



Computational and experimental analysis of the effects  
of manufacturing tolerances on the performance of a  
regenerative liquid ring pump

**Nilla-Helene Donata Karlsen-Davies**  
MEng (Hons.)

This thesis is submitted in partial fulfilment of the requirements for the  
degree of Doctor of Philosophy

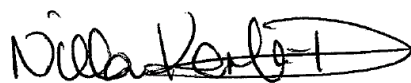
Supervisor:  
Professor George A. Aggidis

Lancaster University  
Faculty of Science & Technology  
Engineering Department  
in collaboration with  
Gilbert Gilkes & Gordon Ltd.

September 2017

## Declaration

The author declares that this thesis has not previously been submitted for award of a higher degree to this or any university, and that the contents, except where otherwise stated, are the author's own work.

Signed: 

Date: 29/09/17

## Abstract

The regenerative liquid ring (RLR) pump is a type of rotodynamic pump which combines the mechanical impulses of the impeller with centrifugal force. The head is increased through recirculation, or regeneration, of the fluid in the impeller blades. The design of the regenerative machine has evolved over many decades and improvements have been made in the design, particularly in the shape and number of impeller blades. However, few publications exist on other design aspects such as the radial and axial clearances between the impeller and the casing, and more crucially most researchers tend to investigate these elements in isolation. This highlights the key driver and novelty of this current research, which applies modern Computational Fluid Dynamics (CFD) tools to systematically assess the effects on pump performance over a large range of impeller-casing clearance parameters and understand their operational behaviour. The sizes of the clearances are dictated by the manufacturer's drawing tolerances on critical pump components.

The results of the parametric clearance analysis showed that there could be a potential variation in head performance by as much as 25%. Furthermore, it highlighted the need to experimentally test a number of pumps within a representative tolerance range. Three test pumps were therefore manufactured and tested. A discrepancy between the CFD and experimental results was observed but the experimental results confirmed that variations in clearances have an impact on the performance, particularly on the developed head. This was more noticeable at higher operational speeds where the pressure differential varied by as much as 19%.

A one-way Fluid-Structure Interaction analysis of the three test impellers was carried out to shed some light on the operational behaviour of the pumps and the effects on the clearances due to non-uniform loading by importing pressure profiles from the corresponding CFD simulations. Assessing the deformation against the computational and experimental pressure, the results indicate that the maximum allowable radial design clearance should be reduced by 35%. Furthermore, with this radial design tolerance the magnitudes of the drive end and non-drive end clearances have a lower impact on the performance. The RLR pump is unique and requires further comparison studies between experimental testing and computational analysis.

## **Keywords**

Regenerative Liquid Ring Pumps, Self-priming Pumps, Computational Fluid Dynamics, Manufacturing Tolerance, Impeller Clearance, Pressure Pulsation, Experimental Testing, Finite Element Analysis, One-way Fluid Structure Interaction.



## **Dedication**

I would like to dedicate this research to my husband and best friend, *James*, whose continued and unfailing love, support and understanding in my pursuits of a Ph.D. degree have provided me with the strength and perseverance I needed to achieve my goals. I am truly grateful for having you in my life.

This work is also dedicated to my Mother, *Mamma*, my inspiration and greatest admirer, who has always loved me unconditionally, supported me in all my pursuits, never doubted my abilities and whose examples have taught me to work hard for the things that I aspire to achieve. I would not be where I am today without you.

## Acknowledgments

Firstly, I would like to thank my supervisor Professor George Aggidis for encouraging me to study a Ph.D., showing continued enthusiasm in this research and for providing support and guidance throughout the course of this project. I would also like to express my sincere gratitude to Dr Stephen Quayle for providing constructive comments and instrumental feedback on this thesis.

My thanks go to Gilbert Gilkes & Gordon Ltd. for sponsoring this research and carrying out the experimental testing. I would specifically like to thank Dr Jo Scott, Anthony Watson and Sam Walker for sharing their experience, providing support and giving insight into this research. I would also like to thank Alan Robinson and Jonathan Martin for contributing to the discussion, and Alan Davies for offering his time and thoughts. Many thanks go out to other Gilkes employees who were involved in this research.

I would like to thank my fellow Ph.D. students from the Hydro and Pump section of the Lancaster University Renewable Energy & Fluid Machinery Group, Dr Audrius Zidonis, Dr Shaun Benzon and Sean Petley, for stimulating discussions, entertaining conversations on CFD and for all the fun we have shared. Many thanks also go to Dr Scott Nash, the last member of our original office, for his support and invaluable inputs on the unwritten rules of Ph.D. research. The working environment created by all of you was second to none.

I was also fortunate to collaborate with Georgios Mousmoulis and Professor Ioannis Anagnostopoulos from the National Technical University of Athens on cavitation detection in centrifugal pumps. Thank you for expanding my horizon within the world of pumps and experimental testing, and for all the interesting and rewarding discussions we have shared.

My thanks go to the reviewers of the academic papers published during this research whose constructive comments helped shape and improve the quality of this work.

Last but not least, I would like to thank my family and friends for their unwavering love, support, guidance and inspiring words throughout what has been a challenging but interesting journey. Besides my husband and Mother, I would particularly like to extend my heartfelt gratitude to Matias and Ernst, my parents-in-law Gill and Peter and my stepfather Torkel. Your love and encouragement mean the world to me.

## List of Journal Publications

1. Mousmoulis, G., Karlsen-Davies, N., Aggidis, G., Anagnostopoulos, J. and Papantonis, D., 2017. Experimental analysis of cavitation in a centrifugal pump using acoustic emission, vibration measurements and flow visualization. *Submitted to Intl. Journal of Applied Acoustics, Under Review.*
2. Karlsen-Davies, N.D. and Aggidis, G.A., 2016. Regenerative liquid ring pumps review and advances on design and performance. *Applied Energy*, 164, pp.815-825.

## List of Conference Publications

1. Mousmoulis, G., Karlsen-Davies, N., Aggidis, G., Anagnostopoulos, A. and Papantois, D., 2017. Experimental analysis of the onset and development of cavitation in a centrifugal pump. In: *Proceedings of the 7th IAHR Meeting of the Working Group on Cavitation and Dynamic Problems in Hydraulic Machinery and Systems (IAHRWG'17)*. 1-3 February 2017, Porto, Portugal.
2. Karlsen-Davies, N. and Aggidis, G., 2016. Computational analysis of the effects of manufacturing tolerances on the performance of a regenerative liquid ring pump. In: *13th European Fluid Machinery Congress*. 3-4 October 2016, The Hague, the Netherlands.
3. Karlsen-Davies, N., 2016. Life Cycle Assessment of a Regenerative Liquid Ring (RLR) pump using CFD coupled with HPC, *High Performance Computing-Based Computational Fluid Dynamics for Offshore Renewable Energy Workshop*. 7-8 April 2016, Lancaster University, Lancaster, UK.
4. Karlsen-Davies, N., 2016. Regenerative Liquid Ring (RLR) Pump Research, *Cavitation Research Seminar*. 22 January 2016, International Institute for Cavitation Research, City University London, London, UK.
5. Karlsen-Davies, N., 2015. Life Cycle Assessment of a Regenerative Liquid Ring (RLR) Pump. *Lancaster University Faculty of Science & Technology Christmas Conference*. 15 December 2015, Lancaster, UK.
6. Karlsen, N. and Aggidis, G., 2014. Review and state of the art of regenerative liquid ring pumps. In: *12th European Fluid Machinery Congress*. 6-7 October 2014, Edinburgh, UK.

## **Academic Achievements**

1. Selected to represent the Engineering Department at the Lancaster University Faculty of Science & Technology Christmas Conference 15 December 2015.
2. Engineering Department nominee for the Lancaster University Faculty of Science & Technology Dean's Award for Excellence in PhD Studies in 1<sup>st</sup> (2014), 2<sup>nd</sup> (2015) and 3<sup>rd</sup> (2016) year.
3. Institution of Mechanical Engineers Best Student Award Certificate November 2013.
4. Institution of Mechanical Engineers Best Project Award Certificate November 2012.

# Table of Contents

Declaration.....	ii
Abstract.....	iii
Keywords.....	iv
Dedication.....	v
Acknowledgments.....	vi
List of Journal Publications.....	vii
List of Conference Publications.....	vii
Academic Achievements.....	viii
Table of Contents.....	ix
List of Figures.....	xiv
List of Tables.....	xxii
Nomenclature.....	xxiv
Mathematical Notation.....	xxvi
List of Acronyms.....	xxvii
1 Introduction.....	1
1.1 The Regenerative Liquid Ring Pump.....	1
1.2 Applications.....	4
1.3 Gilkes 2.5" SX RLR Design.....	5
1.4 Computational Fluid Dynamics.....	8
1.5 Thesis Structure.....	13
2 Background.....	15
2.1 History.....	15
2.2 Operational Advantages.....	22

2.2.1	Low Specific Speed.....	23
2.2.2	Self-priming.....	25
2.2.3	Stable Operating Conditions .....	25
2.2.4	Low Cost.....	25
2.3	Performance Challenges and Losses.....	26
2.3.1	Slip Losses .....	26
2.3.2	Shock Losses.....	27
2.3.3	Circulation Losses.....	27
2.3.4	Peripheral Friction Losses .....	28
2.3.5	Inlet and Outlet Losses.....	28
2.3.6	Leakage Losses .....	28
2.3.7	Operational Wear.....	29
2.3.8	Pressure Pulsation Phenomenon.....	29
2.4	Historical Geometry and Design Optimisation .....	30
2.4.1	Blade Configurations.....	31
2.4.2	Number of Blades .....	34
2.4.3	Impeller Diameter .....	34
2.4.4	Axial and Radial Clearance .....	35
2.4.5	Side Channel.....	35
2.4.6	Stripper.....	37
2.4.7	Suction and Discharge Ports .....	38
2.5	Conclusions and Scope for Further Research .....	41
3	Research Aims and Contribution to Knowledge .....	43
3.1	Research Aims.....	43

3.2	Research Methodology .....	43
3.3	Contribution to Knowledge and Practice .....	43
4	Computational Modelling Methodology .....	45
4.1	Modelling Software.....	45
4.2	CFD Model Assumptions .....	45
4.2.1	Geometric Assumptions.....	46
4.2.2	Modelling Assumptions.....	49
4.3	Simulation Setup and Analysis .....	53
4.3.1	Computational Domain Geometry.....	53
4.3.2	Operating Conditions .....	55
4.3.3	Mesh.....	56
4.3.4	Physics Definition .....	60
4.3.5	Solver Definition.....	68
4.3.6	Analysis of the Results .....	69
4.4	Periodicity .....	74
4.5	Mesh Independence Study .....	76
4.6	Summary of Computational Modelling Methodology .....	80
5	Parametric Clearance Analysis .....	81
5.1	Manufacturing Tolerance Parameters .....	81
5.2	Geometry Preparation .....	84
5.3	Mesh Generation .....	88
5.4	Results and Discussion .....	89
5.5	Summary and Conclusions .....	99
6	Experimental Performance Testing.....	101

6.1	Pump Manufacturing and Part Measurement.....	101
6.2	Pump Test Rig.....	102
6.3	Sensors and Instrumentation.....	105
6.4	Testing Procedure .....	106
6.5	Characteristic Equations .....	109
6.6	Translation of the Test Results to the Specified Speed .....	109
6.7	Estimation of the Uncertainty.....	110
6.7.1	Systematic Uncertainty .....	110
6.7.2	Random Uncertainty.....	111
6.7.3	Overall Uncertainty.....	112
6.8	Test Results .....	114
6.9	Results Comparison and Discussion.....	118
7	Computational Performance Modelling .....	121
7.1	Geometry Preparation .....	121
7.2	Performance Characteristics.....	126
7.3	Performance Effects due to Axial and Radial Clearance Pressure .....	139
7.4	Effects of Impeller Width and Diameter on Performance .....	143
7.5	Summary of Computational Performance Modelling.....	145
8	Comparison of Computational and Experimental Results.....	146
8.1	Performance Curves.....	146
8.2	Discussion of Uncertainties and Errors .....	152
8.2.1	Mechanical Losses.....	152
8.2.2	Critical Review of the Experimental Testing .....	154
8.2.3	Uncertainties due to Manufacturing Tolerances .....	158



8.2.4	Uncertainties due to Surface Roughness .....	160
8.2.5	Limitations of the CFD Model .....	163
8.3	Summary of Computational and Experimental Comparison .....	166
9	Finite Element Analysis (FEA).....	167
9.1	Simulation Setup and Analysis .....	169
9.2	Mesh Refinement Study.....	174
9.3	Results and Discussion .....	176
9.3.1	Impeller Deformation and Stress Analysis .....	176
9.3.2	Comparison of Impeller Deformation and Manufacturing Tolerances.....	185
9.3.3	Comparison of Numerical Predictions and Experimental Measurements.....	187
9.4	Summary and Conclusions .....	189
10	Conclusions and Recommendations .....	191
10.1	Conclusions .....	191
10.2	Recommendations for Future Work .....	193
10.2.1	Advanced Numerical Modelling .....	194
10.2.2	Experimental Investigation of Pressure Pulsation Phenomenon.....	194
10.2.3	Two-way Fluid-Structure Interaction .....	195
10.2.4	Further Experimental Testing of Clearances.....	195
10.2.5	Priming Behaviour.....	196
10.2.6	Cavitation Erosion .....	196
10.2.7	Manufacturing Methods .....	197
10.2.8	Reliability.....	197
	References .....	199

## List of Figures

Figure 1-1: Schematic of a typical regenerative pump (Cooper, 2001). .....	2
Figure 1-2: Location of the tip and side channels in a typical regenerative pump (Cooper, 2001). .....	3
Figure 1-3: Channel cross-section showing flow circulation (MTH Pumps, 2014).....	3
Figure 1-4: Casing cross-section showing helical flow pattern (MTH Pumps, 2014). .....	3
Figure 1-5: Gilkes 2.5" SX pump CAD full assembly. ....	6
Figure 1-6: Gilkes 2.5" SX pump impeller with asymmetrical chevron shaped blades. The blade spacing angle between adjacent blades (half and full blades) is $18^\circ$ ; spacing between identical blades is $36^\circ$ . ....	6
Figure 1-7: Gilkes 2.5" SX pump side channel on (a) the non-drive end side and (b) the drive end side. ....	7
Figure 2-1: Diagram of Addison's liquid ring pump with an eccentrically mounted shaft (Crewdson, 1956). ....	15
Figure 2-2: Flow visualisation study using Perspex glass (Aggidis, 2002). ....	19
Figure 2-3: Performance curves for a typical regenerative pump (Roth Pump Company, 2015). .....	23
Figure 2-4: Specific speed classification for different types of pumps (Krutzsich & Cooper, 1986), where $\psi$ is the head coefficient given by equation (2-2). ....	24
Figure 2-5: Example of pressure pulsation phenomenon in a regenerative pump (Zhang, et al., 2016) for blade angles of $10^\circ$ , $20^\circ$ and $30^\circ$ . Circumferential angle between two adjacent blades is $15^\circ$ . ....	30
Figure 2-6: Regenerative pump impeller (a) single-sided (Moss & Czarnowski, 1996), (b) double-sided (Lytron, 2015). ....	31
Figure 2-7: (a) Straight radial blades, (b) symmetrical chevron blades, (c) meridional geometry of semi-circular blades, (d) meridional section of aerofoil blades (Kidger, et al., 1995; Kusagaya, et al., 2004). ....	33
Figure 2-8: Regenerative pump with (a) circular and (b) rounded side channel shape (Gülich, 2010). ....	36

Figure 2-9: Side channel with soldered in brass strip to reduce helical water circulation (Crewdson, 1956).....	37
Figure 2-10: Schematic of a generic regenerative pump showing the stripper region in relation to the pump suction and discharge (Gülich, 2010).....	38
Figure 2-11: Regenerative pump with axially aligned suction and discharge ports (Quail, et al., 2012). .....	38
Figure 4-1: Port plate on NDE before (left) and after (right) simplification. ....	46
Figure 4-2: Rotating fluid domain with (left) and without (right) additional axial clearance paths. ....	47
Figure 4-3: Modified side channel ring on DE side. ....	48
Figure 4-4: Computational fluid domain with extended outlet (left) and inlet (right) pipes. .	48
Figure 4-5: Pressure pulsations using different turbulence models.....	51
Figure 4-6: Computational fluid model geometry showing (a) main fluid bodies and (b) further decomposition of clearances. ....	54
Figure 4-7: Decomposition of (a) axial clearance and (b) radial clearance flow paths.....	55
Figure 4-8: Mesh arrangement of (a) the total pump fluid region and (b) the impeller fluid region. ....	57
Figure 4-9: Mesh arrangement of (a) DE side channel/inlet pipe and (b) cross-sectional view of side channel showing mesh density regions and inflation layers.....	57
Figure 4-10: Mesh arrangement of (a) one impeller blade fluid region and (b) cross-sectional view of impeller blade pocket showing mesh density regions and inflation layers. ....	58
Figure 4-11: Computational domain in CFX-Pre. ....	61
Figure 4-12: Pressure pulsation trend for four different timesteps. ....	68
Figure 4-13: Location of rotating domain pressure monitoring points. ....	70
Figure 4-14: Position of impeller blade edges relative to the stripper edge on the discharge and the suction side causing the primary pressure peak and the secondary pressure peak.....	72
Figure 4-15: Pressure pulsations over second revolution of the impeller showing the blade passing frequency. Blade spacing between (1) adjacent blades (half and full length blades) and (2) identical blades.....	73

Figure 4-16: Pressure pulsation trend over six revolutions of the impeller. ....	75
Figure 4-17: Results of the mesh independence study, normalised pressure against normalised grid spacing. ....	76
Figure 4-18: Pressure pulsations for the mesh refinement study. ....	79
Figure 5-1: Axial manufacturing tolerance parameters for (a) NDE, (b) impeller and (c) DE. .	82
Figure 5-2: Radial manufacturing tolerance parameters for (a) NDE, (b) impeller and (c) DE.	82
Figure 5-3: Assembly tolerance parameter. The impeller is axially aligned in relation to the DE side of the casing. ....	83
Figure 5-4: Geometry preparation of the axial clearances showing (a) isometric view and (b) cross-sectional view of the axial clearance disk. ....	85
Figure 5-5: Geometry preparation of the radial clearance showing (a) isometric view and (b) cross-sectional view of the radial clearance ring. ....	85
Figure 5-6: Relative positions of the axial clearance disk and the radial clearance ring; in the assembly the axial clearance disks are fitted inside the radial clearance ring. ....	86
Figure 5-7: Clearance geometry parameters; illustrating thin features (highlighted in green) used to create the radial clearance bodies mapped to the impeller fluid. ....	86
Figure 5-8: Clearance geometry parameters; illustrating thin features (highlighted in green) used to create the radial clearance bodies mapped to the axial clearance. ....	87
Figure 5-9: Pressure pulsations for 9 parametric clearance models over 90° revolution of the impeller. ....	92
Figure 5-10: Pressure pulsations for parametric clearance models over four blade passages, arranged into minimum (left), median (middle) and maximum (right) axial clearance groups. ....	93
Figure 5-11: Pressure distribution in the impeller for (a) DE15-NDE47-R176, (b) DE15-NDE47-R278 and (c) DE15-NDE47-R383. ....	94
Figure 5-12: Pressure distribution in the impeller for (a) DE26-NDE36-R278, (b) DE26-NDE51-R278 and (c) DE26-NDE66-R278. ....	95
Figure 5-13: Pressure distribution in the impeller for (a) DE15-NDE77-R176, (b) DE26-NDE66-R176 and (c) DE37-NDE55-R176. ....	96
Figure 5-14: Results of parametric clearance study showing the pump pressure and efficiency. ....	97

Figure 5-15: Results of parametric clearance study showing the power consumption. ....	98
Figure 5-16: Results of parametric clearance study showing the percentage deviation from the pressure performance of the median clearance model (DE= 0.26 mm, NDE=0.51 mm and RAD=0.278 mm). ....	100
Figure 6-1: 2.5" SX pumps used for testing.....	102
Figure 6-2: 3D CAD model of new performance test cell (left hand chamber). ....	103
Figure 6-3: Performance test cell, new Gilkes testing facility in Kendal. ....	104
Figure 6-4: Aerial view of the performance test cell (left hand chamber). ....	104
Figure 6-5: Inside view of the performance test cell. ....	105
Figure 6-6: Experimental test readings of flow rate for pump A, B and C at 2300 rpm. ....	107
Figure 6-7: Experimental test readings of flow rate with 180 second sample interval for pump B at 2300 rpm.....	108
Figure 6-8: Time series of the BEP point of pump B corresponding to point 10 in Figure 6-7. ....	108
Figure 6-9: Overall uncertainty for speed ( $n$ ), torque ( $T$ ), flow rate ( $Q$ ), inlet pressure ( $P_{in}$ ), outlet pressure ( $P_{out}$ ), power ( $N$ ) and efficiency ( $\eta$ ) for pump A at 1200 rpm. ....	112
Figure 6-10: Overall uncertainty for speed ( $n$ ), torque ( $T$ ), flow rate ( $Q$ ), inlet pressure ( $P_{in}$ ), outlet pressure ( $P_{out}$ ), power ( $N$ ) and efficiency ( $\eta$ ) for pump B at 1600 rpm. ....	113
Figure 6-11: Overall uncertainty for speed ( $n$ ), torque ( $T$ ), flow rate ( $Q$ ), inlet pressure ( $P_{in}$ ), outlet pressure ( $P_{out}$ ), power ( $N$ ) and efficiency ( $\eta$ ) for pump C at 2300 rpm. ....	114
Figure 6-12: Experimental pressure head curves for pump A, B and C at 1200, 1600 and 2300 rpm.....	115
Figure 6-13: Experimental efficiency curves for pump A, B and C at 1200, 1600 and 2300 rpm. ....	116
Figure 6-14: Experimental power curves for pump A, B and C at 1200, 1600 and 2300 rpm. ....	117
Figure 7-1: Modifying the impeller width showing (a) isometric view and (b) cross-sectional view; example dimensions are for pump B.....	122
Figure 7-2: Modifying the impeller diameter by adding material; example dimension is for pump A.....	122

Figure 7-3: Experimental test pump parameters; radial, NDE and DE clearance magnitudes for pump A.....	123
Figure 7-4: Experimental test pump parameters; diameter and width of radial clearance ring for pump A. ....	123
Figure 7-5: Experimental test pump parameters; height from hub to tip of DE clearance for pump A.....	124
Figure 7-6: Full computational representation of experimental pump.....	125
Figure 7-7: Pressure pulsations for pump A, B and C at BEP and 0.7BEP at 2300 rpm. ....	127
Figure 7-8: Pressure pulsations for pump A, B and C at BEP and 0.7BEP at 1600 rpm. ....	128
Figure 7-9: Pressure pulsations for pump A, B and C at BEP and 0.7BEP at 1200 rpm. ....	128
Figure 7-10: Computational pressure head curves for pump A, B and C at 1200, 1600 and 2300 rpm.....	129
Figure 7-11: Computational efficiency curves for pump A, B and C at 1200, 1600 and 2300 rpm. ....	130
Figure 7-12: Computational power curves for pump A, B and C at 1200, 1600 and 2300 rpm. ....	130
Figure 7-13: 2.5" SX pump casing cross-sectional view showing location for analysing the circulation flow between the impeller and the deepest section of the side channel. ....	132
Figure 7-14: Pressure distribution in the impeller for pump A, B and C at maximum pressure point of pulsation at 2300 rpm for BEP (top) and 0.7BEP (bottom). ....	134
Figure 7-15: Circulation flow between impeller and side channel for pump A, B and C at maximum pressure point of pulsation at 2300 rpm for BEP (top) and 0.7BEP (bottom). ....	135
Figure 7-16: Circulation flow between impeller and side channel for pump A, B and C at maximum pressure point of pulsation at 2300 rpm for 0.6BEP (top) and 0.4BEP (bottom). ....	136
Figure 7-17: Flow in the NDE (top) and DE (bottom) clearances for pump A, B and C at maximum pressure point of pulsation at 2300 rpm for BEP. ....	137
Figure 7-18: Comparison of pressure pulsation trends for pump A, B and C using the input data corresponding to 0.7BEP for pump A at 2300 rpm.....	138
Figure 7-19: Comparison of the transient average of the generated pressure head, power and efficiency for impeller A, B and C using the input data corresponding to 0.7BEP for pump A at 2300 rpm.....	139

Figure 7-20: Comparison of transient average pressure difference across clearances and total pump pressure at 2300 rpm. ....	140
Figure 7-21: Comparison of transient average pressure difference across clearances and total pump pressure at 1600 rpm. ....	141
Figure 7-22: Comparison of transient average pressure difference across clearances and total pump pressure at 1200 rpm. ....	142
Figure 7-23: Comparison of pressure pulsation trends for impeller A, B and C with pump A clearances at 0.7BEP at 2300 rpm. ....	143
Figure 7-24: Comparison of the transient average of the generated pressure head, power and efficiency for impeller A, B and C with pump A clearances at 0.7BEP at 2300 rpm. ....	144
Figure 8-1: Comparison of experimental and computational pressure head curves for pump A, B and C at 2300 rpm.....	147
Figure 8-2: Comparison of experimental and computational efficiency curves for pump A, B and C at 2300 rpm.....	148
Figure 8-3: Comparison of experimental and computational power curves for pump A, B and C at 2300 rpm.....	148
Figure 8-4: Comparison of experimental and computational pressure head curves for pump A, B and C at 1600 rpm.....	149
Figure 8-5: Comparison of experimental and computational efficiency curves for pump A, B and C at 1600 rpm.....	149
Figure 8-6: Comparison of experimental and computational power curves for pump A, B and C at 1600 rpm.....	150
Figure 8-7: Comparison of experimental and computational pressure head curves for pump A, B and C at 1200 rpm.....	150
Figure 8-8: Comparison of experimental and computational efficiency curves for pump A, B and C at 1200 rpm.....	151
Figure 8-9: Comparison of experimental and computational power curves for pump A, B and C at 1200 rpm.....	151
Figure 8-10: Mechanical losses as percentage of power at BEP.....	153
Figure 8-11: Comparison of computed pressure pulsation history and experimental value at 1.1BEP at 2300 rpm.....	156

Figure 8-12: Comparison of computed pressure pulsation history and experimental value at BEP at 2300 rpm.....	156
Figure 8-13: Comparison of computed pressure pulsation history and experimental value at 0.9BEP at 2300 rpm.....	157
Figure 8-14: Comparison of computed pressure pulsation history and experimental value at 0.6BEP at 2300 rpm.....	157
Figure 8-15: Comparison of 3D scanned NDE body and CAD model. ....	159
Figure 8-16: Comparison of 3D scanned DE body and CAD model.....	160
Figure 8-17: Surface roughness study, results normalised against model with no surface roughness (NSR).....	162
Figure 8-18: Volume splitting of a basic impeller element. ....	165
Figure 8-19: Volume splitting of axial clearance elements. ....	165
Figure 8-20: MultiZone mesh of an impeller fluid volume. ....	165
Figure 9-1: Width and diameter of 2.5" SX impeller for pump A. ....	167
Figure 9-2: Cut-out of impeller showing the expected direction of impeller deformation in relation to the location of the clearance geometries. ....	169
Figure 9-3: One-way Fluid-Structure Interaction schematic.....	169
Figure 9-4: Impeller FEA setup showing rotational speed direction (viewed from NDE). ....	170
Figure 9-5: Imported pressure profiles on (a) impeller surface, (b) NDE, (c) DE and (d) impeller periphery.....	171
Figure 9-6: Equivalent stress contours for imported pressure profile combinations for (a) impeller only, (b), impeller, DE & NDE, (c) impeller, DE, NDE & radial and (d) DE, NDE & radial. ....	172
Figure 9-7: Total deformation contours for imported pressure profile combinations (a) impeller only, (b), impeller, DE & NDE, (c) impeller, DE, NDE & radial and (d) DE, NDE & radial. ....	173
Figure 9-8: Impeller mesh showing refinement on blade edges for Mesh 2 (top) and Mesh 4 (bottom).....	174
Figure 9-9: Results of FEA mesh refinement study, von-Mises stress and deformation against mesh size.....	175



Figure 9-10: Comparison of deformation and stress at maximum pressure pulsation against the corresponding average CFD-calculated pressure head at 2300 rpm. ....	177
Figure 9-11: Comparison of deformation and stress at maximum pressure pulsation against the corresponding average CFD-calculated pressure head at 1600 and 1200 rpm. ....	178
Figure 9-12: Relationship between radial deformation and imported radial pressure profile. ....	179
Figure 9-13: Relationship between axial deformation and imported DE and NDE pressure profiles. ....	180
Figure 9-14: Axial deformation in impeller A at BEP at 2300 rpm. ....	181
Figure 9-15: Total impeller deflection at maximum pressure point at 2300 rpm for BEP and 0.7BEP. ....	183
Figure 9-16: Stress concentration on DE of impeller A at 0.7BEP at 2300 rpm. ....	184
Figure 9-17: Stress concentration on NDE of impeller A at 0.7BEP at 2300 rpm. ....	184
Figure 9-18: Impeller width after deformation against minimum and maximum manufacturing tolerances. ....	185
Figure 9-19: Impeller diameter after deflection against minimum and maximum manufacturing tolerances. ....	186
Figure 9-20: Comparison of total operational impeller width against computational and experimental differential pressure. ....	187
Figure 9-21: Comparison of total operational impeller diameter against computational and experimental differential pressure. ....	188

## List of Tables

Table 2-1: Comparison of methods used to analyse the regenerative operating principle (references refer to focused work within each mode of analysis). .....	20
Table 2-2: Summary of performance challenges and geometrical design optimisation. ....	40
Table 4-1: Initial clearance dimensions.....	49
Table 4-2: Normalised pressure for different turbulence models.....	51
Table 4-3: 2.5" S pump duty point operating conditions used in computational modelling...	55
Table 4-4: Number of elements across each clearance .....	59
Table 4-5: Named selections used on stationary and rotating domain boundaries.....	60
Table 4-6: Simulation boundary conditions .....	64
Table 4-7: Simulation initial conditions.....	65
Table 4-8: Normalised pressure for varied timesteps. ....	67
Table 4-9: Normalised pressure for the periodicity study. ....	75
Table 4-10: Results of the mesh independence study, normalised to the coarsest mesh. ....	76
Table 4-11: Grid Convergence Indexes. ....	78
Table 4-12: Solve times for the mesh independence study.....	79
Table 4-13: Relative numerical uncertainties introduced by various assumptions.....	80
Table 5-1: Manufacturing tolerance parameters (all dimensions given in millimetres). ....	84
Table 5-2: Clearance geometry parameters. ....	87
Table 5-3: Number of elements across each clearance.....	88
Table 6-1: Manufacturing tolerances for the three test pumps.....	102
Table 6-2: Details of the sensors used for the generation of the pump performance curves. ....	106
Table 6-3: The systematic error of each sensor.....	110

Table 6-4: Experimental values at best efficiency point for pump A, B and C at 1200, 1600 and 2300 rpm.....	119
Table 7-1: Experimental test pump parameters.....	124
Table 7-2: Operating points used for the computational performance analysis.....	126
Table 7-3: Calculated values at 0.7BEP for pump A, B and C at 1200, 1600 and 2300 rpm. .	131
Table 7-4: Performance values for the three design combinations, normalised to pump A performance. ....	139
Table 7-5: Performance values for the three impeller sizes, normalised to pump A performance. ....	144
Table 8-1: Roughness values based on manufacturing process. ....	161
Table 8-2: Roughness values based on surface material. ....	161
Table 9-1: Impeller dimensions for pump A, B and C. ....	168
Table 9-2: 2.5" SX impeller material characteristics.....	168
Table 9-3: Results and solve time for imported pressure profile combinations. ....	172
Table 9-4: Results of the FEA mesh refinement study, normalised to the coarsest mesh. ...	175

## Nomenclature

$a$	Acceleration	[m s <sup>-2</sup> ]
$(e_Y)_r$	Random Uncertainty at 95% Confidence (Student's T Distribution)	[-]
$E$	Young's Modulus	[N mm <sup>-2</sup> ]
$f_H$	Systematic Uncertainty for Pressure Transducer	[%]
$f_n$	Systematic Uncertainty for Tachometer	[%]
$f_Q$	Systematic Uncertainty for Flowmeter	[%]
$f_r$	Random Uncertainty	[%]
$f_S$	Total Systematic Uncertainty for Efficiency	[%]
$f_t$	Overall Uncertainty	[%]
$f_T$	Systematic Uncertainty for Torque Transducer	[%]
$(f_Y)_{r95}$	Random Uncertainty at 95% Confidence (Student's T Distribution)	[%]
$F$	Force	[N]
$F_S$	Safety Factor	[-]
$g$	Acceleration due to Gravity	[m s <sup>-2</sup> ]
$\vec{g}$	Gravity Vector	[N m <sup>2</sup> kg <sup>-2</sup> ]
$H$	Hydraulic Head	[m]
$k$	Turbulence Kinetic Energy	[m <sup>2</sup> s <sup>-2</sup> ]
$m$	Mass	[kg]
$n$	Number of Readings	[-]
$n_{Ref}$	Reference Speed for Calculating Mechanical Losses	[rpm]
$n_{sp}$	Specific Speed of Rotation	[rpm]
$p$	Pressure	[Pa]
$p_c$	Order of Convergence	[-]
$p_{in}$	Suction Pressure	[Pa]
$p_{out}$	Discharge Pressure	[Pa]
$\Delta p_T$	Speed Translated Differential Pressure	[Pa]
$p_u$	Momentum	[kg ms <sup>-1</sup> ]
$P$	Power Input	[W]
$P_e$	Bearing Losses	[W]

$P_h$	Hydraulic Power	[W]
$P_m$	Mechanical Losses	[W]
$P_m$	Mechanical Power	[W]
$P_s$	Rotating Disk Losses	[W]
$P_T$	Speed Translated Power Input	[W]
$Q$	Flow Rate	[m <sup>3</sup> h <sup>-1</sup> ]
$Q_{Ref}$	Reference Flow Rate for Calculating Mechanical Losses	[m <sup>3</sup> s <sup>-1</sup> ]
$Q_T$	Speed Translated Flow Rate	[m <sup>3</sup> h <sup>-1</sup> ]
$r$	Radius of Impeller	[m]
$r$	Refinement Ratio	[-]
$R_A$	Average Surface Roughness (in relation to Manufacturing Process)	[μm]
$S$	Surface	[m <sup>-2</sup> ]
$S_y$	Standard Deviation	[-]
$t$	Time	[s]
$t$	Student's T factor	[-]
$T$	Torque	[N m]
$u$	Magnitude of Velocity	[m s <sup>-1</sup> ]
$V$	Volume	[m <sup>3</sup> ]
$\vec{V}$	Velocity Vector	[m s <sup>-1</sup> ]
$\bar{Y}$	Arithmetic Mean of Time Series	[-]
$Y_i$	Time Series	[-]
$\delta_{total}$	Total Deformation	[mm]
$\delta_x$	Deformation in x-direction	[mm]
$\delta_y$	Deformation in y-direction	[mm]
$\delta_z$	Deformation in z-direction	[mm]
$\varepsilon$	Equivalent Sand-grain Roughness	[μm]
$\varepsilon$	Strain	[-]
$\varepsilon$	Turbulence Eddy Dissipation Rate	[m <sup>2</sup> s <sup>-3</sup> ]
$\eta$	Efficiency	[%]
$\mu$	Dynamic Viscosity	[Pa s]
$\nu$	Kinematic Viscosity	[m <sup>2</sup> s <sup>-1</sup> ]

$\rho$	Density	[kg m <sup>-3</sup> ]
$\sigma$	Stress	[N mm <sup>-2</sup> ]
$\psi$	Head Coefficient	[-]
$\omega$	Rotational Frequency	[rad s <sup>-1</sup> ]
$\omega$	Turbulence Eddy Frequency	[s <sup>-1</sup> ]
$\Omega$	Angular Speed	[rad s <sup>-1</sup> ]
$\Omega_s$	Pump Specific Speed	[-]

## Mathematical Notation

$\nabla$	Del Operator
----------	--------------

## List of Acronyms

BEP	Best Efficiency Point
BPF	Blade Passing Frequency
BPP	Blade Passing Period
CAD	Computer Aided Design
CC	Curvature Correction
CEL	CFX Expression Language
CFD	Computational Fluid Dynamics
DAQ	Data Acquisition
DE	Drive End
DES	Detached Eddy Simulation
DM	DesignModeler
DNS	Direct Numerical Simulation
FEA	Finite Element Analysis
FSI	Fluid-Structure Interaction
GCI	Grid Convergence Index
HEC	High End Computing
LES	Large Eddy Simulation
MPI	Message Passing Interface
NDE	Non-Drive End
NPSH	Net Suction Performance Head
R	Radial (Clearance)
RAM	Random Access Memory
RANS	Reynolds-Averaged Navier-Stokes
RLR	Regenerative Liquid Ring
RPM	Revolutions Per Minute
SRS	Scale Resolving Simulation
SST	Shear Stress Transport
SW	SolidWorks
URANS	Unsteady Reynolds-Averaged Navier-Stokes

# 1 Introduction

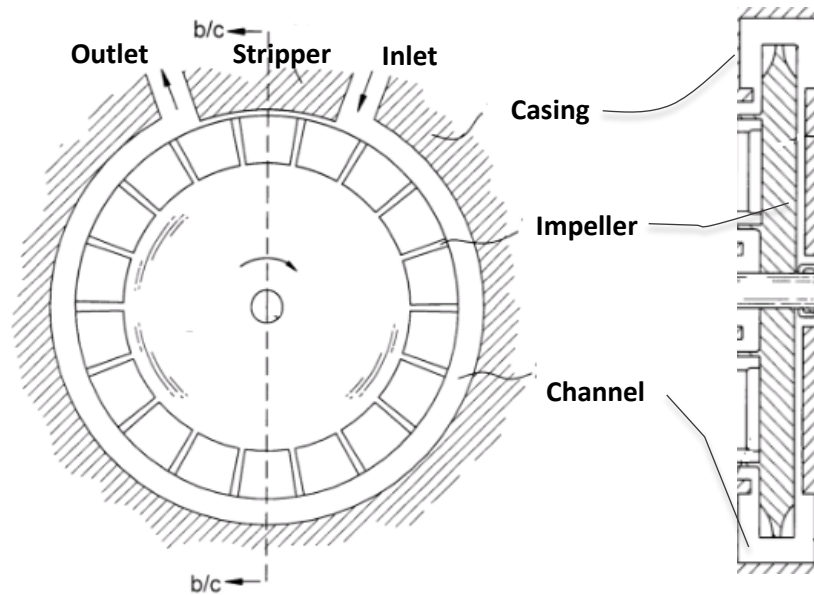
## 1.1 The Regenerative Liquid Ring Pump

The RLR pump is a type of rotodynamic pump which combines mechanical impulses of the impeller with centrifugal force. The increase in head is achieved through a momentum exchange between the impeller and the pumped fluid (Mueller, 2004). However, in contrast to the centrifugal pump, the pressure rise occurs in the peripheral rather than in the radial direction (Lazarkiewicz & Trokolanski, 1965; Quail, et al., 2012). Perhaps what really distinguishes the RLR pump is its ability to develop high heads at relatively low flow rates in only one impeller stage (Yoo, et al., 2005; Quail, et al., 2011a). Compared to a centrifugal pump, it can in many applications offer a more attractive alternative (Mueller, 2004) as discussed in *1.2 Applications*. It also shares similar operating characteristics to another pump classification, positive displacement: the power is directly proportional to head, with a maximum power required at shutoff and a very steep, nearly straight head-capacity curve (Biheller, 1976; Mulley, 2004; Quail, et al., 2010a; Quail, et al., 2011b).

Despite the many advantages over other turbomachines with similar tip speed, one of the main challenges of RLR pumps is to understand and improve the efficiency. The RLR pump requires tight clearances around the impeller to ensure optimum head and efficiency performance. Although these clearances can be affected by operational wear of internal components over time, the initial dimensions are determined by the manufacturing tolerances. Therefore, in order to evaluate the operational performance and subsequently the reliability of the RLR pump, it becomes important to understand how a newly built pump performs in relation to these clearances. In addition, the degradation effects due to erosion, cavitation and natural wear life must be fully understood, as it is closely linked to pump efficiency. The rate of wear will tend to be greater during operation away from best-efficiency conditions. For example, larger clean water pumps can on average drop 5% in efficiency in the first five years of operation, partly due to wear (European Commission, 2001). It therefore becomes important not only to improve the hydraulic design of the RLR pump but also to assess efficiency-degrading parameters during its whole lifecycle.

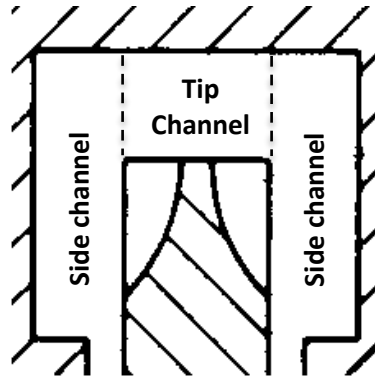


RLR pumps are also sometimes referred to as peripheral, side channel, water-ring, liquid-ring, drag, turbine, traction, tangential, vortex and claw-type pump in literature, often reflecting a variation in geometrical design or preference for a theory of the principle of operation (Burton, 1966; Quail, et al., 2010b; Quail, et al., 2011b).



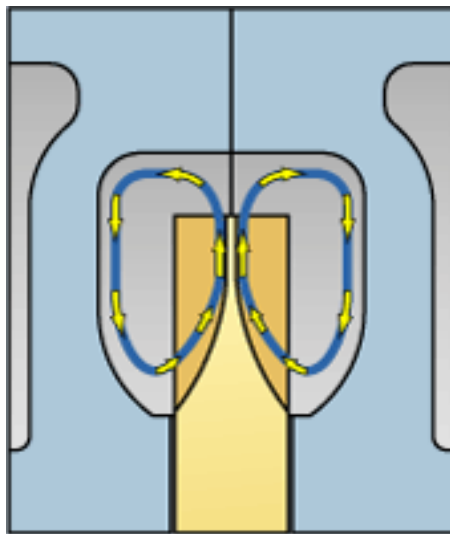
**Figure 1-1: Schematic of a typical regenerative pump (Cooper, 2001).**

Figure 1-1 shows a schematic of a generic RLR pump. It consists of a radially split casing with an annular channel and an impeller (Biheller, 1976) with several, generally 20-50 (Quail, et al., 2011a), radial blades around its perimeter. The annular channel is sometimes separated into the side channel, which are the channels at either side of the impeller, and the tip channel, which is the channel spanning all the way around the periphery of the impeller (Figure 1-2). Gulich (2010) defines the main difference between side channel and peripheral pumps to be the annular channel which in peripheral pumps is placed not only laterally next to the impeller but also around its outer diameter as shown in Figure 1-2.



**Figure 1-2: Location of the tip and side channels in a typical regenerative pump (Cooper, 2001).**

The inlet (suction) and outlet (discharge) ports are separated by a ‘stripper region’ with close clearance to the impeller, which prevents the fluid from flowing back from the outlet to the inlet, so only the fluid between the blades is allowed to pass through. The clearances between the impeller disk and the casing are kept to a minimum to reduce leakage from the high-pressure side back to the low-pressure side (Burton, 1966; Raheel & Engeda, 2002; Raheel & Engeda, 2005).



**Figure 1-3: Channel cross-section showing flow circulation (MTH Pumps, 2014).**

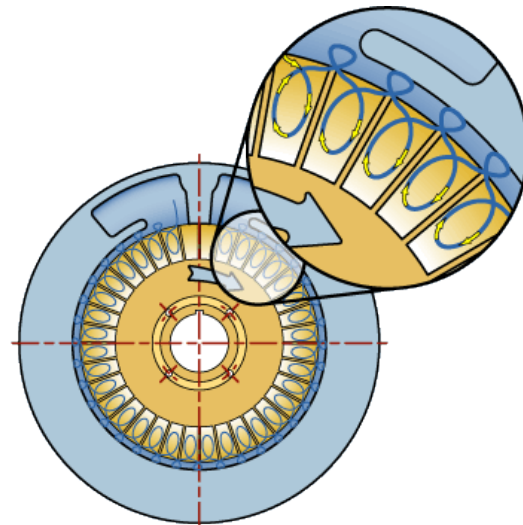


**Figure 1-4: Casing cross-section showing helical flow pattern (MTH Pumps, 2014).**

The increase in head is achieved through an exchange of momentum between the impeller and the fluid. The fluid circulates through the blades as shown in Figure 1-3 due to centrifugal force. The fluid that enters into the lower blade space from the side channel in the direction parallel to the machine axis receives angular momentum by the rotating blades before it is

radially discharged at the blade tip. The blade pocket fluid then transfers the angular momentum to the peripheral flow in the annular open channel, which is driven by shear force due to the rotating blades. The fluid that transfers all the momentum enters into the following blade space, again in an axial direction near the blade hub. This energy exchange process repeats itself from the inlet to the outlet ports, thus the static pressure continues to increase. Thus, the fluid follows a helical path throughout the flow channel (Figure 1-4). It is this repetitive motion of the fluid (regeneration) that allows these pumps to generate high heads at relatively low specific speeds in a single impeller stage.

## **1.2 Applications**

The primary method of use for the regenerative machine has been in the areas of liquid pumping (Crewdson, 1956; Burton, 1966) and mainly for the delivery of water (Senoo, 1948), however considerable modifications have occurred and applications have diversified. Today the RLR pump fulfils a whole range of duties (Burton, 1966) and the regenerative operating principle is also applied in the forms of compressors and turbines.

Regenerative machines are particularly useful for low-viscosity, clean liquid applications (Biheller, 1976; Hollenberg & Potter, 1979) that require low flow rates and relatively high heads. Their inherent ability to provide multi-staging using only one impeller provides much higher heads compared to machines of similar tip speeds (Raheel & Engeda, 2002; Quail, et al., 2010b). The head rise can be increased even further by incorporating several pumping stages on a shared shaft (Quail, et al., 2010a).

The efficiency compares favourably with that of a centrifugal pump of very low specific speed but much less favourably for a large pump of high specific speed. They are an attractive option due to ease of manufacture, relatively low cost, compact design, stable operating conditions, excellent suction characteristics, high temperature capability without internal binding, reliability and excellent priming behaviour (Badami, 1997; Raheel & Engeda, 2005), which in certain applications are often more important than high efficiencies.

In general, the regenerative turbomachines find uses in the fields of biomedical pumping, condensate return, microturbines, automotive and aerospace fuel pumping, shipping and mining, sump service (clean water), laundry, car washers, breweries, spraying systems, chemical and food process industries, control, regulation of lubrication and filtering, booster

systems, refineries and marine (potable water), refrigeration, cryogenic applications in space vehicles, hydrogen gas pipelines, accessory drives on aircraft and missiles, and other applications as regenerative blowers.

In a low-pressure system a small booster pump, such as the RLR pump, can be used to obtain a high-pressure flow and allow the remainder of the system to operate at a lower pressure and reduced power, resulting in reduced energy consumption (Cone, 1980). RLR pumps are also used for petroleum pumping, viscous fluids, chemicals and caustic fluids, and they are particularly ideal for handling volatile or hot fluids due to the fact that they cannot become vapour locked (Wilson, et al., 1955; Biheller, 1976; Badami, 1997; Raheel & Engeda, 2002; Quail, et al., 2011a; MEPCO, 2014).

### **1.3 Gilkes 2.5" SX RLR Design**

The type of RLR pump analysed in this research is the Gilkes 2.5" SX design chosen and provided by the industrial sponsors *Gilbert Gilkes & Gordon Ltd.* (Figure 1-5 - Figure 1-7). The pump inlet is located at the drive end (DE) and the outlet at the non-drive end (NDE). The design features a chevron shaped impeller, consisting of 20 asymmetrical blades as shown in Figure 1-6. The blade spacing angle between adjacent blades (half and full length blades) is  $18^\circ$ , whilst the spacing between identical blades is  $36^\circ$ . In the case of two full length blades this can be described as a "blade pocket". The side channels on either side of the impeller are shown in Figure 1-7. The channels wrap around  $320^\circ$  and  $310^\circ$  of the circumference of the NDE and DE bodies, respectively. The stripper region is the interrupted section of the circumference of the side channels.

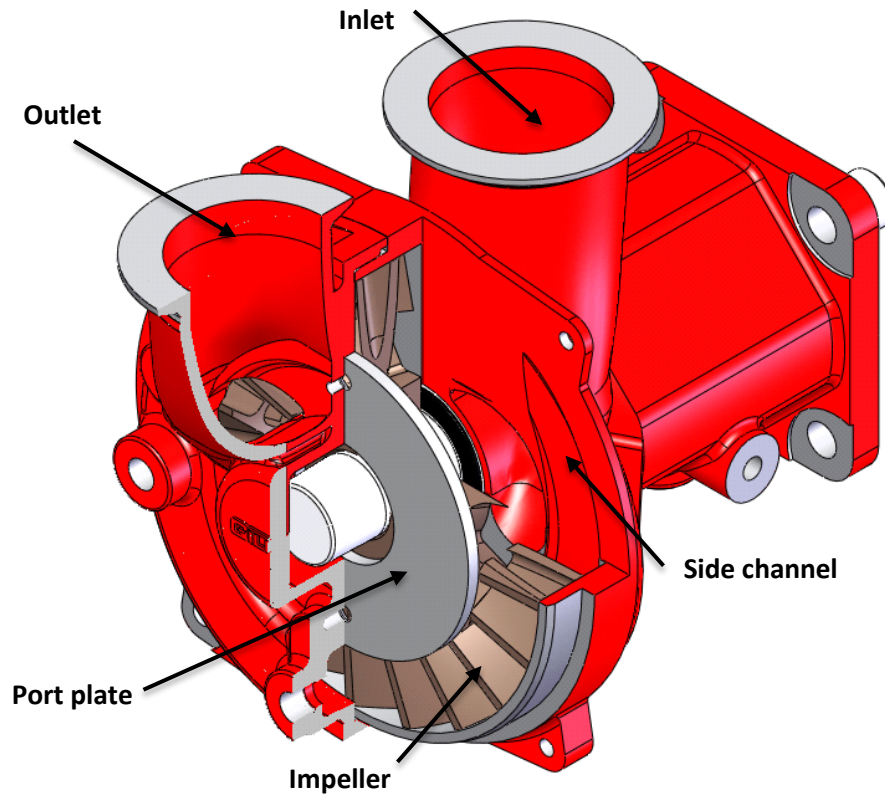


*Figure 1-5: Gilkes 2.5" SX pump CAD full assembly.*

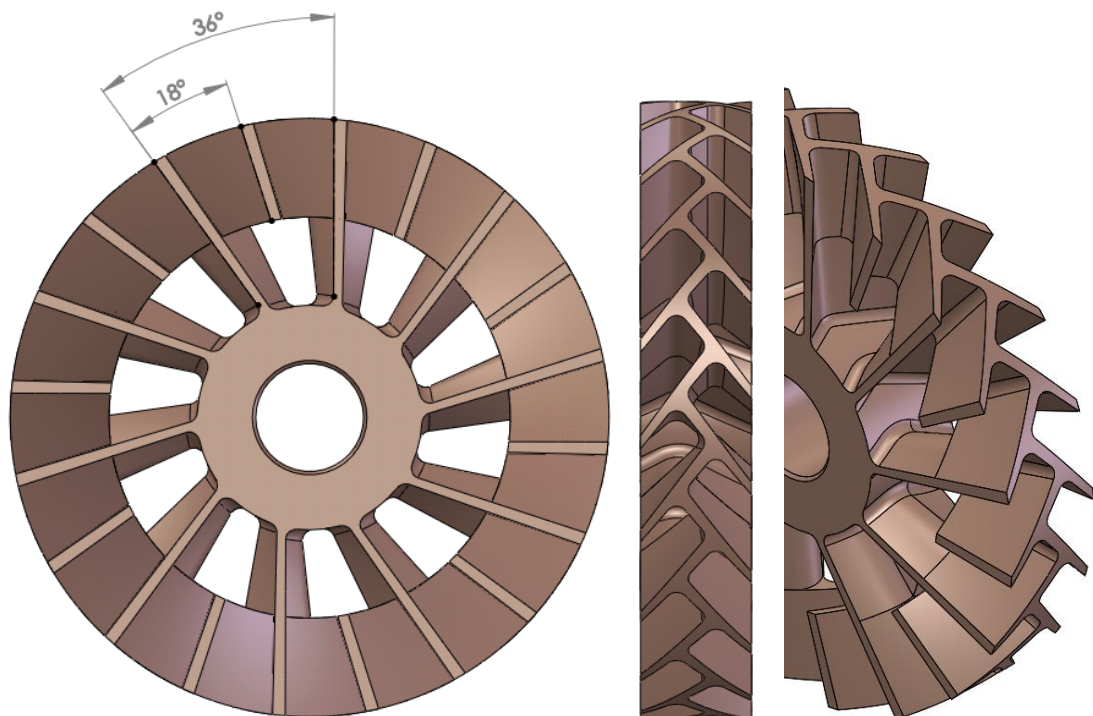


*Figure 1-6: Gilkes 2.5" SX pump impeller with asymmetrical chevron shaped blades. The blade spacing angle between adjacent blades (half and full blades) is 18°; spacing between identical blades is 36°.*

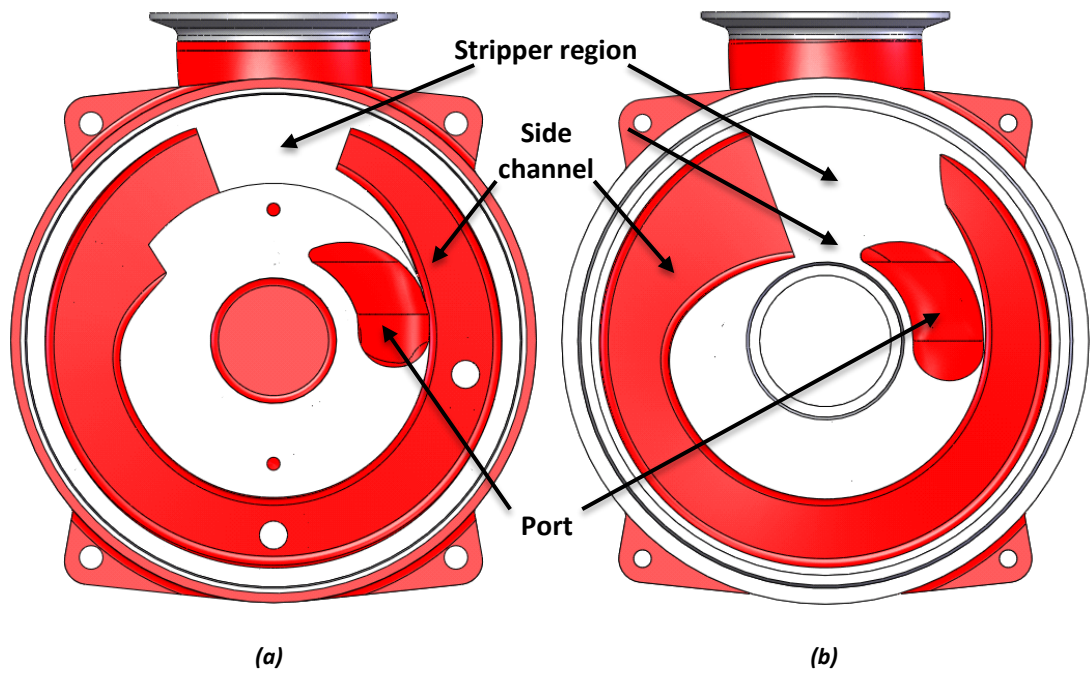


*Figure 1-7: Gilkes 2.5" SX pump side channel on (a) the non-drive end side and (b) the drive end side.*

In a competitive market there has been a renewed focus on improving pump efficiency and extending the lifespan through improved design based on manufacturers' concerns over pump lifetime reliability. The SX pump is one Gilkes' best selling products, however teardown reports show evidence of wear on the impeller. It is not known if the engine cooling water is contaminated or if the damage is due to internal debris passing through the system. RLR pumps such as the SX design require tight clearances around the impeller to ensure optimum head and efficiency performance. Although these clearances can be affected by operational wear of internal components over time, the initial dimensions are determined by the manufacturing tolerances. In order to ensure a consistent pump performance, it becomes important to understand how a newly built pump performs in relation to these clearances and therefore determine improved manufacturing tolerances. This is the motivation for analysing the effects the currently defined manufacturing tolerances have on the pump performance.

## 1.4 Computational Fluid Dynamics

Computational Fluid Dynamics (CFD) is, as the name implies, a very powerful computational tool for predicting fluid flow, heat and mass transfer and chemical reactions. It is part of a larger subject called fluid mechanics where numerical methods are used to solve the governing equations describing the behaviour of viscous, heat conducting flow. The governing equations are based on three fundamental principles of conservation, namely (1) the conservation of mass, (2) the conservation of momentum and (3) the conservation of energy. The derivation of the governing equations can be found in a number of textbooks, such as Versteeg & Malalasekera (2007).

### (1) The Continuity Equation (Conservation of Mass)

The continuity equation relates to the density and velocity of any material particle during motion and can be derived directly by considering a control volume  $dV$ . The mass  $m$  is calculated by a volume integral of the density  $\rho$  and because the total amount of fluid in the control volume is conserved, it may be expressed as equation (1-1).

$$m = \iiint \rho dV \quad (1-1)$$

$$\frac{d}{dt} \iiint \rho dV = 0 \quad (1-2)$$

The mass inside the fixed volume cannot be created or destroyed, hence the rate at which mass is flowing out of the control volume through its surface  $S$  must be equal to the time rate of decrease of mass in inside the control volume:

$$\iint \rho \vec{V} \cdot dS = - \frac{\partial}{\partial t} \iiint \rho dV \quad (1-3)$$

Equation (1-3) is the integral and conservation form of the continuity equation. The control volume is fixed in space thus the limits of the integration are constant, and the time derivative

can be placed inside the integral. Applying the divergence theorem from vector calculus, the surface integral in (1-3) can be expressed as a volume integral:

$$\iint \rho \vec{V} \cdot d\vec{S} = \iiint \nabla \cdot (\rho \vec{V}) dV \quad (1-4)$$

It therefore follows that:

$$\iiint \left[ \frac{\partial \rho}{\partial t} + \nabla \cdot (\rho \vec{V}) \right] dV = 0 \quad (1-5)$$

By taking the partial derivative, equation (1-5) becomes:

$$\frac{\partial \rho}{\partial t} + \nabla \cdot (\rho \vec{V}) = 0 \quad (1-6)$$

Which simplifies to the material derivative in the non-conservation form:

$$\frac{D\rho}{Dt} + \rho \nabla \cdot \vec{V} = 0 \quad (1-7)$$

For an incompressible fluid as in this study, i.e. a liquid, the density remains constant and equation (1-7) therefore becomes:

$$\nabla \cdot \vec{V} = 0 \quad (1-8)$$



## (2) The Momentum Equation (Conservation of Momentum)

The momentum contained at any instant inside the control volume is given by:

$$p_u = \iiint \rho \vec{V} dV \quad (1-9)$$

Newton's Second Law of motion states that the rate of change of momentum of a fluid particle equals the sum of the forces acting on the particle. If the force  $F$  is the total force on the fluid particle, then:

$$F = \frac{d}{dt} \iiint \rho \vec{V} dV \quad (1-10)$$

Thus, it can be shown that equation (1-10) becomes equation (1-11) by applying the material derivative to a vector field:

$$F = \iiint \rho \left( \frac{\partial \vec{V}}{\partial t} + (\vec{V} \cdot \nabla) \vec{V} \right) dV \quad (1-11)$$

The types of forces on fluid particles are distinguished into body and surface forces. Body forces act on each point within the body, these are due to long range forces such as gravity. Surface forces are due to the fluid particle being in contact with a neighbouring particle and act directly on its surface. There are two types: (i) pressure imposed by the outside fluid surrounding the fluid particle, and (ii) shear and normal stresses imposed by friction due to the outside fluid. Thus, the total force experienced by the fluid particle as it is moving through the fixed control volume is given by:

$$F = \underbrace{\iiint \vec{g} \rho dV}_{\text{body force}} - \underbrace{\iiint \nabla p dV}_{\text{pressure force}} + \underbrace{\iiint \mu \nabla^2 \vec{V} dV}_{\text{viscous force}} \quad (1-12)$$

Therefore, it may be implied that by combining equation (1-12) with (1-11), the Navier-Stokes equation for incompressible flow results in:

$$\frac{\partial \vec{V}}{\partial t} + (\vec{V} \cdot \nabla) \vec{V} = \vec{g} - \frac{1}{\rho} \nabla p + \mu \nabla^2 \vec{V} \quad (1-13)$$

### **(3) The Energy Equation (Conservation of Energy)**

The energy equation is derived from the first law of thermodynamics which states that the rate of change of energy inside a fluid particle is equal to the rate of heat addition to the fluid particle plus the rate of work done on the particle due to body and surface forces.

The governing equations, including the Navier-Stokes equations, are presented in their most general form above. These Navier-Stokes equations were developed in the first half of the 19<sup>th</sup> century by the Englishman M. Navier and the Frenchman G. Stokes (Wendt, 2008) and are valid everywhere in the flow field of the flow continuum. Solving the Navier-Stokes equations analytically still remains complex and an almost impossible task due to the number of unknown terms in the partial differential equations. Instead, approximated solutions of the governing equations are obtained through discretised numerical series expansions of the partial differential equations. The linear equations are then computationally solved at discrete points in space and/or time, introducing the concept of mesh and time step. Discretisation methods include finite difference, finite element and finite volume methods. This is the underlying principle of CFD. Assumptions, such as the fluid is isothermal or incompressible, are usually made which enable reduction of some of the terms, or in some cases whole equations can be omitted.

The 'computational cost' is a major limiting factor when using CFD as this suggests a compromise between the accuracy and the timescale. However, CFD methods are constantly being developed and refined. Research and development of regenerative turbomachinery has grown in volume and speed due to the availability of computational techniques in recent times. Together with advances in computing capabilities, CFD has reached the point where analysis of complex machines and flows is possible for a large number of design iterations in a reasonable timescale.

The RLR pump is modelled using the commercial CFD software, ANSYS® CFX®. ANSYS® CFX® has a proven track record in turbomachinery applications. The CFX®-Solver solves the unsteady three-dimensional Reynolds-Averaged Navier-Stokes equations in their conservative form using an element-based finite volume method, which includes the discretisation of space, time and the equations that describe the problem. The spatial domain is discretised using a mesh, where the region of interest is divided into finite control volumes. The equations are discretised and solved iteratively for each of these volumes, resulting in an approximation of the value of each variable at specific points throughout the domain (ANSYS, Inc., 2013). Unlike the finite difference and finite element methods, where the relevant quantities such as mass, momentum and energy must be manually controlled, the finite volume method enforces local conservation over the control volumes that are surrounding each node point on the mesh. The finite volume method is also formulated to allow for unstructured meshes. The CFX®-Solver supports arbitrary mesh topologies, including hexahedral, tetrahedral, wedge and pyramid elements.

This research is based on the Reynolds-Averaged Navier–Stokes (RANS) approach. The Reynolds decomposition proposed by Osborne Reynolds is used to derive the RANS equations from the instantaneous Navier-Stokes equations by decomposing terms like velocity and pressure into their mean and fluctuating parts. The equations are averaged to give the RANS equations, which govern the mean flow. However, the fluctuation in the momentum term means that the velocity fluctuations are still present in the RANS equations, which introduces the concept of Reynolds stress. In order to obtain equations containing only the mean velocity and pressure, the RANS equations must be closed by modelling the Reynolds stress term as a function of the mean flow, eliminating the fluctuating component of the velocity. This is referred to as turbulence closure. One method of doing this is to use the Boussinesq approximation which introduces the concept of eddy viscosity. In CFD, this is modelled most commonly using Two-Equation Turbulence Models. This is described in more detail in *4.2.2.1 Turbulence Model*.

## 1.5 Thesis Structure

This section provides an outline of the thesis and briefly describes the contents of the following chapters.

Chapter 2 - Background: provides an overview of the literature published and establishes the state-of-the-art of research on regenerative liquid ring pumps.

Chapter 3 - Research Aims and Contribution to Knowledge: in this chapter the aims of the research, the methodology of the work and the contribution to knowledge are detailed.

Chapter 4 – Computational Modelling Methodology: introduces the computational modelling methodology and provides justification for the assumptions used. This chapter also contains the mesh independence study and comparison against previously obtained experimental test data.

Chapter 5 - Parametric Clearance Analysis: identifies key manufacturing tolerance parameters that have an effect on the performance of the pump in terms of generated head and efficiency. It also evaluates the pressure pulsation trend observed across the pump for different manufacturing tolerance models at the duty point.

Chapter 6 - Experimental Performance Testing: details of the three experimental test pumps with known manufacturing tolerances are presented in this chapter. The experimental testing procedure, uncertainties and performance curves are also provided.

Chapter 7 - Computational Performance Modelling: in this chapter the exact experimental test setup up and pump geometries are replicated in the CFD model to be able to compare against the results of the experimental testing. In addition, the pressure across the drive end, non-drive end and radial clearances are measured and compared against the total pressure increase in the pump.

Chapter 8 - Comparison of Computational and Experimental Results: provides a comparison of computational and experimental results and discusses the strengths and limitations of the experimental testing and the computational modelling techniques developed during this research.

Chapter 9 - Finite Element Analysis (FEA): an FEA is carried out to investigate operational deformation on the experimental test impellers by importing pressure profiles from the corresponding CFD simulations in Chapter 7. The simulation setup, results, implications on operational performance and limitations of the analysis are presented.

Chapter 10 - Conclusions and Recommendations: presents the outcomes of the research and discusses this in the context of the aims and objectives. This chapter also provides a list of recommendations for future work.

## 2 Background

This chapter provides a background to RLR pumps and establishes the state-of-the-art and current development in this area. The history and development of RLR pumps are also presented followed by a review of performance challenges. The material in this chapter draws heavily on the authors previously published literature reviews (Karlsen & Aggidis, 2014; Karlsen-Davies & Aggidis, 2016a).

### 2.1 History

It is hard to pinpoint exactly when the RLR pump was invented due to its many names and forms. Perhaps one of the earliest concepts to make use of the regenerative operational principle in the United Kingdom was the helical pump by Imray (1874). It consisted of a paddle shaped wheel revolving within a cylindrical casing featuring fixed vanes, similar to parallel-flow turbines, which induced a helical flow pattern to the working fluid before it entered the wheel. Imray's helical pump was later revived by Molloy (1953) and Addison (1954) in the form of a self-priming pump, although in Addison's version the impeller shaft was mounted eccentrically in the casing (similar to Figure 2-1). This was later found to be less efficient than a concentrically mounted impeller (Crewdson, 1956).

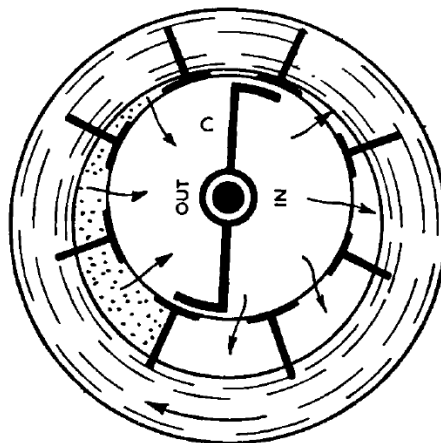


*Figure 2-1: Diagram of Addison's liquid ring pump with an eccentrically mounted shaft (Crewdson, 1956).*

The exact principle of operation of a regenerative pump has been a phenomenon that has intrigued many researchers through the years. It has been investigated using various theoretical models, experimental test studies and more recently computational modelling techniques.

The theoretical models can be a good tool for evaluating different geometry parameters quickly. However, they cannot capture the flow in a realistic manner due to simplified assumptions and the need for experimental correction data, which have a significant effect on the performance prediction. Promising experimental work in the 1940s and 50s (Engels, 1940; Bartels, 1947; Lutz, 1953; Lazo & Hopkins, 1953), which made use of flow visualisation, was successful in determining the nature of the flow pattern but as with any experimental procedure, they can be time consuming and costly, not to mention the issue of capturing adequate detail. Computational modelling has been investigated in recent years, showing good correlation with both theoretically and experimentally determined parameters. This advanced modelling tool offers the ability to investigate the inner flow mechanism of regenerative turbomachinery without the need for expensive test equipment. A summary of the methods used to analyse the regenerative operating principle can be found at the end of this section in Table 2-1.

There are two main theoretical models for describing the flow in regenerative pumps, each relying on a set of basic assumptions. These models can be categorised by the mechanism responsible for the flow pattern: turbulence or angular momentum exchange.

Engels (1940) examined a regenerative pump with semi-circular blades and developed an early one-dimensional model to predict the characteristics of the pump. Based on his findings, he believed that the distinguishing head rise of the pump was caused by a helical flow pattern. However, his model relies on experimentally defined coefficients, which makes it applicable only to the pump geometry tested. He was however able to determine that the flow circulation in the pump increased with decreasing flow rate.

The turbulence mixing theory (Senoo, 1948; Iversen, 1955) considers a turbulence mechanism to be the main driving force of the flow. In some variations of this theory the turbulent stresses are transmitted by the mixing length theory, while in others turbulent shearing stresses are assumed between the impeller and fluid, and between the fluid and casing. Senoo (1948) modelled the internal flow of a radial blade impeller under the condition of an adverse pressure gradient and considered a turbulent friction force to be responsible for the pumping mechanism. In contradiction, Iversen (1955) proposed a viscous model for performance prediction of a radial blade impeller based on the theory that shear stresses are imparted to

the fluid by the impeller. This model included two shear coefficients and an average impeller velocity, which were determined experimentally.

Flow visualisation studies conducted in the 1940s (Engels, 1940; Bartels, 1947) showed that the flow follows a helical pattern in the meridional plane from the inlet to outlet port (see Figure 1-3), which is induced by the centrifugal field of the impeller. This helical flow path cannot be directly described by the theories developed by Senoo (1948) and Iversen (1955). In a discussion of Iversen's model, Wright (Iversen, 1955) suggested an alternative theory based on the momentum transfer between the blade row and the fluid in the channel. He found that by increasing the rotational speed of the pump and giving the blades a suitable backward curvature, the same pressure rise could be achieved, demonstrating the limitations of a purely viscous model.

The circulation-momentum exchange theory (Wilson, et al., 1955) states that the fluid gains momentum in the impeller and imparts this on to the slower moving fluid in the annular channel by circulation (Figure 1-4), increasing the pressure along the annular channel. The fluid then re-enters the impeller with a lower angular momentum. Despite its exclusion of the effects of drag and shear stresses, this theory has been recognised as sufficient to describe the inner flow mechanism and has formed the basis for most publications to date. The model has the ability to explain the helical flow pattern, which the others lacked, formulated the equation for the momentum exchange and identified losses occurring in the pump. In their model Wilson, et al. (1955) assumed that all of the fluid only leaves the tip of the impeller blade, even though experimental analysis had shown that some of the fluid leaves at the side of the blade.

Senoo (1956) reviewed the two theoretical models and showed that they were compatible with each other, but he underlined that neither model is able to take account of the spanwise variations of the flow. They also require significant experimental correction to empirically determine loss coefficients. These are dependent on the exact design and as a result cannot be used to evaluate different geometrical designs. To date, no existing one-dimensional model includes both theories of operation.

A different method based on the adaption of the streamline curvature technique commonly used for axisymmetric through flow calculations in conventional axial and radial flow turbomachines was proposed by Andrew (1990). Although this method could not be used to



calculate the details of flow between the blades, it made it possible to evaluate the likely effects of parameters such as the spanwise variation of the blade angle on overall performance. Spanwise variation was neglected in the turbulent-flow and momentum-exchange theories.

Another limitation of earlier theoretical models is that they can only be used to determine the flow in the region where it is fully developed. There are nonetheless five flow regions in a RLR pump; inlet, acceleration, linear, deceleration and exit regions, all describing different development stages of the flow field (Raheel & Engeda, 2005). Senoo (1954) investigated the effect of the developing region experimentally for various inlet region geometries and found that an increase in channel area in the inlet region could lead to improved head development and efficiency. Despite this it does not provide a full theoretical description of the characteristics of the flow in this region.

Badami (1997), Song et al. (2003) and Yoo et al. (2005) proposed modified theoretical models in order to better correlate internal losses with geometric and hydrodynamic parameters, however a number of empirical coefficients still required extensive experimental determination. Badami (1997) extended the one-dimensional momentum exchange theory to non-radial blades and a comparison between numerical and experimental results showed good corroboration even for varying geometries. Song et al. (2003) developed in their model a method of calculating the circulatory velocity along the channel, which had previously been corrected by a linear region factor (the ratio of the linear region to the fully developed region). Yoo et al. (2005) included the entire flow region from inlet to outlet in their model and were able to predict head and efficiency without any empirical data. Quail et al. (2011a) found that the linear region factor does not provide an adequate representation of the fluid behaviour. They developed a one-dimensional numerical model with the capability of assessing the pump performance without the need of a linear region factor or experimental correction data. In contrast to previous work, their model is applicable to varying geometries.

In parallel to the development of theoretical models to describe the flow pattern of the RLR pump, various experimental studies (see Figure 2-2) have been carried out to better visualise the inner flow mechanism. In 1947 Bartels (1947) discovered scratch marks caused by sand inside a pump casing. He reproduced the scratch marks, which took a helical flow pattern, and measured the helix angle of the flow. Some of the best interpretations of the flow field in

regenerative pumps have come from flow visualisation experiments. Engels (1940) and later Lazo and Hopkins (1953) and Lutz (1953) used a small thread probe to measure the flow directions at different locations in the annular channel of a pump and were able to observe a helical flow pattern.

Burton (1966; 1967) used a pump with Perspex walls to photographically record the flow path of small, energised beads. His work focused on theoretical and experimental analysis of both turbine and pump operation. He was able to affirm that that the fluid is received into the impeller near the root of the impeller blade and leaves near the blade tip during pump operation, and the reverse during turbine operation.



*Figure 2-2: Flow visualisation study using Perspex glass (Aggidis, 2002).*

Hübel et al. (1995) used a laser light sheet technique in combination with digital image processing to perform a visualisation of three-dimensional flow in a regenerative pump. They were able to verify that the inner fluid flow pattern follows helix-shaped streamlines.

**Table 2-1: Comparison of methods used to analyse the regenerative operating principle (references refer to focused work within each mode of analysis).**

Operational Analysis							
Mode of Analysis	Research Area	Method	Advantages	Disadvantages	Reference Index <sup>1</sup>	Most Recent Publication	Comments
Theoretical Models	Turbulent Flow Theory	<ul style="list-style-type: none"> <li>• Turbulent Mixing Length</li> <li>• Turbulent Shearing Stress</li> </ul>	<ul style="list-style-type: none"> <li>• Relatively fast</li> </ul>	<ul style="list-style-type: none"> <li>• Assumptions</li> <li>• Experimental data</li> <li>• Geometry dependant</li> </ul>	1-16	2012	<ul style="list-style-type: none"> <li>• Momentum exchange theory accepted as most suitable</li> <li>• Recent modifications include entire flow region and are independent of empirical data</li> <li>• Can be used for initial design generation</li> </ul>
	Momentum Exchange Theory	<ul style="list-style-type: none"> <li>• Circulation</li> <li>• Violent Mixing</li> </ul>					
Experimental Studies	Flow Visualisation <sup>2</sup>	<ul style="list-style-type: none"> <li>• Probe Measurement</li> <li>• Photographical Recording</li> <li>• Laser &amp; Digital Imaging</li> </ul>	<ul style="list-style-type: none"> <li>• Good visual aid</li> </ul>	<ul style="list-style-type: none"> <li>• Time consuming</li> <li>• Costly</li> <li>• Inadequate detail</li> </ul>	1, 17-22	1995	<ul style="list-style-type: none"> <li>• Determined helical flow pattern and confirmed momentum exchange theory</li> <li>• Showed that fluid enters impeller near the blade root and leaves near the blade tip</li> <li>• Experimental testing can be used to verify optimised design</li> </ul>
Numerical Modelling	Steady State	<ul style="list-style-type: none"> <li>• Frozen Rotor</li> </ul>	<ul style="list-style-type: none"> <li>• Less costly</li> <li>• High repeatability</li> <li>• Accurate</li> </ul>	<ul style="list-style-type: none"> <li>• Processing limitations</li> </ul>	16, 23-30	2016	<ul style="list-style-type: none"> <li>• Has taken the research to new levels</li> <li>• Can be used for performance prediction and parametric studies</li> <li>• Ability to resolve local flow pattern</li> </ul>
	Transient	<ul style="list-style-type: none"> <li>• Moving Reference Frame</li> </ul>					

<sup>1</sup> Index to the references is provided on the following page.

<sup>2</sup> References listed only include studies where experimental investigation has predominantly been used; they do not include experimental verification/comparison of theoretical/numerical modelling.

Index to references provided in Table 2-1:

1. Engels (1940)
2. Senoo (1948)
3. Oeirich (1953)
4. Senoo (1954)
5. Iversen (1955)
6. Wilson et al. (1955)
7. Senoo (1956)
8. Burton (1962)
9. Andrew (1990)
10. Badami (1997)
11. Song et al. (2003)
12. Yoo et al. (2005)
13. Raheel & Engeda (2005)
14. Meakhail & Park (2005)
15. Quail et al. (2011a)
16. Quail et al. (2012)
17. Bartels (1947)
18. Lazo & Hopkins (1953)
19. Lutz (1953)
20. Burton (1966)
21. Burton (1967)
22. Hübel et al. (1995)
23. Weise & Beilke (1998)
24. Quail et al. (2010c)
25. Quail et al. (2011b)
26. Badami & Mura (2012)
27. Fleder & Böhle (2012)
28. Karenth & Sharma (2014)
29. Fleder & Böhle (2015)
30. Zhang, et al (2016)

In the last decade or so CFD methods have been used to investigate the inner flow mechanism of regenerative turbomachinery. In contrast to the one-dimensional models, CFD software does not rely on one restricted model with simplified assumptions, but has the ability to capture the properties of both theoretical models. Prior to this development the most accurate representation of the flow mechanism was from flow visualisation studies. Although experimental testing is beneficial, computational modelling is less costly and time consuming with high repeatability. Furthermore, this advanced tool can be used for performance prediction and parametric studies to find an optimum design point as well as assessing the inner flow pattern. It is also possible to measure the pressure and velocity variations in the pump without having to rely on instrumentation that might introduce errors. However, like all methods, CFD has weaknesses. Often the geometry to be modelled has to be simplified due to limitations in processing capabilities, such as applying a coarse mesh in regions of great detail, which may lead to inaccuracies (Quail, et al., 2012). In spite of this CFD analysis and experimental data have shown good correlation.

Badami and Mura (2012) investigated a regenerative blower with radial, backward and forward orientated blades. They used ANSYS® CFX® to analyse the flow behaviour and the effect of the slope of the blades on the performance, without taking into account leakages. They observed similar results between the CFD and one-dimensional simulations. Their findings show that as soon as the flow rate increases, the fluid enters the impeller blades less frequently, with a lower degree of regeneration and a lower increase in pressure. This agrees with head, power and efficiency relationships of regenerative turbomachinery (Raheel & Engeda, 2002), which was also observed by Engels (1940).

Quail et al. (2011b) were able to use ANSYS® Fluent® on a regenerative pump model to simulate the helical flow pattern previously observed in flow visualisation tests. They found that the local pressure varies across each blade, in contrast to the previously straight linear representation of the pressure distribution (Wilson, et al., 1955; Badami, 1997; Engeda, 2003; Song, et al., 2003; Raheel & Engeda, 2005). Comparing results of the CFD analysis with experimental data they were able to show that CFD has the ability to be used as performance prediction and optimisation tool. Quail et al. (2012) compared performance data from analytical and numerical models with experimental test results. They found that CFD is capable of resolving local flow properties which can be used to make further improvements to the design.

## **2.2 Operational Advantages**

As illustrated in Figure 2-3 the RLR pump is well suited for high head-low capacity applications. High heads are concurrent with low flow rates. The circulatory velocity is higher at lower flow rates, resulting in this higher pressure rise. One effect of the subsequent high heads is a larger power requirement at these low flow rates, with the maximum required at shutoff. Therefore, it can be demonstrated that the maximum efficiency of an RLR pump occurs at comparatively faster flow (Raheel & Engeda, 2002). The efficiency curve features a sharp peak close to 50%. The increased power demand at reduced flow rates can lead to overloading of electric drive motors designed to meet the demand at the duty point (Nesbitt, 2006).

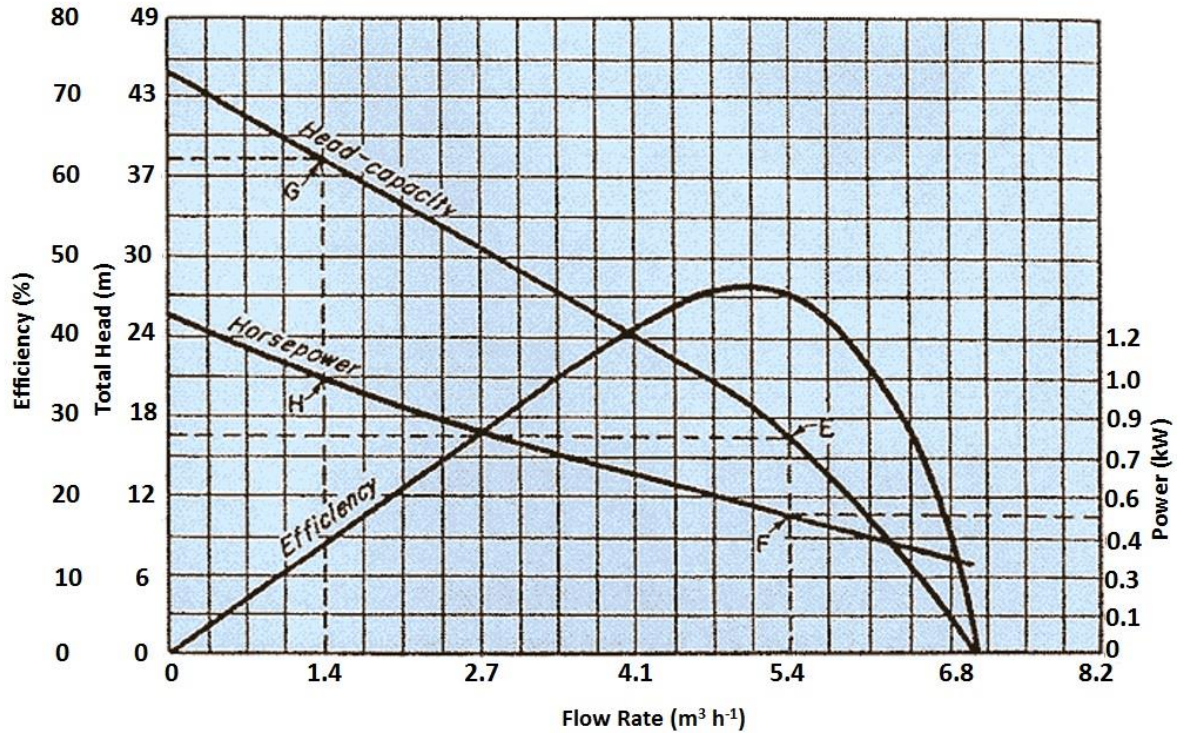


Figure 2-3: Performance curves for a typical regenerative pump (Roth Pump Company, 2015).

### 2.2.1 Low Specific Speed

Despite the low efficiency, typically in the range of 35-50% (Crewdson, 1956; Quail, et al., 2010c), it is evident from Figure 2-4 that in the low specific speed range for delivery of small quantities of fluid at a high pressure, the RLR pump compares favourably with other more complex multistage rotodynamic machines. The dimensionless specific speed,  $\Omega_s$ , is given by equation (2-1):

$$\Omega_s = \frac{\Omega \sqrt{Q}}{(g\Delta H)^{3/4}} \quad (2-1)$$

Where  $\Omega$  is the angular speed,  $Q$  is the flow rate,  $g$  is acceleration due to gravity and  $H$  is the total head at the best efficiency point.

The head coefficient in Figure 2-4 is given by equation (2-2):

$$\psi = g\Delta H(\Omega^2 r^2) \quad (2-2)$$

Where  $r$  is the impeller radius.

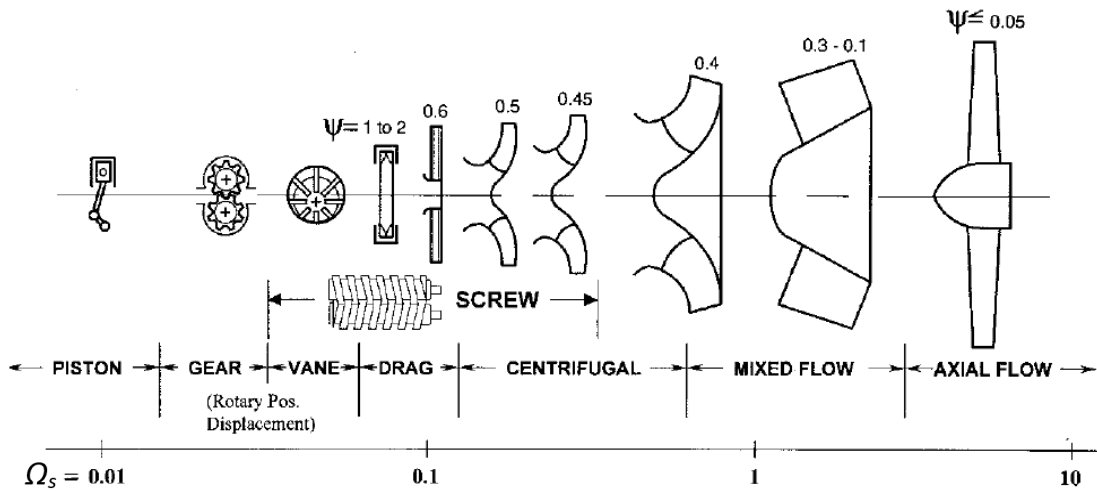


**Figure 2-4: Specific speed classification for different types of pumps (Kurtzsch & Cooper, 1986), where  $\psi$  is the head coefficient given by equation (2-2).**

A comparative study (Quail, et al., 2010a) of a centrifugal and regenerative pump showed that the latter was capable of delivering a head nearly three times higher at a much greater efficiency, underlining the importance of pump selection. Based on data collected for the European Commission study in 2008 (European Commission, 2001), better pump selection was estimated to give cost effective energy savings of 3% (or 1.1TWh pa) within a 15-year timeframe.

It should however be noted that Hollenberg & Potter (1979) carried out an efficiency-specific speed study which indicated that higher efficiencies may be achievable at higher specific speeds.

### **2.2.2 Self-priming**

A typical horizontal centrifugal pump is sensitive to the presence of air and other gases in the pumped liquid, if the circumstances exceed the capability of the pump it might lose its prime or completely stop pumping (Lazarkiewicz & Trokolanski, 1965; Marty, 2012). RLR pumps on the other hand have excellent priming behaviour. The self-priming ability is ensured by correct arrangement of the inlet and outlet ports and external elbow joints, so that a portion of fluid always remains within the pump cavity. When the impeller begins to rotate, the remaining fluid is thrown around the casing to form a ring of liquid (Lazarkiewicz & Trokolanski, 1965; Burton, 1966; Gülich, 2010), hence the alternative name *liquid ring pump*. Due to the gradual increase in pressure across the pump, any vapour bubbles occurring in the fluid will collapse gently over a relatively long time. This makes the RLR pump able to handle gases or a mixture of gas and liquid. Under the same conditions a centrifugal pump would be subjected to cavitation as the bubbles will collapse violently due to the sudden increase in pressure (Mueller, 2004; Quail, et al., 2010c). Most positive displacement types are capable of handling in excess of 50% gas without modification (Parker, 1994). The amount of entrained gases the RLR pump can handle varies but numbers ranging from 20-50% have been reported (Quail, et al., 2010c; Marty, 2012).

### **2.2.3 Stable Operating Conditions**

As the gradient of the head-capacity curve is very steep, the RLR pump can maintain a relatively stable flow within a range of pressure pulsations by throttling a valve. In contrast, typical centrifugal pumps have a parabolic shaped curve whereby the flow rate can change dramatically with pressure (Marty, 2012). When a regenerative pump is applied as a gas compressor there is an additional advantage of no surge or instability (Meakhail & Park, 2005).

### **2.2.4 Low Cost**

For the simple designs featuring elementary radial impeller blades and casing, this type of pump can be easier and cheaper to manufacture than centrifugal pumps with intricate vanes and volutes. The RLR pumps are also more compact and require fewer stages than centrifugal pumps (Badami, 1997; Raheel & Engeda, 2002). Fewer components and less material indicate that the initial environmental impact, in form of raw material extraction and energy consumption during the manufacturing process, will in comparison be less for a RLR pump.



This is an important factor to consider when assessing the life cycle cost in terms of energy usage.

## **2.3 Performance Challenges and Losses**

The highest reported efficiency for any water-ring self-priming pump was measured by Crewdson in 1956 (Crewdson, 1956) at 50%. The low efficiency can partly be assigned to the inherent fluid dynamic behaviour of the pump; the input power is used for developing the increase in head as well as being consumed by the circulatory flow through the impeller blades (Sixsmith & Altmann, 1977; Badami, 1997; Raheel & Engeda, 2002). However, the pumping efficiency is significantly reduced when the circulatory flow decreases (Crewdson, 1956).

As much as 40-50% of the supplied power is believed to be consumed by losses that are related to the geometry of the machine (Engeda, 2003), of which losses due to slip make up the largest contribution (Sixsmith, 1981; Marty, 2012). The performance of the RLR pump is also affected by other types of losses, such as shock losses, circulation losses, peripheral friction losses, losses at the inlet and outlet ports and leakage losses (Lazarkiewicz & Troskolanski, 1965; Burton, 1966; Raheel & Engeda, 2002; Engeda, 2003), which are explained in more detail in the subsequent sections.

Improvements in the design should be aimed at increasing the efficiency at high pressures and low flow rates due to the large corresponding increase in power consumption (Shirinov & Oberbeck, 2011a). As soon as the flow rate increases, the fluid enters the impeller blades less frequently, with a lower degree of regeneration and a lower increase in pressure (Engels, 1940; Burton, 1967; Raheel & Engeda, 2002).

### **2.3.1 Slip Losses**

Burton (1967) described losses due to slip as “imperfect guidance of the flow by the blades”. As the fluid traverses through the impeller the pressure between each adjacent blade will be different due to the adverse peripheral pressure gradient, giving rise to a secondary circulation which forces the fluid exiting the blade to flow backward with respect to the rotational direction of the impeller (Lazarkiewicz & Troskolanski, 1965; Raheel & Engeda, 2005; Yoo, et al., 2005). The slip loss increases with the peripheral pressure gradient (El Hag, 1979; Raheel & Engeda, 2002). The actual mean peripheral fluid velocity at the blade exit is less than the

theoretical velocity based on the outlet blade angle (velocity triangle). It is this difference that provides the energy required to maintain the circulation (Sixsmith, 1981). The reduction in peripheral velocity is accounted for by introducing a slip factor which is defined as the ratio of the mean peripheral velocity to the velocity of the blading (Sixsmith, 1981; Yoo, et al., 2005). To reduce these losses, Sixsmith (1981) suggested to increase the inlet blade angle and reduce the outlet angle. The amount of slip at zero head gives an indication of the drag (or 'hold') which the blades have on the fluid (Crewdson, 1956).

### **2.3.2 Shock Losses**

In contrast to the slip effect, shock (or incidence) losses occur at the entry to the blades and predominantly at operating conditions outside the duty point. It is believed that the loss is due to the difference in angle between the blade and the flow when the fluid enters the blade (Lazarkiewicz & Trokolanski, 1965; Meakhail & Park, 2005; Raheel & Engeda, 2005) as a result of the difference in angular momentum between the slower moving fluid in the channel and the faster moving fluid in the impeller. The shock effect is accounted for by an incidence factor which is defined as the ratio of the mean peripheral fluid velocity at the blade inlet to the velocity of the blading (Yoo, et al., 2005).

### **2.3.3 Circulation Losses**

During operation the RLR pump experiences hydraulic losses as the flow circulates between the impeller blades and the annular channel (Lazarkiewicz & Trokolanski, 1965; Raheel & Engeda, 2002; Engeda, 2003). This type of loss can be separated into three loss mechanisms (Meakhail & Park, 2005; Raheel & Engeda, 2005; Yoo, et al., 2005; Quail, et al., 2011a). The first occurs due to turning of the fluid in both the annular channel and in the blades. More specifically the channel turning loss can be assigned to the sharp corners of the channel. The second loss mechanism is due to the mixing of faster moving flow in the impeller with the slower moving flow in the annular channel. Thirdly, when the flow circulates through the impeller it will experience a sudden change in flow area when it enters or leaves the blades.

### **2.3.4 Peripheral Friction Losses**

Peripheral head losses are caused by the natural curvature of the annular channel which gives rise to wall shear stresses (Andrew, 1990; Raheel & Engeda, 2005). It can be evaluated in the same way as classical pipe losses occurring in bends and contraction, expansion and straight ducts (Song, et al., 2003; Yoo, et al., 2005; Quail, et al., 2011a).

### **2.3.5 Inlet and Outlet Losses**

The losses that occur at the inlet and outlet ports of the pump are primarily caused by the difference in the flow area between the ports and the channel (Quail, et al., 2011a), which causes rapid changes in fluid velocities.

### **2.3.6 Leakage Losses**

There are two major types of leakage losses occurring in the RLR pump: firstly through the axial and radial clearances between the impeller and the pump casing and secondly between the inlet and outlet ports across the stripper. The latter is the largest and has a greater effect on the pump performance (Iversen, 1955; Burton, 1962; Lazarkiewicz & Trokolanski, 1965; Burton, 1966; Sixsmith, 1981; Badami, 1997). During pumping operation, the high-pressure fluid near the discharge port, assisted by the impeller blades which are moving in the same direction, will attempt to leak back through the stripper clearance to the low-pressure suction port. This occurs due to the pressure difference existing between the fluid in the impeller blades and the fluid in the side channel and due to the drag of the impeller. To avoid excessive backflow the stripper clearance must be kept to a minimum. However, Sixsmith & Altmann (1977) believed that only small improvements in performance could be gained. Sixsmith (1981) later identified that multistaging could reduce the loss of efficiency due to the reduction of the backflow by nearly a half. Burton (1966) also identified a third type of leakage loss that occurs between the side channel and the central blade “pocket” (area between two successive blades), however it turned out to only have a minor effect on the pump performance compared with the losses through the stripper section.

### **2.3.7 Operational Wear**

RLR pumps are generally very robust compared to other pumps and offer long service life, however performance challenges can arise due to operational wear of internal components. Although it is important to ensure tight clearances for optimum head and efficiency (Hollenberg & Potter, 1979), it does not come without its price. Abrasives in the pumped fluid will cause rapid wear on the impeller and casing, making the RLR pumps poor at handling solids of any appreciable size (Biheller, 1976; Hollenberg & Potter, 1979; Gülich, 2010; MEPCO, 2014). This kind of fluid contamination has a tendency to cause premature failure in mechanical seals and erosion of the impeller blades, as particles get stuck between the impeller and the casing (Gülich, 2010; Lytron, 2015). For different applications it becomes important to identify parameters that affect component wear and consequently performance as these will directly affect how the energy consumption will change over time, with the added benefit of improving pump reliability. Ensuring that proper maintenance of existing pumps is carried out can also make substantial energy savings. Replacing worn pump parts will reduce internal leakage and maintain pump efficiency. An added benefit of this is the reduction of the life cycle impact on the environment by refurbishing rather than replacing the whole pump.

Due to the gradual increase in pressure from the suction to the discharge side, there is a radial and axial load on the impeller (Crewdson, 1956; Lazarkiewicz & Troskolanski, 1965). It is important that the pump reaches a pressure equilibrium within a reasonable period of time to ensure proper axial balancing of the impeller (Lytron, 2015). Until this point the impeller is sensitive to sudden changes in pressure, due to pressure valves or other conditions, which could cause it to rub against the casing. During operation some deformation of the impeller can take place due to increase in temperature, adversely affecting the clearances and alignments within the pump. In comparison, the radial clearance is typically less subject to wear (Badami, 1997).

### **2.3.8 Pressure Pulsation Phenomenon**

Another disadvantage of the regenerative pump is the high noise level caused by the blade passing frequency (BPF) corresponding to the rotational frequency times the number of blades, which in turn is due to the recirculating flow and the associated losses (Gülich, 2010). Weise & Beilke (1998) reported sound power levels as high as 110 dB for a peripheral fan, the measurements included mufflers. The interaction of the circulation flow with the blades edges

and the port plates creates a pulsation in the pressure history of the pump (Weise & Beilke, 1998) as illustrated in Figure 2-5.

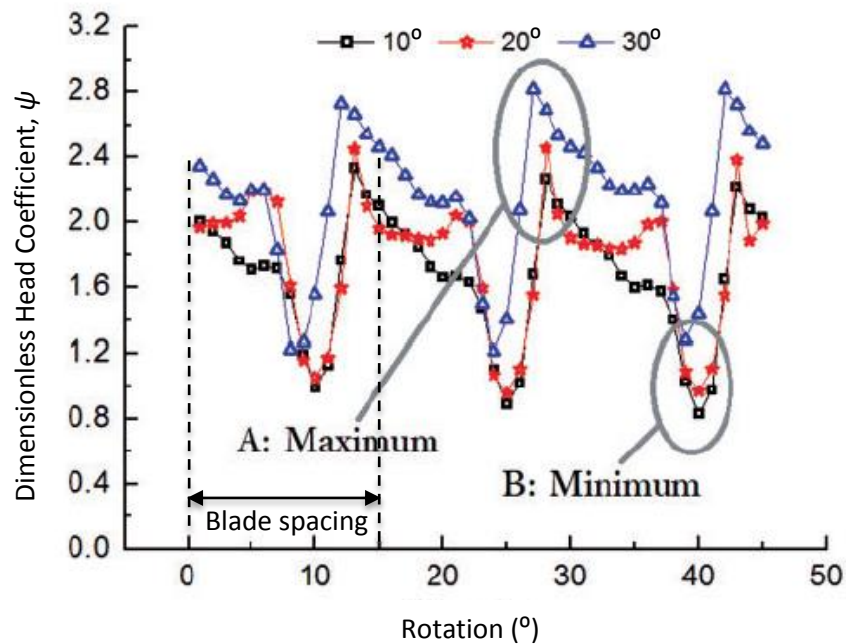


*Figure 2-5: Example of pressure pulsation phenomenon in a regenerative pump (Zhang, et al., 2016) for blade angles of 10°, 20° and 30°. Circumferential angle between two adjacent blades is 15°.*

Similarly to the pressure pulsation history produced by Zhang, et al. (2016) in Figure 2-5, Böhle & Müller (2009) and Fleder & Böhle (2012; 2015) have also identified a distinct pulsation trend in the computationally predicted pressure differential. Weise & Beilke (1998) were able to demonstrate a similar characteristic periodic pressure pulsation pattern using both transient computational calculations and experimental measurements, however as far as the author is aware no other experimental verification of the pressure pulsation phenomenon exists.

## 2.4 Historical Geometry and Design Optimisation

The design of the regenerative machine has evolved over many decades. Similar to the concept of the paddlewheel (Imray, 1874) most of the earlier designs of regenerative turbomachines consisted of a basic geometrical configuration with simple vanes either cast or machined into the impeller. Throughout the years researchers have investigated the correlation between performance and geometrical features, focusing on the design of the blade shape, the side channel, the inlet and the outlet.

### 2.4.1 Blade Configurations

The design of the impeller blades has a significant effect on the performance due to the influence on the fluid flow and the energy transfer to the fluid (Shirinov & Oberbeck, 2011a), this is perhaps why most of the design improvements have centred on the geometry of the blading. The impeller blades of regenerative turbomachinery can have different profiles including radial, non-radial, semi-circular and aerofoil blades. These profiles can be configured into a single- or double-sided impeller (see Figure 2-6). The latter, also sometimes referred to as a webbed impeller as it features a “web” between the blades, promotes equal pressure distribution on both sides, which in turn makes the impeller self-adjust axially and reduces the chances of wear (Lazarkiewicz & Trokolanski, 1965). This is probably why this type historically was the most common form used for commercial units (Iversen, 1955; Shimosaka, 1960). Symmetrical blade profiles have also been shown to increase the efficiency due to improved energy transfer between the impeller and the fluid (Sixsmith & Altmann, 1977). This can be assigned to the reduction of so called “dead zones” of fluid between adjacent blades which do not take part in the circulation (Zozulya, 1982).

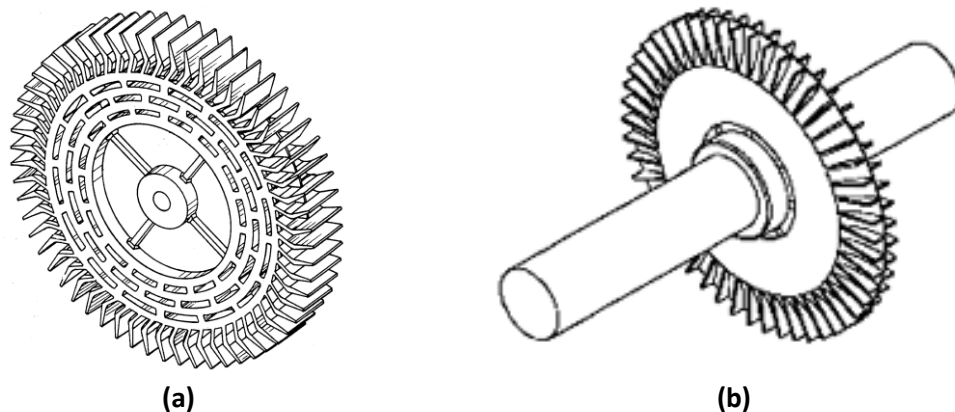


*Figure 2-6: Regenerative pump impeller (a) single-sided (Moss & Czarnowski, 1996), (b) double-sided (Lytron, 2015).*

The most widely used blade profile is the straight radial blade (Figure 2-7a), which is perpendicular to the perimeter of the impeller and can rotate in either direction (Senoo, 1948; Senoo, 1954; Iversen, 1955; Wilson, et al., 1955; Shirinov & Oberbeck, 2011a; Choi, et al., 2013). Different variations of this profile exist. Particularly, a circular shape in the meridional section (applying a radius to the corners) has been found to reduce turbulence and promote better flow circulation by reducing the incidence angle (Dewitt, 1957; Lazarkiewicz & Trokolanski, 1965; Kang, et al., 2004).

Non-radial blades have a similar profile but can either be forwardly or backwardly inclined in relation to the impeller's direction of rotation (Burton, 1966; Burton, 1967; Yamazaki & Tomita, 1971; Yamazaki, et al., 1972; Tomita, et al., 1973; Yamazaki & Y, 1974; Grabow, 1975; Choi, et al., 2013). A recent experimental study found that the head performances of both forward and backward bladed impellers deteriorate as the blade angle increases, underlining that straight radial blades are more efficient in comparison (Choi, et al., 2013). However, out of the two, the forwardly inclined blade performs better (Grabow, 1975).

The chevron shaped blades (Figure 2-7b), angled with respect to the axial direction, are in some ways similar to a Pelton turbine as the fluid is scooped up by the blade shape, rendering them more efficient if rotated in the direction of the blade inclination. Chevron impellers have not been subjected to as much study as radial blades, but have been found to provide improved performance compared with radial blades. This is due to the reduction in incident loss at the blade inlet and subsequently higher circulation (Crewdson, 1956; Burton, 1966; Burton, 1967; Hübel, et al., 1995; Badami, 1997). Furthermore, the radial clearance is reduced as the chevron impeller features a continuous surface around the periphery circle, which limits the leakage losses (Burton, 1972). Both Burton (1972) and Badami (1997) found that the head produced by the chevron bladed impeller is around twice that of a radial blade impeller. One study found the optimum chevron angle of around  $30^\circ$  (Choi, et al., 2013). While another study (Raheel & Engeda, 2005) on the other hand determined it to be between  $45^\circ$  and  $60^\circ$ , which makes it rather difficult to select an ideal angle from a design point of view. As is the case for centrifugal pumps, the parametric design of the RLR pump is dependent upon the operational parameters.

Only limited research exists into semi-circular profile blades (Figure 2-7c) (Grabow, 1975; Hollenberg & Potter, 1979), they have however been shown to have a complete absence of the dead zones and a minimum wetted surface perimeter in the case of viscous liquids (Zozulya, 1982).

Aerofoil blades (Figure 2-7d) have a circular contour and project axially into the channel, they have mostly been used in regenerative compressor designs (Sixsmith & Altmann, 1977; Abdallah, 1981; Sixsmith, 1981; Song, et al., 2003). Aerofoil profiles are usually fitted with a core for guiding the flow and reducing the vortex formation at the blade tips (Sixsmith & Altmann, 1977). Sixsmith & Altmann (1977) found that the aerofoil blades produced more

pressure rise than any other blade shapes. Although the efficiency was improved compared to the radial blade impeller, the efficiency remained around 40%. They suggested to use properly contoured aerofoil blading to increase the efficiency further. As with other blade profiles, symmetrical blading gave a higher efficiency.

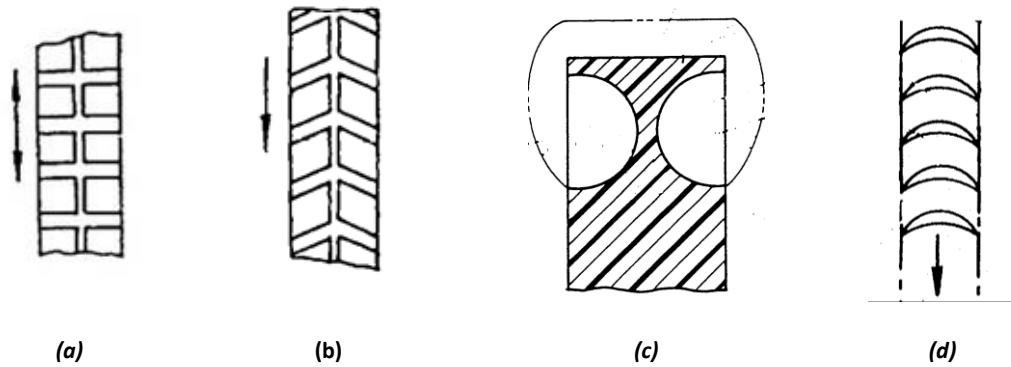


**Figure 2-7: (a) Straight radial blades, (b) symmetrical chevron blades, (c) meridional geometry of semi-circular blades, (d) meridional section of aerofoil blades (Kidger, et al., 1995; Kusagaya, et al., 2004).**

Interestingly, Shirinov & Oberbeck (2011b) found that aerofoil blades are superior to the other blades types tested for pressures higher than 20 kPa, while symmetrical chevron blades outperform in the 100 Pa to 20 kPa range because they allow the best momentum transfer from the impeller to the fluid in the side channel.

Meakhail & Park (2005) carried out a CFD study to investigate the complex flow field of a regenerative pump using an impeller with twisted blades, which combines a chevron inlet blade angle and a backwardly inclined angle at the side-blade exit. They were able to show that part of the fluid leaves the impeller at the side of the blade, in contrast to the assumptions made by Wilson et al. (1955). Based on their results they determined that the side-blade exit angle has a significant effect on the performance. Angles less than  $90^\circ$  gave higher efficiencies due to the fact that the flow angle is close to the blade angle, which reduces or eliminates vortex formation behind the blade.

Fleder & Böhle (2012) compared the performance of an impeller with straight radial rectangular blades to an impeller with triangular shaped blades (in the radial plane) and found that the latter generates a higher head due a higher circulation frequency, much like a chevron shaped impeller. Zhang et al. (2016) investigated both numerically and experimentally the effect of the suction side blade profile on the performance of a side channel pump with radial



blades, using base angles of  $10^\circ$ ,  $20^\circ$  and  $30^\circ$ . They found that a larger angle provided a higher head coefficient, although the effects on the efficiency were less noticeable.

Regardless of blade profile, blade angles matching the fluid angles provide a better performance as the fluid will have a smoother entry and exit of the blades (Sixsmith, 1981).

#### **2.4.2 Number of Blades**

Some researchers (Senoo, 1954; Iversen, 1955; Crewdson, 1956; Shimosaka & Yamazaki, 1960; Grabow, 1975; Shirinov & Oberbeck, 2011a; Karenth & Sharma, 2014) have also successfully improved the impeller performance by varying the number of impeller blades. The number of blades has an effect on the head developed by the pump (Badami, 1997) due to the effect on the slip factor (Iversen, 1955; Mason, 1957; Lazarkiewicz & Troskolanski, 1965). As the number of blades is reduced the losses due to slip are increased by a large amount. Raheel & Engeda (2005) did a study involving radial blade profiles and concluded that 75 to 90 blades should mitigate this problem. However, a further increase could have an adverse effect on the circulation between the blades as well as increasing the friction losses.

However, as with all design criteria, the exact number of blades will vary for different designs and conditions. Iversen (1955) and later Shirinov & Oberbeck (2011b) determined that the optimal size, number and spacing of the blades are strongly related to the diameter of the impeller and the size of the side channel. For an increase in the cross-sectional area of the side channel, the optimum impeller will feature larger but fewer blades in a more sparse formation. On the other hand, if the diameter of the impeller is increased while the side channel area is unchanged, the ideal number of blades will increase relative to the diameter.

#### **2.4.3 Impeller Diameter**

Losses arising from shock and slip are mainly due to misalignment of the blade and fluid angles. Therefore it comes as no surprise that these losses are also affected by the impeller tip radius. Raheel & Engeda (2005) found that these could be minimised by increasing the impeller tip radius and decreasing the hub radius.

#### **2.4.4 Axial and Radial Clearance**

Research (Shimosaka & Yamazaki, 1960; Yamazaki, et al., 1972; Badami, 1997; Horiguchi, et al., 2009; Badami & Mura, 2012; Fleder & Böhle, 2015) has shown that a decrease in axial clearances for a radial bladed impeller will provide an increase in efficiency due to reduction in backflow from the high-pressure discharge to the low-pressure suction side. There is no definite number for the optimum clearance. Sixsmith (1981) determined it to be less than 0.3 mm to prevent excessive backflow. Through comparison of experimental and theoretical results of different axial clearance values (0.01-0.08 mm), Badami (1997) found that 0.01 mm provided a higher head and better efficiency.

Less attention has been given to the radial clearance. Raheel & Engeda (2005) found that for a radial bladed impeller the radial clearance has an effect on losses due to shock, turning of the blades, and channel and blade mixing. These were minimised for a radial bladed impeller by increasing the radial clearance.

#### **2.4.5 Side Channel**

Typically, the side channel wraps around 270° to 320° of the circumference (Gülich, 2010). The water ring created by the remaining water in the pump casing rotates concentrically and ineffectively in the casing if the side channels are not interrupted at one point of the circumference as shown in Figure 2-9.

The shape and cross-sectional area of the side channel have an effect on the performance of the pump. An unnecessary amount of power is lost in sustaining the circulatory flow against the resistance due to fluid friction and turbulence (caused by violent mixing of slower and faster moving fluids) in the channel (Sixsmith & Altmann, 1977). It becomes important to reduce this resistance to a minimum. Particularly, a circular cross-section or rounded shape (Figure 2-8) assists with the circulatory flow and reduces turbulence (Lazarkiewicz & Trokolanski, 1965; Sixsmith, 1981).

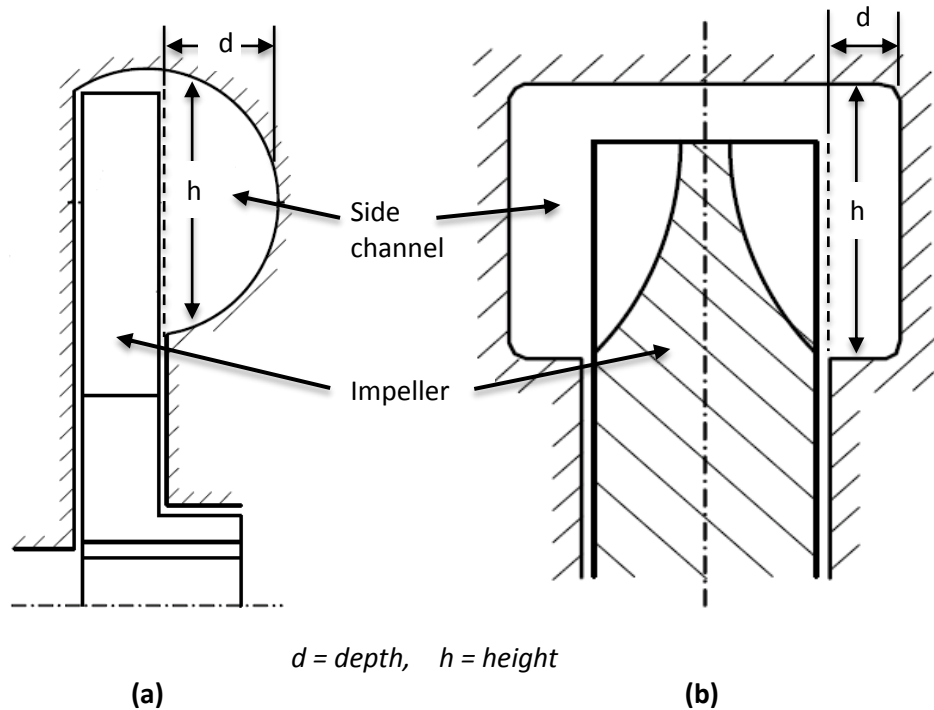


**Figure 2-8: Regenerative pump with (a) circular and (b) rounded side channel shape (Gülich, 2010).**

Studies by Senoo (1954) and Badami (1997) have also shown that an increase in cross-sectional area at the inlet region initiates the circulatory flow and improves head development and efficiency. In addition, increasing the depth of the open area of the side channel decelerates the circulatory flow and reduces the kinetic energy, which in turn provides the power required to support the circulation against the friction (Sixsmith & Altmann, 1977). The depth of the side channel also has an effect on shock and channel turning losses, notably a sharp drop in efficiency occurs for large channel depths (Raheel & Engeda, 2005).

Attempts have also been made to control the circulatory flow by including a central core in the side channel (Engels, 1940; Crewdson, 1956; Pfaff, 1961). Crewdson (1956) soldered a thin brass strip along the middle of the side channel, dividing it into two parts, to affect any radially inward flowing circulatory flow (Figure 2-9). From the performance curves established, he was able to conclude that the pumping efficiency was significantly reduced with decreasing circulatory flow.

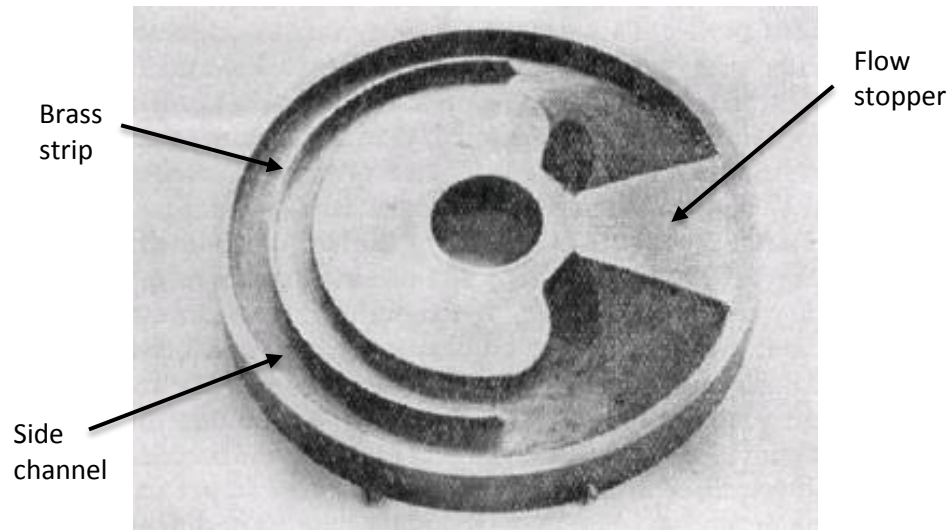


*Figure 2-9: Side channel with soldered in brass strip to reduce helical water circulation (Crewdson, 1956).*

Based on previous research carried out by Pfaff (1961), Burton (1972) investigated the use of fixed return blades at the root of the side channel and near the tip of the impeller, both improved the performance by altering the torque balance between the impeller and the side channel and by guiding the fluid back into the impeller blade area, respectively.

#### **2.4.6 Stripper**

The stripper (also referred to as 'interrupter' or 'flow stopper') is situated between the suction and discharge ports (Figure 2-10) and plays an important role as it forces the fluid to leave through the outlet rather than flowing back to the inlet region. Limited research exists on the stripper region and investigation into the effects of key parameters such as its length and form should be carried out. A small stripper angle (the angle between the inlet and the outlet ports) gives a corresponding larger pumping area and increases the interaction time between the fluid and the impeller. However, more flow will leak through the stripper gap from the discharge to the suction (Quail, et al., 2010b). The shape of the stripper also has an important influence on the noise level (Gülich, 2010).

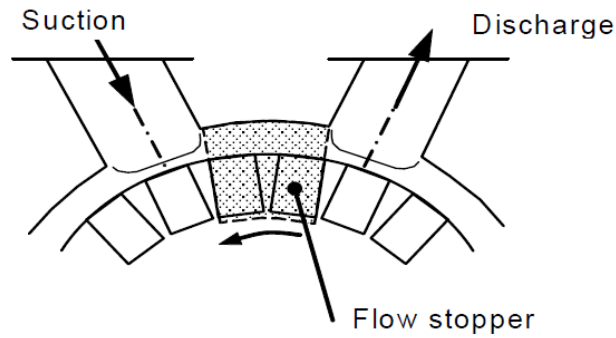


**Figure 2-10: Schematic of a generic regenerative pump showing the stripper region in relation to the pump suction and discharge (Gülich, 2010).**

#### 2.4.7 Suction and Discharge Ports

The design of the inlet controls how the fluid will interact with the impeller blades. The majority of RLR pumps feature straight, vertical ports leading into the channel in a radial direction (Quail, et al., 2012), however studies have shown that this arrangement induces large losses at the inflow (Quail, et al., 2011b). This can be mitigated by realigning the fluid flow so it enters and leaves the pump in an axial direction (Figure 2-11), ensuring that the fluid is directed towards the inlet edge of the impeller blades with the velocity required to ensure smooth entry at the design pressure (Bicard, 1957; Sixsmith, 1981; Karenth & Sharma, 2014).

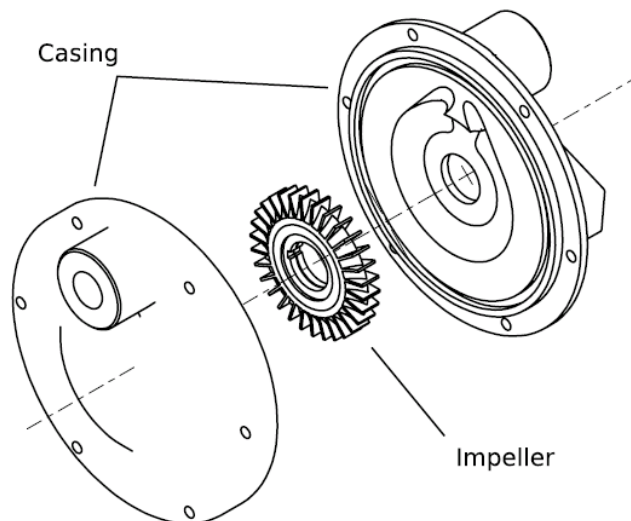


**Figure 2-11: Regenerative pump with axially aligned suction and discharge ports (Quail, et al., 2012).**

Senoo (1956) found that the pump performance is sensitive to the pressure drop that occurs when the fluid enters through the inlet port, indicating that the shape and position of the inlet

are parameters that should be investigated further. Sixsmith (1981) also suggested having a tapered diffuser after the discharge port to reduce the velocity of the fluid and translating some of the kinetic energy to an extra increase in pressure. The axial arrangement of the suction and discharge ports proposed by Quail et al. (2012), shown in Figure 2-11, will also minimise axial thrust on the impeller.

The performance challenges and geometrical design optimisation of the RLR pump are summarised in Table 2-2. Below is an index to the reference column in Table 2-2.

1. Iversen (1955)
2. Shimosaka (1960)
3. Lazarkiewicz & Troskolanski (1965)
4. Raheel & Engeda (2005)
5. Senoo (1948)
6. Senoo (1954)
7. Wilson, et al. (1955)
8. Crewdson (1956)
9. Dewitt (1957)
10. Mason (1957)
11. Shimosaka (1960)
12. Burton (1966)
13. Burton (1967)
14. Yamazaki & Tomita (1971)
15. Yamazaki et al. (1972)
16. Burton (1972)
17. Tomita, et al. (1973)
18. Yamazaki & Tomita (1974)
19. Grabow (1975)
20. Sixsmith & Altmann (1977)
21. Hollenberger & Potter (1979)
22. Sixsmith (1981)
23. Zozulya (1982)
24. Badami (1997)
25. Kang, et al. (2004)
26. Meakhail & Park (2005)
27. Shirinov & Oberbeck (2011a)
28. Shirinov & Oberbeck (2011b)
29. Fleder & Böhle (2012)
30. Choi, et al. (2013)
31. Karenth & Sharma (2014)
32. Zhang, et al. (2016)
33. Horiguchi et al. (2009)
34. Fleder & Böhle (2015)
35. Engels (1940)
36. Pfaff (1961)
37. Quail et al. (2010b)
38. Senoo (1956)
39. Bicard (1957)
40. Quail, et al. (2011b)
41. Quail, et al. (2012)

**Table 2-2: Summary of performance challenges and geometrical design optimisation.**

<b>Geometry and Performance</b>					
<b>Geometry</b>	<b>Performance Effects</b>	<b>Geometrical Parameter / Configuration</b>	<b>Reference Index<sup>3</sup></b>	<b>Most Recent Publication</b>	<b>Comments</b>
<b>Impeller</b>	<ul style="list-style-type: none"> <li>• Axial thrust</li> <li>• Misalignment of blade and fluid angles</li> </ul>	<ul style="list-style-type: none"> <li>• Single-sided</li> <li>• Double-sided</li> <li>• Diameter</li> </ul>	1-4	2005	<ul style="list-style-type: none"> <li>• Double-sided promotes equal pressure distribution, reduces chances of wear</li> <li>• Increasing impeller tip radius and decreasing hub radius mitigate shock and slip losses</li> </ul>
<b>Blade</b>	<ul style="list-style-type: none"> <li>• Misalignment of blade and fluid angles</li> </ul>	<ul style="list-style-type: none"> <li>• Profile</li> <li>• Angle</li> <li>• Number</li> </ul>	4-32	2016	<ul style="list-style-type: none"> <li>• Symmetrical profiles more efficient</li> <li>• Aerofoil and chevron blades perform better</li> <li>• Blades matching fluid angles ensure smooth entry and exit of fluid</li> </ul>
<b>Clearance</b>	<ul style="list-style-type: none"> <li>• Backflow</li> <li>• Entry to blade</li> <li>• Circulation</li> </ul>	<ul style="list-style-type: none"> <li>• Axial</li> <li>• Radial</li> </ul>	4, 22, 24, 34	2015	<ul style="list-style-type: none"> <li>• No definite number for optimal clearance</li> <li>• Less attention given to radial clearance</li> </ul>
<b>Side-channel</b>	<ul style="list-style-type: none"> <li>• Resistance</li> <li>• Turbulence</li> <li>• Circulation</li> </ul>	<ul style="list-style-type: none"> <li>• Shape</li> <li>• Width</li> <li>• Depth</li> </ul>	3-4, 6, 8, 16, 22, 24, 34-36	2015	<ul style="list-style-type: none"> <li>• Rounded shape assist circulation and reduces turbulence</li> <li>• Increasing width reduces power consumption loss</li> <li>• Return vanes for improved fluid guidance</li> </ul>
<b>Stripper</b>	<ul style="list-style-type: none"> <li>• Backflow</li> </ul>	<ul style="list-style-type: none"> <li>• Length</li> <li>• Width</li> <li>• Shape</li> </ul>	37	2010	<ul style="list-style-type: none"> <li>• Limited research exists</li> </ul>
<b>Suction / Discharge</b>	<ul style="list-style-type: none"> <li>• Initial fluid interaction</li> <li>• Axial thrust</li> </ul>	<ul style="list-style-type: none"> <li>• Alignment</li> <li>• Shape</li> <li>• Auxiliary fittings</li> </ul>	22, 38-41	2012	<ul style="list-style-type: none"> <li>• Axial arrangement ensures alignment of fluid</li> <li>• Diffuser at discharge to reduce velocity</li> </ul>

<sup>3</sup> Index to references provided on the previous page.

## 2.5 Conclusions and Scope for Further Research

Despite the fact that the exact principle of operation of the RLR pump has been a phenomenon not fully understood, it has nevertheless been widely applied for over a century in areas of liquid pumping. Its interesting design makes it suitable for a wide range of applications, particularly when efficiency is of less importance than stable operating conditions. Due to the low specific speed, it is an excellent choice when small quantities of liquid are to be delivered against high heads. Research and development of other regenerative turbomachinery has grown in volume and speed due to the availability and increasing usage of CFD in recent times; models can be continually refined and then verified with experimental testing in a shorter timeframe. However, the literature reviewed has demonstrated a need to establish the state-of-the-art for three-dimensional numerical analysis for RLR pumps in order to bridge this gap in knowledge.

The main challenges identified for further improvement in the performance of RLR pumps include the ability to fully comprehend the highly complex and turbulent internal flow field and the associated losses that occur. Early research made an attempt at this through various mathematical models, however they could not fully represent the three-dimensional helical flow pattern and also required experimental correction data. The design of the regenerative machine has evolved in parallel to this work over many decades. Improvements have been made, particularly in the shape and number of impeller blades, though very few published works are available that look at other design aspects such as radial and axial clearances, and more crucially most researchers tend to investigate these elements in isolation. This highlights the key driver of this current research, which aims to systematically assess the effect on pump performance of a large range of geometrical features, such as variations in impeller-casing clearance size combinations. The initial dimensions of these clearances are determined by the drawing manufacturing tolerances and by analysing a wide range of combinations, optimum clearances can be ensured from inception.

There is also no research investigating potential impeller deformation during operation and how this affects the magnitude of the axial and radial clearances, highlighting an important area for further study that has not been identified before. RLR pumps are subject to high rotational speeds and pressure loads which induce undesired effects such as mechanical



vibration and noise, which is likely to cause some deformation of the impeller and subsequently the shape and the thickness of the clearances.

## **3 Research Aims and Contribution to Knowledge**

### **3.1 Research Aims**

The main aim of this industry funded Ph.D. is to assess the relationship between manufacturing tolerances and pump performance of a Gilkes RLR pump using a commercial Computational Fluid Dynamics (CFD) code and experimental testing. Based on differences in pump performance, reasonable estimates of product lifetime can be ascertained, allowing the manufacturer to better predict pump service times. To achieve this, the following objectives were set:

1. To develop a computational model to analyse the flow through the RLR pump using modern CFD tools.
2. To analyse the effects on pump performance for a large range of impeller-casing clearance combinations using the chosen CFD model.
3. To validate the results obtained using the CFD model by comparison with experimental testing.

### **3.2 Research Methodology**

The research approach is listed below:

1. Review of literature to establish suitable numerical modelling techniques for RLR pumps.
2. Based on prominent techniques found in literature, develop a CFD model using assumptions to reduce the computational cost while ensuring accuracy of the model.
3. Determine parameters for impeller-casing clearance analysis.
4. Test and evaluate suitability of chosen CFD model.
5. Finite Element Analysis (FEA) of test pumps under hydraulic loading.
6. Develop improved manufacturing design tolerance limits for the 2.5" SX pump.

### **3.3 Contribution to Knowledge and Practice**

Systematic parametric clearance modelling: Although some studies exist on the effects of different clearance magnitudes on the pump performance, they are limited in the number of impeller-casing clearance combinations. Furthermore, the studies feature relatively simple

geometries with radial blades. The chevron shaped impeller in the Gilkes design has a complex geometry and a larger wetted surface in the peripheral circumference. The results of the extensive study showed that large performance gains can be made with tighter manufacturing tolerances, particularly the ones affecting the radial clearance size. The findings can be combined with a performance-cost analysis to better understand the life cycle of a RLR pump from manufacture to decommissioning and ensure optimum impeller-casing clearances from inception. Larger clearances are likely to reduce the rate of internal wear and increase the operational life of the pump. In contrast, tighter clearances provide improved performance at the cost of an increased rate of wear, as well as an increase in cost due to higher manufacturing specification.

Impeller deformation modelling: Due to the inherent periodically unsteady flow-induced impeller oscillations occurring in the regenerative pump coupled with high rotational speeds, undesired effects such as mechanical vibration, noise and impeller deformation occur in regenerative pumps. This research has for the first time investigated and shown how the impeller deformation during operation can affect the magnitude of the axial and radial clearances, highlighting an important area for further study that has not been identified before.

Maximum manufacturing tolerance design limits for optimum performance: This research has determined the maximum manufacturing tolerances of a 2.5" SX pump using a combination of modern CFD tools, experimental testing and FEA to ensure a consistent pump performance, providing the manufacturer with the tools to better tailor their designs to meet the needs of their customers and reduce the total cost of ownership either by improving the efficiency or extending the lifespan through improved design. With the current 2.5" SX design, the maximum allowable radial design clearance should be reduced by 35%. With this radial design tolerance the magnitudes of the drive end and non-drive end clearances have a lower impact on the performance. In addition to a lower maximum radial tolerance, the maximum assembly tolerance (the axial alignment of the impeller in relation to the casing) should be reduced by 14%.

## 4 Computational Modelling Methodology

This chapter introduces the Computational Fluid Dynamics (CFD) model chosen for this research based on available resources, literature and the ability of the industrial sponsors, *Gilbert Gilkes & Gordon Ltd.*, to easily incorporate and adapt the model into their systems. Areas of importance when developing a CFD model are turbulence modelling, mesh generation, application of boundary conditions, data processing and efficient use of the computational resources available. The details of computational models used and assumptions are described in this chapter together with the modelling techniques used for the operational performance and clearance analysis. This chapter also examines the potential errors introduced by various modelling assumptions to reduce computational costs while maintaining an acceptable numerical accuracy. Finally, the mesh independence study is presented to quantify the discretisation error.

### 4.1 Modelling Software

The RLR pump is modelled using the commercial CFD software, ANSYS® CFX®. The version of CFX® used was 15.0 and it was originally used within the ANSYS® Workbench® platform, however when access to the Lancaster High End Computing (HEC) cluster became available halfway through the project, the standalone version was used. Domain geometries were created using the commercial CAD packages SolidWorks® 14.0 and ANSYS® DesignModeler®. The meshes were created using the ANSYS® Meshing® tool.

### 4.2 CFD Model Assumptions

The development and initial verification of the computational model used in the clearance analysis of the RLR pump are detailed here. The model focuses on a duty point provided by the industrial sponsors but other head-flow rate points are also investigated in order to compare the simulation results to available experimental test data. The CFD model is then analysed, modified and enhanced to reduce the computational expense while maintaining an acceptable level of accuracy. The assumptions introduced to achieve this have been divided into *4.2.1 Geometric Assumptions* and *4.2.2 Modelling Assumptions*.

### 4.2.1 Geometric Assumptions

Contrary to typical turbomachines, such as the centrifugal pump, the RLR pump does not have any symmetry or periodicity and therefore the full fluid region incorporating all the major flow paths (suction, discharge, side channels, impeller and clearances) has to be modelled. The complex geometry requires careful modelling and potentially large meshes to capture relevant detail, subsequently increasing the amount of computational resources required to analyse the flow mechanism in the pump. However, there are some simplifications that can be made. The simplifications and geometrical assumptions used to create the CFD model are detailed below.

#### 4.2.1.1 Port Plate Simplification

The particular design of RLR pump used in this research features side channels on either side of the impeller. The side channel ring is discontinued by port plates to limit the available leakage flow path, i.e. axial clearance. For the non-drive end (NDE) side of the pump, the port plate is a separate part to the casing, as seen in Figure 4-1. When extracting the fluid region, small and complex geometrical shapes are created where the interfaces are not fully lining up. In order to avoid this the port plate was incorporated into the NDE body in a similar manner as on the drive end (DE) body.

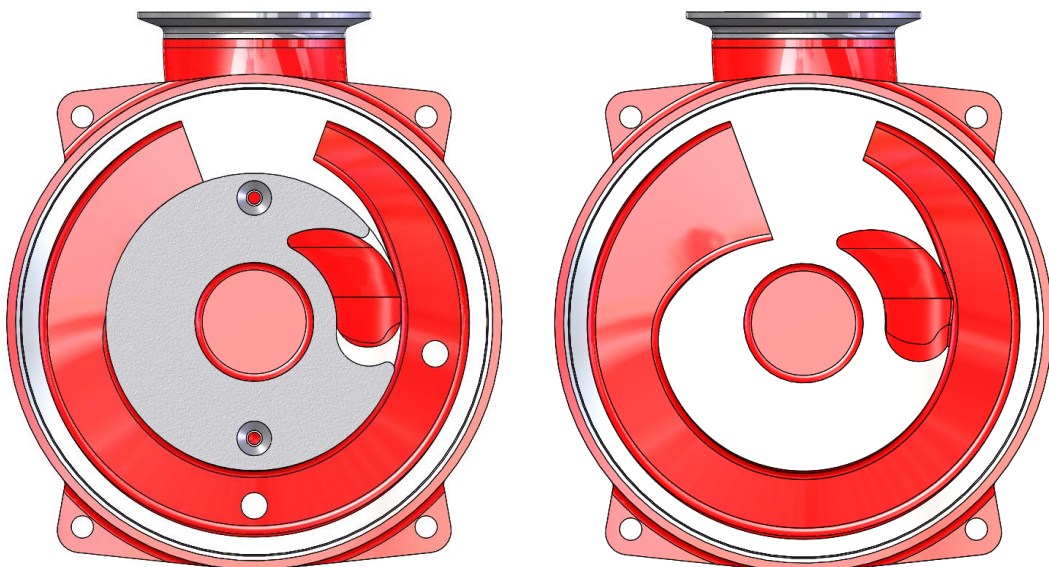


*Figure 4-1: Port plate on NDE before (left) and after (right) simplification.*

#### **4.2.1.2 Axial Clearance Reduction**

In reality the axial clearance 'disks' on either side of the impeller extends all the way to the shaft (see Figure 4-2). However, these inner flow paths are not uniform in thickness leading to additional complexity of the fluid domain geometry. Furthermore, eliminating these inner disks simplifies and streamlines the geometry generation for the parametric clearance study (5 *Parametric Clearance Analysis*).

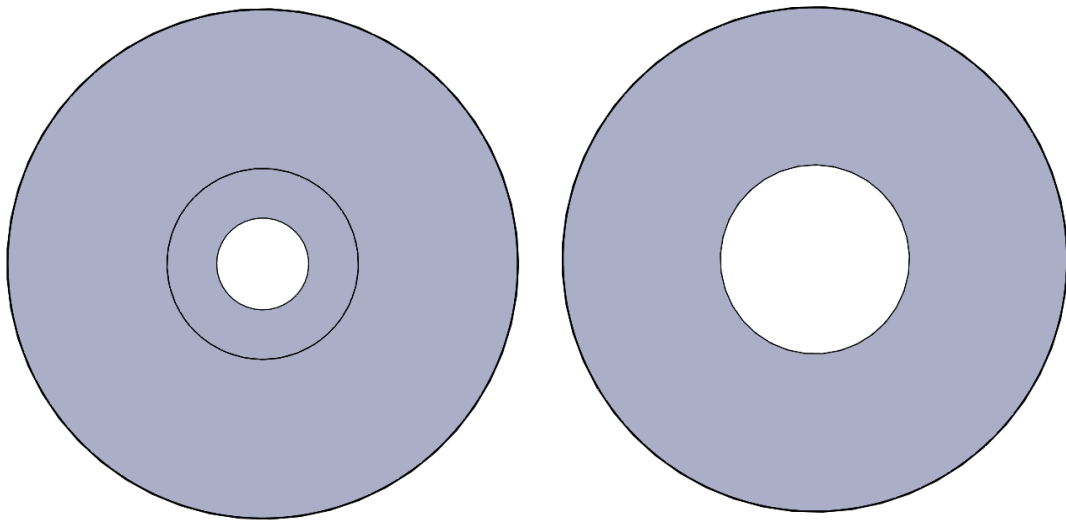


**Figure 4-2: Rotating fluid domain with (left) and without (right) additional axial clearance paths.**

A test case has been run with these additional axial clearance paths, assumed to be uniform in thickness, showing that only small differences in pressure exist when compared to a case without the additional flow paths.

#### **4.2.1.3 Side Channel Simplification**

As can be seen in Figure 4-3 the end tip of the side channel ring on the right hand side of the DE body is very narrow and slim, which becomes problematic during the meshing process due to the creation of poor quality elements in the boundary layer. Therefore a small segment was sliced off increasing the mesh quality significantly.

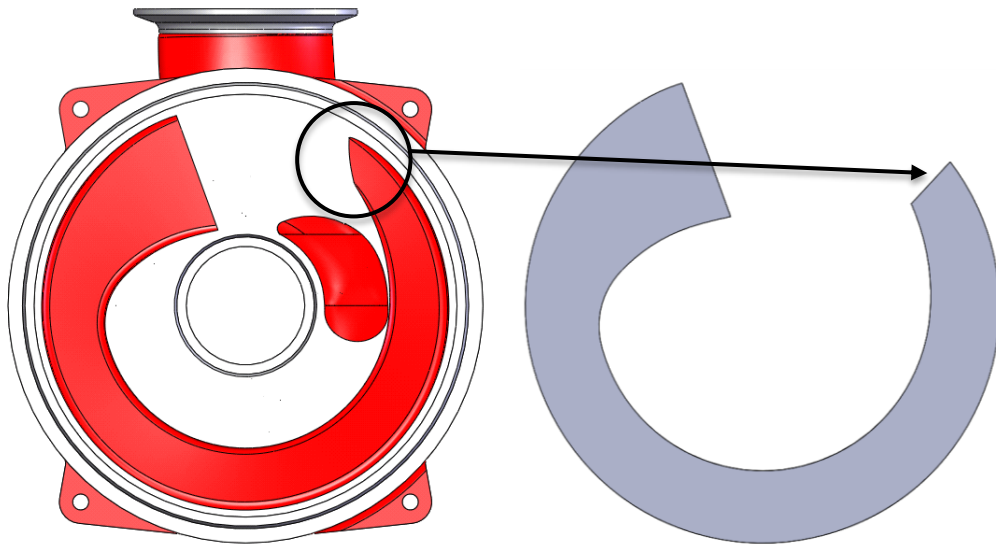


*Figure 4-3: Modified side channel ring on DE side.*

#### **4.2.1.4 Inlet and Outlet Pipe Extension**

As the exact setup of the previous experimental tests were unknown, the outlet and inlet of the computational model were extended five diameters upstream (of the pump suction) and downstream (of the pump discharge), see Figure 4-4. This is to allow the flow field to fully develop before it enters the impeller and to avoid recirculation at the outlet (Spence & Amaral-Teixeira, 2008; Škerlavaj, et al., 2011).

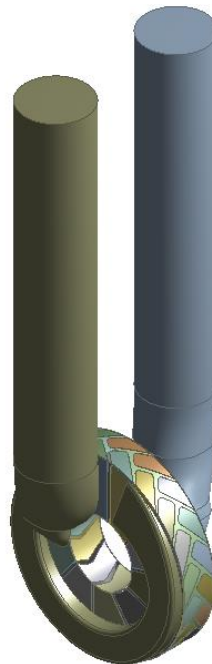


*Figure 4-4: Computational fluid domain with extended outlet (left) and inlet (right) pipes.*

#### 4.2.1.5 Clearance Dimensions

The initial dimensions of the clearances were based on a median value of the manufacturing tolerances and are given in Table 4-1 below, along with the designated abbreviations used during the clearance analysis.

*Table 4-1: Initial clearance dimensions.*

	<b>Unit</b>	<b>Drive End</b>	<b>Non-drive End</b>	<b>Radial</b>
<b>Dimension</b>	[mm]	0.26	0.51	0.278
<b>Abbreviation</b>	[-]	DE	NDE	R

#### 4.2.2 Modelling Assumptions

In addition to the geometric simplifications of the fluid domain, a series of assumptions relating to the physics of the problem must also be defined. This will inform the selection of the most suitable numerical techniques. This section details the selection and assumption process and provides justification in the form of evidence found in literature or sensitivity analyses carried out on the CFD model.

##### 4.2.2.1 Turbulence Model

Turbulence is a complex phenomenon characterised by fluid motion with chaotic changes in pressure and flow velocity, where the transported quantities of mass and momentum alter in space and time (Batchelor, 2012). Turbulent flows occur over a large range of length and time scales and in many cases involve length scales that are smaller than what can be captured in an affordable mesh resolution. A complete description of a turbulent flow, in which the flow variables are known as a function of space and time, can only be obtained by numerically solving the Navier-Stokes equations. However, this Direct Numerical Simulation (DNS) of turbulence requires unrealistic computational resources (Škerlavaj, et al., 2011). Other options, which resolve the large energy-containing scales while also modelling the influence of the scales smaller than the mesh, such as Scale Resolving Simulation (SRS), are available. In ANSYS® CFX®, the SRS options are Large Eddy Simulation (LES) and Detached Eddy Simulation (DES) (ANSYS, Inc., 2013). If the resolution of large scales is important these options provide more accurate results, however it necessitates the use of a very fine mesh and small timesteps



in order to capture the eddy formation. This results in simulations that are time intensive and generate large quantities of data.

As an alternative to these intensive techniques, statistical models based on Unsteady Reynolds-Averaged Navier-Stokes (URANS) equations are used, in which all the scales of the turbulence are modelled rather than solved. The most widely used are the Two-Equation Turbulence Models which provide a good compromise between computational expense and numerical accuracy. The  $k$ - $\epsilon$  and  $k$ - $\omega$  models include additional separate equations to solve for turbulent kinetic energy ( $k$ ), turbulent dissipation ( $\epsilon$ ) and turbulence frequency ( $\omega$ ). One of the most used two-equation turbulence models in ANSYS® CFX® is the  $k$ - $\omega$  Shear Stress Transport (SST) model (ANSYS, Inc., 2013). It is a combination of the  $k$ - $\epsilon$  and  $k$ - $\omega$  models where the  $k$ - $\epsilon$  model is used in the freestream zone while the  $k$ - $\omega$  model is used near the wall.

Due to the lack of research into turbulence modelling in regenerative pumps, a few simulations were run with the following turbulence models to assess their influence on the flow and the computational cost:  $k$ - $\omega$ ,  $k$ - $\epsilon$  and the  $k$ - $\omega$  SST model with the 2<sup>nd</sup> order and then the high resolution turbulence scheme selected. These were compared against a modified SST turbulence model with curvature correction (SST-CC), the results are presented in Table 4-2 and Figure 4-5.

Although the SST model can accurately predict the onset and the amount of flow separation under adverse pressure gradients, the flow recovery can be too slow and the separation area may become too large. The two-equation models are not always capable of capturing the effects of streamline curvature and system rotation. It is possible to implement a curvature-correction (CC) term to the SST model, i.e. a SST-CC model, which is much more accurate than the SST model over a wide range of flows (Menter, et al., 2003).

**Table 4-2: Normalised pressure for different turbulence models.**

Turbulence Model	Unit	k- $\omega$ SST (2 <sup>nd</sup> order)	k- $\omega$ SST (high resolution)	k- $\epsilon$	SST-CC
<b>Timestep</b>	[s]	$3.52 \times 10^{-5}$			
<b>Mass Flow Rate</b>	[kg s <sup>-1</sup> ]	5.9			
<b>Rotational Speed</b>	[rpm]	2300			
<b>Normalised Pressure</b>	[%]	100.00	100.51	103.56	98.63
<b>Solve Time</b>	[h, min]	30h, 33min	33h, 10min	27h, 13min	33h, 39min

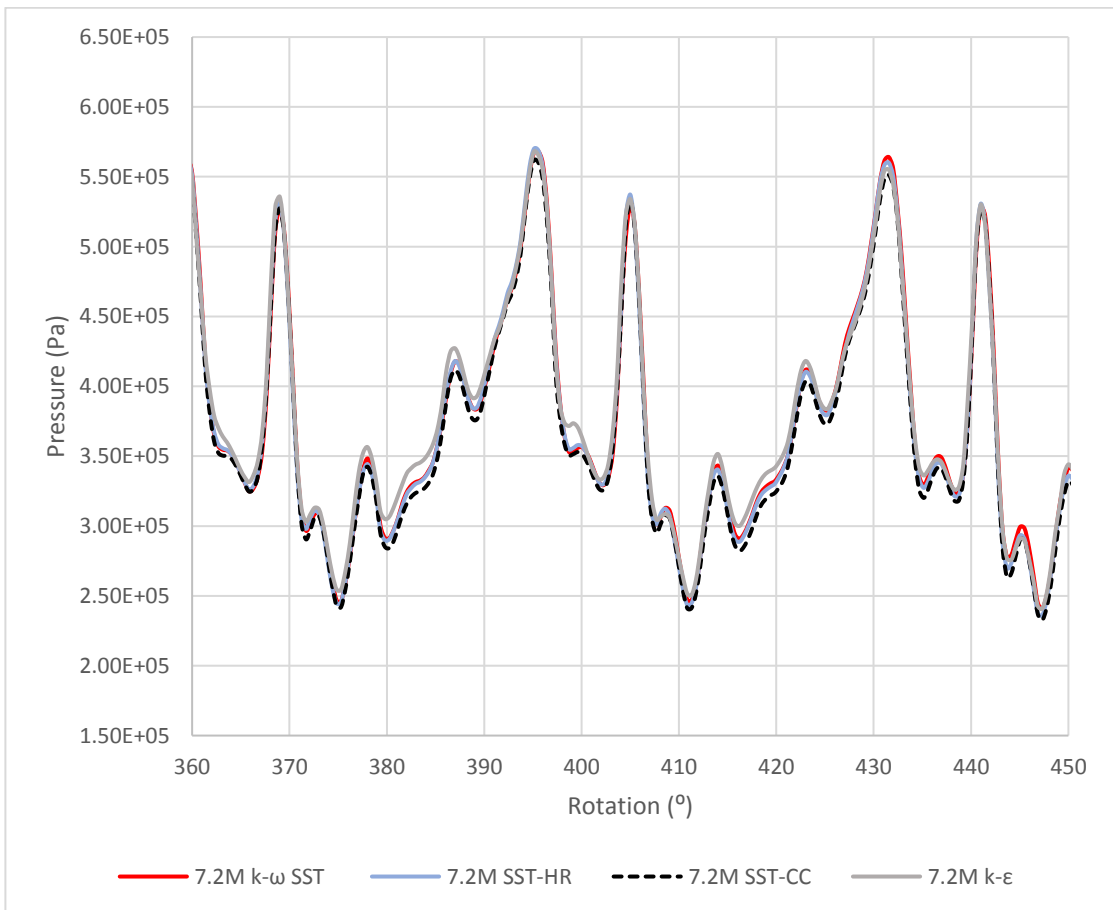


**Figure 4-5: Pressure pulsations using different turbulence models.**

Despite the benefits of the SST-CC model, little research into its use in regenerative pumps has been carried out. In this application, the k- $\omega$  SST model provided results closer to the true experimental value than the SST-CC model (the experimental performance curves are discussed in more detail in *6.9 Results Comparison and Discussion*), within a reasonable

timescale. It is also robust and generally preferred in pump applications, re-affirming that it is a suitable model for this research.

#### **4.2.2.2 Precision**

Where possible the use of double precision for transient simulations with fast mesh motions is advised. However, running in double precision mode can become computationally expensive. A test case was carried out to compare single and double precision, showing insignificant difference in pressure (approximately 0.5%) and therefore the single precision mode was used.

#### **4.2.2.3 Unsteady Calculations**

When modelling a fluid flow with rotating and stationary domains coupled together, such as in this research, there are different methods for solving the flow field. In ANSYS® CFX®, there are three types of frame change models available; Frozen Rotor, Stage and Transient Rotor-Stator. In the 'Frozen Rotor' approach, the two frames of reference have a fixed relative position throughout the calculation, analogous to freezing the impeller in a specific position and observing the instantaneous flow field at that point. The rotating flow field is solved in a rotating frame of reference and the Coriolis force is accounted for by the source terms while the stationary flow is solved in a fixed frame of reference. This model produces a steady state solution to the multiple frame of reference problem and the Reynolds-Averaged Navier-Stokes (RANS) equations are solved. As a result, it does not model unsteady (transient) effects at the frame change interface. The 'Stage' model is an alternative to the Frozen Rotor model, enabling steady state predictions to be obtained for multistage machines.

Most of the published work on numerical analysis of RLR pumps is carried out using steady state calculations. For steady state calculations, the flow characteristics do not change with time and steady state conditions are assumed to be reached after a relatively long time interval. However, due to the kidney-shaped inlet/outlet ports, only a few impeller pockets will be exposed to the flow during steady state simulations. In reality the circulatory flow is driven by the periodic passage of the impeller blades past the kidney-shaped ports, therefore the flow is expected to be highly unsteady. The characteristic pressure pulsations observed for transient (unsteady) simulations are not captured in steady state simulations, however the pressure can be observed to oscillate in the form of periodic sinusoidal waves. Steady state

simulations are mainly performed to obtain good initial conditions (i.e. details of the flow-field) before starting a transient analysis. A key part of this research is to fully understand the effects of different clearances on the performance and operational life of the pump, and it is important to be able assess the effects of the blades moving past the kidney shaped inlet/outlet ports at different clearances.

The simulations therefore require transient analysis using a rotating frame of reference. The 'Transient Rotor-Stator' approach solves the unsteady RANS equations, accounting for the transient interaction effects of the flow between the rotating and stationary domains. The interface position is updated at each timestep as the relative motion between the domains is simulated.

### **4.3 Simulation Setup and Analysis**

This section details the setup of the RLR pump simulation based on the assumptions discussed in *4.2 CFD Model*. It also covers the methodology to determine the performance of the pump from the computational results.

#### **4.3.1 Computational Domain Geometry**

The full fluid domain used for the computational analysis was created using the CAD geometry for the 2.5" SX pump provided by the industrial sponsors (Figure 1-5). The computational domain consists of a rotational domain (impeller, radial and axial clearances) and two stationary domains (side channels, suction and discharge pipes). The pump simulation fluid domain was created by extracting the fluid cavity using ANSYS® DesignModeler® (Figure 4-6), an inbuilt parametric geometry software of ANSYS® Workbench®. The fluid domain was then optimised using a combination of the commercial CAD software SolidWorks® and DesignModeler®.

The full fluid region was divided into three parts (1-suction, 2-discharge and 3-impeller) and subsequently split into a number of fluid bodies for modelling: [1A] the suction pipe, [1B] the suction side channel, [2A] the discharge pipe, [2B] the discharge side channel, [3A] the leakage flow paths containing the radial and axial clearances and [3B] the pump impeller, as seen in Figure 4-6(a). This allows each fluid region to be meshed individually and tailored to the modelling requirements in that particular region. The axial and radial clearances were

incorporated into the rotating impeller fluid region [3] and separated into several smaller bodies for ease of mesh control as illustrated in Figure 4-6(b). The inlet of the pump is located on the DE (right hand side), while the outlet is located on the NDE (left hand side).

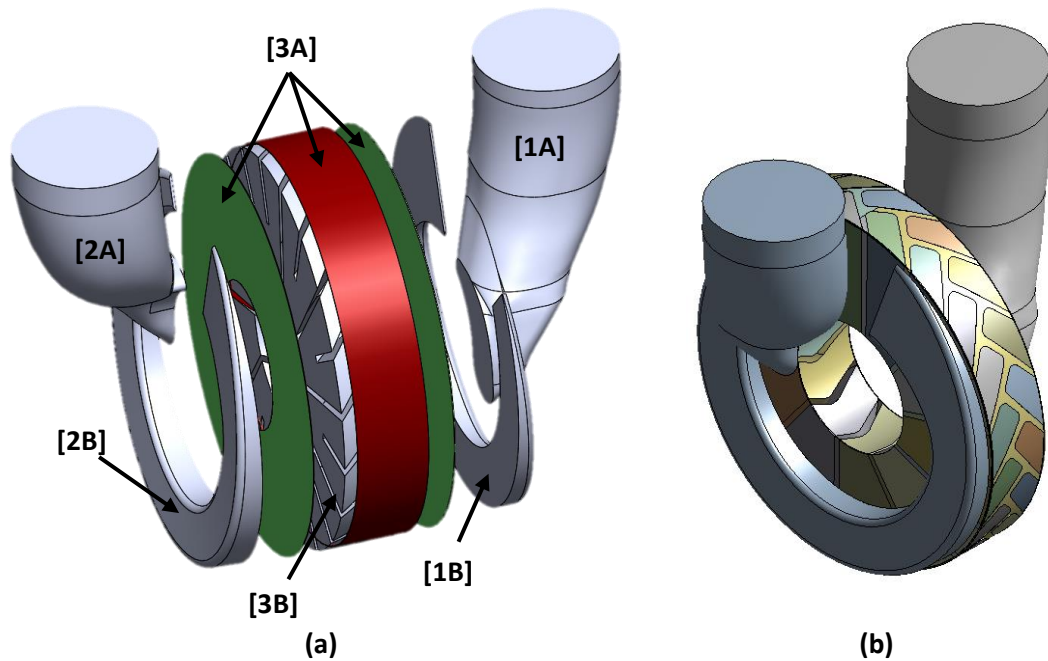


**Figure 4-6: Computational fluid model geometry showing (a) main fluid bodies and (b) further decomposition of clearances.**

The axial clearance 'disks' are decomposed by extruding the faces of impeller fluid bodies outwards in the axial direction of the clearances, effectively slicing the axial clearance flow paths into the shapes shown in Figure 4-7(a). There are a total of 40 axial clearance bodies on each side of the impeller. The extrude feature cannot be applied in the radial direction, therefore the peripheral faces of the impeller fluid bodies are extended outwards using the 'thin' feature in which the defined thickness corresponds to the dimension of the radial clearance 'ring'. The newly created thin radial clearance bodies are then merged with the radial clearance flow path, effectively slicing the ring into the chevron shaped body shown in Figure 4-7(b). The chevron shaped ring is then divided up further by using the thin feature to extend the thin peripheral faces of the axial clearance bodies in the radial direction, creating thin slices which are then merged with the chevron ring. These two processes create a total of 120 radial clearance bodies.

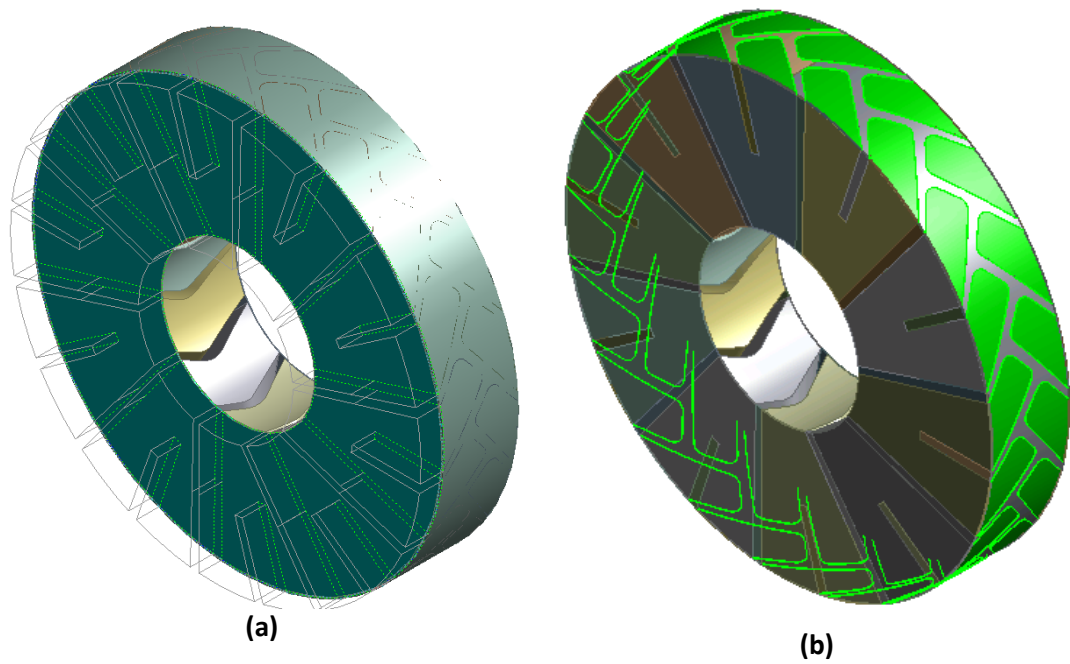


**Figure 4-7: Decomposition of (a) axial clearance and (b) radial clearance flow paths.**

### 4.3.2 Operating Conditions

The operating conditions used for the pump simulations were based on previous *Gilbert Gilkes & Gordon Ltd.* internal experimental testing, the duty point conditions provided are detailed in Table 4-3.

**Table 4-3: 2.5" S pump duty point operating conditions used in computational modelling**

	<b>Unit</b>	<b>Value</b>
Inlet diameter	[mm]	63.50
Inlet area	[mm <sup>2</sup> ]	3166.92
Rotational Speed	[rpm]	2300
Mass Flow Rate	[kg s <sup>-1</sup> ]	5.88
Inlet Velocity	[m s <sup>-1</sup> ]	1.86
Pressure Differential	[kPa]	310.26

### **4.3.3 Mesh**

The meshes used for the computational modelling were generated using the ANSYS® Meshing® software. This software was chosen due to its user friendliness. ANSYS® CFX® is a mesh based CFD technique that uses the Eulerian specification of fluid flow. The domain is discretised using finite volume elements. The extended pipes could be meshed with structured hexahedral elements near the walls because of their simplistic shapes. However, unstructured tetrahedral elements were used for generating the mesh on the lower pipes, side channels and the rotating domain due to the more complex geometries.

Due to the complexity of the pump geometry, care was taken regarding the distribution of the mesh elements in the model. Figure 4-8 provides an indication of the mesh distribution. A larger element size in the suction and discharge pipes is acceptable for the computational modelling (Fleder & Böhle, 2015) as the regions of critical importance are the axial and radial clearances surrounding the impeller. The sizes were selected based on the need to accurately represent the nature of the complex flow field but also to obtain an acceptable mesh quality. The orthogonal quality was kept above 0.1 and the skewness below 0.95. The meshing methodology for the stationary and rotating domains is detailed in this section.

#### **4.3.3.1 Stationary Domains**

The stationary domains consist of 1.8 million mesh elements. The lower pipes and side channels feature tetrahedral elements, while the upper pipes consist of hexahedral elements in the boundary layer (10 layers). Figure 4-9 shows the detailed meshing of the stationary domain bodies, denser mesh sizing closer to the impeller entry/exit and larger elements further afield.

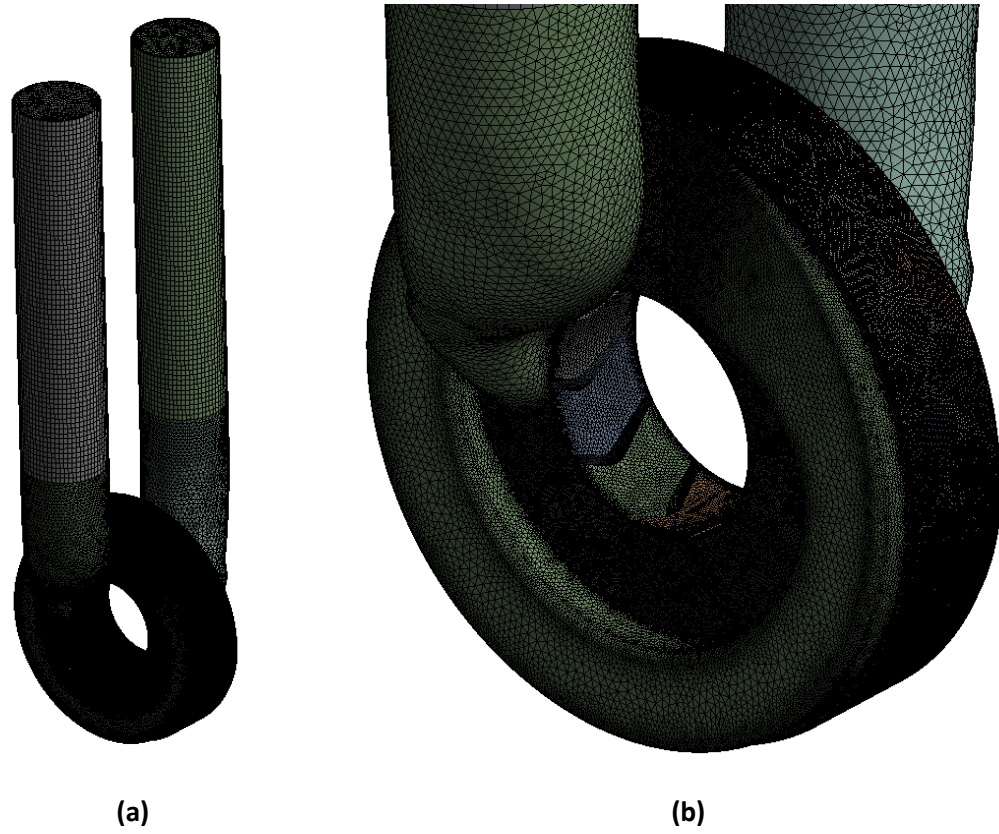


**Figure 4-8: Mesh arrangement of (a) the total pump fluid region and (b) the impeller fluid region.**

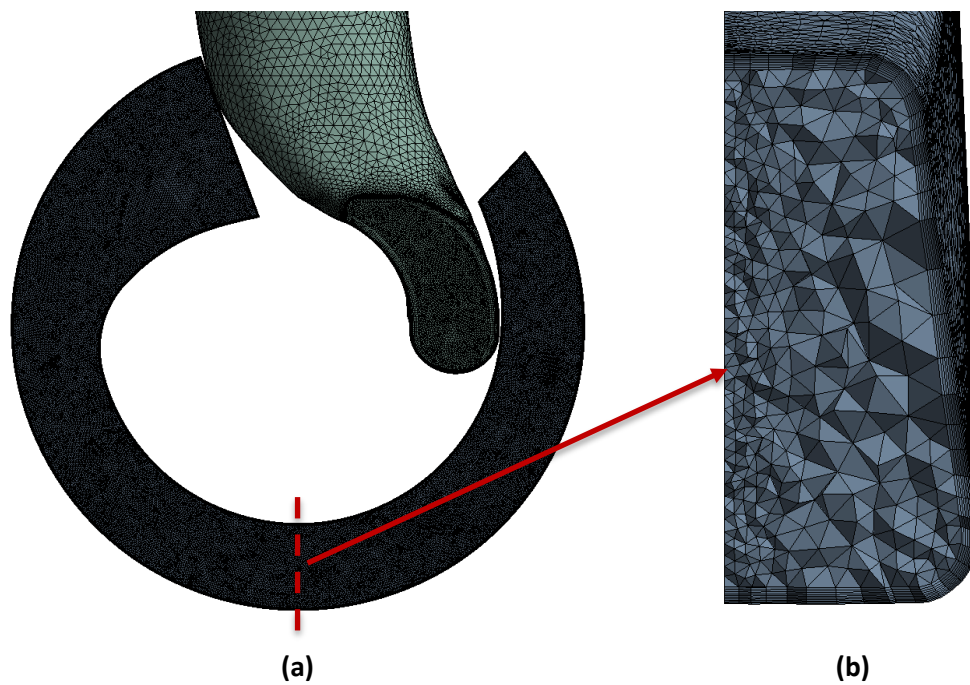


**Figure 4-9: Mesh arrangement of (a) DE side channel/inlet pipe and (b) cross-sectional view of side channel showing mesh density regions and inflation layers.**



### 4.3.3.2 Rotating Domain

The rotating domain consists of 5.4 million mesh elements. The impeller fluid region (fluid filled pockets between the impeller blades), see Figure 4-10(a), was meshed as an unstructured tetrahedral mesh due to the complexity of the geometry, including wedge and pyramid shaped cells due to the inflation layers at the wall boundaries. The inflation layers shown in Figure 4-10(b) consist of 10 layers.

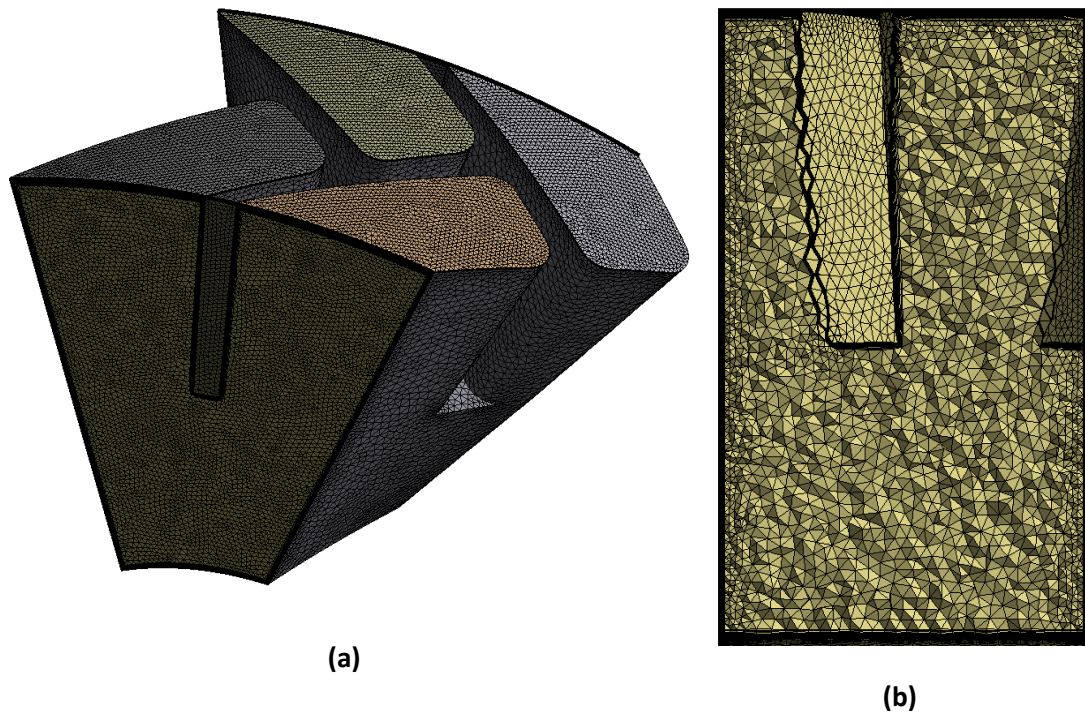


**Figure 4-10: Mesh arrangement of (a) one impeller blade fluid region and (b) cross-sectional view of impeller blade pocket showing mesh density regions and inflation layers.**

The axial and radial clearances around the impeller are very small, often less than 0.5 mm. It is essential to be able to capture the behaviour of the flow at these points of interest. As the thickness can be different for the DE, NDE and radial clearances, a set element size of 0.04 mm was used to distribute the elements equally within each clearance space. This was controlled by the means of a sweep mesh feature. The element size across these clearances was then decreased in increments of 0.01 mm during the mesh independence analysis. The number of elements generated across each clearance based on the element sizes used in the mesh independence study are shown in Table 4-4.

**Table 4-4: Number of elements across each clearance**

<b>Clearance Name</b> [-]	<b>Clearance Dimension</b> [mm]	<b>Element Size</b> [mm]	<b>No. of Elements</b> [-]
Drive End (DE)	0.26	0.04	7
		0.03	9
		0.02	13
Non-drive End (NDE)	0.51	0.04	13
		0.03	17
		0.02	26
Radial (R)	0.278	0.04	7
		0.03	9
		0.02	14

The overall mesh design was improved further by ensuring that the element size on each of the domain interfaces was matched to warrant smooth transitions of the flow field across the interfaces.

The computational domain was meshed in five stages:

1. Impeller fluid region
2. Axial clearances
3. Radial clearance
4. Side channels and lower pipes
5. Extended pipes

Named selections were defined in ANSYS® Meshing® in order to streamline the process of meshing and setting up the simulation. Names were applied to all faces in the domains, which are called upon when applying mesh controls and setting up the solver physics in CFX-Pre. The named selections used for the stationary and rotating domains are shown in Table 4-5.

**Table 4-5: Named selections used on stationary and rotating domain boundaries**

	<b>Selection Name</b>	<b>Description</b>
<b>Stationary Domains</b>	inlet	Inlet five diameters upstream from pump inlet
	outlet	Outlet five diameters upstream from pump exit
	Sint_de	Interface surface between stationary and rotating domains on DE
	Sint_nde	Interface surface between stationary and rotating domains on NDE
	walls_fluid_in	Internal walls of pipe and side channel on DE
	walls_fluid_out	Internal walls of pipe and side channel on NDE
<b>Rotating Domain</b>	Rint_de	Interface surface between rotating and stationary domains on DE
	Rint_nde	Interface surface between rotating and stationary domains on NDE
	walls_imp	Impeller walls
	stat_walls	Internal casing walls around the periphery of the impeller

The naming convention for the named selections shown in Table 4-5 are consistent throughout the computational modelling studies. The meshing sequence and sizing were automated using *Worksheet*, which creates a record of the meshing operations and allows them to be used again for future mesh generations.

#### **4.3.4 Physics Definition**

The definition of the simulation physics was carried out in CFX-Pre, a pre-processor for ANSYS® CFX®, where the mesh is imported and the simulation is set up (Figure 4-11). The named selections defined in ANSYS® Meshing® (4.3.3 Mesh) were carried through to CFX-Pre and used to define the boundary conditions and monitor points.

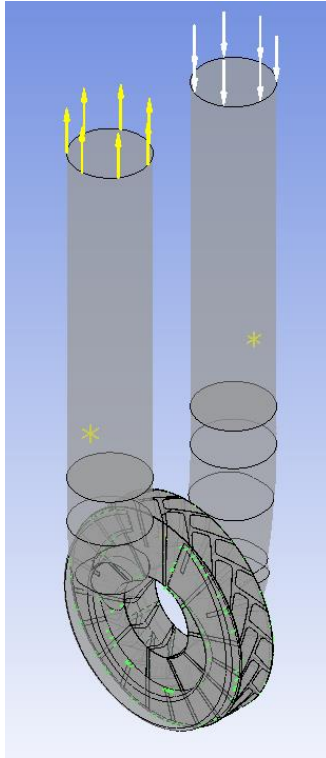


**Figure 4-11: Computational domain in CFX-Pre.**

#### **4.3.4.1 User Defined CEL Expressions**

A number of user defined expressions can be created in ANSYS® CFX® to control the simulation and calculate the output parameters of interest. These output parameters can also be monitored as the simulation progresses. The expressions used in the pump simulations are detailed below.

EXPRESSIONS:

$$\text{DeltaT} = \text{TimePerRev}/80/20$$

*Defines the time per timestep.*

$$\text{RotSpeed} = 2300 \text{ [rpm]}$$

*Defines the rotational speed of the impeller at the duty point.*

$$\text{TimePerRev} = 2*2*\pi/\text{RotSpeed}$$

*Defines the total simulation time in terms of revolutions of the impeller (two in this case).*

InletPressure = areaAve(Pressure)@inlet

*Calculates the static pressure at the far inlet.*

OutletPressure = areaAve(Pressure)@outlet

*Calculates the static pressure at the far outlet.*

PressureDrop = areaAve(Pressure)@outlet-areaAve(Pressure)@inlet

*Calculates the pressure increase across the pump.*

InterfaceDE = areaAve(Pressure)@interface\_DE Side 1

*Calculates the static pressure at the interface between the rotating and stationary domains on the DE.*

InterfaceNDE = areaAve(Pressure)@interface\_NDE Side 1

*Calculates the static pressure at the interface between the rotating and stationary domains on the NDE.*

Pin = areaAve(Pressure)@P in

*Calculates the static pressure at the pump inlet.*

Pout = areaAve(Pressure)@P out

*Calculates the static pressure at the pump outlet.*

MassFlowIn = massFlow@inlet

*Calculates the mass flow rate at the far inlet.*

MassFlowOut = massFlow@outlet

*Calculates the mass flow rate at the far outlet.*

Torque = (torque\_z)@impeller

*Calculates the torque on the impeller shaft.*

myFlowRate = 21.23609 [m<sup>3</sup> h<sup>-1</sup>]

*Defines the volumetric flow rate for the power output calculation.*

myMassFlowRate = 5.881218 [kg s<sup>-1</sup>]

*Defines the mass flow rate at the inlet.*

myVelocity = 1.86267 [m s<sup>-1</sup>]

*Defines the velocity at the inlet for the stationary domain initialisation.*

PowerIn = RotSpeed\*Torque

*Calculates the required input power.*

PowerOut = myFlowRate\*PressureDrop

*Calculates the output power.*

Efficiency = PowerOut/PowerIn

*Calculates the efficiency of the pump.*

Head = PressureDrop/(myRho\*g)

*Calculates the head produced by the pump.*

VelocityIn = ave(Velocity)@inlet

*Calculates the velocity at the inlet.*

VelocityOut = ave(Velocity)@outlet

*Calculates the velocity at the outlet.*

myRho = massFlowAve(Density)@inlet

*Calculates the density of the fluid entering the computational domain.*

#### **4.3.4.2 Materials**

The simulation contained only one fluid which was defined under isothermal conditions and constant fluid properties. The fluid was water at 25°C with a density of 997 kg m<sup>-3</sup> and a dynamic viscosity of 8.899\*10<sup>-4</sup> kg m<sup>-1</sup> s<sup>-1</sup>.

#### **4.3.4.3 Domain Interfaces**

The dynamic interfaces between the stationary and rotating domains were set to Fluid-Fluid interface with a General Connection and a Transient Rotor Stator Frame Change model to model the transient effects using a rotating frame of reference method. The Pitch Change option was set to 'None' as the full pump was modelled and the interface surfaces are aligned with each other.

#### 4.3.4.4 Boundary Conditions

Table 4-6: Simulation boundary conditions

	Boundary Name	Location	Type	Boundary Details
Stationary Domains	inlet	inlet	Inlet	Flow Regime: Subsonic Mass and Momentum: Total pressure Value: 1 [atm] Flow Direction: Normal to Boundary Condition Turbulence: Medium (Intensity = 5%)
	outlet	outlet	Outlet	Flow Regime: Subsonic Mass and Momentum: Mass Flow Rate Value: myMassFlowRate
	walls	walls_fluid_in, walls_fluid_out	Wall	Mass and Momentum: No Slip Wall Wall Roughness: Smooth Wall
	interface_DE_Side 1	Sint_de	Interface	Mass and Momentum: Conservative Interface Flux Turbulence: Conservative Interface Flux
	interface_NDE_Side 1	Sint_nde	Interface	Mass and Momentum: Conservative Interface Flux Turbulence: Conservative Interface Flux
Rotating Domain	clearwall	walls_hub	Wall	Mass and Momentum: No Slip Wall Wall Roughness: Smooth Wall
	impeller	walls_imp	Wall	Mass and Momentum: No Slip Wall Wall Roughness: Smooth Wall
	statwalls	stat_walls_shroud	Wall	Mass and Momentum: No Slip Wall Wall Velocity: Counter Rotating Wall Wall Roughness: Smooth Wall
	interface_DE_Side 1 1	Rint_de	Interface	Mass and Momentum: Conservative Interface Flux Turbulence: Conservative Interface Flux
	interface_NDE_Side 1 1	Rint_nde	Interface	Mass and Momentum: Conservative Interface Flux Turbulence: Conservative Interface Flux

Boundary conditions must be specified in order to solve the differential form of the governing equations, these are detailed in Table 4-6.

Total pressure was imposed at the inlet as the boundary condition, while the mass flow rate normal to the boundary was set at the outlet. The static pressure at the outlet is part of the solution, which is very apt for this application. This boundary condition configuration is one of the recommended options for ANSYS® CFX® and is deemed as robust (ANSYS, Inc., 2013). Test cases showed similar values for the pressure differential for other boundary condition combinations, such as mass flow rate at the inlet and pressure at the outlet.

#### 4.3.4.5 Initial Conditions

The initial conditions for the stationary and rotating domains are detailed in Table 4-7 below.

*Table 4-7: Simulation initial conditions*

	Parameter	Option	Value
Stationary Domains	Cartesian Velocity Components	Automatic with Value	U = 0 [m s <sup>-1</sup> ] V = -myVelocity [m s <sup>-1</sup> ] W = 0 [m s <sup>-1</sup> ]
	Static Pressure	Automatic with Value	Relative Pressure = 1 [atm]
Rotating Domain	Cartesian Velocity Components	Automatic with Value	U = 0 [m s <sup>-1</sup> ] V = 0 [m s <sup>-1</sup> ] W = 0 [m s <sup>-1</sup> ]
	Static Pressure	Automatic with Value	Relative Pressure = 1 [atm]



#### 4.3.4.6 Timestep

For a transient simulation the time dependant behaviour is specified through time duration (length of the simulation in real time) and timestep (real time intervals at which the CFX-Solver solves for the flow field). The timestep is an important factor in any transient simulation. The Courant number is often used as an indicator for numerical stability of a transient simulation and is defined as:

$$\text{Courant number} = \frac{udt}{dx} \quad (4-1)$$

The number indicates the number of mesh cells the fluid has to pass through during each timestep. The maximum value of the Courant number changes with the method used to solve the discretised equations. In explicit methods, a direct computation of the dependent variables can be made in terms of known quantities. Implicit methods, however, use a matrix or iterative technique to obtain the solution when the dependent variables are defined by coupled sets of equations. It is desirable to have a Courant number below 1 so that the fluid does not move across more than one cell during a single timestep. In CFX®, the Courant number is calculated for each timestep as a multidimensional generalisation of equation (4-1).

The Courant number will be the highest in regions where the flow with the highest velocity is travelling through the densest regions of the mesh. For the RLR pump this will be when the fluid enters the rotating impeller blades, and for this reason the Courant number is monitored here. The timestep is defined by the CEL expression, *DeltaT*, which specifies a rotational advance of the impeller.

Initially a timestep was chosen to keep the RMS Courant number below 1, however a timestep independence study was also carried out to determine the effect of the timestep size on the accuracy of the results while monitoring the computational cost. It is important to balance the need for accuracy against the run-time cost. As an implicit code, ANSYS® CFX® generally allows for larger timestep sizes than explicit codes whilst being more computationally demanding. However, for some transient calculations it might be that the Courant number needs to be small in order to accurately resolve transient details (ANSYS, Inc., 2013). It can be shown that an explicit method would be unstable if the Courant number is > 1. To maintain numerical

stability of the iterative solution for higher timestep sizes, implicit methods increase the under-relaxation parameters. This increased damping leads to inaccuracies in the transient behaviour. Furthermore, for the simulation to be time dependant rather than time averaged, a low Courant number is desirable.

The initially chosen timestep size was equivalent to a physically convenient angle of rotation (blade spacing), i.e.  $0.9^\circ$  rotation of the impeller per timestep, corresponding to a  $\Delta t$  of  $6.52 \times 10^{-5}$  s. The timestep size was then decreased in increments of 50% to a  $\Delta t$  of  $8.15 \times 10^{-6}$  s, corresponding to  $0.1125^\circ$  impeller rotation per timestep.

The normalised percentage differences in the transient average pressure for the timestep study are shown in Table 4-8 and the pressure trend for these simulations is shown in Figure 4-12. The pressure pulsations follow the same trend but are more pronounced for the smaller timesteps. Despite this, the drop in the normalised pressure between the smallest timestep of  $8.15 \times 10^{-6}$  s and the largest timestep of  $6.52 \times 10^{-5}$  s is relatively large (2.1%). Based on these results, a timestep of  $3.52 \times 10^{-5}$  s was chosen as the difference in the normalised pressure is only 0.5% compared to the smallest timestep but the solve time is nearly 81 hours shorter.

*Table 4-8: Normalised pressure for varied timesteps.*

<b>Timestep</b>	<b>[s]</b>	<b><math>8.15 \times 10^{-6}</math></b>	<b><math>1.63 \times 10^{-5}</math></b>	<b><math>3.52 \times 10^{-5}</math></b>	<b><math>6.52 \times 10^{-5}</math></b>
<b>Rotation step</b>	<b>[<math>^\circ</math>]</b>	0.1125	0.225	0.45	0.9
<b>Mass Flow Rate</b>	<b>[<math>\text{kg s}^{-1}</math>]</b>	5.9			
<b>Rotational Speed</b>	<b>[rpm]</b>	2300			
<b>Normalised Pressure</b>	<b>[%]</b>	100.00	99.95	99.45	97.92
<b>Solve Time</b>	<b>[h, min]</b>	111h, 15min	53h, 13min	30h, 36min	17h, 59min

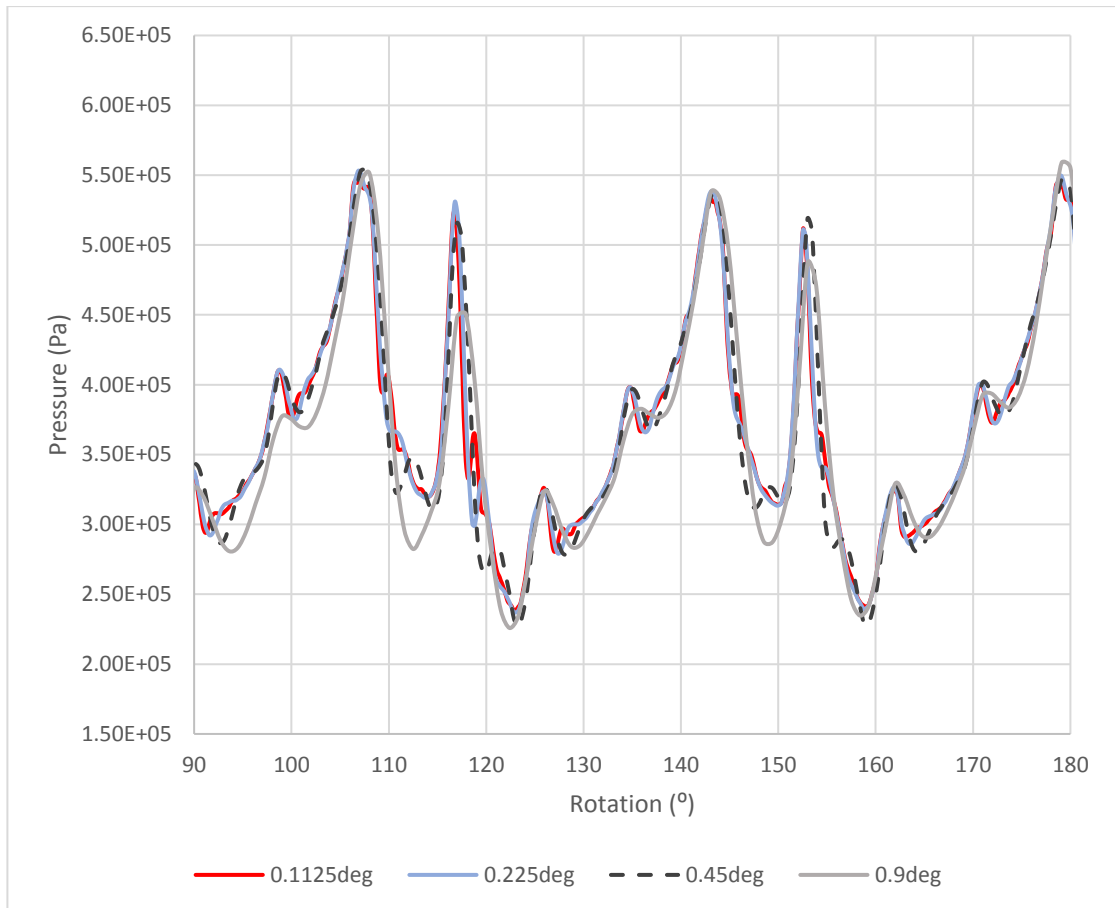


Figure 4-12: Pressure pulsation trend for four different timesteps.

### 4.3.5 Solver Definition

#### 4.3.5.1 Solver Control

The High Resolution advection scheme was chosen for the simulations, which uses a blending factor between Fourth Order numerics and Second Order near pressure extrema. This is recommended by the ANSYS® CFX-Solver Modeling Guide as it provides a good balance between robustness and accuracy (ANSYS, Inc., 2013). The Second Order Backward Euler implicit time-stepping scheme was chosen as this is generally recommended for transient runs in CFX®. As the name implies this scheme is second order accurate in time. The second order interprets the solution in the middle of the timestep instead of at the end of the timestep such as in the First Order Backward Euler Scheme.

#### 4.3.5.2 Residual Target

The ANSYS® CFX-Solver Modeling Guide prescribes a 1e-4 residual target as being adequate for most engineering applications (ANSYS, Inc., 2013). Nevertheless, two simulations were run with residual targets of 1e-5 and 1e-4. The timestep was set to a conservative value of  $8.15 \times 10^{-6}$  s, which relates to 0.1125° rotation per timestep, giving a Courant number of around 0.6.

The results showed a 1e-4 residual target reduced the simulation time by 47%, while only giving a 0.68% difference in normalised pressure compared to a 1e-5 target.

#### 4.3.5.3 Solver Settings

The MeTIS partitioning algorithm was used to divide the domain into four, and the simulation was run using the Platform MPI Local Parallel method on a quad core Intel Xeon, 3.4GHz processor with 32GB memory RAM. The simulations were later run on the Lancaster High End Computing (HEC) cluster when access became available.

#### 4.3.6 Analysis of the Results

Once the simulation has finished, the data is extracted in tabular form and analysed. Information from previous experimental testing is based on a head-flow performance curve, therefore the primary output from these simulations is the pressure increase across the pump from the inlet to the outlet. Another reason is of course due to the fact that the RLR pumps are unique in their capability of producing very large pressures at low flow rates, an inherent feature to be monitored and assessed.

The pressure differential  $\Delta p$ , given in equation (4-2) below, varies with each timestep, creating pressure pulsations due to the influence of the impeller blades.

$$\Delta p = p_{out} - p_{in} \tag{4-2}$$

Where  $p_{out}$  is the discharge pressure<sup>4</sup> and  $p_{in}$  is the suction pressure<sup>5</sup>.

---

<sup>4</sup> Instantaneous pressure is computed at the far outlet shown in Figure 4-11 at each timestep.

<sup>5</sup> Instantaneous pressure is computed at the far inlet shown in Figure 4-11 at each timestep.

These pulsations are calculated and plotted for each timestep using the expressions detailed in 4.3.4.1 *User Defined CEL Expressions*. The average pressure is then calculated over the second revolution of the impeller, as described in 4.4 *Periodicity*. Figure 4-15 shows the pressure pulsations across the pump and at locations within the rotating domain, updated at each timestep. The four locations within the rotating domain are situated close to the DE ('imp\_1' and 'imp\_2') and the NDE ('imp\_3' and 'imp\_4'). Two are initially located at the top half of the domain ('imp\_1' and 'imp\_3') and two at the bottom ('imp\_2' and 'imp\_4') as shown in Figure 4-13.

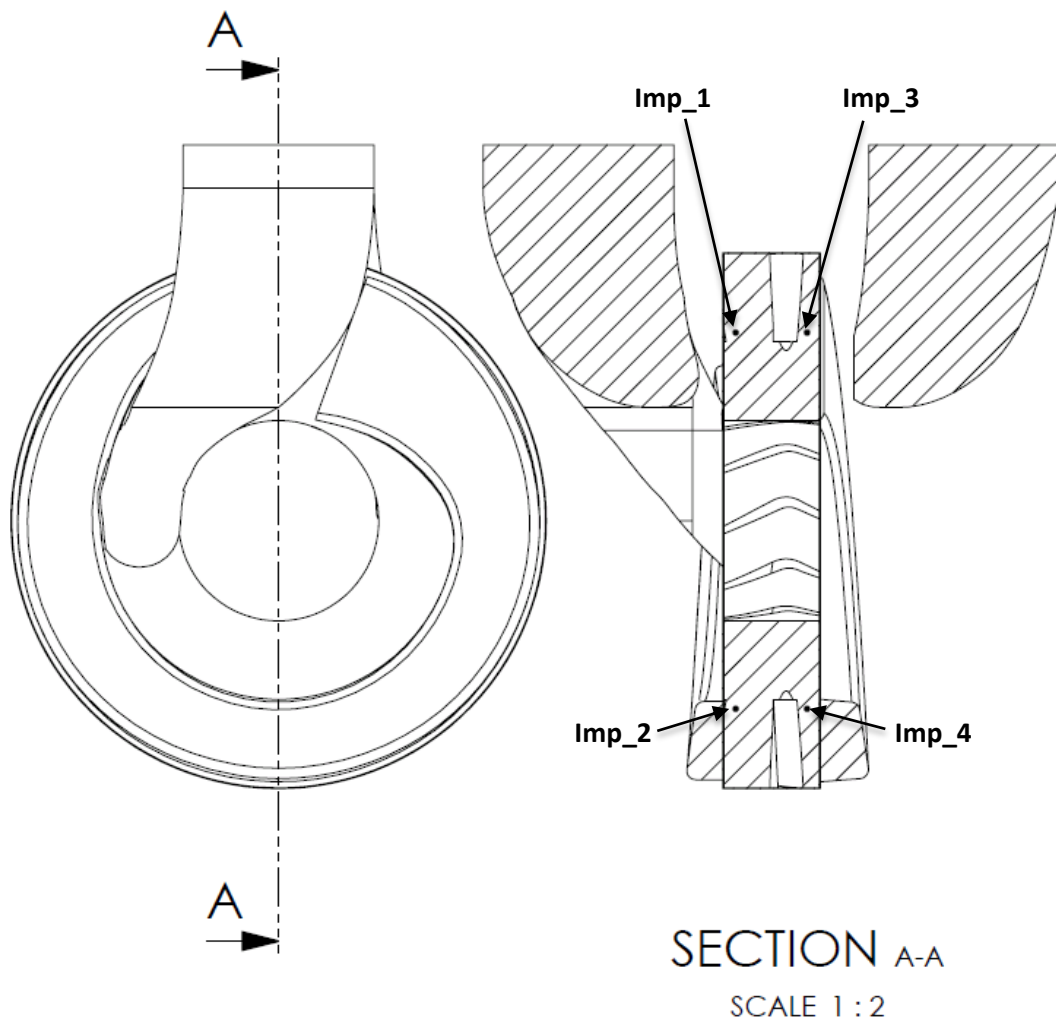


**Figure 4-13: Location of rotating domain pressure monitoring points.**

Review of literature confirms that pressure pulsations are an occurring phenomenon in both regenerative (Weise & Beilke, 1998; Böhle & Müller, 2009; Fleder & Böhle, 2015; Zhang, et al., 2016) and centrifugal pumps (Spence & Amaral-Teixeira, 2008; Spence & Amaral-Teixeira,

2009). The developed pressure has a periodic pattern with peaks and troughs, corresponding to the local pressure variations as the fluid passes through the impeller blade pocket. The pressure pulsations match the blade passing frequency (BPF), i.e. for the impeller with 20 blades there are 20 pulsations in one revolution. These pulsations are caused by the interaction of the circulating flow with the blade edges and the stripper region (Weise & Beilke, 1998).

The frequency of the pressure pulsations can be validated by calculating the BPF, which is defined using equation (4-3):

$$BPF = \frac{\text{No. blades} \times RPM}{60} [Hz] \quad (4-3)$$

For a pump with 20 blades rotating at a speed of 2300 rpm, the BPF can be calculated to be 766.67 Hz. The corresponding blade passing period (BPP) is calculated to be 0.00135 seconds using equation (4-4).

$$BPP = \frac{1}{BPF} \quad (4-4)$$

The time it takes to complete one revolution of the impeller at the above speed can be calculated to be 0.0261 seconds using equation (4-5).

$$\text{Time per rev} = \frac{2\pi}{\omega} \quad (4-5)$$

Dividing this number by the number of blades results in the BPP, confirming that the pressure pulsations correlate to the passing blades.

For the impeller used in this study the blade spacing angle between adjacent blades (half and full length blades) is 18°, whilst the spacing between identical blades is 36° (see Figure 1-6). The first and largest pressure peak appears when a full length blade has reached the stripper edge on the discharge side, this is also the point when a full blade pocket (area between two successive full length blades) is flush against the port plate as shown in Figure 4-14 (top, left).

The effects on the pressure pulsations measured across the pump ( $\Delta p$ ) can be seen in Figure 4-15. Due to the asymmetric design of the impeller, the blade edges on the suction (drive end) and discharge (non-drive end) sides are offset by  $9^\circ$  (Figure 4-14), which causes the secondary lower pressure peak seen in Figure 4-15. After  $9^\circ$  rotation of the impeller a full length blade has reached the stripper edge on the suction side as seen in Figure 4-14 (bottom, right).

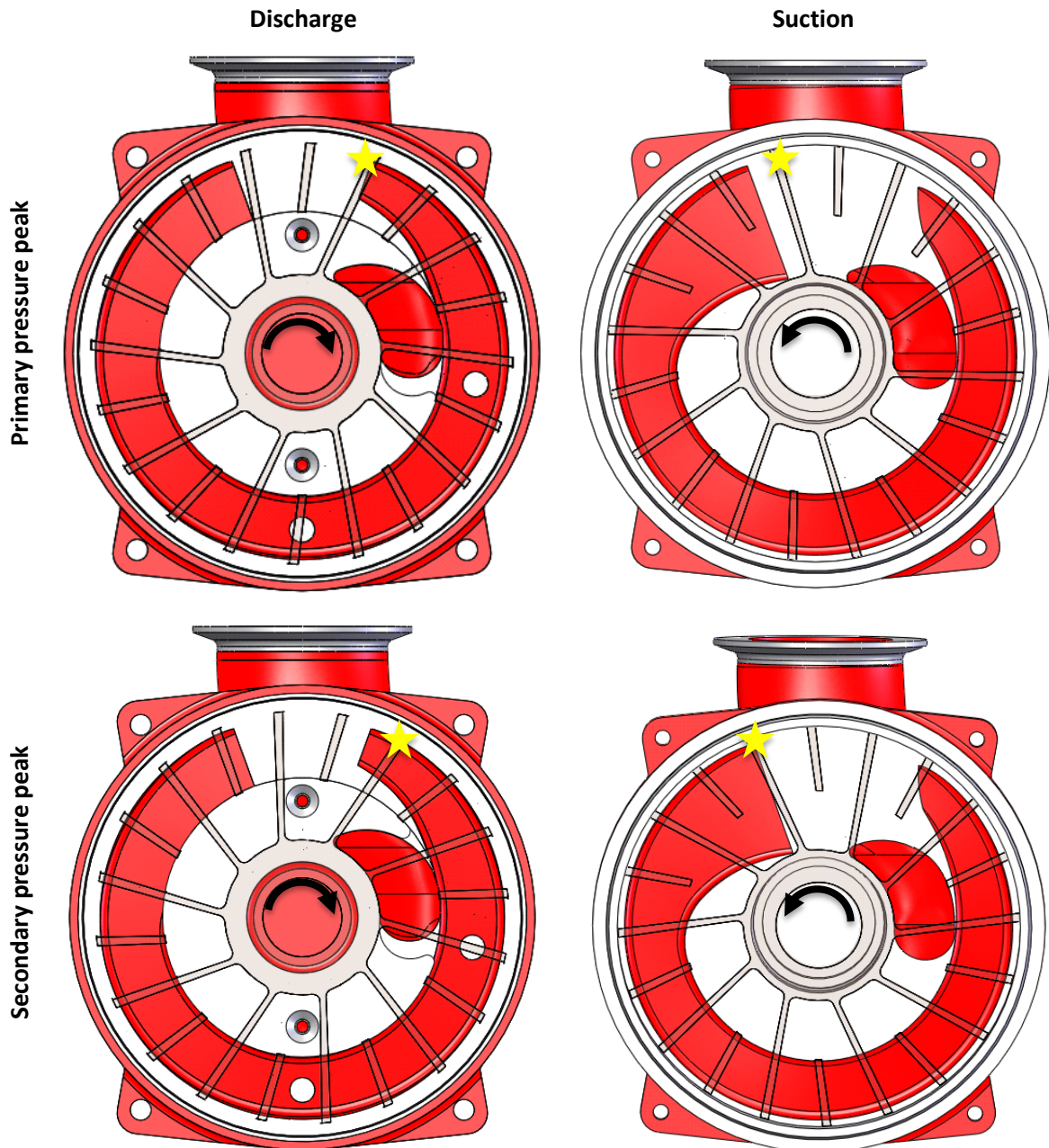


**Figure 4-14: Position of impeller blade edges relative to the stripper edge on the discharge and the suction side causing the primary pressure peak and the secondary pressure peak.**

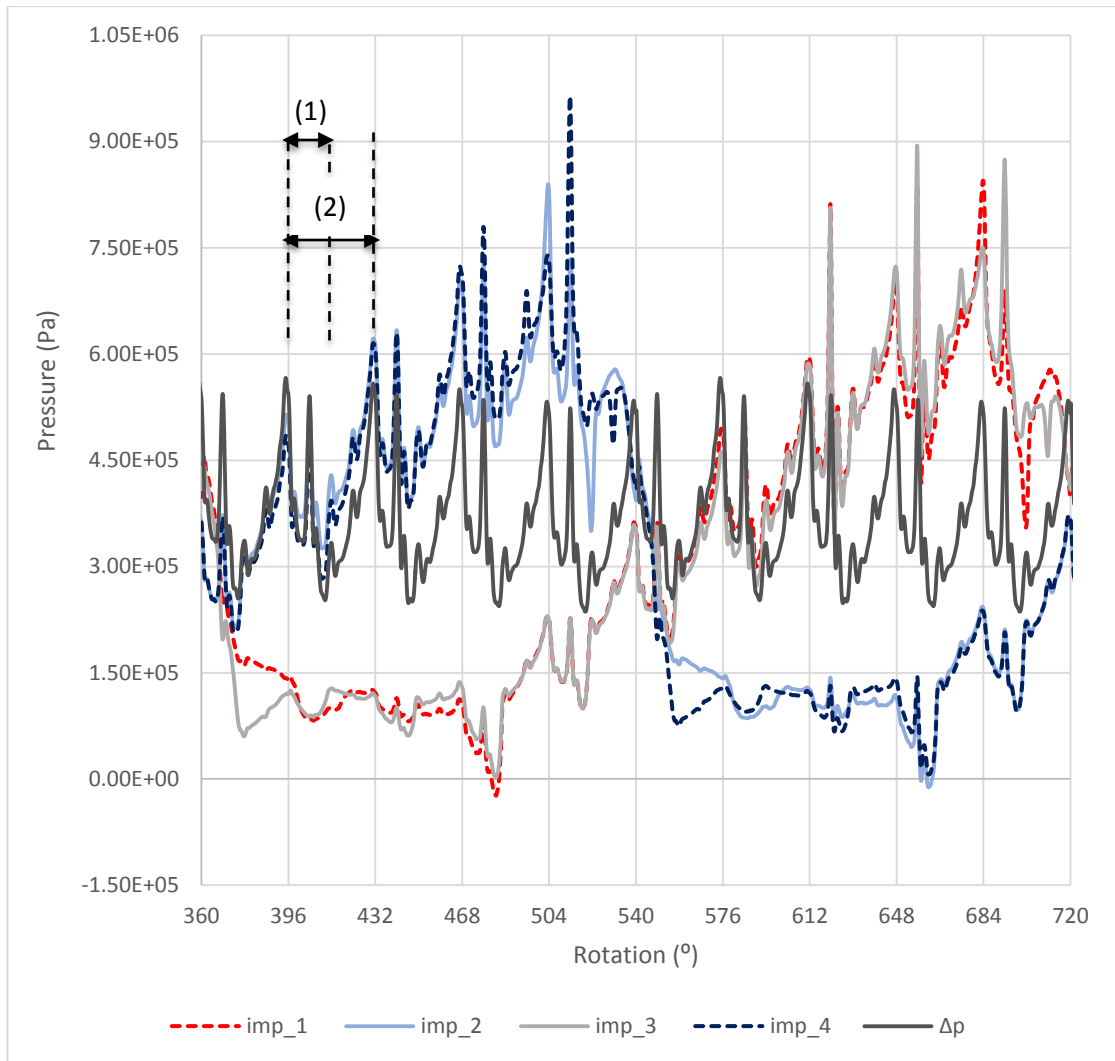


**Figure 4-15: Pressure pulsations over second revolution of the impeller showing the blade passing frequency. Blade spacing between (1) adjacent blades (half and full length blades) and (2) identical blades.**

The amplitudes of the pressure pulsations measured across the pump are relatively large, ranging from approximately 250 kPa to 470 kPa (see Figure 4-15). However, the values are in a similar range to results published by Zhang et al. (2016) (see Figure 2-5). The reason for large pressure amplitudes in regenerative pumps compared to centrifugal ones might be due to the dampening effects of the volute. This research focuses on the pressure increase across the pump however most of the reviewed literature is concerned with pressure pulsations in or near the impeller. Computational modelling in this project has shown that pressure pulsations do occur in the impeller as seen in Figure 4-15 but with a more irregular pattern than at the outlet. However, the distinct trend for the rotating domain is similar for each revolution of the impeller, confirming the periodic nature of the pressure pulsations. The pressure measured in



a blade pocket starting at the bottom of the impeller (imp\_2 and imp\_4) increases steadily for 180° until it reaches the port plate when the pressure drops rapidly.

Other outputs of interest include pump hydraulic efficiency  $\eta$ , given in equation (4-6) below, which is also calculated for each timestep.

$$\eta = \frac{\rho g H Q}{T \omega} = \frac{(p_{out} - p_{in}) Q}{T \omega} \quad (4-6)$$

Where  $\rho$  is the density of water,  $g$  is the acceleration due to gravity,  $H$  is the hydraulic head,  $Q$  is the flow rate,  $T$  is the torque measured on the impeller shaft,  $\omega$  is the angular velocity,  $p_{out}$  is the discharge pressure and  $p_{in}$  is the suction pressure.

As with the pressure, the efficiency fluctuates for each timestep (it is linked to the pressure increase across the pump) and the average must be calculated. This is done throughout the simulation using the expression defined in 4.3.4.1 *User Defined CEL Expressions* and the average value is then calculated over the second revolution of the impeller.

#### 4.4 Periodicity

The numerical calculation must continue until the transient pulsations of the flow field become periodic due to the unsteady nature of the flow. A periodicity study was carried out to determine when the calculation becomes fully periodic which was defined by the pressure pulsations at key locations in the fluid domain. The timestep was fixed at 0.225° rotation per timestep. The pressure increase across the pump over one revolution is calculated by taking the average value of the pressure pulsations at each timestep. The dataset over six revolutions of the impeller has been normalised so that the average pressure over the first revolution is equal to 100%, which is the datum for normalising the results. Every value thereafter is given as a percentage in relation to the first value.

After the first revolution the difference in normalised pressure is very small (less than 0.5%) for each subsequent revolution as seen in Table 4-9. Approximately two revolutions of the impeller are necessary to obtain a periodic converged solution, this value was also determined by Böhle, et al. (2016). The key locations chosen are the boundaries corresponding to the inlet

and outlet of the pump and the impeller. The pressure trend measured across the pump is periodic in nature and very similar over six revolutions of the impeller as seen in Figure 4-16.

**Table 4-9: Normalised pressure for the periodicity study.**

Revolution of impeller	[-]	1	2	3	4	5	6
Mass Flow Rate	[kg s <sup>-1</sup> ]	5.9					
Rotational Speed	[rpm]	2300					
Normalised Pressure	[%]	100.00	98.31	98.14	97.66	98.96	98.14

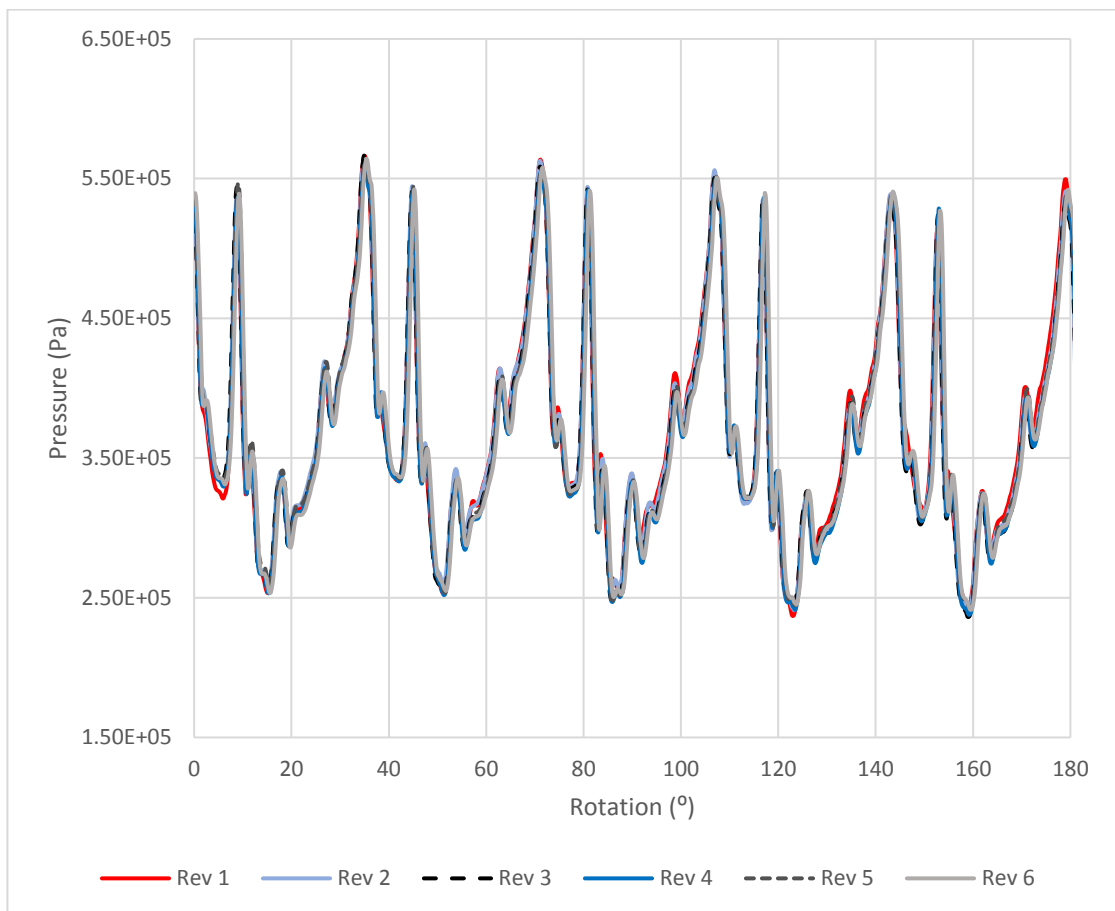


**Figure 4-16: Pressure pulsation trend over six revolutions of the impeller.**

## 4.5 Mesh Independence Study

In order to investigate the discretisation error, a mesh independence study was carried out using the 7.2M element full pump mesh described in 4.3.3 *Mesh*. The Grid Convergence Index (GCI) proposed by Roache (1994) was applied. A refinement ratio of 1.5 was used to generate three meshes, with the coarsest mesh containing 7.2M elements and the finest mesh containing 40.7M elements. The results are normalised to the coarsest mesh, shown in Table 4-10 below and plotted in Figure 4-17.

*Table 4-10: Results of the mesh independence study, normalised to the coarsest mesh.*

Mesh [-]	Normalised Grid Spacing [-]	Number of Elements [Million]	Normalised Average Pressure [%]
1	1.00	7.2	100.00
2	0.67	15.9	102.43
3	0.44	40.7	102.48

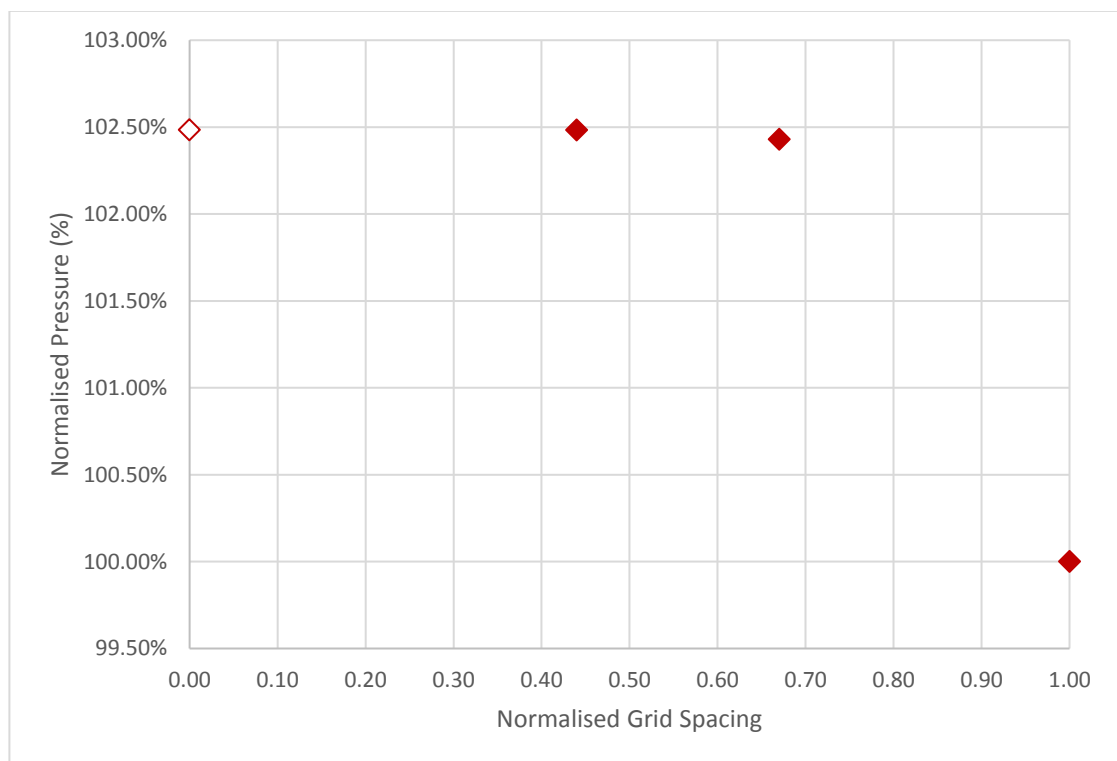


*Figure 4-17: Results of the mesh independence study, normalised pressure against normalised grid spacing.*

As the grid spacing is reduced, the modelled pressure approaches the asymptotic zero grid spacing value. The order of convergence,  $p_c$ , can be calculated using equation (4-7) below.

$$p_c = \frac{\ln\left(\frac{p_1 - p_2}{p_2 - p_3}\right)}{\ln(r)} \quad (4-7)$$

Where  $p_n$  is the normalised average pressure for each mesh and  $n$  is the grid number. Index 1 denominates the coarsest mesh while index 3 denominates the finest mesh.

Once the order of convergence is obtained, the average pressure at zero grid spacing,  $p_{h=0}$ , can be determined using a Richardson extrapolation of the two finest mesh.

$$p_{h=0} = p_3 + \frac{p_3 - p_2}{2^{p_c} - 1} \quad (4-8)$$

This gives a zero grid spacing average pressure of 102.48% which is also plotted in Figure 4-17.

The order of convergence can also be used to calculate the GCI. For mesh convergence studies using three meshes or more, Roache (1994) suggests using a safety factor  $F_s$  of 1.25. The GCI for Mesh 3 & 2 and Mesh 3 & 1 can be calculated as follows:

$$GCI_{32} = \frac{F_s \left( \frac{p_3 - p_2}{p_3} \right)}{r^{p_c} - 1} \quad (4-9)$$

$$GCI_{31} = \frac{F_s \left( \frac{p_3 - p_1}{p_3} \right)}{r^{p_c} - 1} \quad (4-10)$$

The grid convergence indexes are given in Table 4-11 below.

**Table 4-11: Grid Convergence Indexes.**

<b>Refinement Ratio</b>	$r$	1.5
<b>Order of Convergence</b>	$p_c$	9.41
<b>Safety Factor</b>	$F_s$	1.25
<b>GCI for Meshes 3 and 2</b>	$GCI_{32}$	0.0015%
<b>GCI for Meshes 2 and 1</b>	$GCI_{21}$	0.0668%
<b>GCI for Meshes 3 and 1</b>	$GCI_{31}$	0.0682%

Equation (4-11) can be applied to determine if the solutions are within the asymptotic range.

$$\frac{GCI_{21}}{r^{p_c} \times GCI_{32}} = 1.001 \quad (4-11)$$

The result is nearly 1 which indicates that the solutions are well within the asymptotic range.

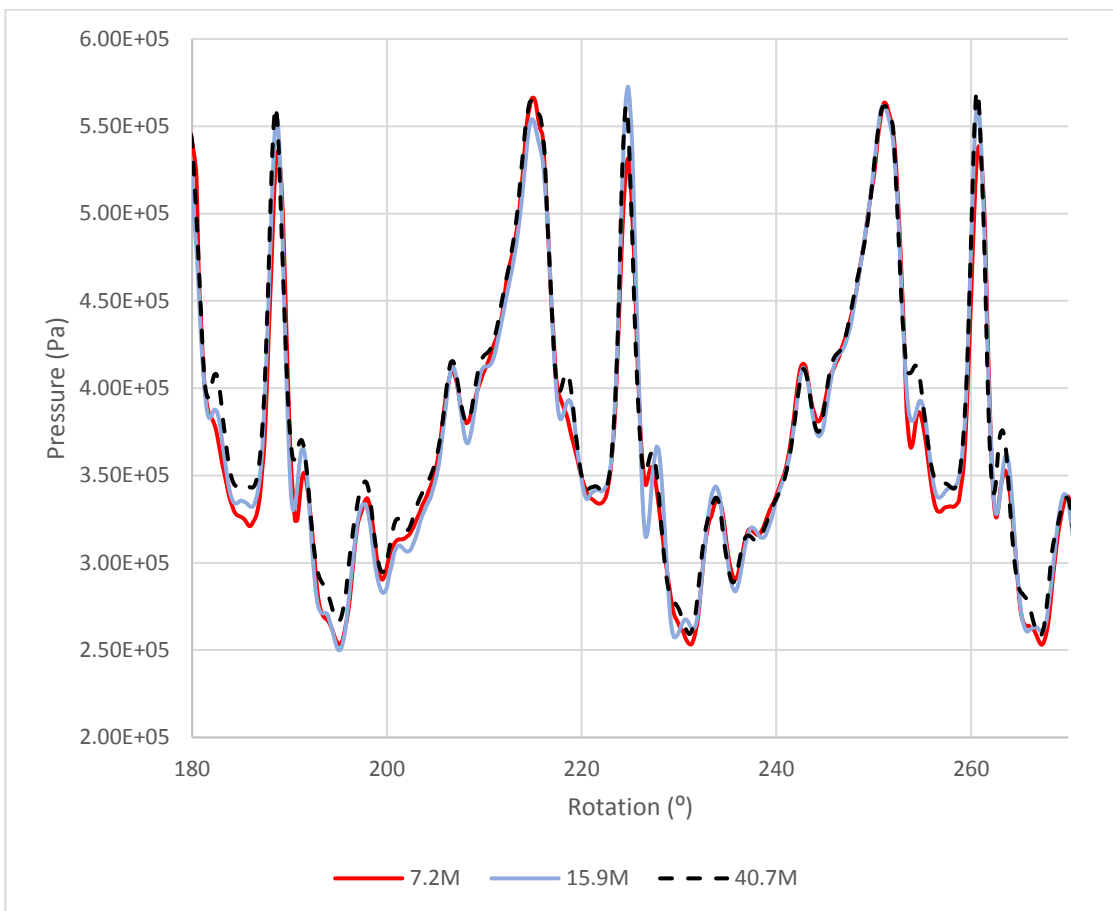
Figure 4-18 shows the pressure pulsations across the pump for each mesh analysed in the independence study. Despite the fact that 0.45° rotation of the impeller per timestep was shown to produce accurate results in 4.3.4.6 *Timestep*, meshes with smaller elements require smaller timesteps for problems with identical velocities. Therefore, the timestep was fixed for each simulation at a value of 0.225° rotation per timestep, providing a good compromise between accuracy and computational cost. The results show a similar trend for the three meshes, however as the mesh density is increased the difference between the peak pressures are reduced.

Table 4-12 shows the time taken for each simulation in the mesh independence study to run on 64 cores on the Lancaster HEC cluster. The results of this study has shown that Mesh 1 (coarse mesh) will be suitable for the studies in 5 *Parametric Clearance Analysis* and 7 *Computational Performance Modelling* as the absolute error (given in Table 4-11) is 0.0682% and it is assumed that this error can be negated when comparing different clearance combinations. The simulation time is also low enough (at just over 2 days) to allow a wide range of clearance variations and operational points to be analysed. Mesh 2 will be used periodically to verify the results achieved using Mesh 1. The percentage difference between

Mesh 2 and Mesh 3 is less than 0.06%, however the solve time is significantly longer for Mesh 3.

**Table 4-12: Solve times for the mesh independence study.**

	Unit	Mesh 1	Mesh 2	Mesh 3
<b>No. Elements</b>	[M]	7.2	15.9	40.7
<b>Timestep</b>	[s]	1.63*10 <sup>-5</sup> s		
<b>Solve time</b>	[d, h]	2d, 5h	4d, 6h	17d, 2h



**Figure 4-18: Pressure pulsations for the mesh refinement study.**

## 4.6 Summary of Computational Modelling Methodology

The general CFD principles used to analyse the RLR pump are discussed in this chapter and the simplifications and assumptions are justified and quantified where possible. The modelling domains, meshes, definitions of the solver physics and general setup of the simulations as well as results analysis have also been discussed.

The relative numerical uncertainties introduced by the assumptions discussed in this chapter are given in Table 4-13 below. The numerical error of the sources listed were calculated using standard deviation to quantify the amount of variation of the set of computed values of interest in one study (here listed under 'Source of Error'). The total numerical error is 0.46%, calculated using the root-sum-square method. There could, however, be further additional sources of error not included, such as surface roughness and from the turbulence model used. Although a number of Two-Equation URANS models were analysed, it was not compared to an SRS model which would be more accurate but also computationally more expensive.

*Table 4-13: Relative numerical uncertainties introduced by various assumptions.*

<b>Source of error</b>	<b>Numerical Error <math>\delta</math> [%]</b>
Single precision	0.05
Timestep	0.20
Periodicity	0.23
Residual Target	0.34
Domain Discretisation (Mesh)	0.07
<b>Total (Root-Sum-Square)</b>	<b>0.46</b>

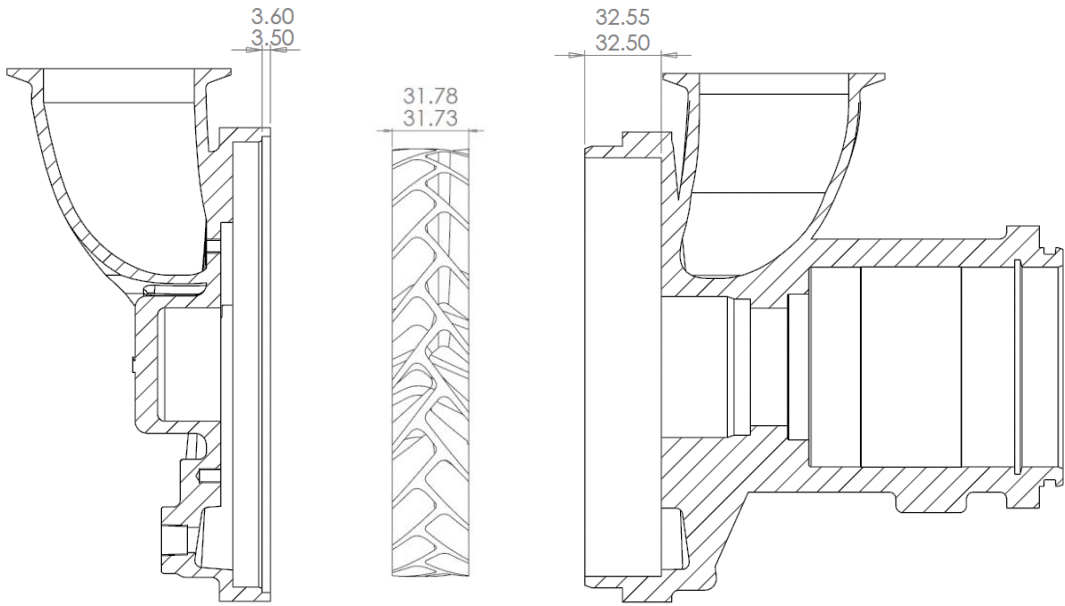
## 5 Parametric Clearance Analysis

This chapter details the study carried out to assess the effects on the pump performance by varying the clearances between the impeller and the casing. The RLR pump requires tight clearances around the impeller to ensure optimum head and efficiency performance. Although these clearances can be affected by operational wear of internal components over time, the initial dimensions are determined by the manufacturing tolerances. Therefore, in order to evaluate the operational performance and subsequently the reliability of the RLR pump, it becomes important to understand how a newly built pump performs in relation to these clearances. The derivation of different clearance combinations is detailed below followed by the geometry preparation of the computational model. All the simulations are run using the coarse mesh described in *4.5 Mesh Independence Study*. Following this, the results are presented, compared and discussed. The initial results of this parametric clearance analysis were published in a paper looking at the computational effects of manufacturing tolerances on a regenerative liquid ring pump (Karlsen-Davies & Aggidis, 2016b).

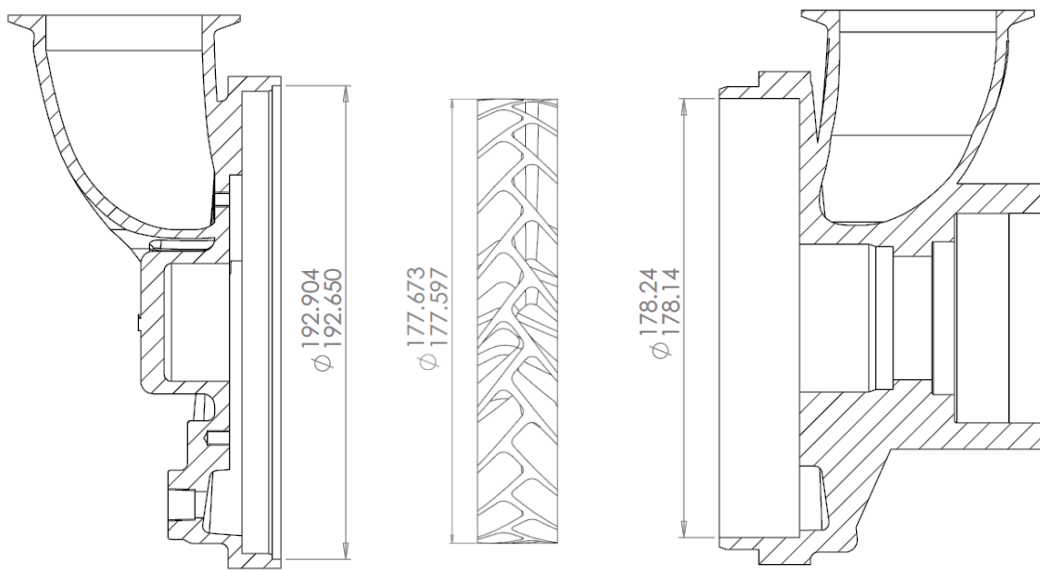
### 5.1 Manufacturing Tolerance Parameters

A parametric study of “worst-case” to “best-case” scenario sizes of axial and radial clearances is used to look at the impact on the pressure increase and the efficiency at the duty point detailed in *4.3.2 Operating Conditions*. The study covers a wide range of axial and radial clearances, derived from the minimum, median and maximum values of the manufacturing tolerances of the drawings for the impeller, the casing on the drive end (DE) side, the casing on the non-drive end (NDE) side and the drive shaft (Figure 5-1 and Figure 5-2). In addition, the axial alignment of the impeller in relation to the casing is determined by the drawing assembly tolerance on the DE of the impeller (Figure 5-3).





(a) (b) (c)  
**Figure 5-1: Axial manufacturing tolerance parameters for (a) NDE, (b) impeller and (c) DE.**



(a) (b) (c)  
**Figure 5-2: Radial manufacturing tolerance parameters for (a) NDE, (b) impeller and (c) DE.**

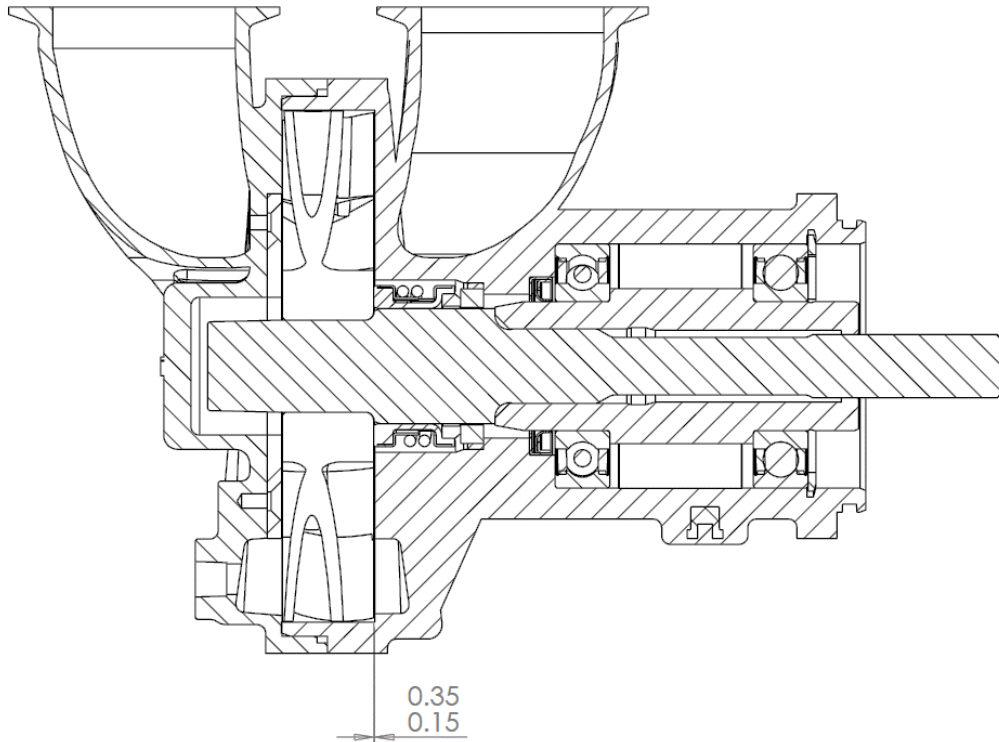


**Figure 5-3: Assembly tolerance parameter. The impeller is axially aligned in relation to the DE side of the casing.**

The “worst-case” to “best-case” scenarios are derived using tolerance stack-ups, where for example the minimum axial manufacturing tolerance is a resultant of the maximum axial tolerance of the impeller and the minimum axial tolerance of the casing. Conversely, the maximum axial manufacturing tolerance is calculated using the minimum axial tolerance of the impeller and the maximum axial tolerance of the casing. This method provides the total axial clearance available. A similar approach is taken for the radial manufacturing tolerances. As the notation implies, the median manufacturing tolerance is the median value of the minimum and maximum dimensions.

The assembly tolerance given on the DE of the impeller makes it possible to determine a range of values which can then be used to calculate the corresponding dimensions on the NDE for a given total axial clearance. For each of the combinations of DE and NDE clearances there will also be a range of radial clearances to take into account. If keeping to the style of minimum, median and maximum scenarios, a total of 27 tolerance models can be generated. The dimensions of the parametric models are displayed in Table 5-1.

**Table 5-1: Manufacturing tolerance parameters (all dimensions given in millimetres).**

	Axial Minimum		Axial Median		Axial Maximum	
<b>Total Axial Clearance →</b>	0.62		0.77		0.92	
<b>DE ↓</b>	<b>NDE</b>	<b>Radial</b>	<b>NDE</b>	<b>Radial</b>	<b>NDE</b>	<b>Radial</b>
0.15	0.47	0.176	0.62	0.176	0.77	0.176
		0.278		0.278		0.278
		0.383		0.383		0.383
0.26	0.36	0.176	0.51	0.176	0.66	0.176
		0.278		0.278		0.278
		0.383		0.383		0.383
0.37	0.25	0.176	0.40	0.176	0.55	0.176
		0.278		0.278		0.278
		0.383		0.383		0.383

## 5.2 Geometry Preparation

In order to streamline the clearance study, the clearance geometries were redrawn in SolidWorks® to parametrise the relevant dimensions. To simplify the process, the width and the height of the impeller are assumed constant, only the magnitude of the clearances is varied. Figure 5-4 and Figure 5-5 show the process of parameterising the axial and radial clearances, respectively. The axial clearance body was redrawn as a rectangle from a cross-sectional perspective where the width (in this example 0.37 mm) corresponds to the axial clearance magnitude. The sketch was then revolved in the direction shown in Figure 5-4 to create the full axial clearance disk. In order to import this parameter into DesignModeler®. A list of the parameters used for the clearance study are included in Table 5-2.

In a similar fashion, the radial clearance body was redrawn as a rectangle from a cross-sectional perspective where the height (in this example 0.278 mm) corresponds to the radial clearance dimension. The width is also parameterised so it can be updated in line with the different axial clearance magnitudes (the radial clearance ring wraps around the impeller fluid pockets as well as the axial clearances). To create the full radial clearance ring, the sketch is revolved in the direction shown in Figure 5-5. Figure 5-6 shows the relative positions of the axial clearance disks and the radial clearance ring once assembled.

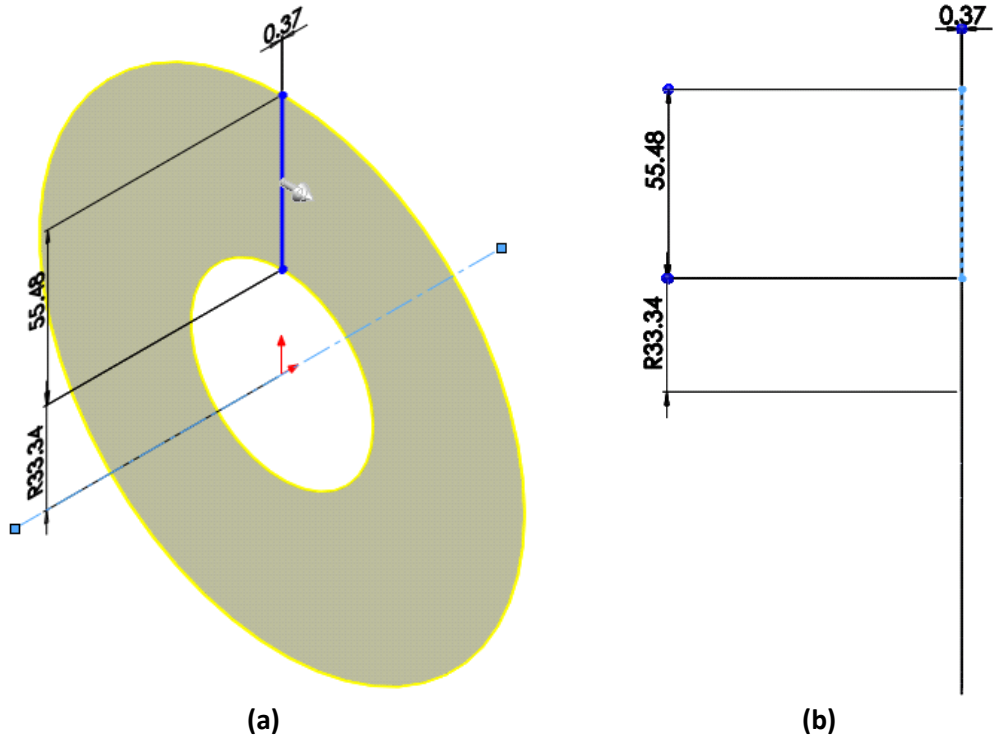


Figure 5-4: Geometry preparation of the axial clearances showing (a) isometric view and (b) cross-sectional view of the axial clearance disk.

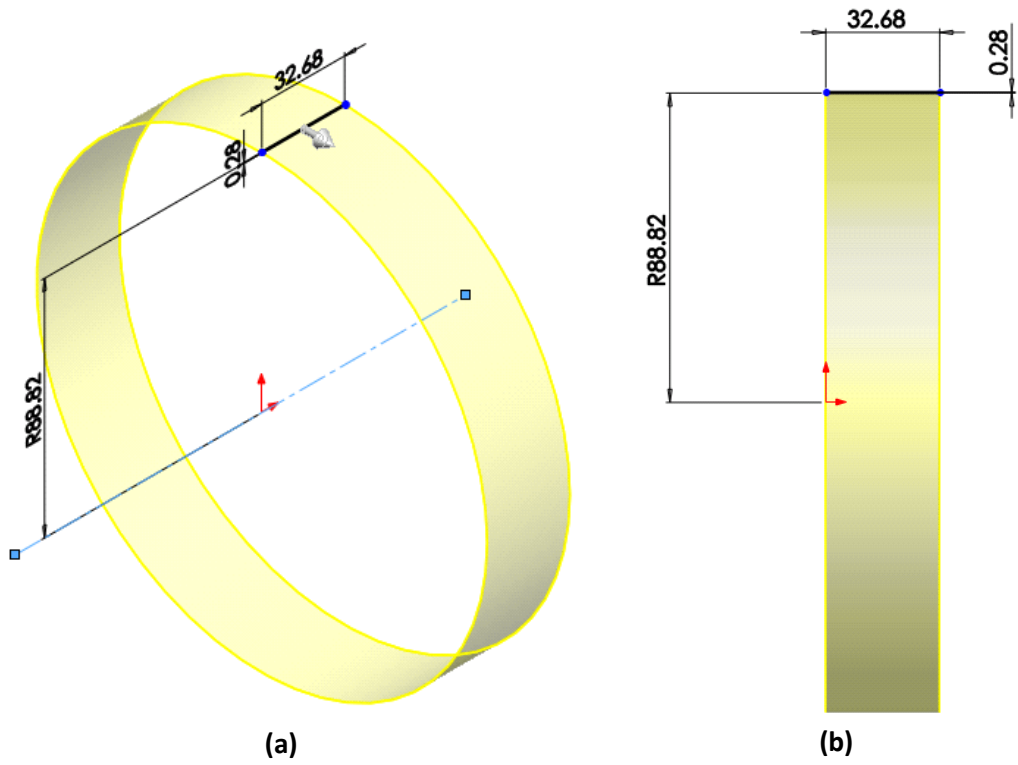
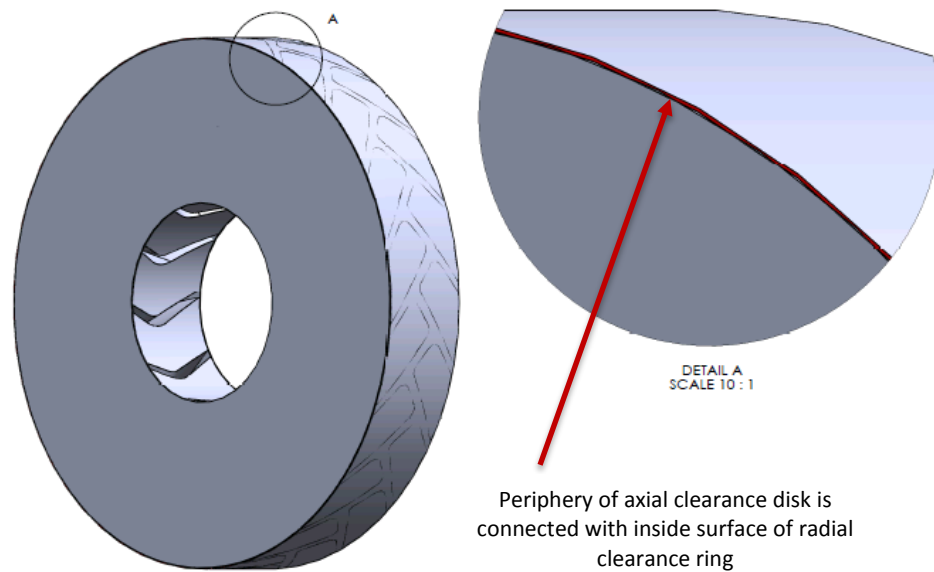
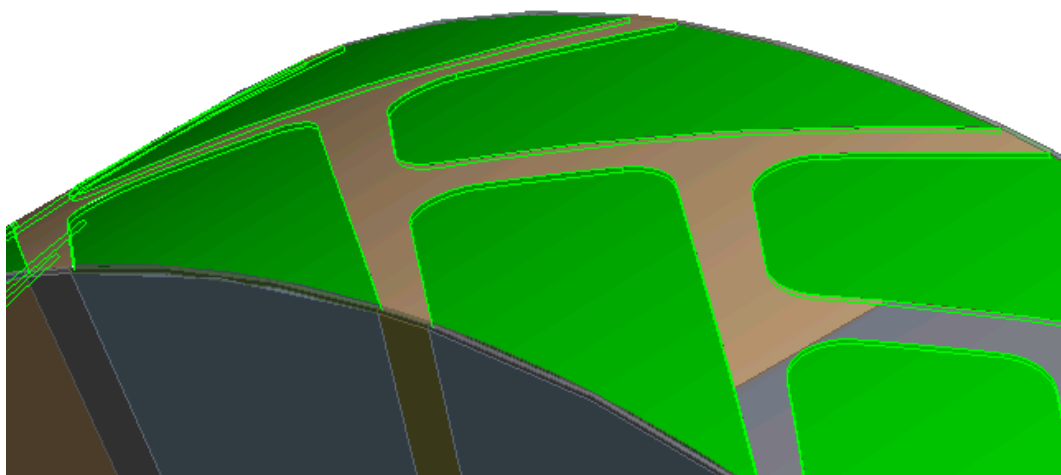


Figure 5-5: Geometry preparation of the radial clearance showing (a) isometric view and (b) cross-sectional view of the radial clearance ring.



**Figure 5-6: Relative positions of the axial clearance disk and the radial clearance ring; in the assembly the axial clearance disks are fitted inside the radial clearance ring.**

Once the fluid domain is imported into DesignModeler®, it is decomposed into several smaller bodies as explained in 4.3.1 *Computational Domain Geometry* (see Figure 4-7). The magnitude of the thin features (Figure 5-7) used to create the radial clearance bodies, corresponding to the designated dimension of the radial clearance ring, is parameterised and updated in line with the imported SolidWorks® parameters.



**Figure 5-7: Clearance geometry parameters; illustrating thin features (highlighted in green) used to create the radial clearance bodies mapped to the impeller fluid.**

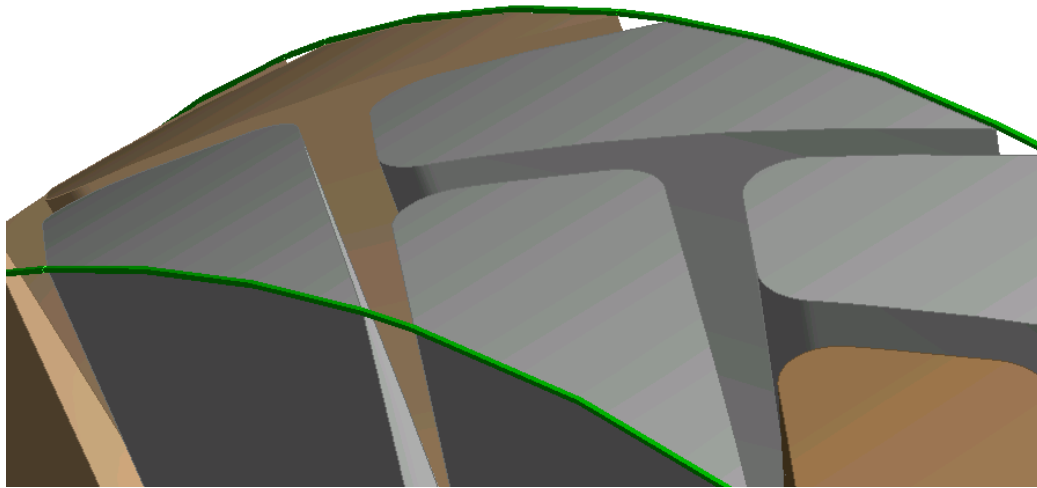


**Figure 5-8: Clearance geometry parameters; illustrating thin features (highlighted in green) used to create the radial clearance bodies mapped to the axial clearance.**

**Table 5-2: Clearance geometry parameters.**

<b>Parameter</b> [-]	<b>Example Value<sup>6</sup></b> [mm]
DE/NDE axial clearance dimension	0.370
Radial clearance dimension	0.287
Inner radius of axial clearance disk <sup>7</sup>	33.340
Outer radius of axial clearance disk	55.480
Inner radius of radial clearance ring <sup>8</sup>	88.820
Width of radial clearance ring	32.680
Magnitude of impeller fluid bodies in radial direction <sup>9</sup>	0.287
Magnitude of axial clearance bodies in radial direction <sup>10</sup>	0.287

<sup>6</sup> Example values correspond to dimensions shown in Figure 5-4 and Figure 5-5.

<sup>7</sup> The total radius (i.e. 33.34 mm + 55.48 mm) for the axial clearance disk is equal to the inner radius of the radial clearance ring.

<sup>8</sup> The inner radius does not include the magnitude of the radial clearance, i.e. the outer radius would be 89.11 mm (88.82 mm + 0.287 mm).

<sup>9</sup> Example magnitude corresponds to dimension assigned to thin feature used to create the radial clearance bodies mapped to the impeller fluid shown in Figure 5-7.

<sup>10</sup> Example magnitude corresponds to dimension assigned to thin feature used to create the radial clearance bodies mapped to the axial clearance fluid shown in Figure 5-8.

### 5.3 Mesh Generation

Generating the mesh for each clearance model was simplified due to the parameterisation, however the number of elements across the radial and axial clearances had to be updated for each model. The values in Table 5-3 correspond to an element size of approximately 0.04 mm in line with the coarse mesh statistics.

*Table 5-3: Number of elements across each clearance.*

Clearance Name [-]	Clearance Dimension [mm]	No. of Elements [-]
Drive End (DE)	0.15	4
	0.26	7
	0.37	9
Non-drive End (NDE)	0.47	12
	0.62	16
	0.77	19
	0.36	9
	0.51	13
	0.66	17
	0.25	6
	0.40	10
Radial (R)	0.55	14
	0.176	4
	0.278	7
	0.383	10

The rest of the mesh statistics were kept the same, however the order of the meshing process had to be adapted for some of the clearance models to avoid low quality elements. This was particularly true for models featuring a small NDE clearance.

## 5.4 Results and Discussion

The characteristic periodic pressure pulsations for a representative number of clearance models are plotted over 90° revolution of the impeller in Figure 5-9, clearly showing the effects of variations in axial and radial clearances. The trend is the same for each model, however there is approximately a 250 kPa shift between the lowest and highest pressure pulsation.

Furthermore, a distinct pattern can be observed. The pulsations can be divided into three sets of three trends. The highest pressure set of these corresponds to the minimum radial clearance (dotted lines in Figure 5-9), the second set with the median radial clearance (lines in Figure 5-9) and the third set at the lowest pressure with the maximum radial clearance (dashed lines in Figure 5-9). Each set can then be sub-divided by the minimum (black), median (red) and maximum (blue) axial clearance. The minimum axial clearance provides the highest pressure, which then tapers down as the axial clearance is increased to its maximum value. In other words, the pressure increases as the radial clearance approaches the minimum and, if the radial clearance remains static, the pressure increases as the axial clearance approaches its minimum.

In Figure 5-10, the results are grouped into the minimum, median and maximum axial clearance, showing the pressure pulsations over four blade passages (two full blades and two half blades). As one would expect, the amplitudes of the pressure pattern are largest for the minimum axial group and smallest for the maximum axial group. The heights of the primary peaks are quite different. For the maximum axial group, the peaks appear to be roughly the same height but as the axial group clearance decreases the difference between these two peaks also increases. In addition, the 'intermediate' peaks (two-three peaks between the primary peaks) are more pronounced for the minimum axial group.

The pressure pulsations are caused by the interaction of the circulating flow with the blade edges and the stripper edge (port plate). A pressure maximum occurs when the area between these edges decreases very quickly, which is the moment of maximal deceleration of the circulating flow. The pressure peak can therefore be interpreted as a suddenly decelerated flow. A smaller clearance is likely to increase the unsteadiness and strengthen the effects of viscosity, which could explain the more pronounced peaks.



The pressure pulsations in Figure 5-9 are displayed after a full revolution of the impeller, showing a high pressure at  $360^\circ$ . The next pressure peak appears at  $396^\circ$  when a long blade has reached the stripper edge on the discharge (NDE) side, this is also the point when a full blade pocket (area between two adjacent long blades) is flush against the port plate. Then as the blade passes the port plate, the low pressure side of the blade reaches the port plate which causes a sharp decrease in the pressure. Then, as the impeller blade continues past the port plate the pressure rises rapidly. The secondary lower pressure peak seen in Figure 5-9 is due to the asymmetric design of the impeller. The blade edges on the suction (DE) and discharge (NDE) sides of the impeller are offset by  $9^\circ$ , this causes the secondary pressure peak when a full length blade has reached the stripper edge on the suction side after  $9^\circ$  rotation of the impeller (see Figure 4-14).

It is evident that the total axial clearance (space envelope for the impeller) has an effect on the head performance which stems from the variation in the pressure pulsation formation as seen in Figure 5-10. The difference in amplitude within each axial clearance group decreases as the axial envelope increases. Within each axial group the pressure pulsations are clearly clustered together into radial groups, i.e. minimum (0.176 mm), median (0.278 mm) and maximum (0.383 mm).

A smaller radial clearance ensures a higher generated pressure head and it is therefore not surprising that the pressure pulsations are higher on the y-axis. This also reinforces the conclusion that the radial clearance has a significant effect on the performance of an RLR pump with a chevron shaped impeller. This is due to the continuous surface around the periphery circle of the impeller compared to a radial bladed impeller, reducing the radial clearance and subsequently the amount of leakage through the radial clearance more efficiently (Burton, 1972).

In Figure 5-11 the pressure distribution in the impeller is compared for one radial group within the minimum axial group, i.e. DE = 0.15 mm, NDE = 0.47 mm and R = 0.176/278/383 mm. The distribution depicts a gradual increase in pressure from the inlet to the outlet. As the radial clearance increases, the areas of high pressure decrease both in appearance and value. Similarly, in Figure 5-12 the pressure distribution in the impeller is compared for one assembly group within the median radial group, i.e. DE = 0.26 mm, NDE = 0.36/0.51/0.66 mm and R = 0.278 mm. The highest regions of pressure are observed for the smallest axial group (NDE =

0.36 mm). Lastly, the pressure distribution in the impeller is also compared for three models in the maximum axial group with a constant radial clearance, i.e.  $DE = 0.15/0.26/0.37$  mm,  $NDE = 0.77/0.66/0.55$  mm and  $R = 0.176$  in Figure 5-13. In this comparison the axial envelope remains the same and there are more high pressure regions for the  $DE = 0.37$  mm and  $NDE = 0.55$  mm combination. These pressure distributions correspond to the average pressure values calculated for each clearance model.

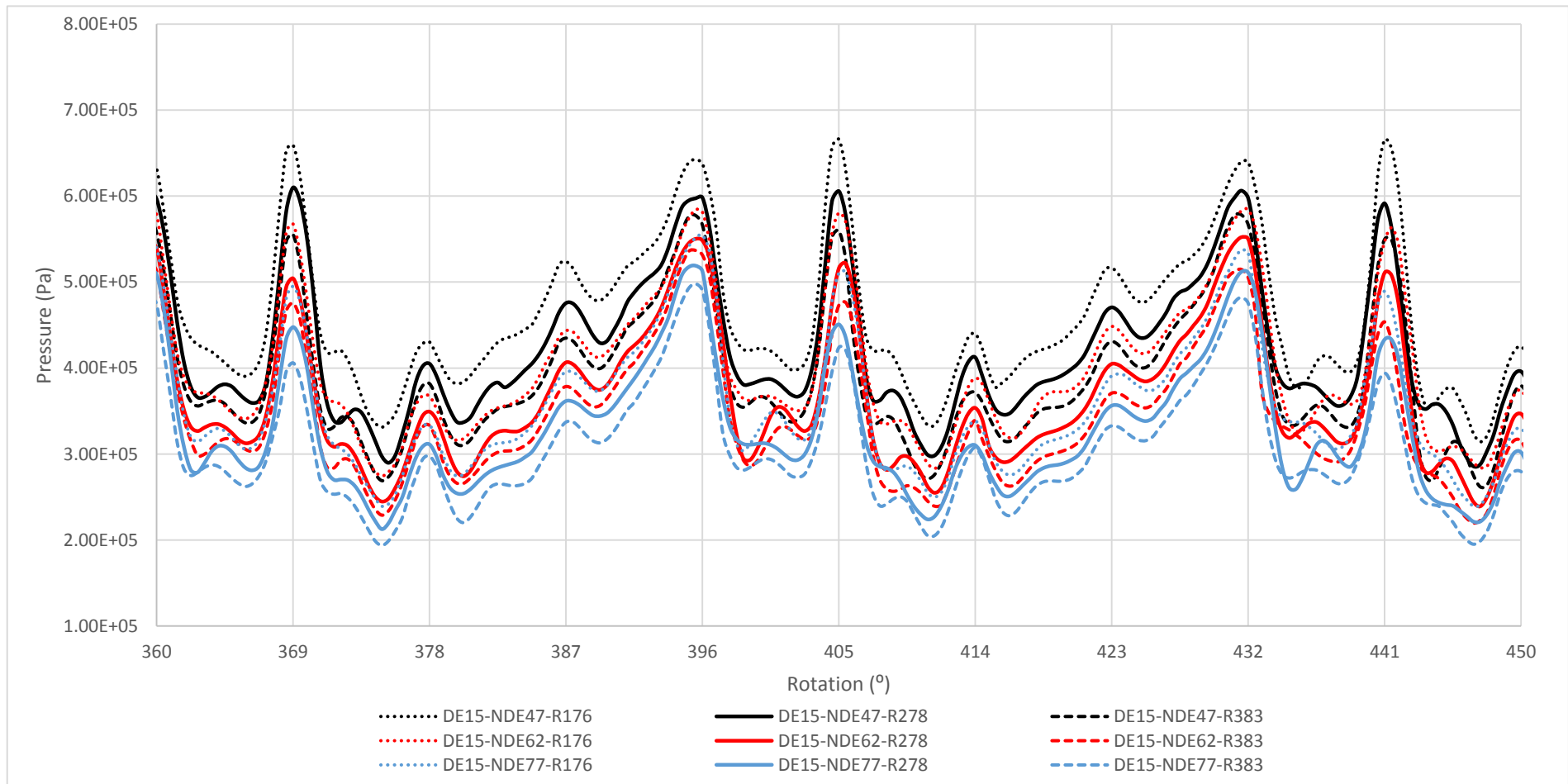


**Figure 5-9: Pressure pulsations for 9 parametric clearance models over 90° revolution of the impeller.**

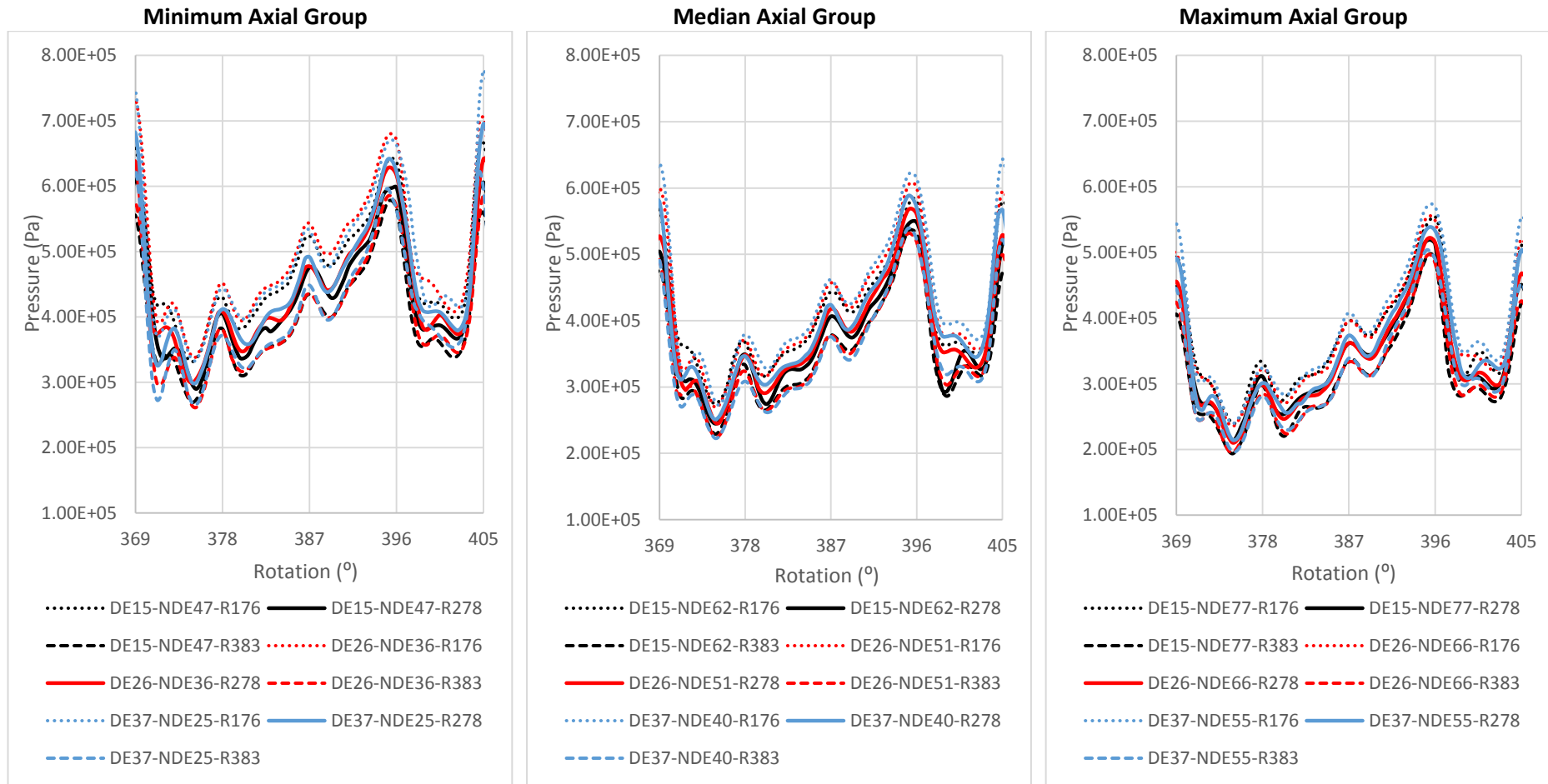


Figure 5-10: Pressure pulsations for parametric clearance models over four blade passages, arranged into minimum (left), median (middle) and maximum (right) axial clearance groups.

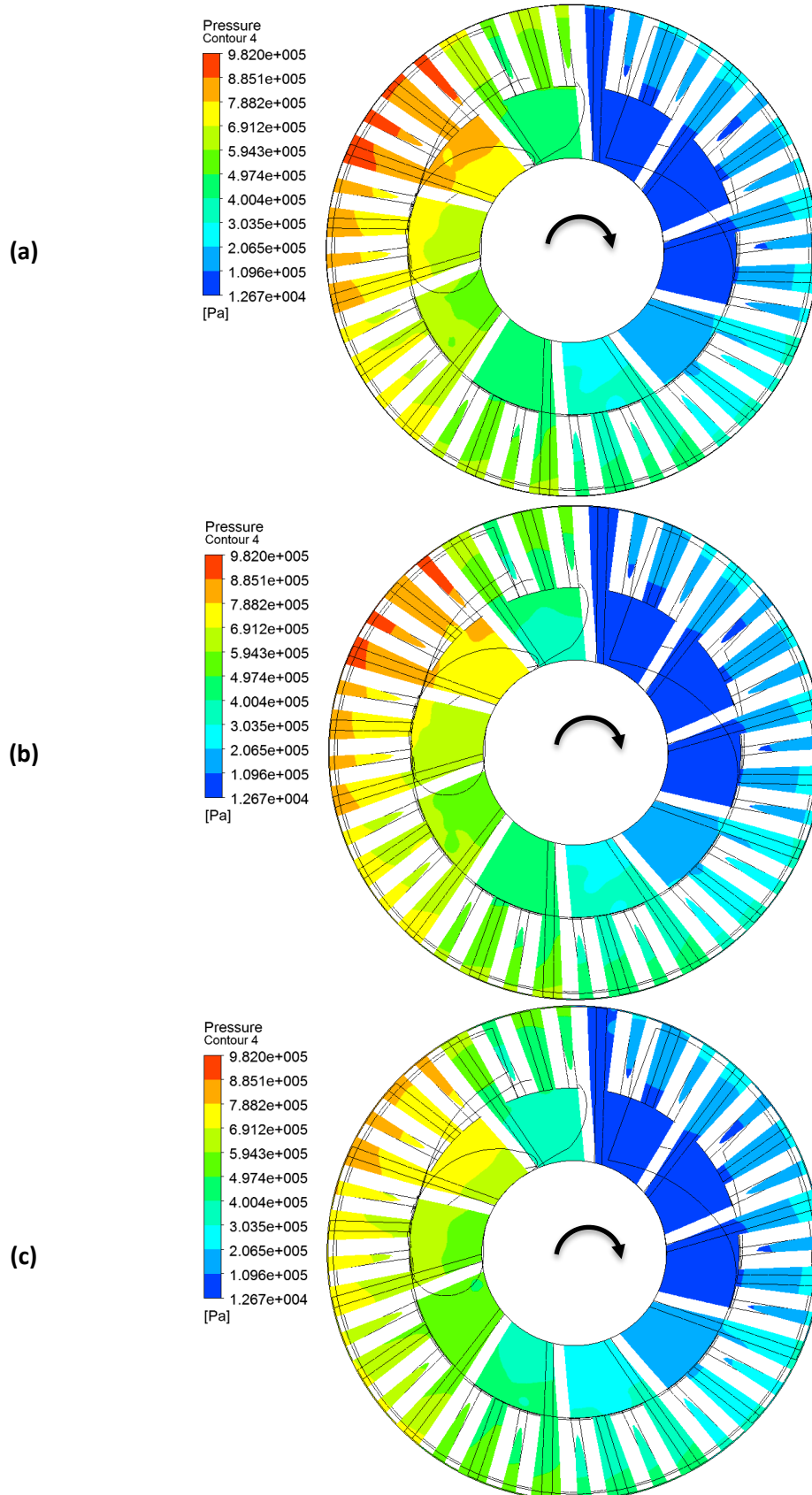


Figure 5-11: Pressure distribution in the impeller for (a) DE15-NDE47-R176, (b) DE15-NDE47-R278 and (c) DE15-NDE47-R383.

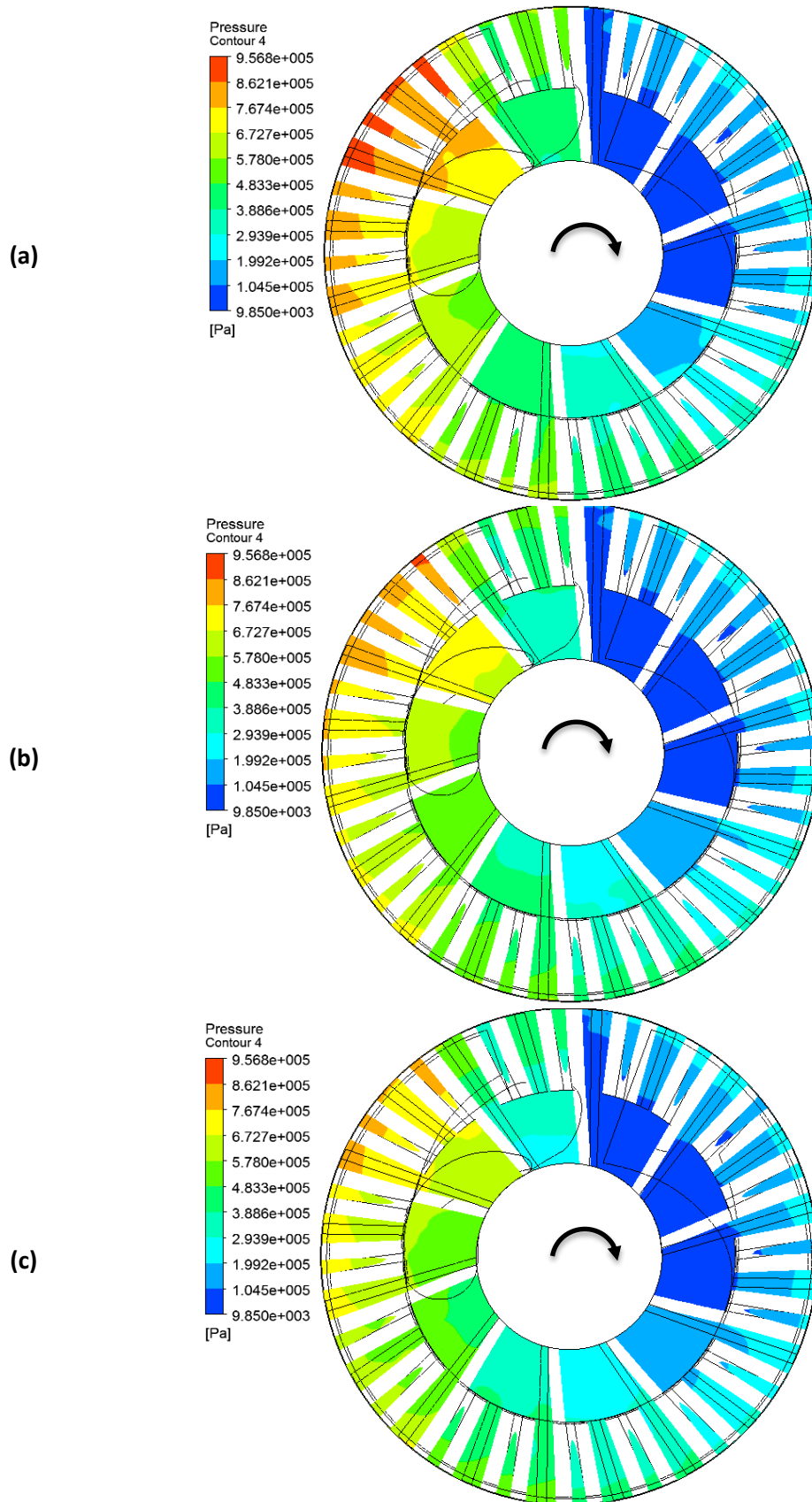


Figure 5-12: Pressure distribution in the impeller for (a) DE26-NDE36-R278, (b) DE26-NDE51-R278 and (c) DE26-NDE66-R278.

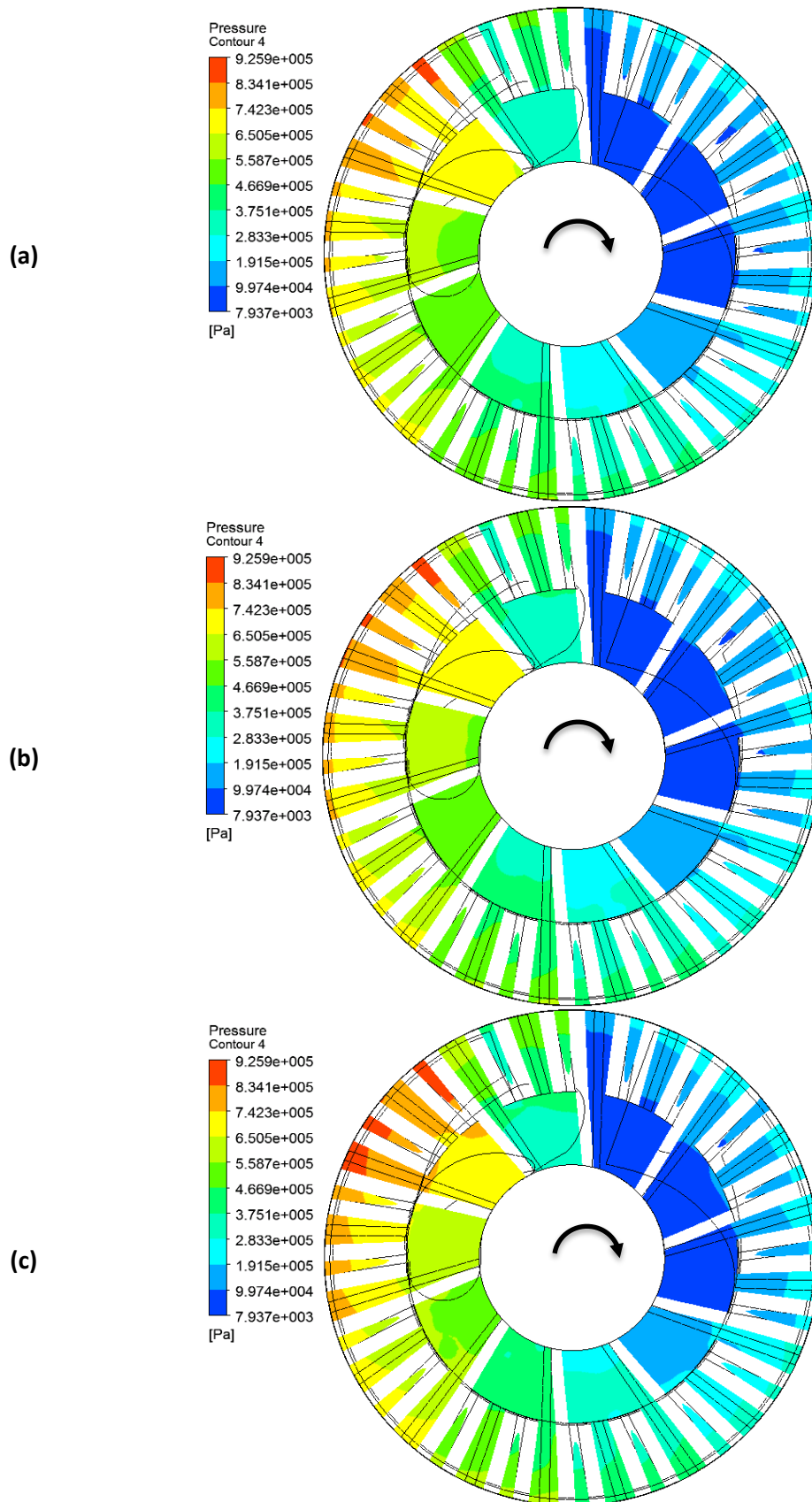
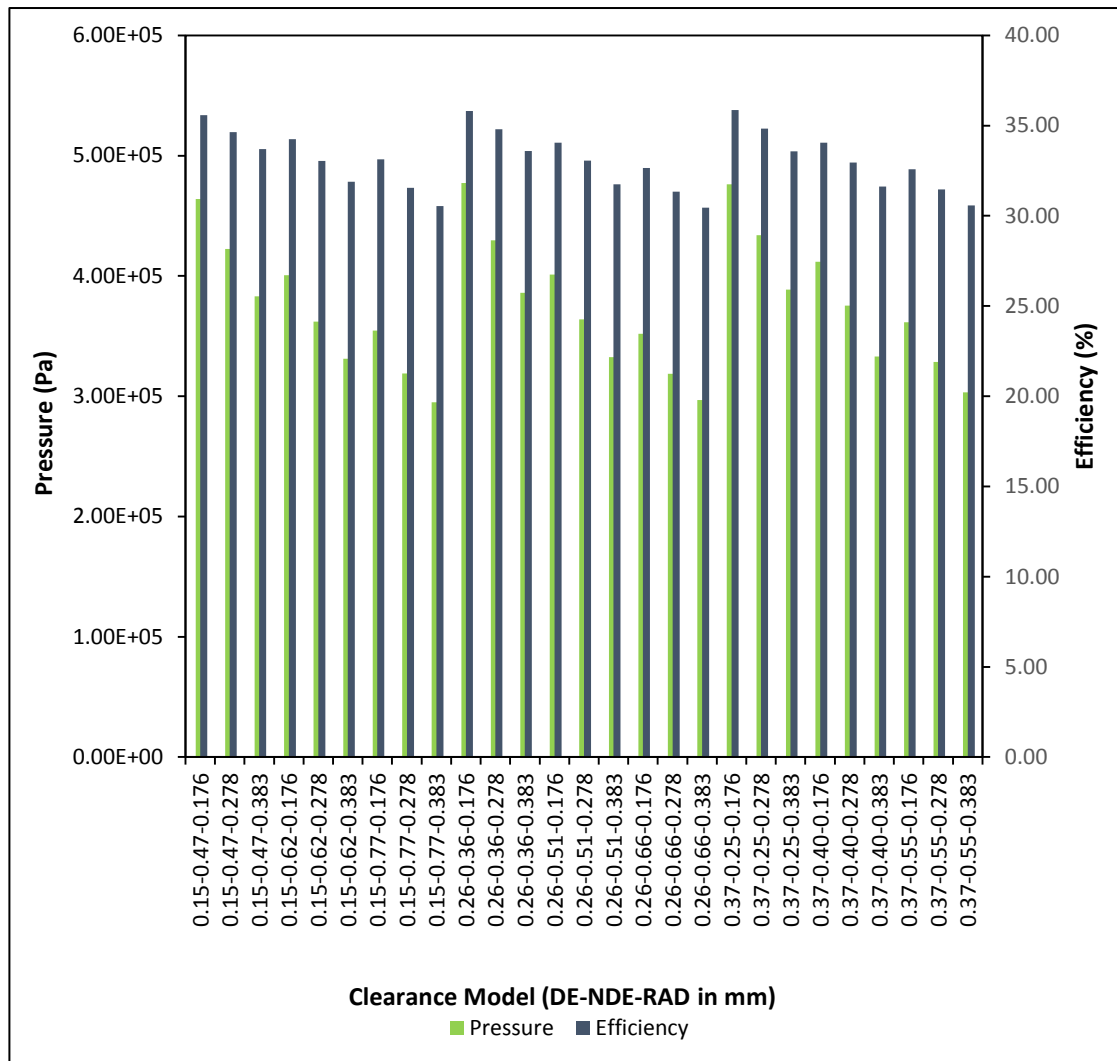


Figure 5-13: Pressure distribution in the impeller for (a) DE15-NDE77-R176, (b) DE26-NDE66-R176 and (c) DE37-NDE55-R176.

The pump efficiency and pressure for each clearance model are plotted in Figure 5-14, showing a clear trend when the models are arranged by ascending DE clearance on the x-axis. For the first nine models on the x-axis, the efficiency and pressure decrease follow an almost straight line. This trend can also be observed for the following nine models and the nine after that.



**Figure 5-14: Results of parametric clearance study showing the pump pressure and efficiency.**

The results indicate that, for this rotational speed and mass flow rate, the radial clearance has a significant effect on both the pump efficiency and generated pressure. This is because the radial clearance between the impeller disk and the casing should be kept to a minimum to reduce leakage from the high-pressure (discharge) side back to the low-pressure (suction) side. Furthermore, the chevron impeller has a large wetted surface, resulting in a continuous thin clearance between the outer radius of the impeller and the casing. Secondly, to improve the performance of the pump it is more important to have a smaller total axial clearance. The



assembly tolerance (axial alignment of pump in relation to the DE) has lower impact on the performance. It appears that a smaller clearance on the NDE (discharge side) than at the DE (suction side) provides a slightly better pump performance. However, the clearance on the suction side is more likely to influence the priming abilities of the pump as this affects its suction performance, which is another area of possible future investigation into the operational life cycle of the RLR pump.

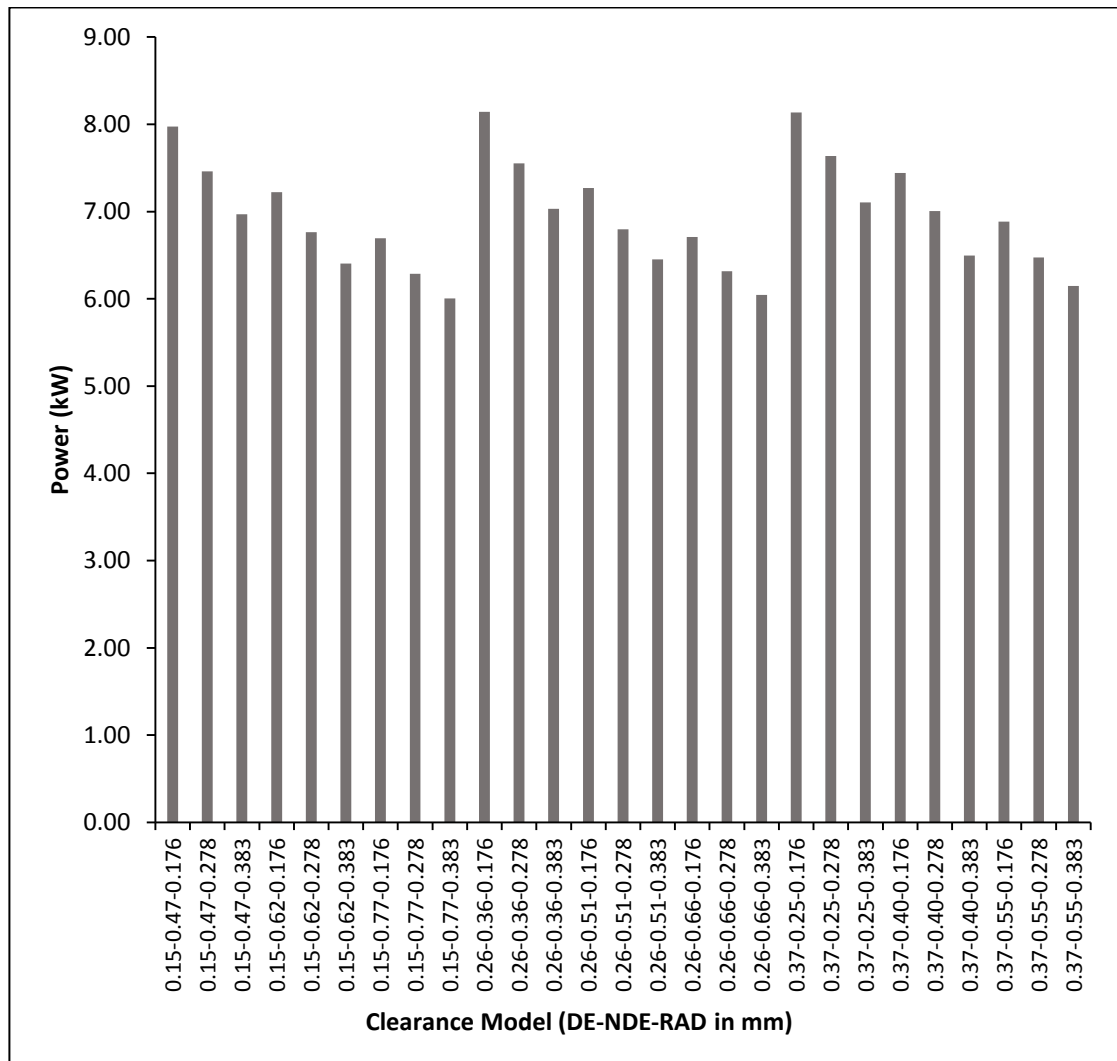


**Figure 5-15: Results of parametric clearance study showing the power consumption.**

The power values follow a similar trend to the pressure and efficiency. The results of the power for each clearance model can be seen in Figure 5-15, which indicates that a higher power consumption leads to a higher pressure generation and improved efficiency. This concurs with the circulation-momentum exchange theory described in Chapter 2 Background; a higher degree of circulation between the impeller blades and the side channels provides a higher

pressure but at the cost of a larger power consumption. The input power is used to generate the pressure increase as well as being consumed by the circulatory flow through the impeller blades, however the efficiency of the pump is significantly reduced when the circulatory flow decreases.

## 5.5 Summary and Conclusions

The results from this analysis suggest that large performance gains can be made with tighter manufacturing tolerances. More interestingly, the results can be used to better understand the life cycle of an RLR pump from manufacture to decommissioning and ensure optimum impeller-casing clearances from inception. This is particularly evident in Figure 5-16 where the results of the 27 different combinations of clearances are plotted against the percentage deviation from the head performance of the median clearance model (i.e. DE = 0.26 mm, NDE = 0.51 mm and R = 0.278 mm), showing that even for a newly built pump the head can be out by as much as  $\pm 25\%$  based on the current manufacturing drawing tolerances. If evaluating the clearance models with the same DE clearance size in Figure 5-16, i.e. 0.15 mm, 0.26 mm and 0.37 mm, against each other, two conclusions can be made. Firstly, the radial clearance clearly has the highest impact on the generated pressure. Secondly, it appears that a larger NDE clearance size provides a slightly better pressure performance.

As would be expected, a pump with tighter clearances due to minimum manufacturing tolerances performs better, while a pump with maximum manufacturing tolerances performs poorly in comparison. The axial and radial clearances have the greatest effect on the pressure performance, while the performance varies only slightly with the axial alignment of the impeller, i.e. the assembly tolerance.

Furthermore, it is possible to combine these findings with a performance-cost analysis. Larger clearances are likely to reduce the rate of internal wear and increase the operational life of the pump. In contrast tighter clearances provide improved performance at the cost of an increased rate of wear, as well as an increase in cost due to higher manufacturing specification. Based on the findings of this study it became evident that it would be necessary to test a number of pumps with a representative range of manufacturing tolerances.

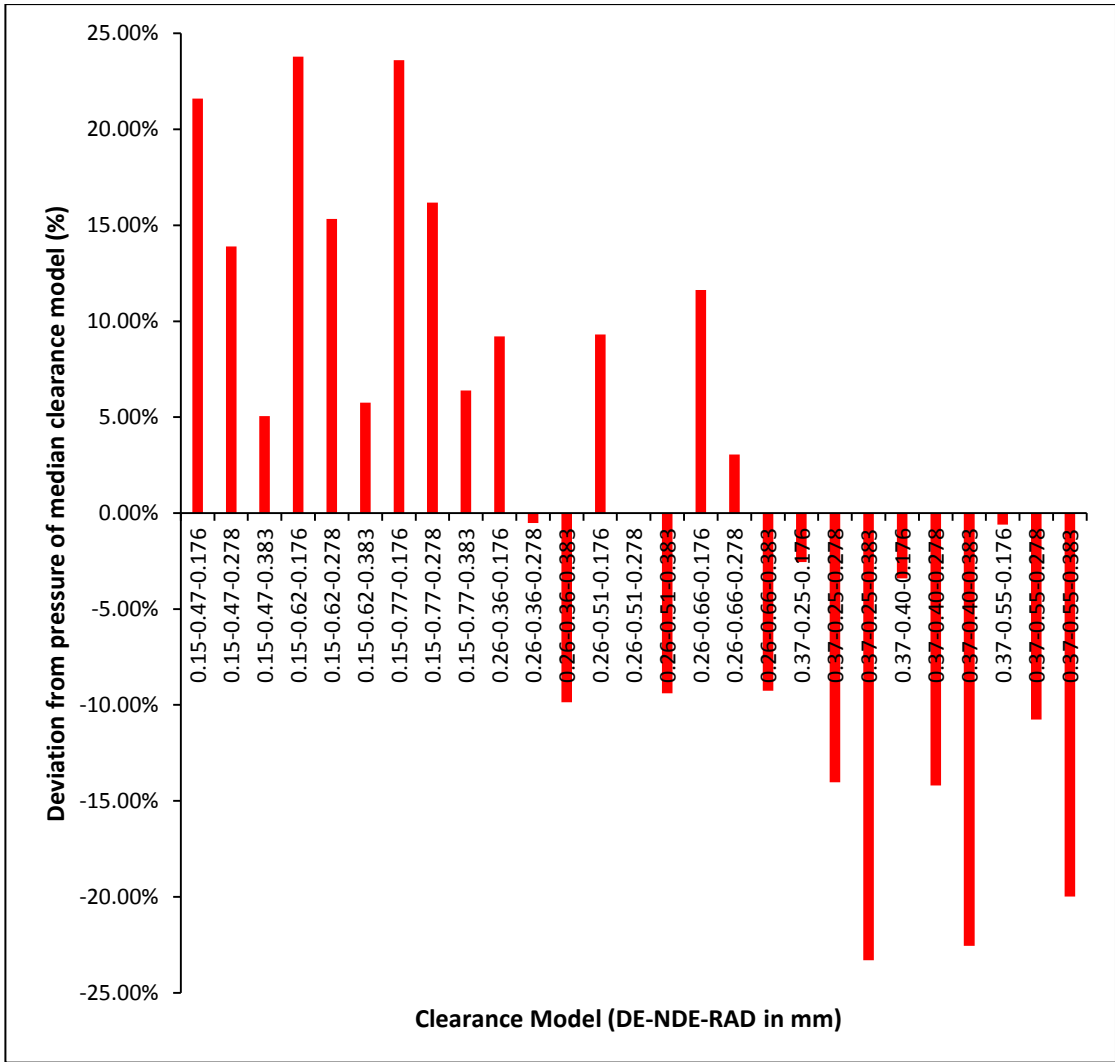


Figure 5-16: Results of parametric clearance study showing the percentage deviation from the pressure performance of the median clearance model (DE= 0.26 mm, NDE=0.51 mm and RAD=0.278 mm).

## 6 Experimental Performance Testing

This chapter describes the experimental performance testing of three 2.5" SX pumps with different axial and radial clearances. The testing took place at the new Gilkes pump testing facility in Kendal according to BS EN ISO 9906:2012 (British Standards Institution, 2012). The tests were carried out by a Gilkes employee with the author invited to observe the initial testing of one pump. A short summary of the manufacture of the pumps is provided, followed by details of the performance cell and equipment used during testing. The characteristic equations used to calculate the performance of the pumps and the performance curves are also provided. The systematic uncertainty is then established. As only one set of tests could be carried out due to commercial constraints, it was not possible to determine the random uncertainty. At the end of the chapter, the results are presented, compared and discussed.

### 6.1 Pump Manufacturing and Part Measurement

Gilkes machine and quality test all their pumps in-house. The drive end (DE) body, non-drive end (NDE) body and impeller are sand cast. The port plate faces and the periphery of the impeller are then machined to create the correct axial and radial clearances in the casing. Similarly, the axial faces of the impeller are also machined.

Based on the manufacturing tolerances provided by Gilkes and the results of the parametric tolerance study (detailed in *5 Parametric Clearance Analysis*), three test pumps were manufactured. The number of test pumps reflected the need to provide a reasonable range of manufacturing tolerance scenarios but limit the cost and time of manufacturing, quality control and testing. It should however be noted that the axial clearance (DE and NDE combined) and the radial clearances are based on the median tolerance range. Table 6-1 below shows the dimensions of the axial and radial clearances and the dimensions of the impellers. The manufactured test pumps are depicted in Figure 6-1.

*Table 6-1: Manufacturing tolerances for the three test pumps.*

Pump	NDE Clearance	DE Clearance	Radial Clearance	Impeller	
				Width	Diameter
<b>A</b>	0.401	0.344	0.265	31.755	177.660
<b>B</b>	0.468	0.305	0.250	31.750	177.660
<b>C</b>	0.527	0.257	0.255	31.740	177.650

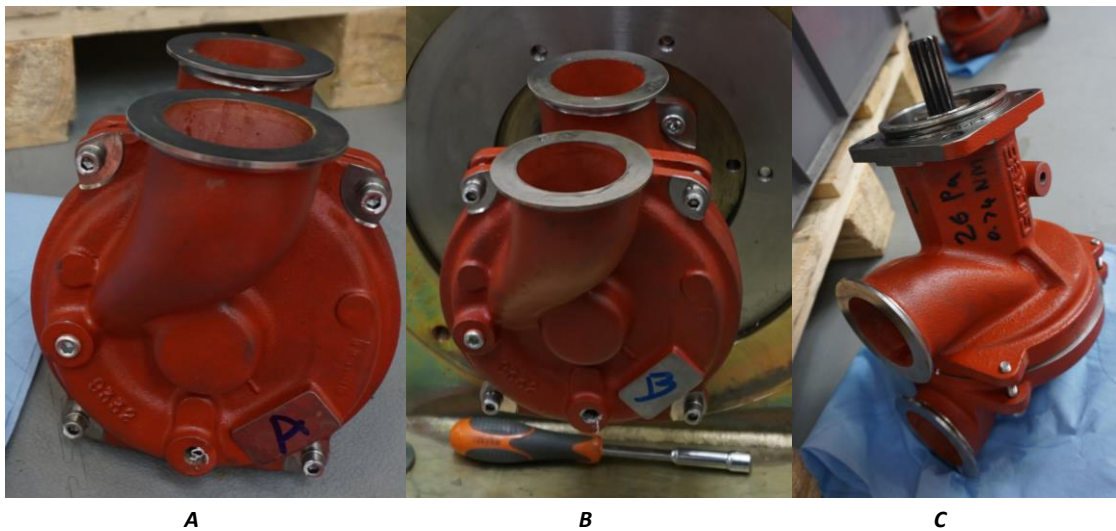


*Figure 6-1: 2.5" SX pumps used for testing.*

## 6.2 Pump Test Rig

The newly built Gilkes pump testing facility features a test cell for establishing the performance, a seal technology cell for analysing pump seal designs and two endurance test cells (coolant and seawater applications) for determining the number of operational hours. The 3D CAD design of the performance test cell (and sealing technology cell) is shown in Figure 6-2 and the physical rig in Figure 6-3 and Figure 6-4.

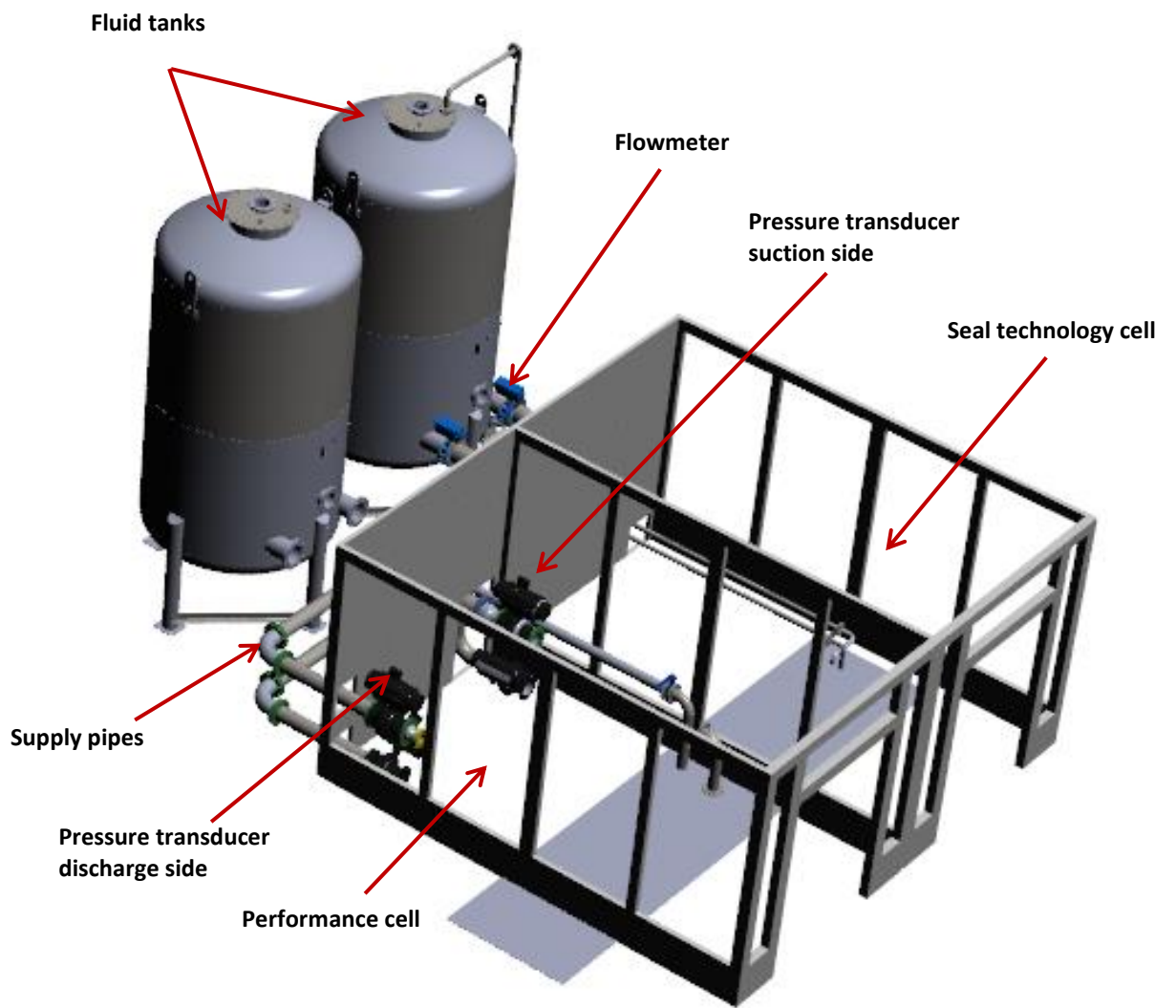


*Figure 6-2: 3D CAD model of new performance test cell (left hand chamber).*

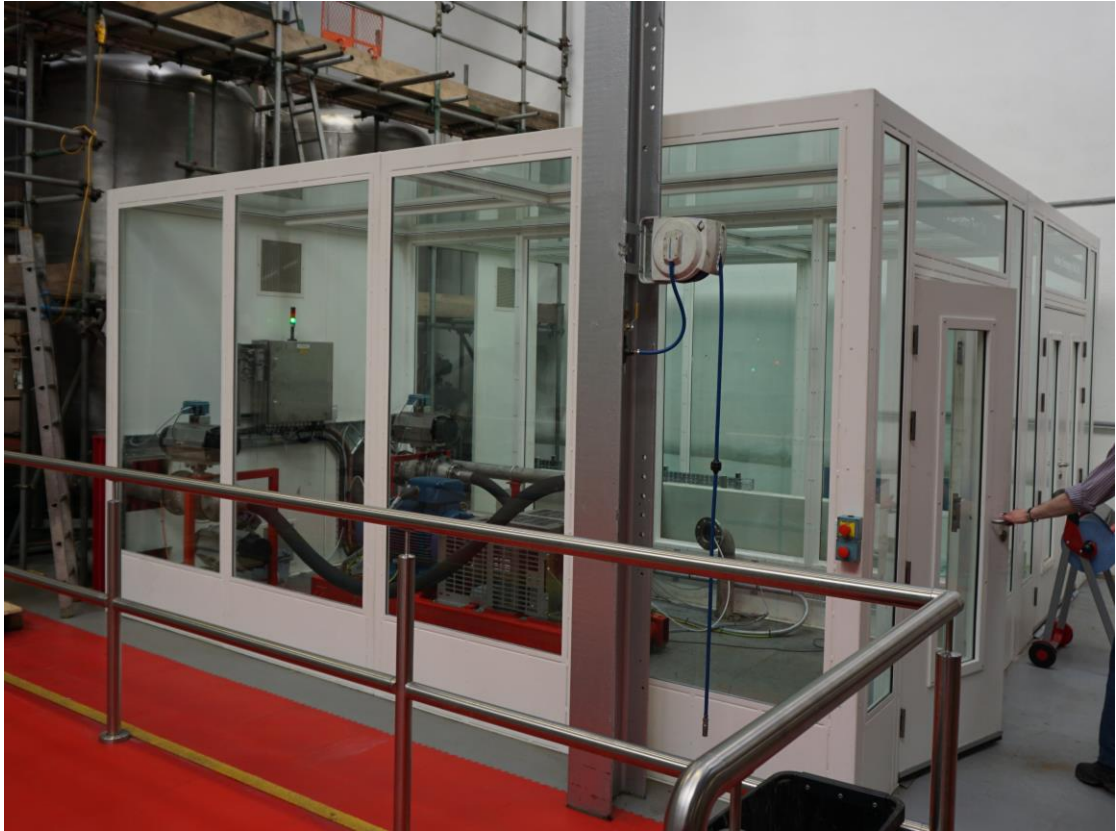


*Figure 6-3: Performance test cell, new Gilkes testing facility in Kendal.*



*Figure 6-4: Aerial view of the performance test cell (left hand chamber).*



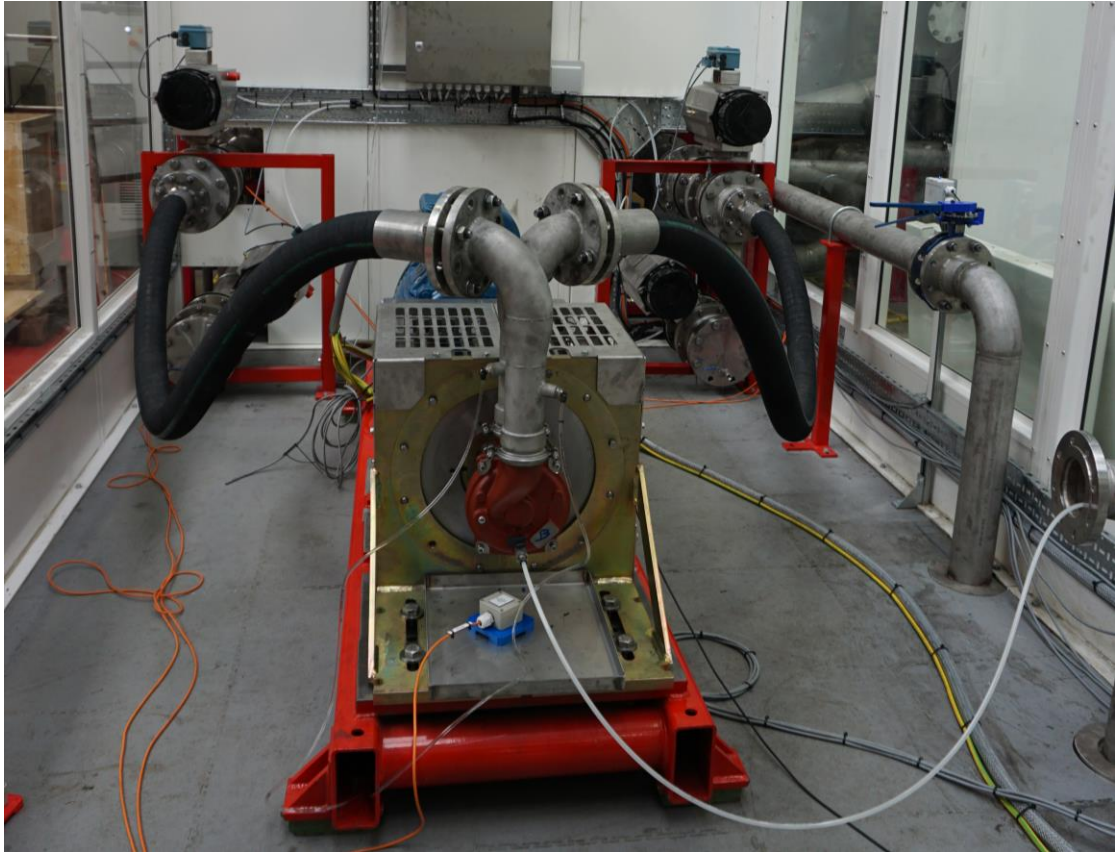


*Figure 6-5: Inside view of the performance test cell.*

The inlet/outlet pipes connected to the pump are attached to flexible hoses which feed into the pipework (see Figure 6-5). The suction is at the DE of the pump, i.e. the right-hand side, while the discharge is on the NDE, i.e. the left-hand side. Pneumatic tubes are fitted in the immediate inlet/outlet pipes and are connected to the pressure transducers, which are positioned towards the back of the cell, one for the suction side and one for the discharge side. The flowmeter is positioned upstream of the pressure transducers, behind the back wall of the cells. The torque transducer is located on the shaft running between the motor and the pump in the metal cage.

### **6.3 Sensors and Instrumentation**

The location of the pressure and torque transducers and the flowmeter in relation to the test rig are described in 6.2 *Pump Test Rig* and shown in Figure 6-2. The sensors used in the pump performance test cell and the details of their operation are given in Table 6-2.



**Table 6-2: Details of the sensors used for the generation of the pump performance curves.**

<b>Instrument</b>	<b>Manufacturer and Model</b>	<b>Measured Parameter</b>	<b>Measuring Range</b>	<b>Accuracy</b>
Pressure Transducer	IFM, PM2654	Pressure head (bar), $H$	0.5-10 bar	$\pm 0.6\%$
Flowmeter	Meatest, M910E-V2020 8"	Flow rate ( $\text{m}^3 \text{h}^{-1}$ ), $Q$	0.1-10 $\text{m s}^{-1}$	$\pm 0.5\%$
Torque Transducer / Tachometer <sup>11</sup>	Datum Electronics, M425	Torque (Nm), $T$ / Rotational speed (rpm), $n$	0-250 Nm / 0-8,000 rpm	$\pm 0.1\%$

## 6.4 Testing Procedure

With the exception of one ‘trial’ pump, the 2.5” SX pumps were the first pumps to be tested in the newly built testing facility. The pumps were initially tested at operational speeds of 2300, 1600 and 1200 rpm twice, once with automatic motor control and then manually.

For the automatic tests, the flow rate was increased from 0 until the valve was fully open before the flow rate was gradually decreased and readings were taken at every second. The manual measurements were started at 50% valve opening. The change in flow rate was achieved by adjusting the percentage valve opening which was reduced in increments of 5% at intervals of 30 seconds with the intention of allowing the flow to stabilise before moving on to the next point. Readings were taken every second. However, upon analysing the results it was clear that the flow was not allowed to stabilise at a given operating point, hence the measurements were not taken at steady state conditions as stated in BS EN ISO 9906:2012.

---

<sup>11</sup> The tachometer is part of the torque transducer system.

For the second set of tests only manual measurements were done. As before the tests were started at 50% valve opening but the flow was reduced in increments of 2% at intervals of approximately 180 seconds. For every second of test reading, measurements are taken of the rotational speed, inlet pressure, outlet pressure, flow rate, pump torque, power input and fluid temperature. The readings of flow rate for pump A, B and C at 2300 rpm are shown in Figure 6-6. From these readings the efficiency, output power and differential pressure head can be calculated. The test fluid was water at room temperature. The intermediate ‘transitional’ data between operating points has not been used. Instead the average was taken for each of the ‘stable’ sample times ensuring a constant number of 150 samples for each point for consistency. This resulted in 13-14 operating points (this number varies with the test pump and speed).

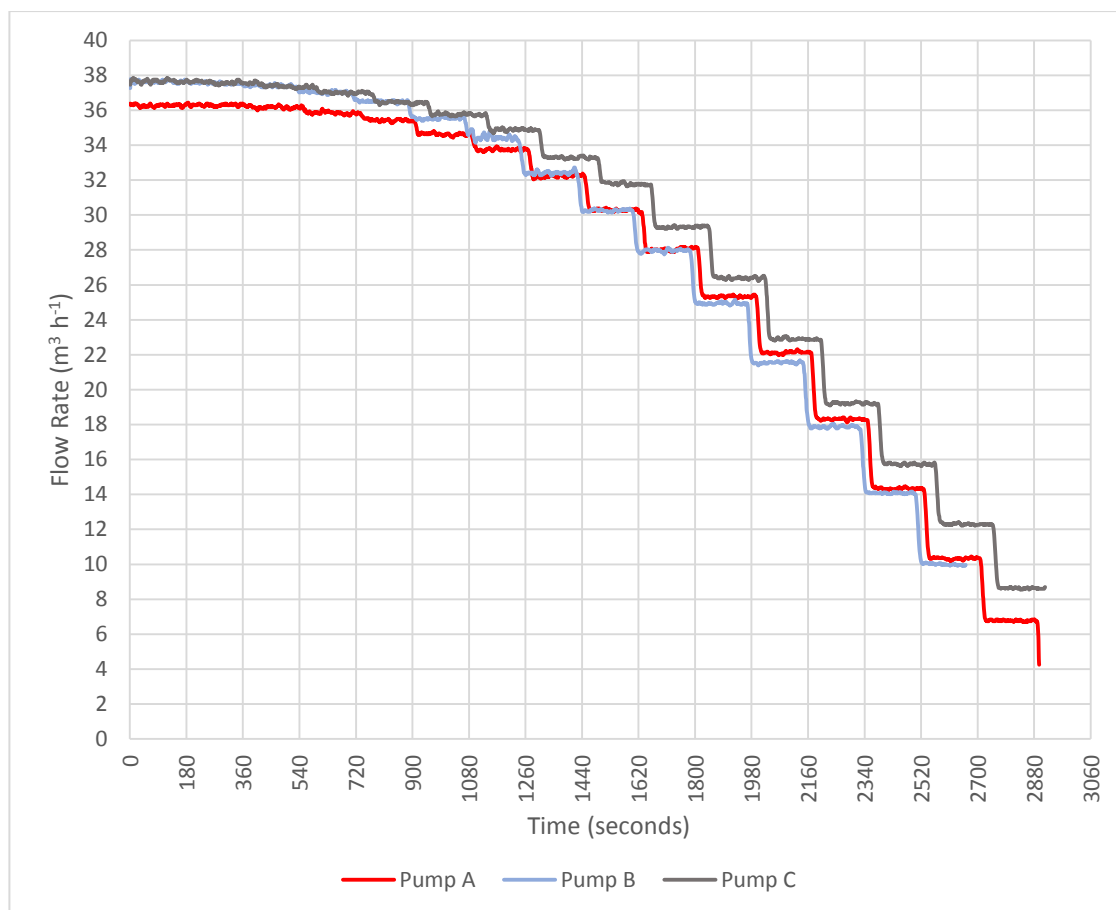


**Figure 6-6: Experimental test readings of flow rate for pump A, B and C at 2300 rpm.**

The intermediate measurements when the valve position is adjusted are removed in Figure 6-7 to show the operating points for pump B at 2300 rpm. As can be seen the difference between the operating points increases as the valve opening is reduced.

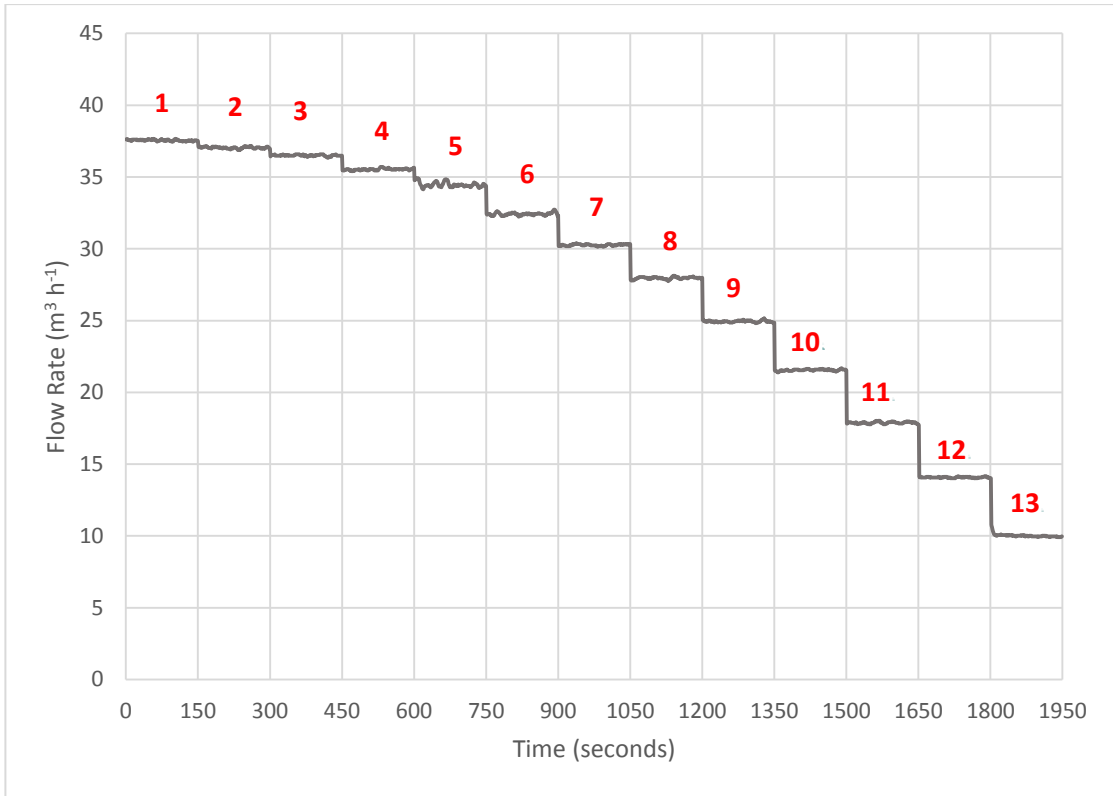


**Figure 6-7: Experimental test readings of flow rate with 180 second sample interval for pump B at 2300 rpm.**

Figure 6-8 shows the time series of the best efficiency point (BEP) for pump B, point 10 in Figure 6-7, in more detail. These measurements correspond to only one operating point, making it possible to determine an average representative value of the flow rate as well as the random uncertainty of the flow rate at that specific operating point.

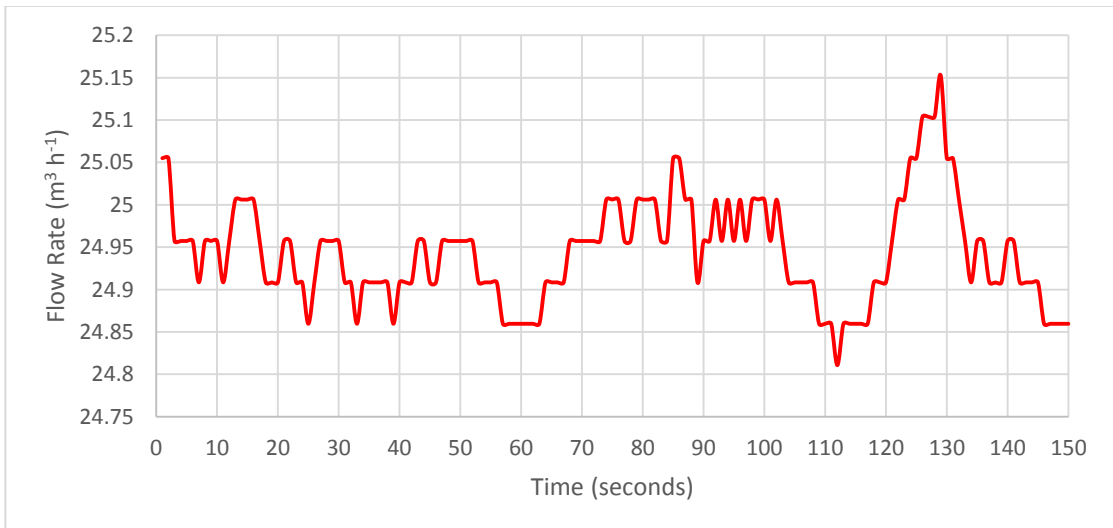


**Figure 6-8: Time series of the BEP point of pump B corresponding to point 10 in Figure 6-7.**

## 6.5 Characteristic Equations

The characteristic equations (6-1)-(6-3) used to define the operation and performance of the test pumps are given below.

$$P_m = T\omega \quad (6-1)$$

$$P_h = \rho gHQ = (p_{out} - p_{in})Q \quad (6-2)$$

$$\eta = \frac{P_h}{P_m} \quad (6-3)$$

Where  $P_m$  is the mechanical power,  $T$  is the torque measured on the pump shaft,  $\omega$  is the angular velocity,  $P_h$  is the hydraulic power,  $\rho$  is the density of water,  $g$  is the acceleration due to gravity,  $H$  is the hydraulic head,  $Q$  is the flow rate,  $p_{out}$  is the discharge pressure,  $p_{in}$  is the suction pressure and  $\eta$  is the efficiency. For consistency throughout the project pressure head has been used to define the performance of the pump rather than hydraulic head.

## 6.6 Translation of the Test Results to the Specified Speed

The BS EN ISO 9906:2012 states that all test data obtained at the speed of rotation,  $n$ , in deviation from the specified speed of rotation,  $n_{sp}$ , must be translated to the specified speed of rotation. If the deviation does not exceed the permissible variation of  $\pm 20\%$ , the measured flow rate,  $Q$ , the differential pressure,  $\Delta p$ , and the power input,  $P$ , can be converted using the below equations (6-4)-(6-6).

$$Q_T = Q \left( \frac{n_{sp}}{n} \right) \quad (6-4)$$

$$\Delta p_T = \Delta p \left( \frac{n_{sp}}{n} \right)^2 \quad (6-5)$$

$$P_T = P \left( \frac{n_{sp}}{n} \right)^3 \quad (6-6)$$

where  $T$  denotes the speed translated value and  $sp$  the specified speed of rotation.

## 6.7 Estimation of the Uncertainty

Uncertainty is an inevitable part of any measurement, even if the procedures and equipment used, as well as the methods of analysis, fully conform to good practice and requirements set out by international standards. This section estimates the total systematic uncertainty for the efficiency and the overall random uncertainty of each operating point.

### 6.7.1 Systematic Uncertainty

The systematic uncertainty for each instrument used during the testing is given in Table 6-3 below. These values are well within the permissible values for instrumental uncertainties (Grade 1) defined by BS EN ISO 9906:2012.

*Table 6-3: The systematic error of each sensor.*

Instrument	Symbol	Systematic Uncertainty
Pressure Transducer ( $H$ )	$f_H$	$\pm 0.6\%$
Flowmeter ( $Q$ )	$f_Q$	$\pm 0.5\%$
Torque Transducer ( $T$ )	$f_T$	$\pm 0.1\%$
Tachometer ( $n$ )	$f_n$	$\pm 0.1\%$

The total systematic uncertainty for the efficiency,  $f_s$ , can be calculated using the root-sum-squared method in equation (6-7) below, given in the IEC 60193:1999 (International Electrotechnical Commission, 1999). The total systematic uncertainty in the efficiency,  $\eta$ , was calculated as  $\pm 0.79\%$ .

$$f_s = \pm \sqrt{f_H^2 + f_Q^2 + f_T^2 + f_n^2} \quad (6-7)$$

The systematic uncertainties cannot be reduced by repeating the measurement if the same instruments and the same measurement procedure are used. The main objective of the experimental testing was to compare the clearance combinations of three test pumps for which the systematic uncertainty can be cancelled out and it is only the random uncertainty which determines the error in the comparison.

### 6.7.2 Random Uncertainty

Unfortunately, due to commercial restraints and limited access to the testing equipment the tests could not be repeated to account for any random uncertainty due to the characteristics of the measuring system or the variations of the measured quantity by taking repeat measurements at a single operating point. It is however possible to estimate the overall random uncertainty of each operating point by calculating the uncertainty for the measured quantities, i.e. pressure, flow rate and torque, and calculated quantities, i.e. power and efficiency. The methodology is taken from Annex L (*Analysis of random uncertainties for a test at constant operating conditions*) of the international testing standard (IEC 60193:1999).

For example, if  $n$  is the number of readings, the arithmetic mean,  $\bar{Y}$ , of the time series  $Y_i (i = 1 \dots n)$  can be determined using equation (6-8).

$$\bar{Y} = \frac{1}{n} \sum_{i=1}^n Y_i \quad (6-8)$$

The standard deviation,  $S_y$ , of these observations is calculated using equation (6-9) below.

$$S_y = \sqrt{\frac{1}{n-1} \sum_{i=1}^n (\bar{Y} - Y_i)^2} \quad (6-9)$$

The random uncertainty associated with the mean value at 95% confidence level, using the Student's t-distribution, is given by equation (6-10) and (6-11).

$$(e_Y)_r = \pm \frac{t \times S_y}{\sqrt{n}} \quad (6-10)$$

$$(f_Y)_{r95} = \pm \frac{(e_Y)_r}{\bar{Y}} \times 100\% \quad (6-11)$$

Where  $t$  is the Student's T factor and can be approximated using equation (6-12).

$$t = 1.96 + \frac{2.36}{n-1} + \frac{3.2}{(n-1)^2} + \frac{5.2}{(n-1)^{3.84}} \quad (6-12)$$

### 6.7.3 Overall Uncertainty

The overall uncertainty,  $f_t$ , for each operating point can be calculated using equation (6-13) (IEC 60193:1999) below.

$$f_t = \sqrt{f_s^2 + f_r^2} \quad (6-13)$$

The overall uncertainty for each of the measured and calculated quantities can then be plotted against the operating point for each test pump and operational speed. Figure 6-9 - Figure 6-11 show the overall uncertainty for pump A at 1200 rpm, pump B at 1600 rpm and pump C at 2300 rpm, respectively.

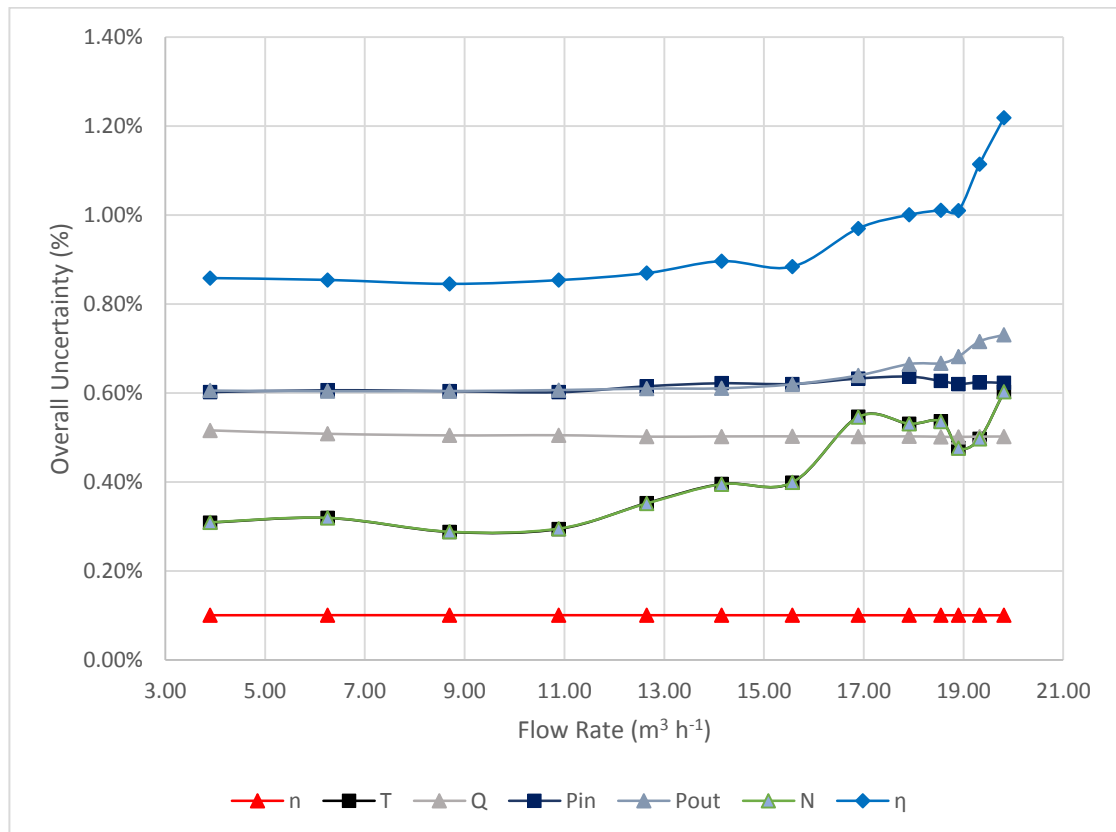
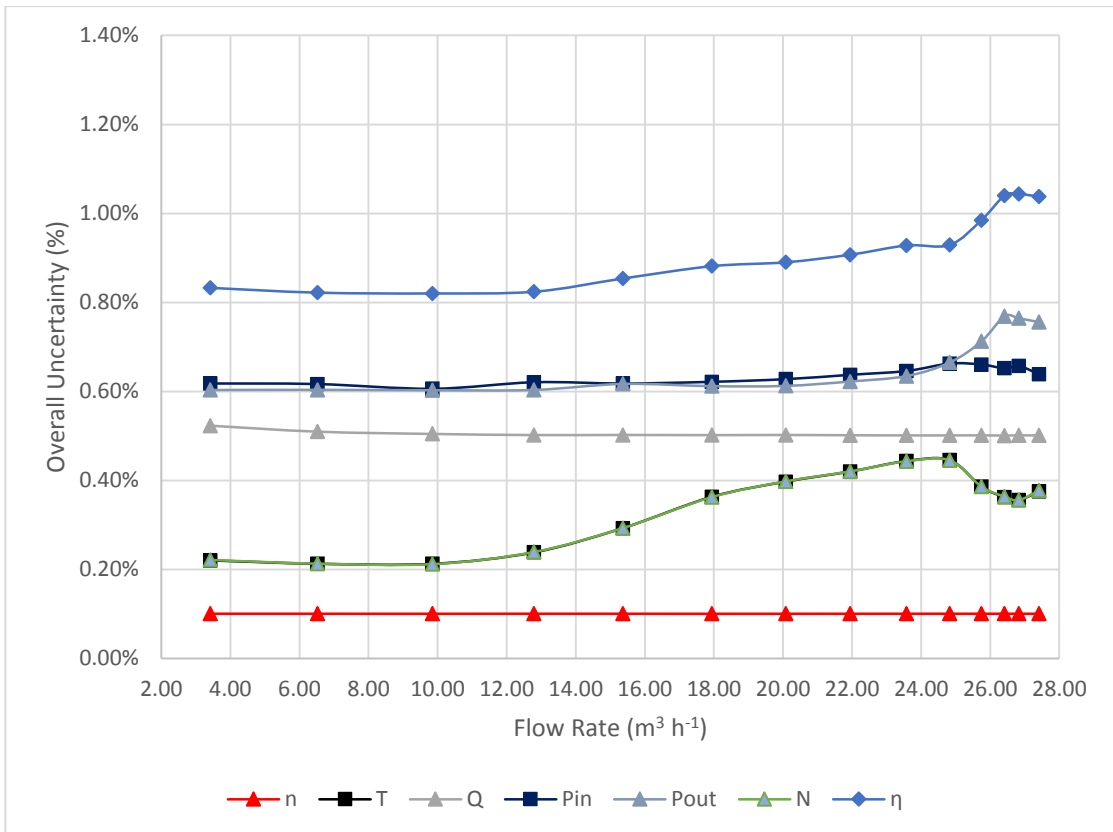


Figure 6-9: Overall uncertainty for speed ( $n$ ), torque ( $T$ ), flow rate ( $Q$ ), inlet pressure ( $P_{in}$ ), outlet pressure ( $P_{out}$ ), power ( $N$ ) and efficiency ( $\eta$ ) for pump A at 1200 rpm.



**Figure 6-10: Overall uncertainty for speed ( $n$ ), torque ( $T$ ), flow rate ( $Q$ ), inlet pressure ( $P_{in}$ ), outlet pressure ( $P_{out}$ ), power ( $N$ ) and efficiency ( $\eta$ ) for pump B at 1600 rpm.**

The figures are intended to depict a general picture of the overall uncertainty. The trends are similar for each pump and operational speed tested. As can be observed in Figure 6-9 and Figure 6-10, there appears to be a higher degree of uncertainty of torque in particular, and subsequently power and efficiency, at the higher flow rates measured at 1200 and 1600 rpm. At higher flow rates, more fluid is moving through the impeller which increases the inertial force. The motor is turning one way, whilst the impeller is being resisted by the fluid presence. It therefore becomes harder for the motor to deliver the required torque due to slip and as a result the speed needs to be constantly adjusted.

The uncertainties are more consistent at 2300 rpm, which is the optimal operational speed of the pump, see Figure 6-11. Typically, the uncertainty will increase at the design limits of the measurement equipment, i.e. at closed and fully open valve conditions. Furthermore, it could be that the flexible hoses attached up- and downstream of the pump suction and discharge, see Figure 6-5, are inducing more vibration at higher flow rates and thus contributing to non-optimal operating conditions. However, the values are well within the permissible values for overall uncertainties (Grade 1) defined by BS EN ISO 9906:2012.



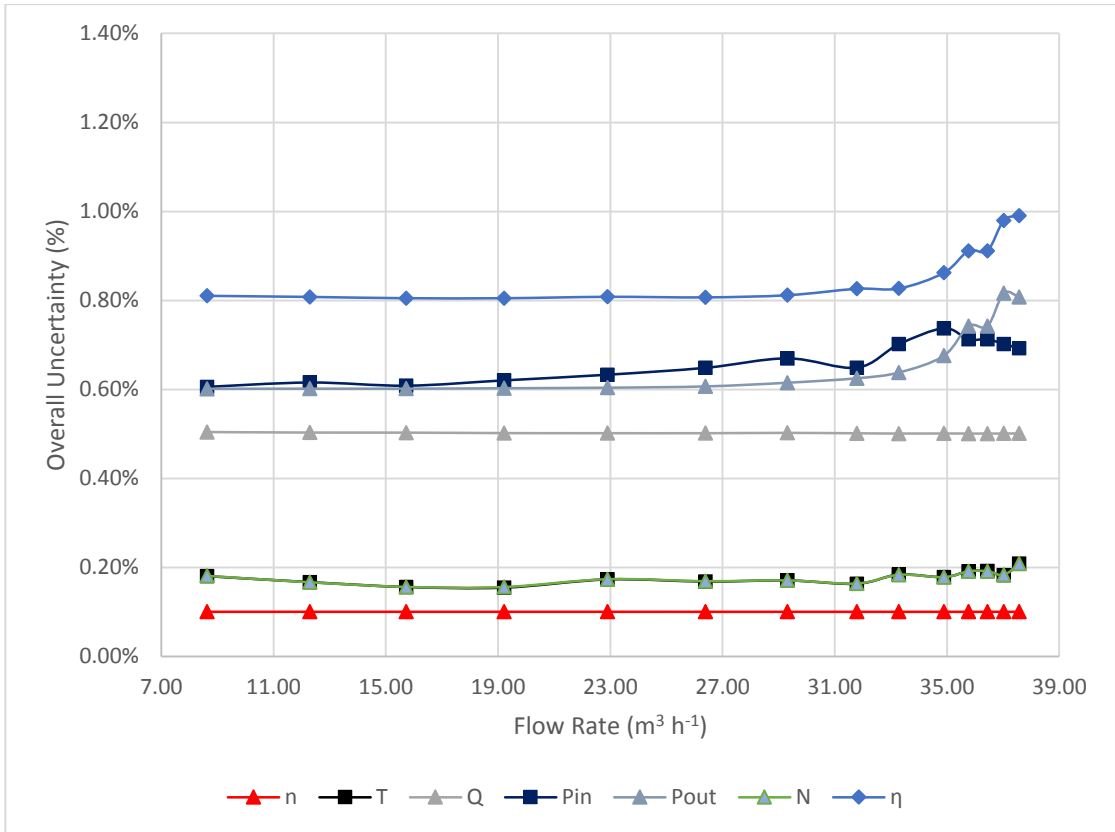


**Figure 6-11: Overall uncertainty for speed ( $n$ ), torque ( $T$ ), flow rate ( $Q$ ), inlet pressure ( $P_{in}$ ), outlet pressure ( $P_{out}$ ), power ( $N$ ) and efficiency ( $\eta$ ) for pump C at 2300 rpm.**

### 6.8 Test Results

The results of the three different 2.5" SX test pumps are collated in three graphs shown in Figure 6-12, Figure 6-13 and Figure 6-14 for the pressure head, the efficiency and the power input, respectively. This makes it possible to directly compare the effect of different manufacturing tolerances on the performance of the test pumps.

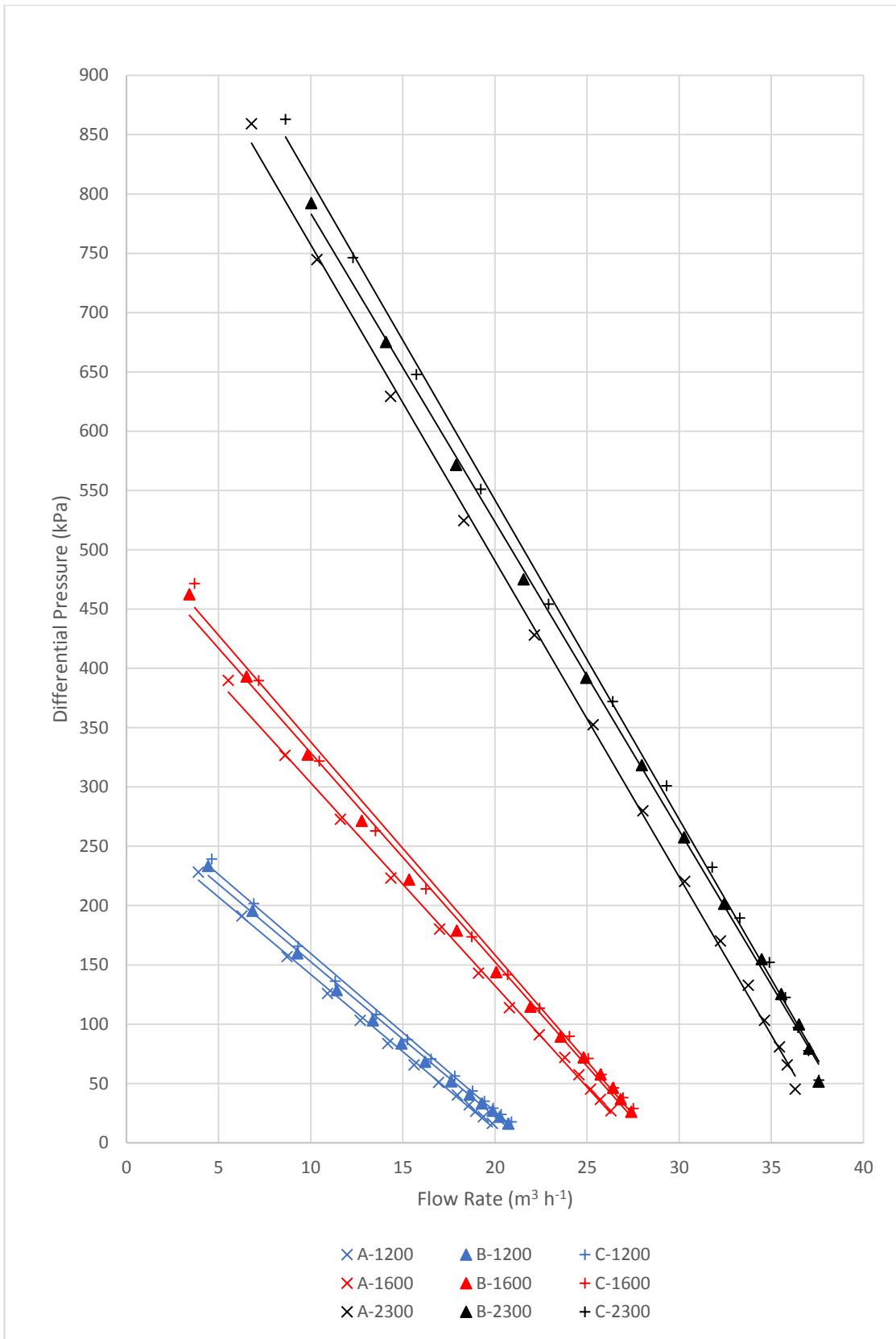


**Figure 6-12: Experimental pressure head curves for pump A, B and C at 1200, 1600 and 2300 rpm.**

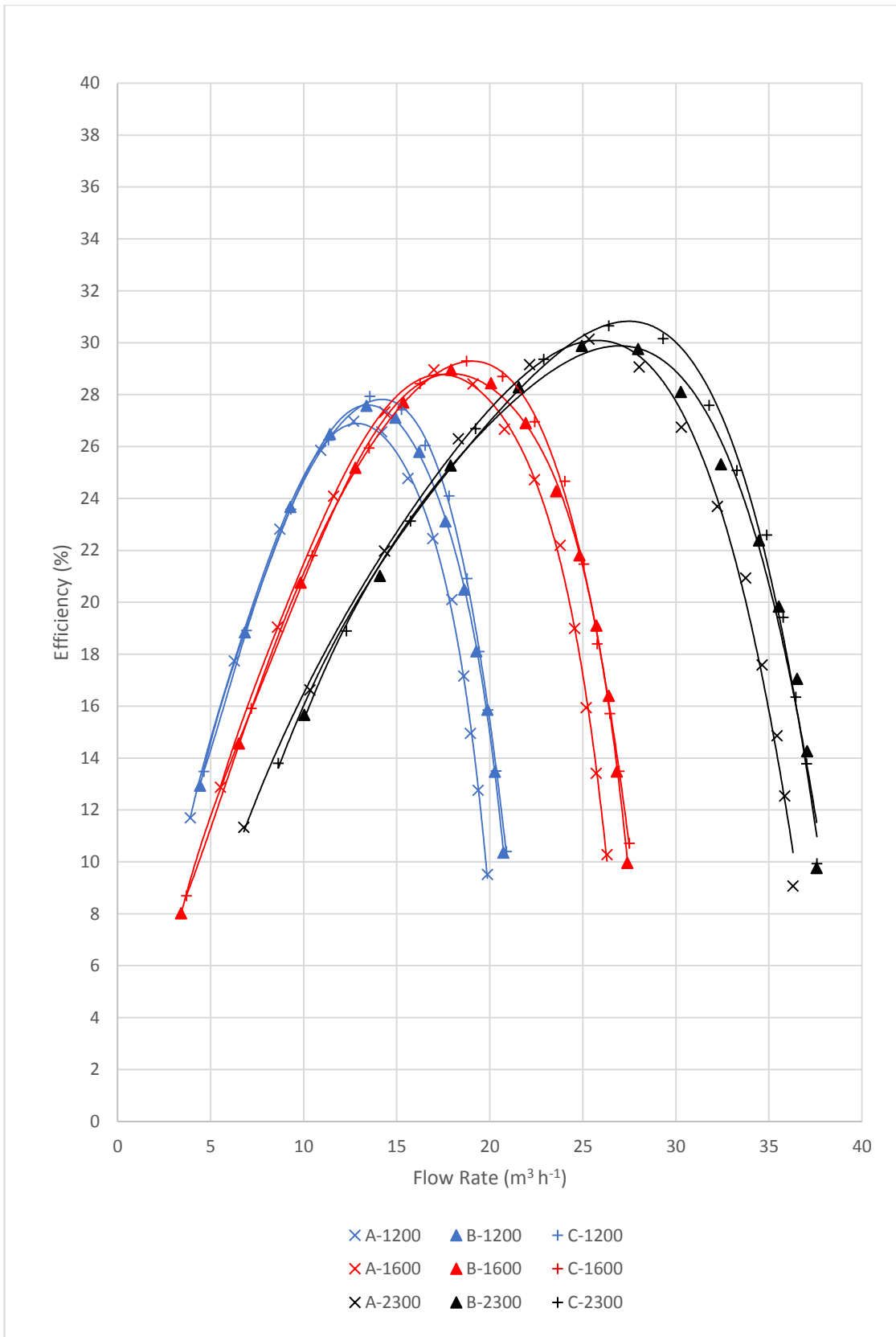


Figure 6-13: Experimental efficiency curves for pump A, B and C at 1200, 1600 and 2300 rpm.

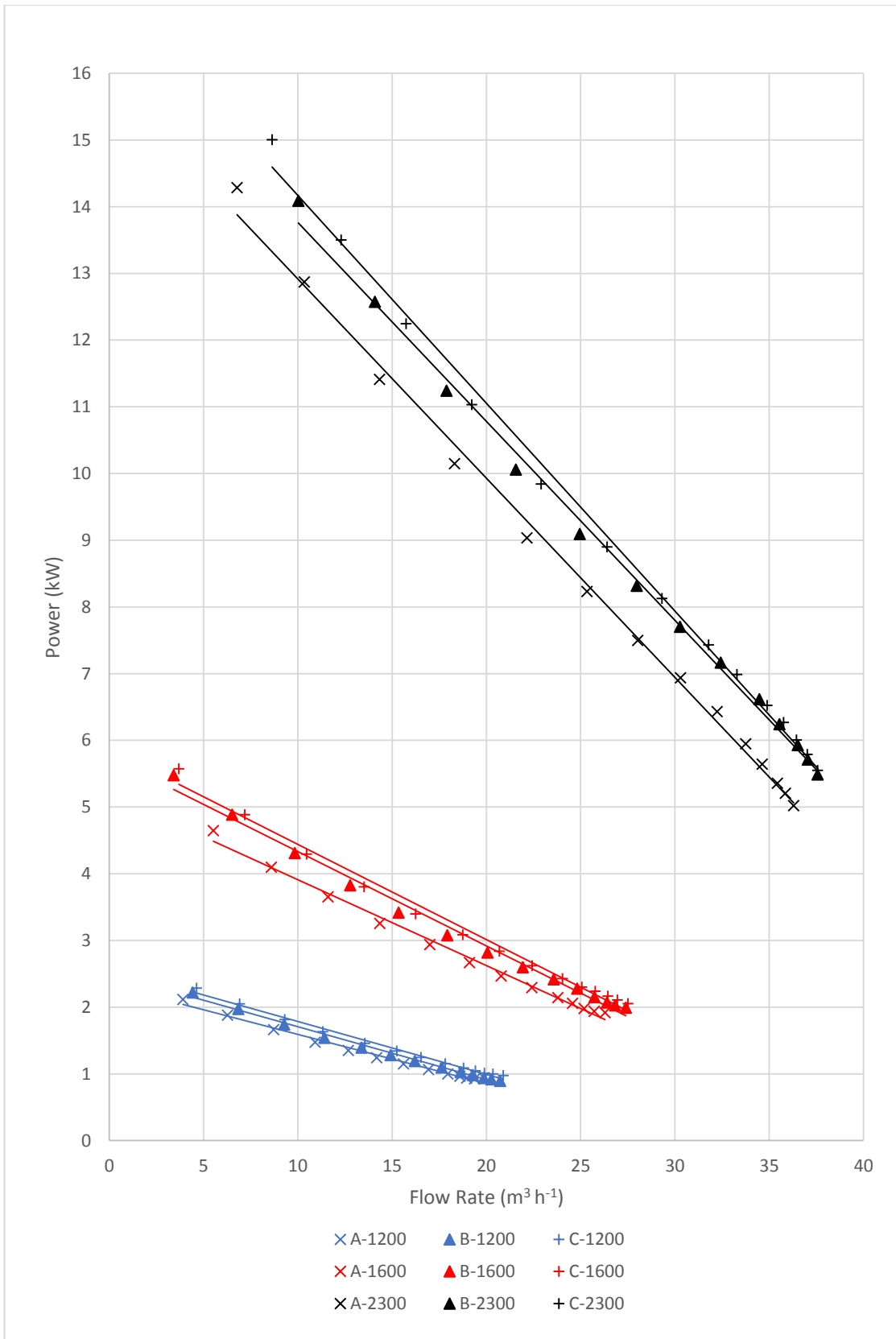


Figure 6-14: Experimental power curves for pump A, B and C at 1200, 1600 and 2300 rpm.

## 6.9 Results Comparison and Discussion

The experimental results of the three 2.5" SX test pumps are compared and discussed in this section analysing the effects of the change in manufacturing tolerances on the performance of the pumps.

Figure 6-12 shows that test pump C produces a higher differential pressure at all the rotational speeds tested. The better pressure performance is more notable at the highest speed of 2300 rpm with smaller gains as the speed is reduced. The lowest pressure is categorically produced by test pump A, again the reduction compared to the two other test pumps being more notable at 2300 rpm. It is clear that out of the three operational speeds tested 2300 rpm is the optimal, which can lead one to conclude that ideal operational conditions can be reached at higher operational speeds. However, limitations exist and there might be other factors to take into account such as increased vibration and higher rate of mechanical wear. No evidence of the RLR pump tested at higher speeds than 2300 rpm is available for comparison. The results from the computational modelling (see 7.2 *Performance Characteristics*) show that the amplitude of the pressure pulsations increase with operational speeds, subsequently also increasing undesired effects such as vibration and noise.

Similar trends can be observed for the efficiency in Figure 6-13. However, the efficiencies are relatively similar for lower flow rates, while the efficiency of test pump C is notably higher around the best efficiency point (BEP) for all three rotational speeds. At each operational speed the largest difference in efficiency occurs at higher flow rates. This is particularly evident for pump A. At flow rates lower than the BEPs for each pump, the difference in efficiency is minimal (almost identical at 1200 rpm), however after the BEP there is a clear drop in efficiency for pump A compared to the other two pumps. The difference between pump B and C is small, although pump C is slightly more efficient over four flow rates after the BEP. Based on these findings one can conclude that a smaller DE and larger NDE clearance combination (i.e. pump C) is more efficient in the mid-to-high flow rate spectrum (refer to Table 6-1 for manufacturing tolerances for each test pump).

The trends for the shaft power represented in Figure 6-14 are almost identical to pressure curves in Figure 6-12. The power consumption for pump B and C is similar while pump A consumes noticeably the least power. One can therefore conclude that, generally, a more

efficient pump also consumes more power. This concurs with the results of the parametric clearance study in chapter 5.

It is interesting to note that when comparing the produced pressure head at the BEP for each test pump, the operational speed has a clear influence. At 1200 rpm the highest pressure head is produced by test pump C (in descending order: C-B-A), at 1600 rpm by test pump A (in descending order: A-B-C) and at 2300 rpm by test pump B (in descending order: B-C-A). The percentage difference between the largest and lowest pressure value at these BEPs vary by 4.56%, 3.61% and 10.09% for each speed, respectively. The BEP values are included in Table 6-4.

*Table 6-4: Experimental values at best efficiency point for pump A, B and C at 1200, 1600 and 2300 rpm.*

	1200 rpm			1600 rpm			2300 rpm		
	A	B	C	A	B	C	A	B	C
<b>Flow Rate (m<sup>3</sup> h<sup>-1</sup>)</b>	12.68	13.37	13.55	17.00	17.93	18.75	25.33	24.95	26.40
<b>Differential Pressure (kPa)</b>	103.24	103.29	108.17	180.05	178.92	173.56	352.41	391.94	372.01
<b>Shaft Power (kW)</b>	1.35	1.39	1.46	2.94	3.08	3.09	8.23	9.09	8.90
<b>Efficiency (%)</b>	26.97	27.56	27.93	28.95	28.96	29.29	30.13	29.87	30.65

A higher operational speed will increase the centrifugal force and subsequently the radial deflection (Krutzsich & Cooper, 1986), in other words the radial clearance is likely to reduce at higher speeds as the impeller is deflected outwards. A smaller radial clearance is likely to reduce the backflow from the high pressure (NDE) side to the low pressure (DE) side. As pump B has the smallest radial clearance (0.25 mm), the leakage losses are likely to be lower, leading the pump to generate a higher pressure head than the other pumps at 2300 rpm. Conversely, the centrifugal force and deflection will be lower at a lower operational speed.

Despite pump C having a larger radial clearance (0.255 mm) than pump B, it generated the highest pressure head at 1200 rpm, however the difference between the largest and lowest pressure value is significantly smaller than at 2300 rpm. The impeller in pump C has the smallest diameter. As the centrifugal force also increases with decreasing radius this could

explain the difference in pressure at 1200 rpm. The maximum measured pressure head is notably lower as the operational speed decreases so it could be that there is a lower pressure force acting on the impeller in the axial direction as the speed decreases which means that the axial clearances are closer to their design values. If this is the case, it reinforces the conclusion that a smaller DE clearance is more important for a higher pressure head than the NDE clearance. The difference between the largest and lowest pressure value at 1600 rpm is even smaller and so it might be that the difference is purely down to inconsistencies in the testing procedure and conditions. The centrifugal and axial deflections are investigated further in Chapter 9 *Finite Element Analysis (FEA)* by importing pressure profiles from the CFD analyses in Chapter 7 *Computational Performance Modelling* into a structural analysis.

It is clear that whichever pump can push through the largest amount of fluid per measurement of time (i.e. flow rate) is the most efficient of the three operational speeds measured. For each speed, pump C has the highest best efficiency point, if only by 0.3-1%. The flow rate at that point is higher than the BEP for pump A and B. There is less consistency in the pressure head and power input required. At 1200 rpm pump C produces the highest pressure head and consumes the most power, however at 1600 rpm pump C still consumes the most power but produces the lowest pressure head. At 2300 rpm pump B consumes the most power and produces the highest pressure head. One can conclude that the pump that consumes the most power generally also produces the highest pressure, which concurs with the circulating flow theory. A higher degree of circulation between the impeller blades and the side channels provides a higher pressure but at the cost of a larger power consumption.

Based on these findings it appears that a pump with a larger NDE clearance and smaller DE clearance (i.e. pump C) gives the highest BEP for the three different speeds tested. The radial clearance of pump A is 0.01 mm larger than that of pump C and 0.015 mm larger than that of pump B, so the difference between pump B and C is very small. The difference in DE and NDE clearances are however more significant (refer to Table 6-1), leading one to conclude that the radial clearance ultimately has a greater effect on the pump performance.

## 7 Computational Performance Modelling

This chapter details the studies carried out to computationally assess the performance of the three 2.5" SX pumps detailed in *Chapter 6 Experimental Performance Testing*. The CFD model is altered to replicate the experimental test pumps and the exact experimental setup and operating conditions are used. The results are presented in the form of pressure pulsation characteristics and performance curves. In addition, the pressure across the DE, NDE and radial clearances are measured and compared against the total pressure increase in the pump. Following this, the sensitivity of the impeller width and diameter is assessed. A full comparative analysis of the experimental and computational modelling is detailed in *Chapter 8 Comparison of Computational and Experimental Results*.

All the simulations are run using the coarse mesh described in *4.5 Mesh Independence Study* with test cases using the medium mesh. A one-way Fluid-Structure Analysis is then carried out in *Chapter 9 Finite Element Analysis (FEA)* using the results obtained in this chapter to further understand the relationship between the axial and radial clearances and the pump performance.

### 7.1 Geometry Preparation

As with the parametric clearance study in *Chapter 5 Parametric Clearance Analysis* the geometry was prepared in SolidWorks® before being imported into DesignModeler®. As only three computational pump geometries were required, the width and the diameter of the impeller fluid domain were also altered. The change in impeller width was accommodated by slicing off excess material as shown in Figure 7-1, while the change in impeller diameter was incorporated by adding material to the periphery of one impeller fluid region and then using a circular pattern feature as shown in Figure 7-2. Similar preparation methods as in *Chapter 5* were applied to the axial and radial clearances, however the direction of added material was outwards from the impeller fluid domain to accommodate the change in impeller width.



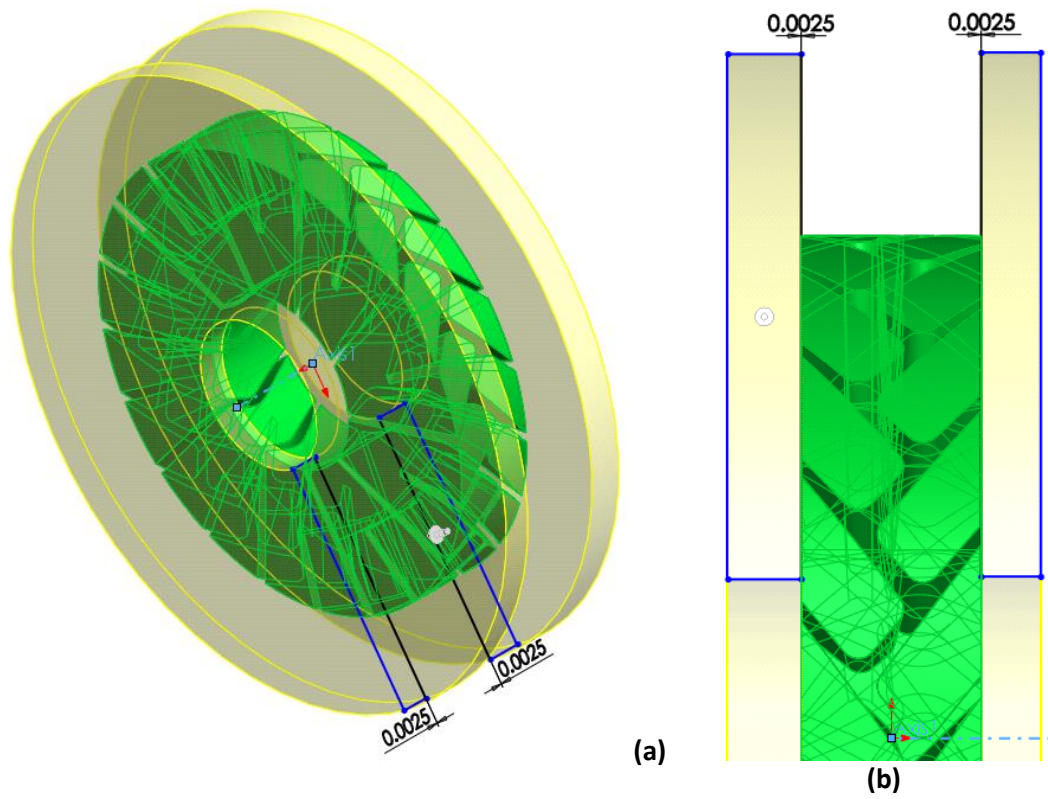


**Figure 7-1: Modifying the impeller width showing (a) isometric view and (b) cross-sectional view; example dimensions are for pump B.**

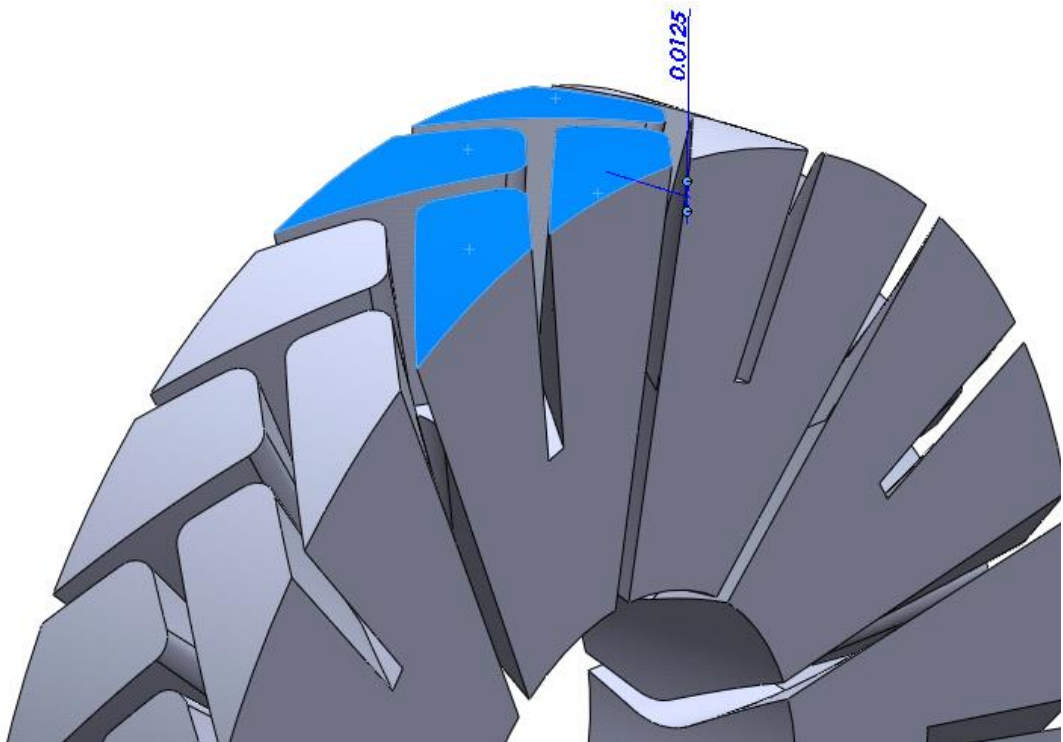


**Figure 7-2: Modifying the impeller diameter by adding material; example dimension is for pump A.**

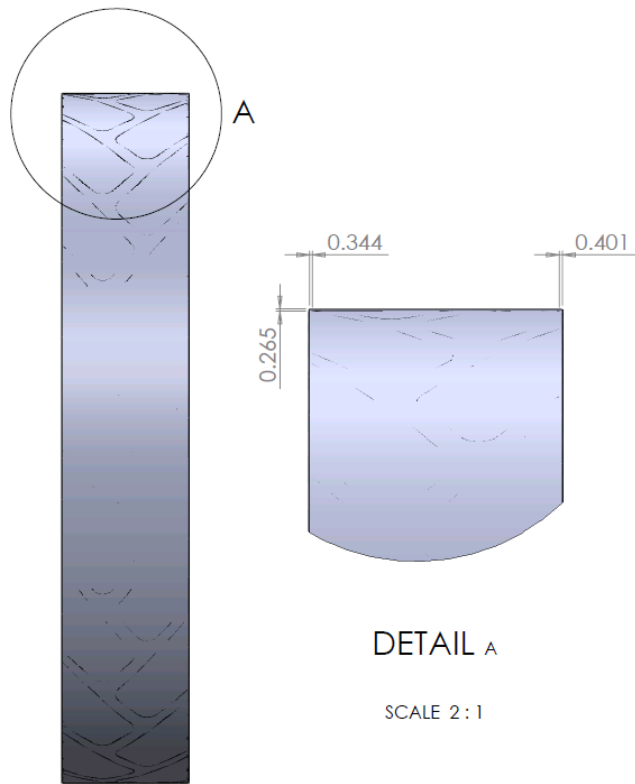


**Figure 7-3: Experimental test pump parameters; radial, NDE and DE clearance magnitudes for pump A.**

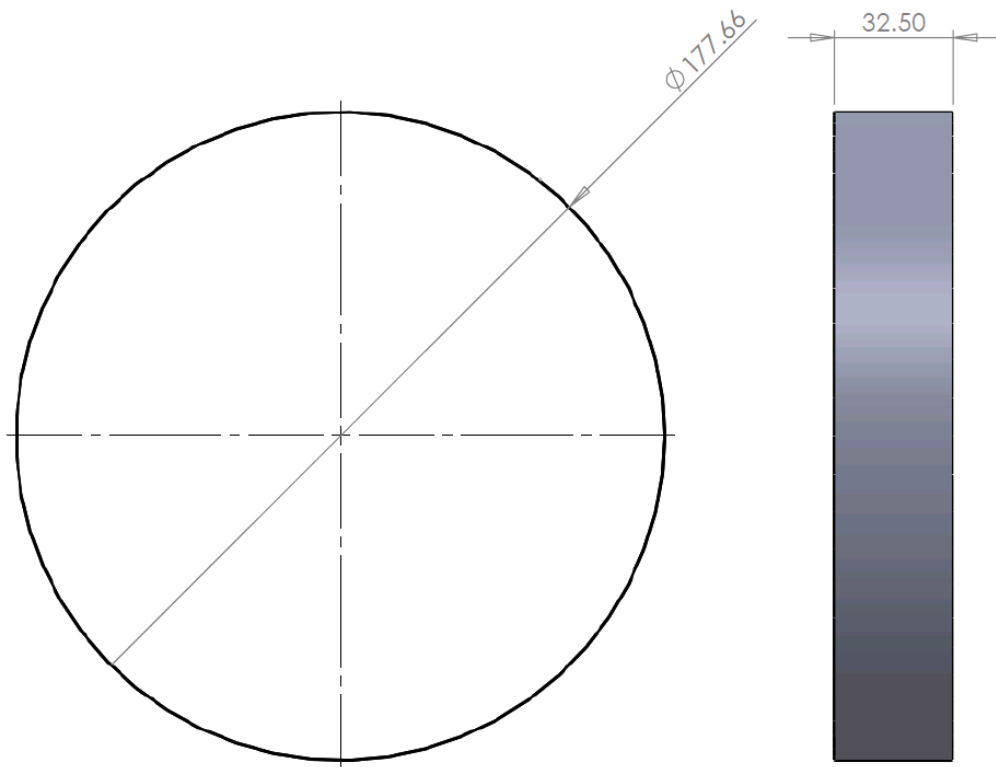


**Figure 7-4: Experimental test pump parameters; diameter and width of radial clearance ring for pump A.**

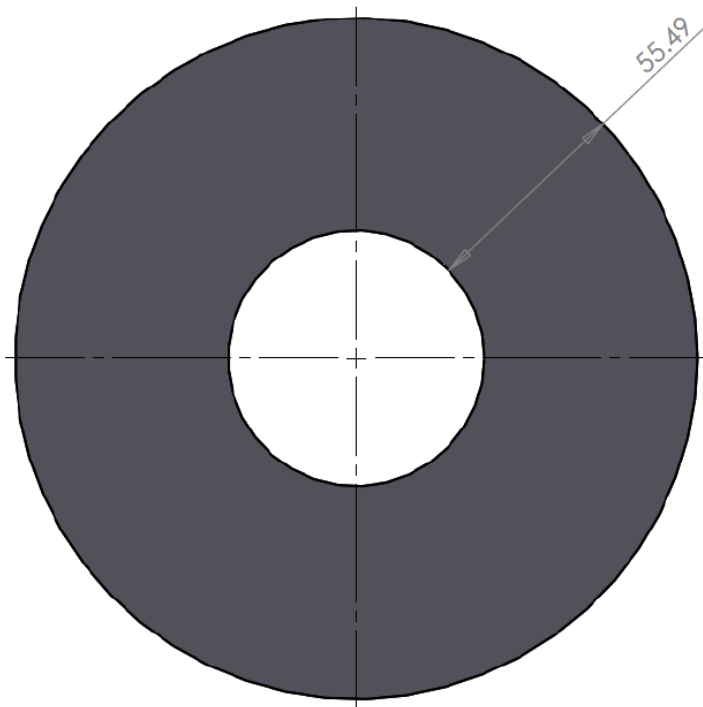


**Figure 7-5: Experimental test pump parameters; height from hub to tip of DE clearance for pump A.**

A list of the parameters used for this study are included in Table 7-1.

**Table 7-1: Experimental test pump parameters.**

Parameter Description [-]	Figure Reference [-]	Pump A [mm]	Pump B [mm]	Pump C [mm]
Dimension of peripheral cut of NDE axial clearance to reduce impeller width	Figure 7-1	N/A	0.0025	0.0075
Dimension of peripheral cut of DE axial clearance to reduce impeller width		N/A	0.0025	0.0075
Additional material added to impeller fluid bodies in radial direction to increase impeller diameter	Figure 7-2	0.0125	0.0125	0.0075
Radial clearance dimensions	Figure 7-3	0.265	0.250	0.255
NDE axial clearance dimensions		0.401	0.468	0.527
DE axial clearance dimensions		0.344	0.305	0.257
Radius of radial clearance ring	Figure 7-4	88.830	88.830	88.825
Width of radial clearance ring		32.500	32.523	32.524
Distance from hub to tip of DE axial clearance	Figure 7-5	55.490	55.490	55.485
Distance from hub to tip of NDE axial clearance		55.490	55.490	55.485

The inlet and outlet pipes were also modified to represent the experimental setup, see Figure 7-6. Extra monitoring points were created at several sections of the inlet/outlet pipes to assess the pressure pulsation trend at these locations.

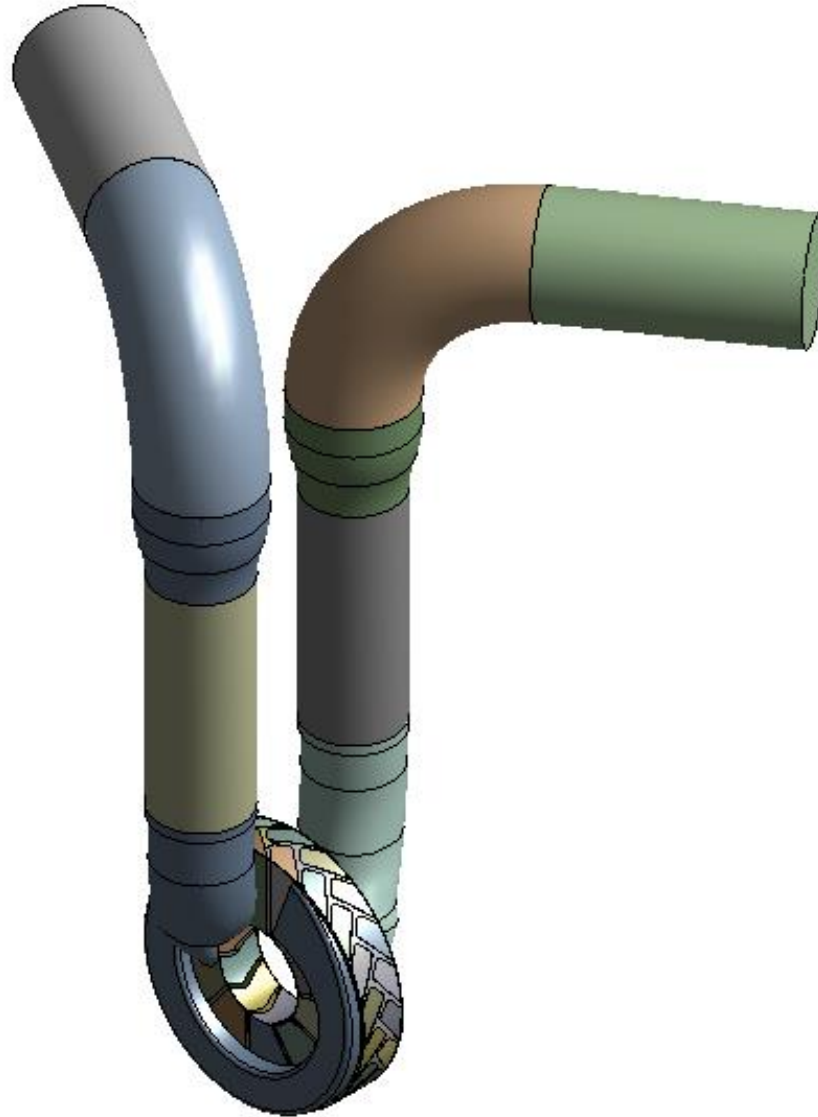


*Figure 7-6: Full computational representation of experimental pump.*

## 7.2 Performance Characteristics

Four operating points are analysed for each pump at three different speeds, corresponding to the experimental test data in *Chapter 6 Experimental Performance Testing*. A list of the operating points is included in Table 7-2, the points are denoted as a fractional quantity of the flow rate in relation to the best efficiency point (BEP). An extra two operating points at 2300 rpm were also included in the analysis.

**Table 7-2: Operating points used for the computational performance analysis.**

		Pump A	Pump B	Pump C
Speed [rpm]	Fraction of BEP [-]	Flow Rate [m <sup>3</sup> h <sup>-1</sup> ]		
2300	1.1 BEP	28.03	27.97	29.32
	BEP	25.33	24.95	26.40
	0.9 BEP	22.15	21.56	22.91
	0.7 BEP	18.32	17.90	19.23
	0.6 BEP	14.34	14.09	15.74
	0.4 BEP	10.34	10.03	12.30
1600	1.1 BEP	19.10	20.07	20.69
	BEP	17.00	17.93	18.75
	0.7 BEP	11.61	12.78	13.51
	0.4 BEP	5.52	6.51	7.18
1200	1.1 BEP	14.19	14.93	15.25
	BEP	12.68	13.37	13.55
	0.7 BEP	8.72	9.28	9.31
	0.3 BEP	3.90	4.43	4.64

In order to predict the computational performance of the test pumps, the transient average value resulting from the total timesteps of pressure pulsations over the second revolution is used (see Figure 7-7, Figure 7-8 and Figure 7-9) as validated in *4.4 Periodicity*. This value is then utilised to produce the performance curves shown in Figure 7-10, Figure 7-11 and Figure 7-12.

For each operational speed it can be observed that higher pressure differences between the outlet and the inlet result in higher amplitudes of the peaks in the pressure traces. This is

further enhanced by the operational speed, i.e. the amplitudes of the peaks are comparatively larger for higher speeds. The characteristic form of the pressure histories remains the same for each operational speed. There is little difference between intermediate and main peaks and troughs of the different pumps, however there is a shift along the y-axis. This corresponds to the total generated pressure of each pump, evaluated in terms of transient average value. At 2300 rpm the pressure pulsations of pump A and pump B more or less overlap while there is a significant negative shift for that of pump C. However, this shift decreases as the flow rate increases. Contrary, at 1600 and 1200 rpm, there is a visible shift in pressure pulsations between all the pumps, which again decreases with increasing flow rate.

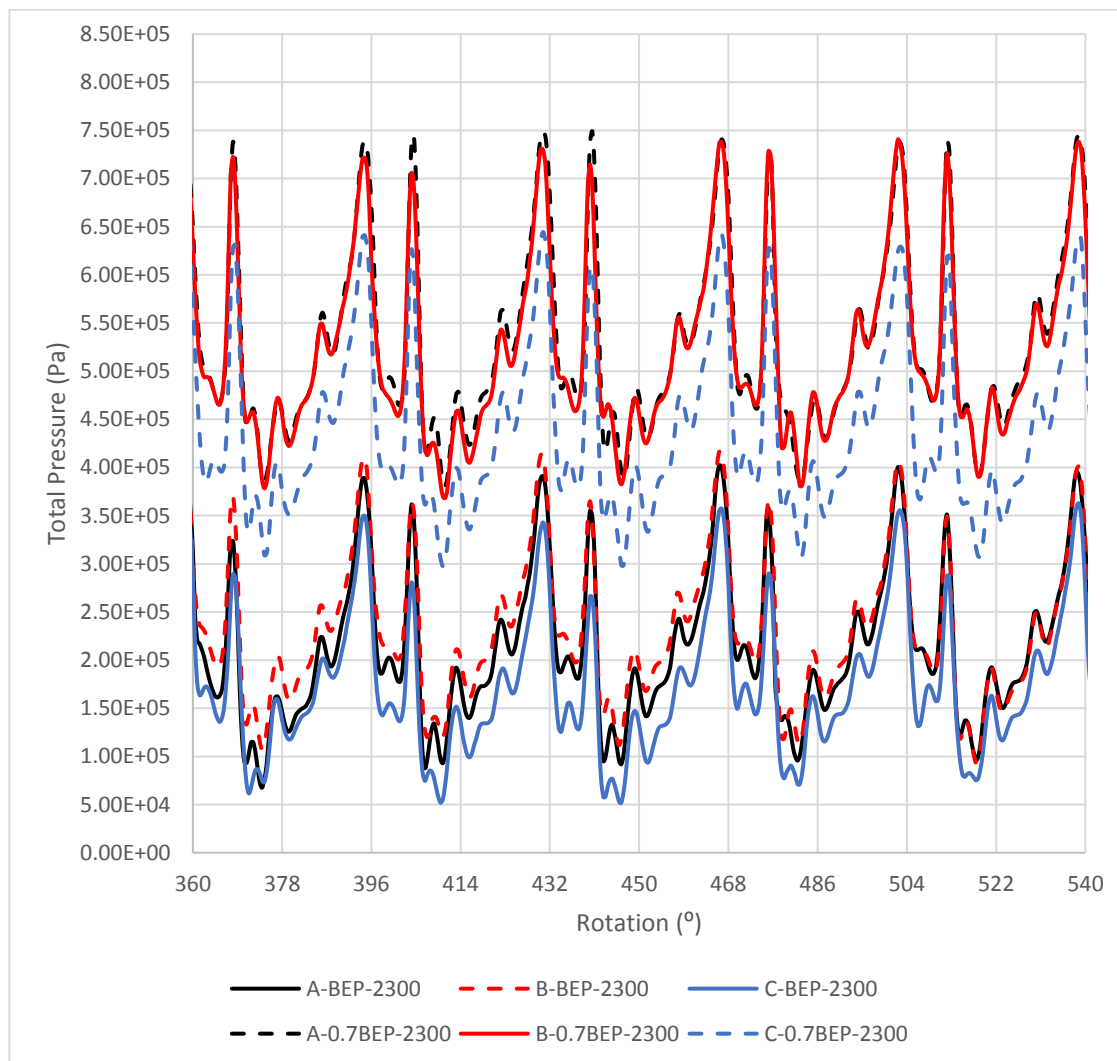


**Figure 7-7: Pressure pulsations for pump A, B and C at BEP and 0.7BEP at 2300 rpm.**

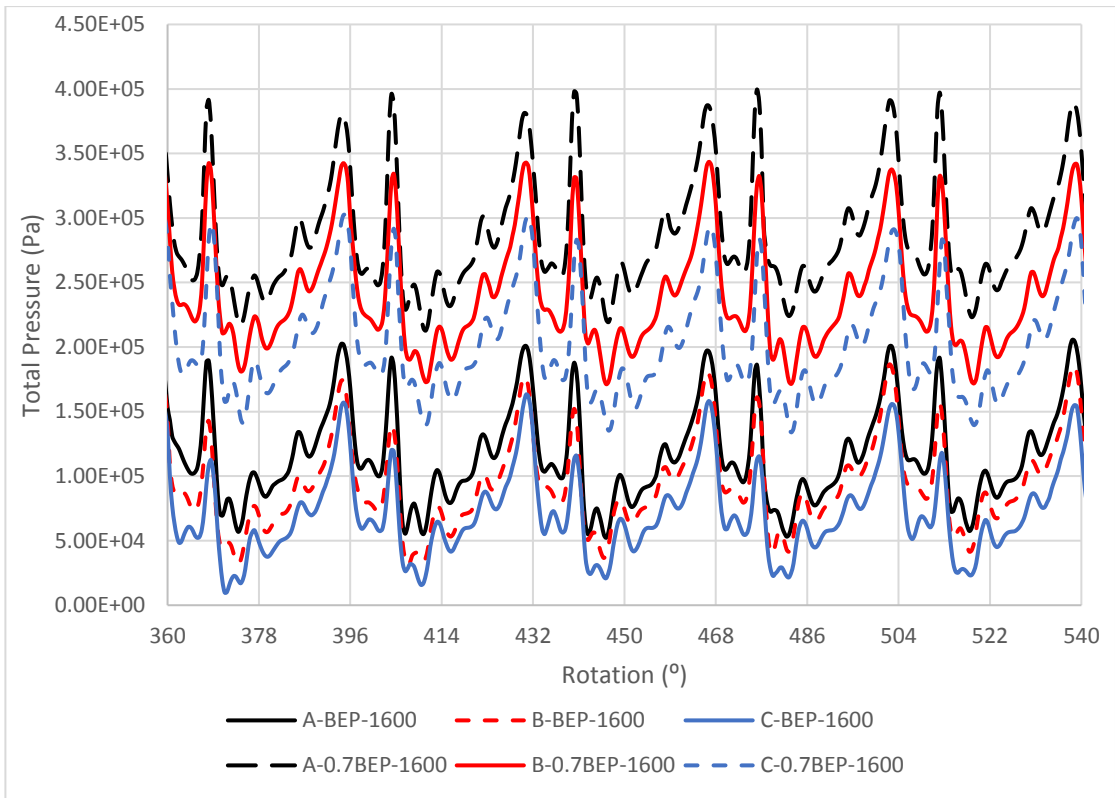


**Figure 7-8: Pressure pulsations for pump A, B and C at BEP and 0.7BEP at 1600 rpm.**

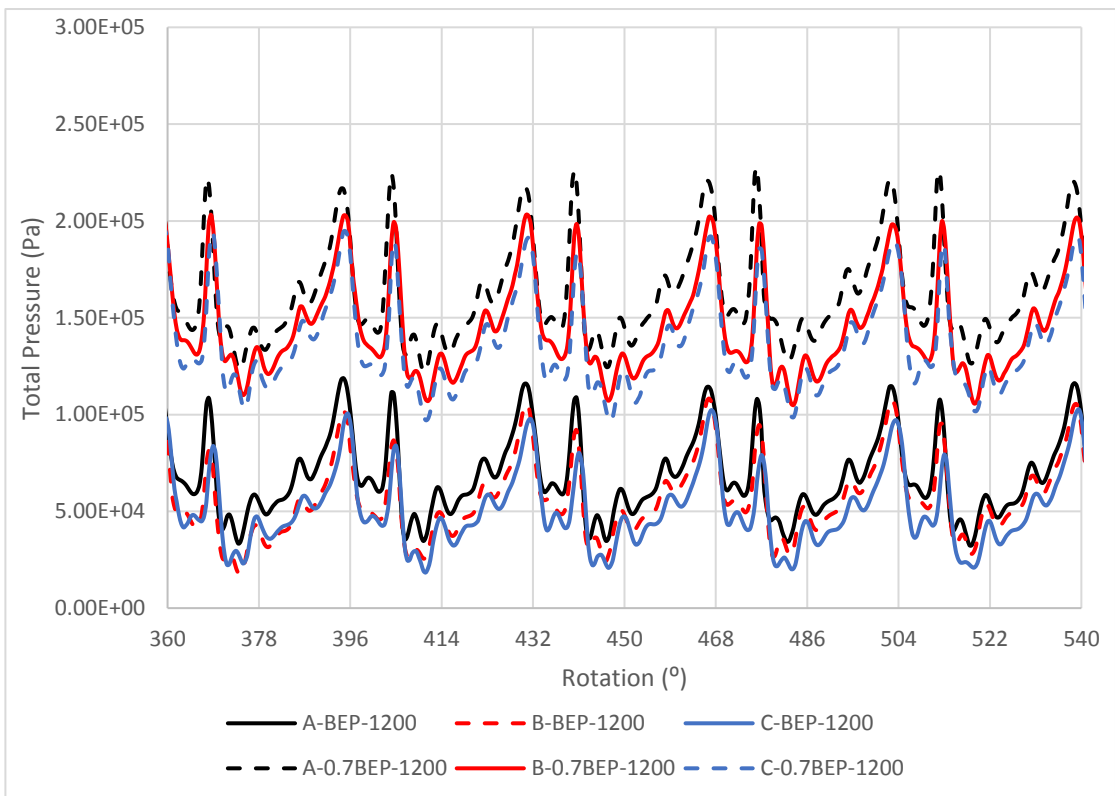


**Figure 7-9: Pressure pulsations for pump A, B and C at BEP and 0.7BEP at 1200 rpm.**

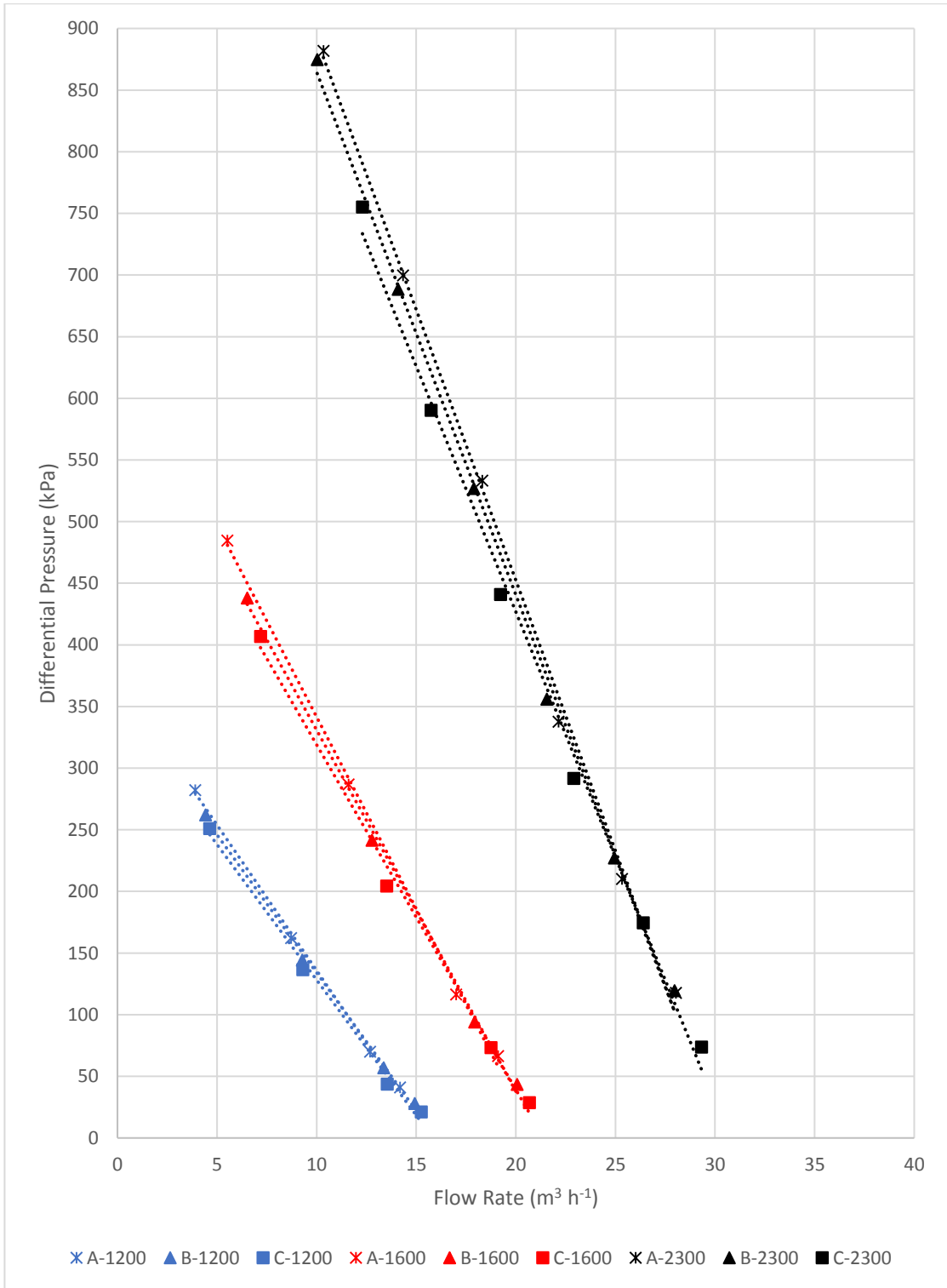


**Figure 7-10: Computational pressure head<sup>12</sup> curves for pump A, B and C at 1200, 1600 and 2300 rpm.**

<sup>12</sup> The total pressure corresponds to the pressure differential,  $\Delta p$ , given in equation (4-2).



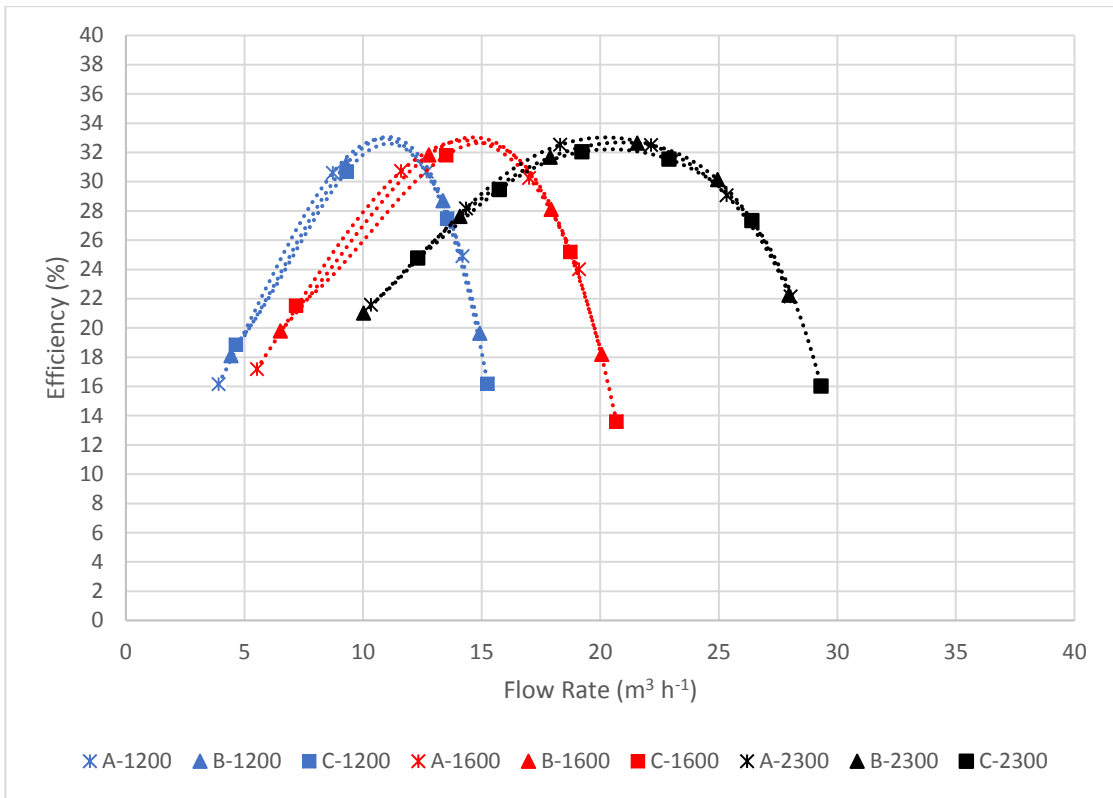


Figure 7-11: Computational efficiency curves for pump A, B and C at 1200, 1600 and 2300 rpm.

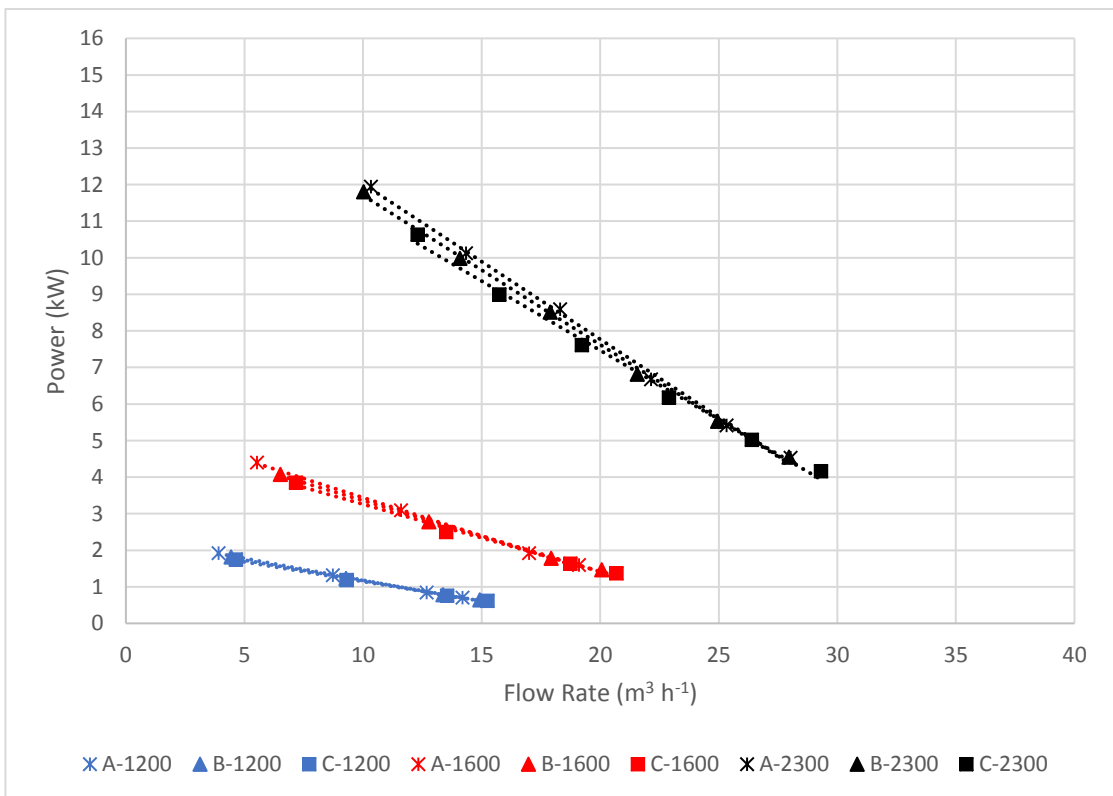


Figure 7-12: Computational power curves for pump A, B and C at 1200, 1600 and 2300 rpm.

The pressure pulsation characteristics and the performance curves indicate that pump A and B produce a notably higher pressure head when compared to pump C. At the higher flow rates at 2300 rpm, pump B has the best performance in terms of pressure and efficiency, however the highest efficiency at the lower flow rates is observed in pump A at 0.7 BEP and in pump C at 0.6 and 0.4 BEP. Pump A generates the highest pressure for the lowest flow rates. At the lower operational speeds of 1600 and 1200 rpm pump A generates the highest pressure head. However, pump B has the highest efficiency at 0.7 BEP while pump C has the highest efficiency at 0.4 BEP.

For all three pumps the computational BEP corresponds to 0.7 times the flow rate of the experimental BEP. The 0.7BEP values are included in Table 7-3.

**Table 7-3: Calculated values at 0.7BEP for pump A, B and C at 1200, 1600 and 2300 rpm.**

	1200 rpm			1600 rpm			2300 rpm		
	A	B	C	A	B	C	A	B	C
<b>Flow Rate (m<sup>3</sup> h<sup>-1</sup>)</b>	8.72	9.28	9.31	11.61	12.78	13.51	18.32	17.90	19.23
<b>Differential Pressure (kPa)</b>	162.03	144.16	136.47	286.86	241.41	204.21	533.17	526.74	440.76
<b>Shaft Power (kW)</b>	1.32	1.23	1.18	3.09	2.78	2.50	8.59	8.51	7.61
<b>Efficiency (%)</b>	30.60	31.16	30.70	30.72	31.83	31.81	32.52	31.67	32.05

The trends for the shaft power represented in Figure 7-12 are similar to the pressure head chart in Figure 7-10. It can be observed that the pump with the highest pressure generation also consumes the most power, which was also observed for the experimental test pumps. The input power is used for developing the increase in head as well as being consumed by the circulating flow through the impeller blades.

The pressure distribution in the impeller (viewed from the NDE) for pump A, B and C are compared in Figure 7-14 for the BEP and 0.7BEP at 2300 rpm; the arrow represents the direction of rotation. The distribution depicts a gradual increase in pressure from the inlet to the outlet. The areas of high pressure decrease both in appearance and value when comparing

pump A and B to pump C, corresponding to the trend observed for the generated pressure head at the BEP. At 0.7 BEP the pressure distribution for pump B has a larger appearance of high pressure regions compared to pump A although pump A has a slightly larger total generated pressure head (approximately 1.2%). This difference is most likely due to a higher pressure for pump B at this particular maximum pressure point.

In Figure 7-15 and Figure 7-16 the circulation flow between the impeller and the deepest section of the side channels (casing cross-sectional view; DE on the left and NDE on the right) are compared for pump A, B and C at 2300 rpm for the BEP and 0.7BEP, and for 0.6BEP and 0.4BEP, respectively. The exact location of the cross-sectional plane is shown in Figure 7-13.

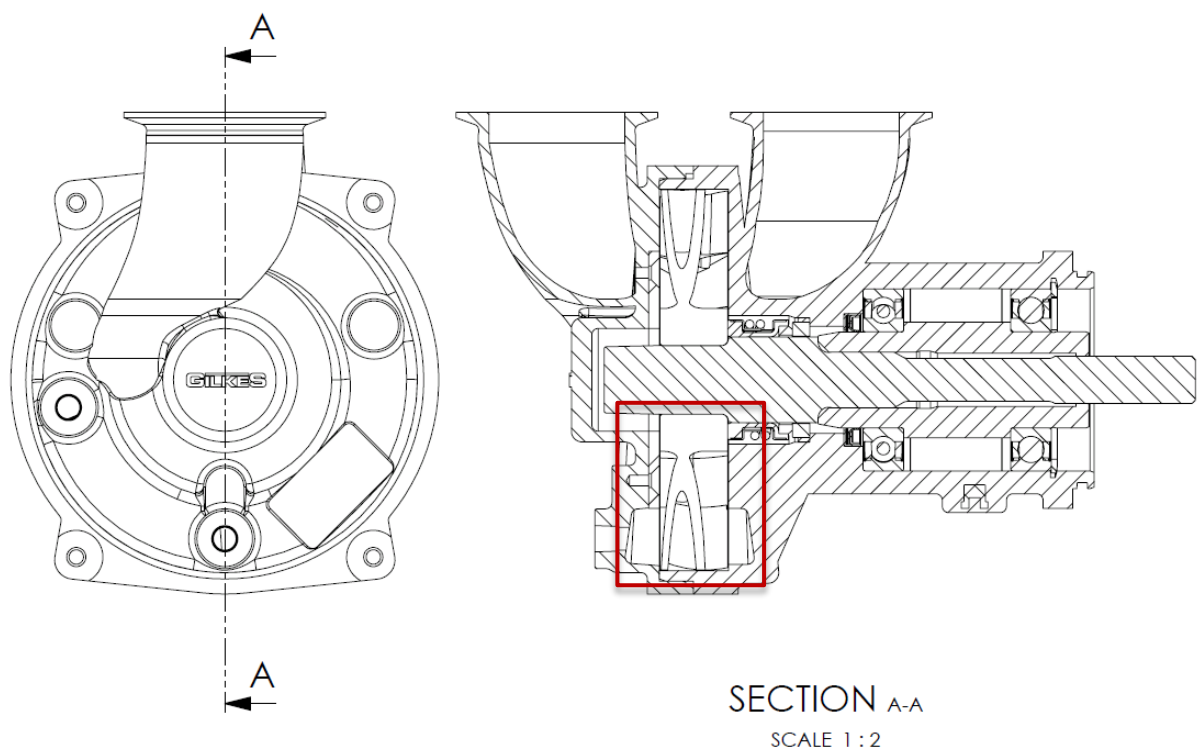


**Figure 7-13: 2.5" SX pump casing cross-sectional view showing location for analysing the circulation flow between the impeller and the deepest section of the side channel.**

The centre of the circulation flow can generally be located at the same position of the blade height regardless of the pump geometry, however it varies for each operating point. At the BEP, the centre is approximately at 2/3 of the blade height on the suction side (DE), while at the other points a vortex can be observed on both sides. The position of the vortex on the pressure side (NDE) is shifted along the blade length towards the tip as the flow rate decreases, whereas it is generally shifted closer to the blade root on the suction side. Furthermore, the

vortex on the pressure side is more pronounced than the one on the suction side for pump B and C, however the opposite is true for pump A.

The velocity in the side channel on both the suction and pressure sides is higher than the velocity in the impeller. This is because the fluid moves at its fastest when it is ejected at the impeller tip and enters the side channels. The velocity is close to zero near to the vortices in the impeller, which correlates to the fluid exiting the impeller.

The velocity contours in the middle of the NDE and DE clearances are shown in Figure 7-17 for the BEP at 2300 rpm, in addition to the streamlines of the flow. High velocity regions can be observed where the blade edges on the NDE and DE meet the port plate. When the fluid encounters a constriction, the velocity must increase due to mass conservation and subsequently the pressure drops as shown in Figure 7-14. This is also the reason why the velocity is higher along the lower half of the full blade edges which are passing the restricted space between the impeller hub and the casing walls. The streamlines show that there is more flow recirculation where the side channels meet the impeller.

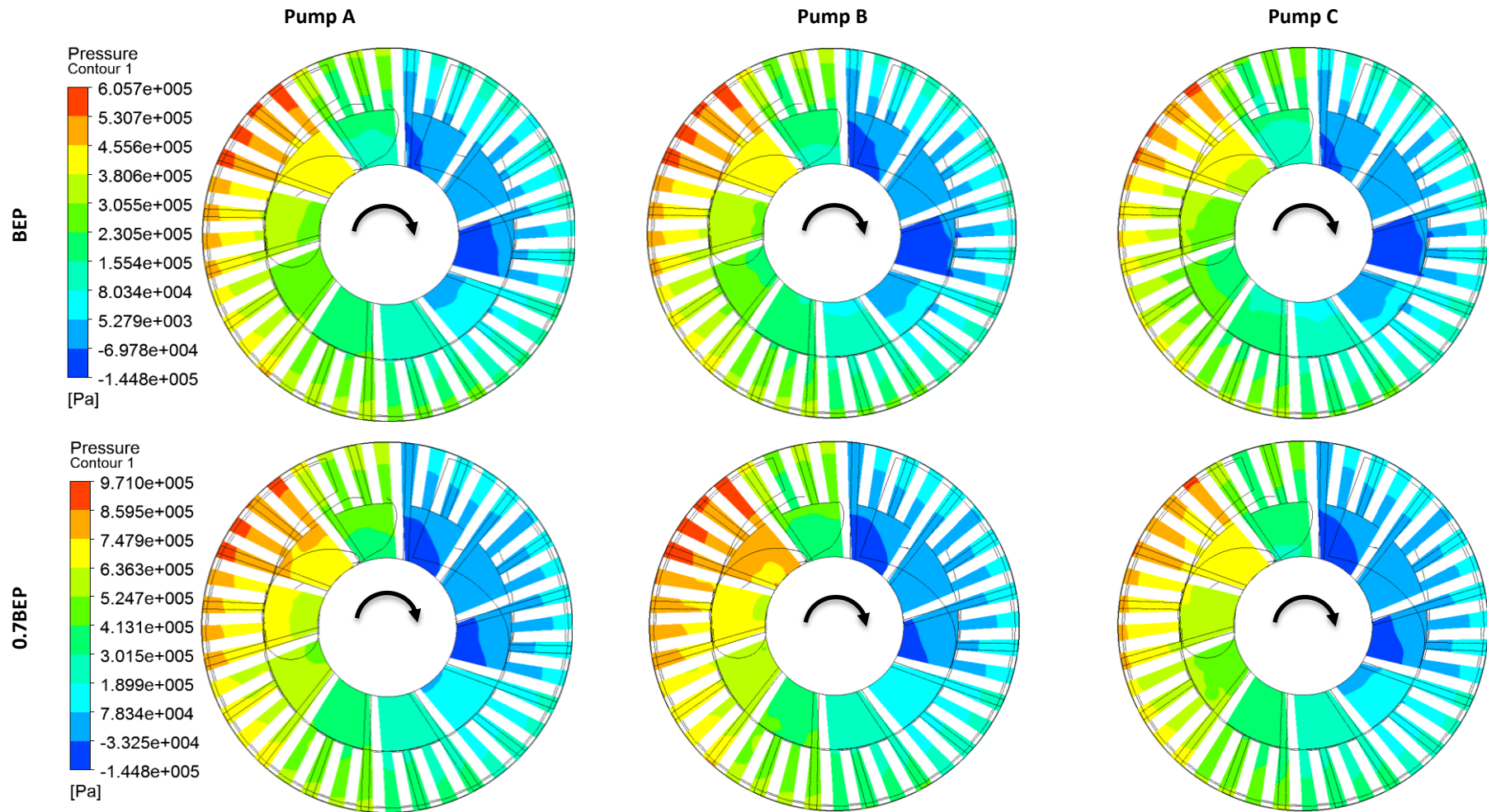


Figure 7-14: Pressure distribution in the impeller for pump A, B and C at maximum pressure point of pulsation at 2300 rpm for BEP (top) and 0.7BEP (bottom).

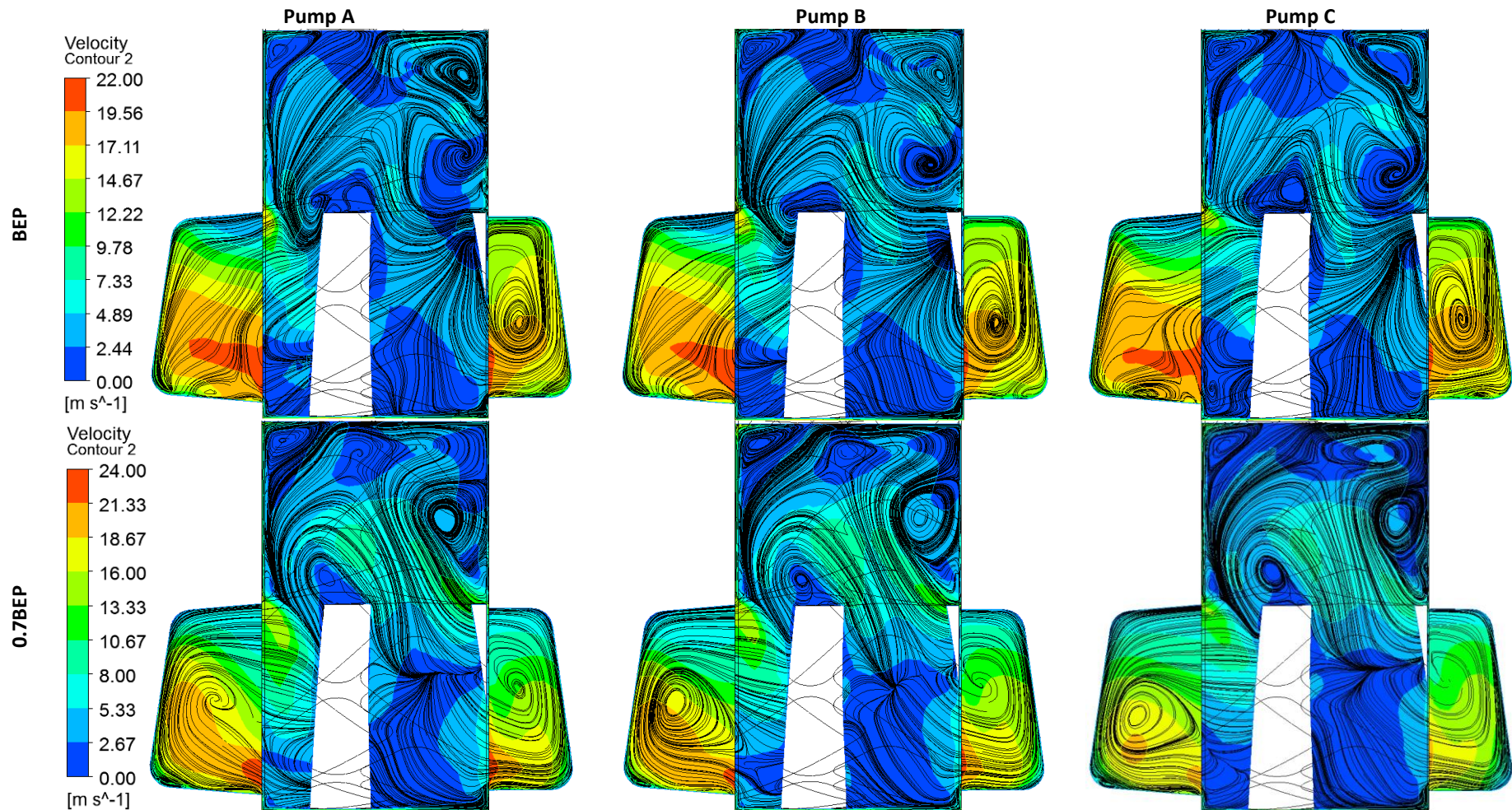


Figure 7-15: Circulation flow between impeller and side channel for pump A, B and C at maximum pressure point of pulsation at 2300 rpm for BEP (top) and 0.7BEP (bottom).



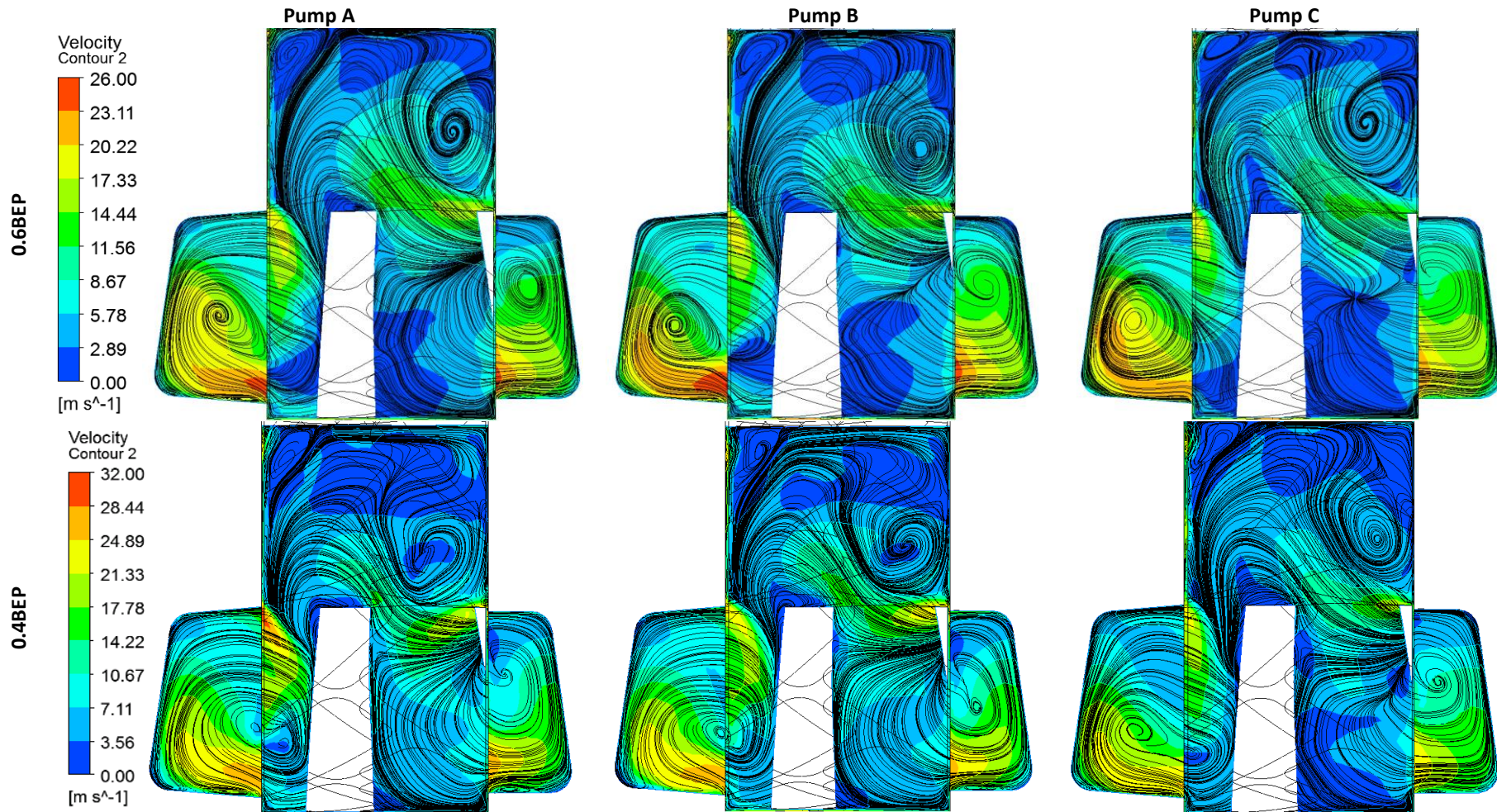
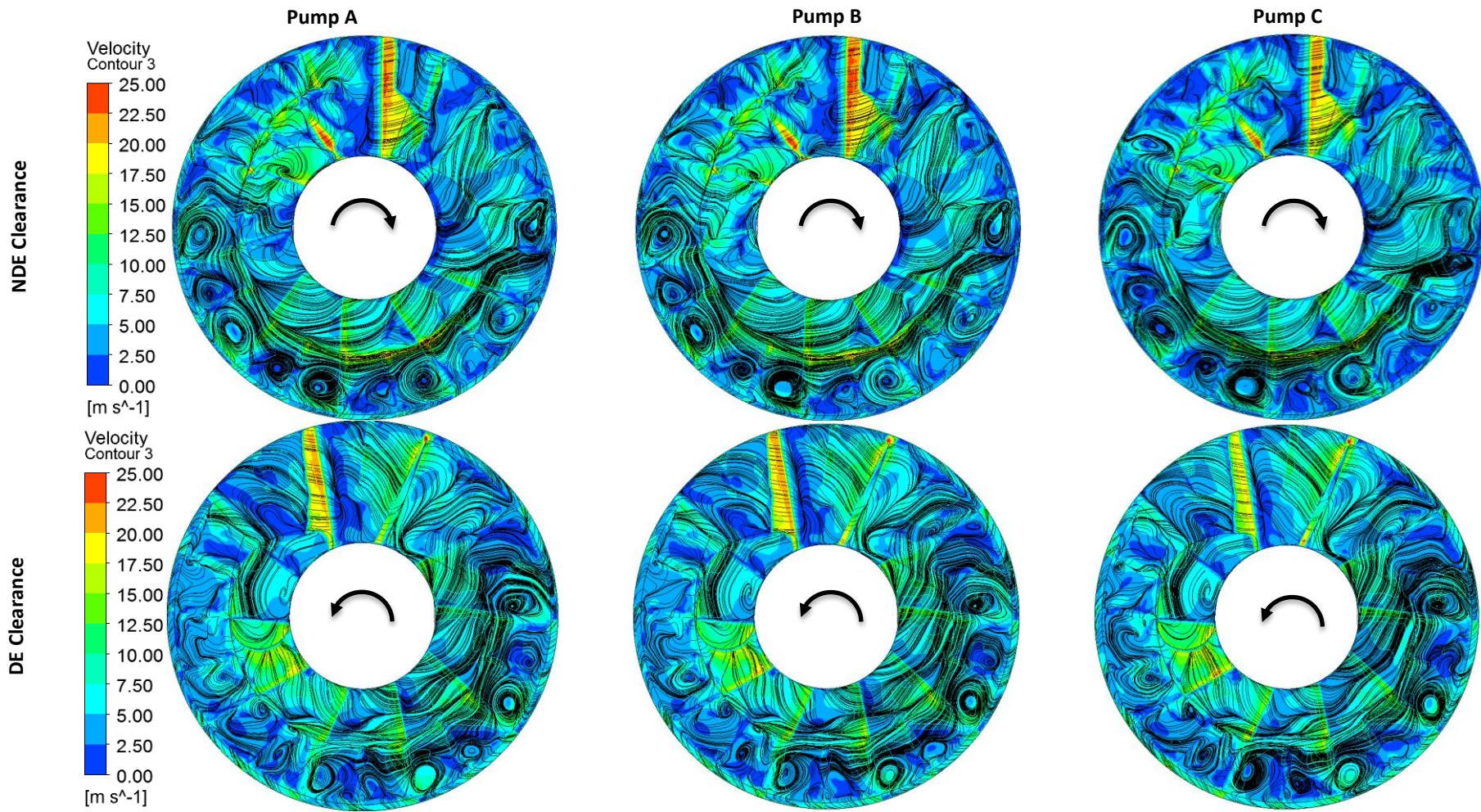


Figure 7-16: Circulation flow between impeller and side channel for pump A, B and C at maximum pressure point of pulsation at 2300 rpm for 0.6BEP (top) and 0.4BEP (bottom).





*Figure 7-17: Flow in the NDE (top) and DE (bottom) clearances for pump A, B and C at maximum pressure point of pulsation at 2300 rpm for BEP.*



Due to the characteristics of the test pumps, the operating inputs, such as mass flow rate and inlet pressure, are not identical. In order to make a direct performance comparison between the pumps it was decided to analyse pump B and C using the input data corresponding to 0.7 BEP for pump A at 2300 rpm.

The results are presented in Figure 7-18 and Figure 7-19 in terms of pressure pulsations and then the transient average of the generated pressure head, shaft power and efficiency, respectively.

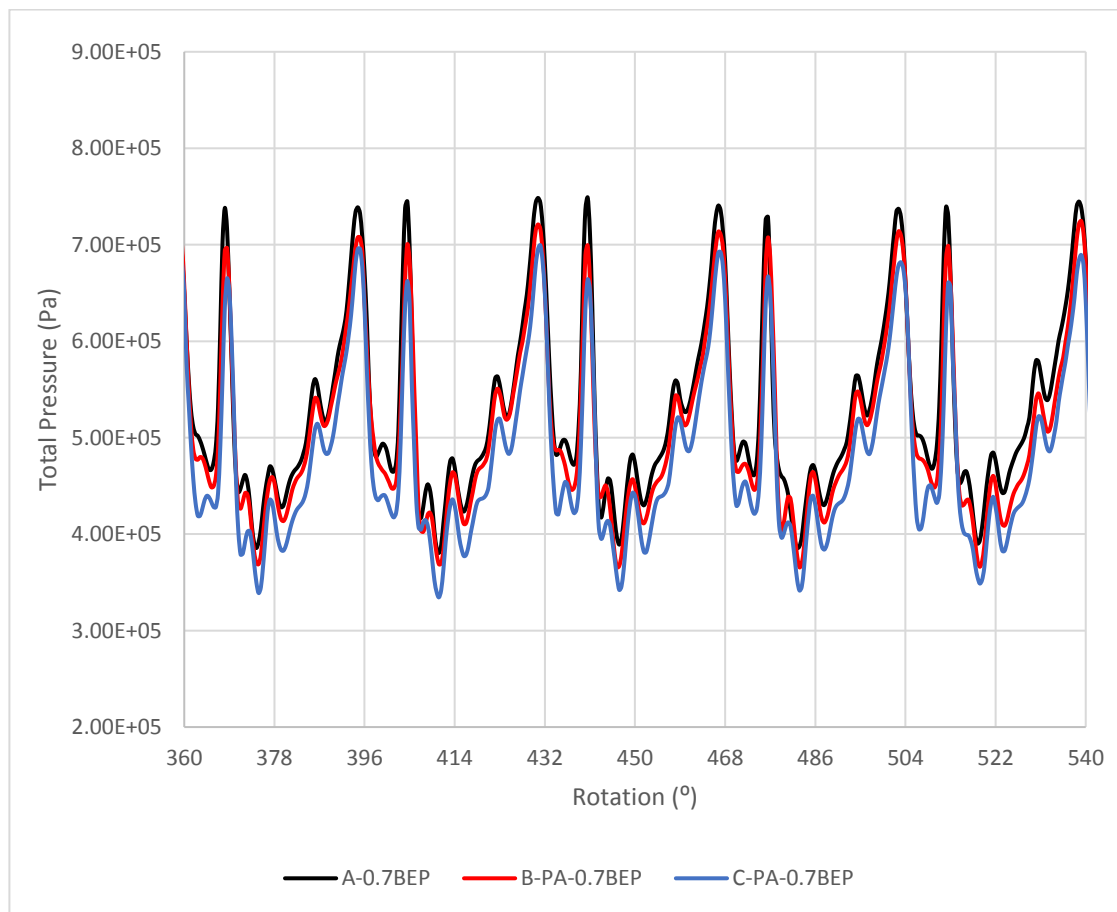


**Figure 7-18: Comparison of pressure pulsation trends for pump A, B and C using the input data corresponding to 0.7BEP for pump A at 2300 rpm.**

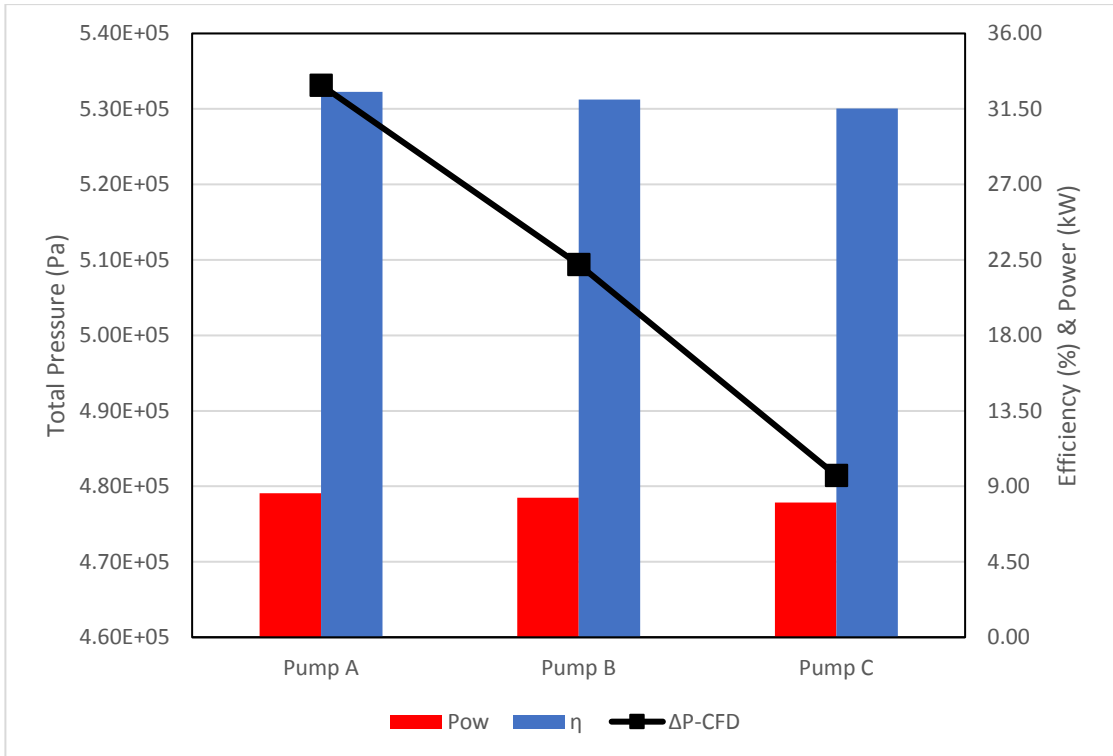


**Figure 7-19: Comparison of the transient average of the generated pressure head, power and efficiency for impeller A, B and C using the input data corresponding to 0.7BEP for pump A at 2300 rpm.**

It is clear that pump A has the best performance in terms of generated pressure head and efficiency, albeit only by a small percentage (see Table 7-4), but it requires a higher input power to sustain the pressure head. As with most of the results at the other operating points pump C has a notably worse performance in terms of pressure.

**Table 7-4: Performance values for the three design combinations, normalised to pump A performance.**

	Unit	Pump A	Pump B	Pump C
Normalised Pressure		100.00	95.54	90.30
Normalised Power	[%]	100.00	96.97	93.43
Normalised Efficiency		100.00	98.62	96.92

### 7.3 Performance Effects due to Axial and Radial Clearance Pressure

In order to assess which clearance primarily drives the pressure rise across the pump, the pressure was monitored at either side of the clearances:

1. For the radial clearance; casing side of clearance ring and impeller side.
2. For the NDE clearance; discharge side of clearance disk and impeller side.
3. For the DE clearance; suction side of the clearance disk and impeller side.

The difference in the transient average pressure between the two sides was then calculated and compared against the total pressure across the pump, the results are shown in Figure 7-20, Figure 7-21 and Figure 7-22.

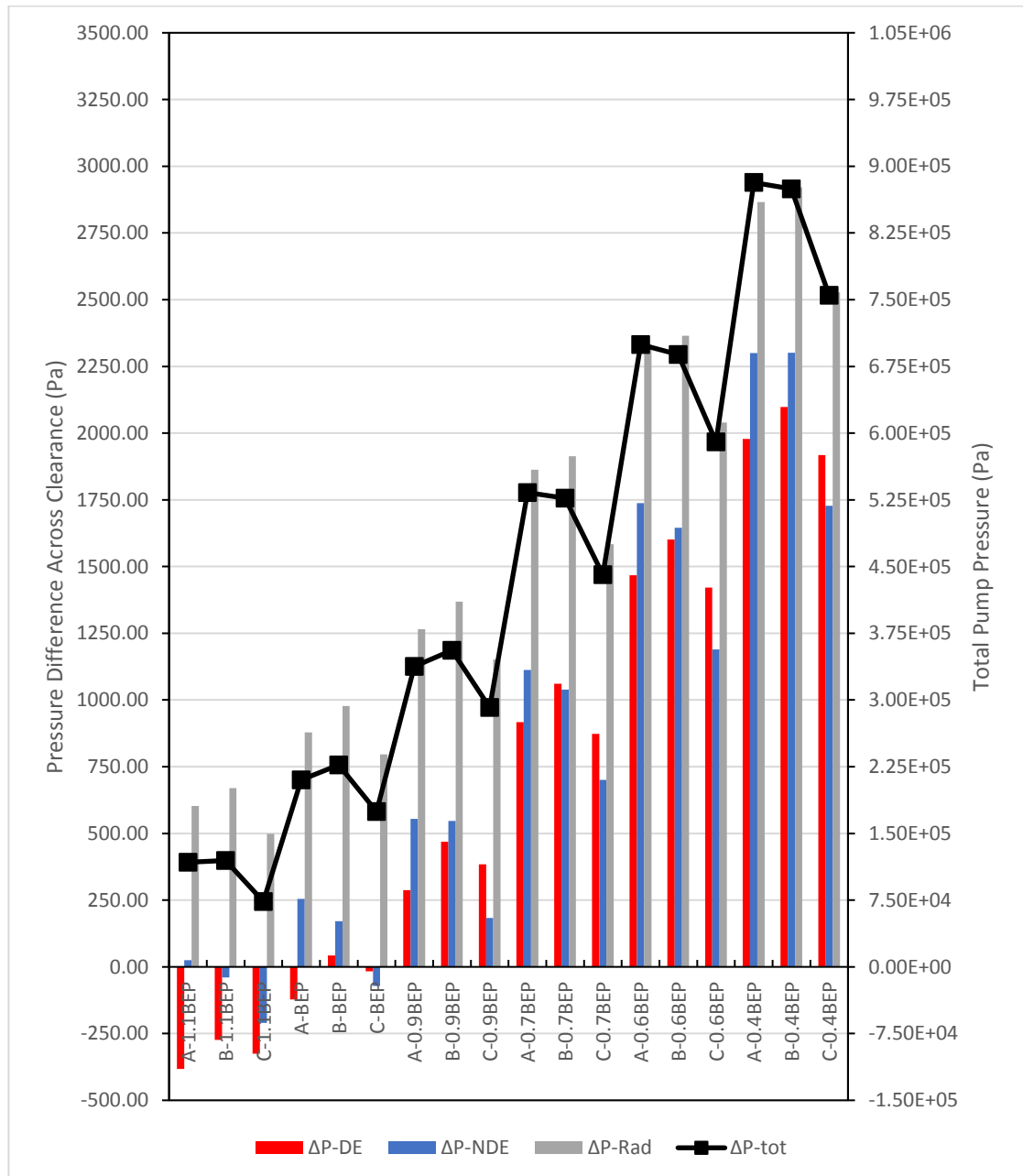
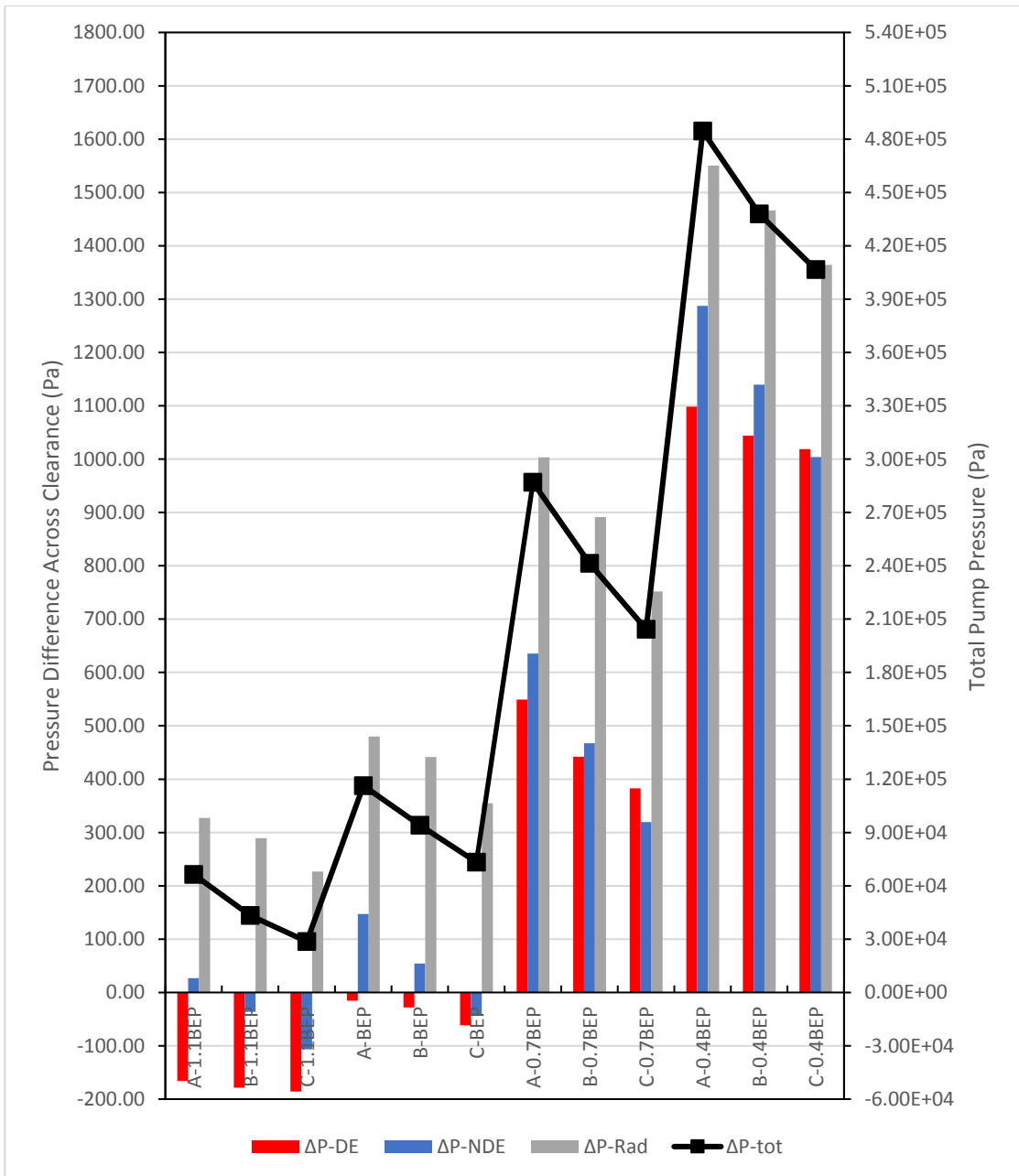
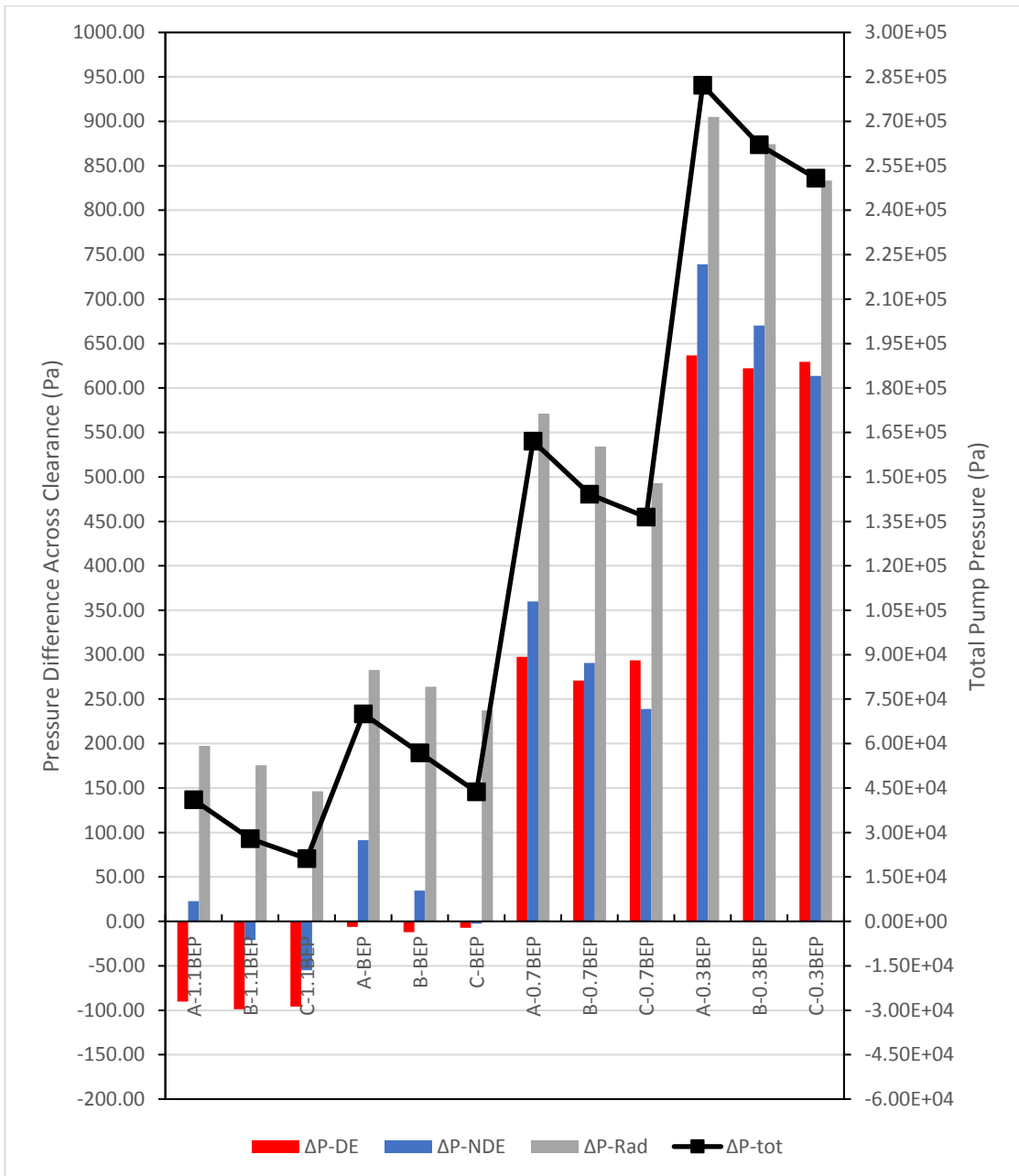


Figure 7-20: Comparison of transient average pressure difference across clearances and total pump pressure at 2300 rpm.



**Figure 7-21: Comparison of transient average pressure difference across clearances and total pump pressure at 1600 rpm.**

The results confirm that the radial clearance has the greatest influence on the total generated pressure of the pump. The pressure across the radial clearance and the total pressure clearly follow the same trend for all points analysed; whichever pump has the largest radial pressure difference also generates the largest pressure head. At 1200 and 1600 rpm, pump A produces the highest pressure while pump C produces the lowest pressure at every mass flow rate measured. However, at 2300 rpm pump B has the best pressure head performance.



**Figure 7-22: Comparison of transient average pressure difference across clearances and total pump pressure at 1200 rpm.**

It is less straightforward to find a clear trend for the pressure across the DE and NDE clearances. For most of the cases, it appears that the increase in pressure is more significant across the NDE clearance when compared to the DE clearance which correlates with the findings in the parametric clearance study in *Chapter 5*. However, the trend is reversed for pump C.

## 7.4 Effects of Impeller Width and Diameter on Performance

The previous analyses have focused on assessing the effects of the axial and radial clearances on the pump performance. Both the experimental and computational results show that there are noticeable differences. However, the test pumps feature different impeller tolerances as well as clearance sizes. Although the variations in impeller width and diameter are small, it is interesting to investigate the effects these might have on the pump performance. It was decided to keep the clearances constant using the measurements for pump A in combination with the measured tolerances for impeller B and impeller C, resulting in two new geometries (see Table 6-1 for the manufacturing tolerances used). The performance of the new combinations are analysed at 0.7BEP for pump A at 2300 rpm and compared against the performance of pump A at the same point.

The results are presented in Figure 7-23 and Figure 7-24 in terms of pressure pulsations and then the transient average of the generated pressure head, shaft power and efficiency, respectively.

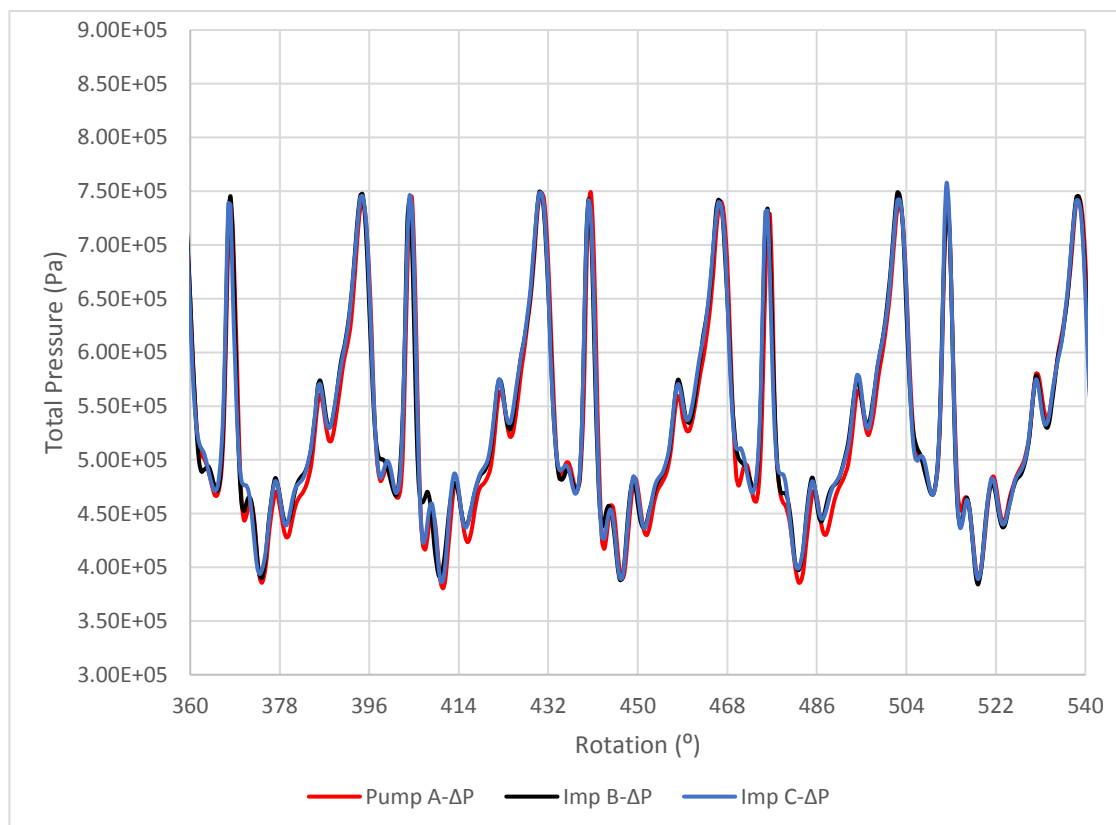


**Figure 7-23: Comparison of pressure pulsation trends for impeller A, B and C with pump A clearances at 0.7BEP at 2300 rpm.**

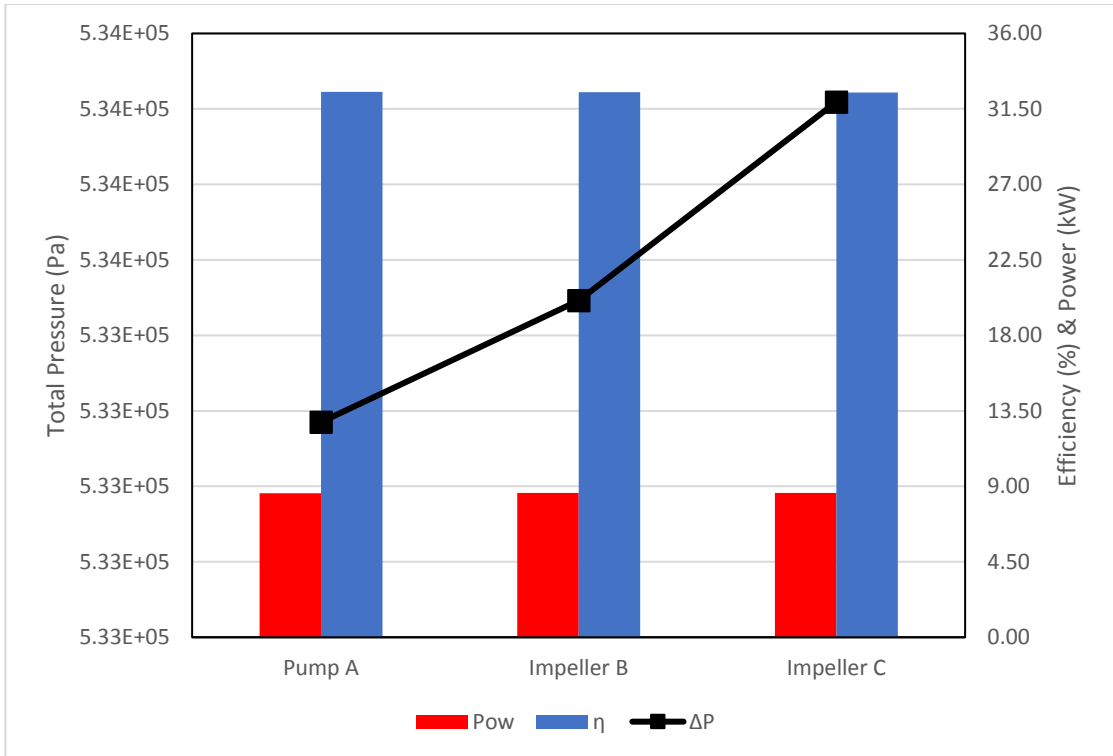


**Figure 7-24: Comparison of the transient average of the generated pressure head, power and efficiency for impeller A, B and C with pump A clearances at 0.7BEP at 2300 rpm.**

As would be expected, due to the small variations in impeller tolerances, the results show that there are only small differences in the performance between the three design combinations. The normalised performance values using pump A as the baseline are included in Table 7-5.

**Table 7-5: Performance values for the three impeller sizes, normalised to pump A performance.**

	Unit	Pump A	Impeller B	Impeller C
<b>Normalised Pressure</b>		100.00	100.06	100.16
<b>Normalised Power</b>	[%]	100.00	100.12	100.25
<b>Normalised Efficiency</b>		100.00	99.93	99.87

The impeller C design has the smallest width and diameter and generates a slightly higher pressure at the cost of a higher power consumption and lower efficiency which correlates with the circulating flow theory. The only difference between the impeller A and B designs is the width. As before the smaller design, i.e. impeller B, produces a higher pressure, consumes more power and has a lower efficiency. However, the efficiency performance is still slightly better than that of the impeller C design.

Based on these results one can conclude that the main driver for the performance deviation between the test pumps are due to the clearance combinations and not the impeller tolerances.

## **7.5 Summary of Computational Performance Modelling**

In this chapter the performance of the experimental pumps was investigated computationally by replicating the geometrical properties and operating conditions of the test pumps. The characteristic pressure pulsations and performance curves have been plotted showing that there is a relatively small difference between pump A and B. Pump C on the other hand performs relatively poorly in comparison apart from at the lowest tested flow rate of 0.4BEP. There is a clear link between the pressure across the radial clearance and the total generated pressure head. An impeller width and diameter sensitivity study showed that a smaller impeller provides a better pressure head performance, however compared to the effects of the size of the clearances the improvement is minimal. The results in this chapter will be compared against the experimental test data in Chapter 8 *Comparison of Computational and Experimental Results*.



## 8 Comparison of Computational and Experimental Results

This chapter provides a detailed discussion of the achieved results and includes comparisons of the computational predictions and the experimental measurements in order to determine the performance of a regenerative pump in relation to manufacturing tolerances and to identify the limitations of this research. The computational and experimental performance curves are presented. Following this, the various factors leading to discrepancies between the results are presented and discussed. This includes mechanical losses, inconsistencies in experimental testing, uncertainties due to manufacturing and limitations of the computational models and techniques developed during this research.

### 8.1 Performance Curves

The computational simulations of the experimental test pumps were carried out at the 1.1BEP, BEP, 0.7BEP and 0.4 BEP for 2300, 1600 and 1200 rpm. An additional two points at 0.9BEP and 0.6BEP were also analysed at 2300 rpm. The experimental pump geometries, setup and operating conditions were replicated in the computational modelling with the aim of making a direct comparison against the experimental test data. The computational and experimental performance curves showing pressured head, efficiency and power consumption are plotted in Figure 8-1 - Figure 8-9.

For all three operational speeds the difference between the computed and measured pressure head decreases with the flow rate until the computed curves cross the measured curves and the computational model over-predicts. The crossover point is different for each test pump but remains the same across the three operational speeds. For pump A the best correlation can be observed at 0.7BEP, for pump B at 0.6BEP and for pump C at 0.4BEP. Computationally, pump A also appears to have the best fit at higher flow rates while pump C is at lower flow rates. This is most likely due to the size of the drive end (DE) clearance. Pump A has the largest DE clearance whereas pump C has the smallest by approximately 25%. The computational model struggles to predict the pump performance at higher flow rates and this is particularly evident for pump C which is much more sensitive to volumes of water with regards to the DE clearance. As the DE clearance increases the sensitivity of the model decreases. The correlation between the computational and experimental value at the crossover points is best

for the highest speed of 2300 rpm; 1.65% for pump A, 1.94% for pump B and 1.19% for pump C.

The experimental efficiency curves are flatter than the computational ones, this is observed for all the operational speeds, however this is not unusual. At 2300 rpm the computational model over-predicts the efficiency at lower flow rates, correlates relatively well at both the BEP and 0.9BEP, and then under-predicts at higher flow rates. However, the efficiency is only a fraction of the hydraulic power and the shaft power which relies on the computed pressure head and torque which differ from the measured values and therefore cannot be directly compared against the experimental efficiencies.

The computationally predicted torque on the shaft is consistently smaller than the measured value for all operating points and speeds. The computational model captures the basic trend, although the discrepancy reduces with decreasing flow rates which manifests itself in the power curves.

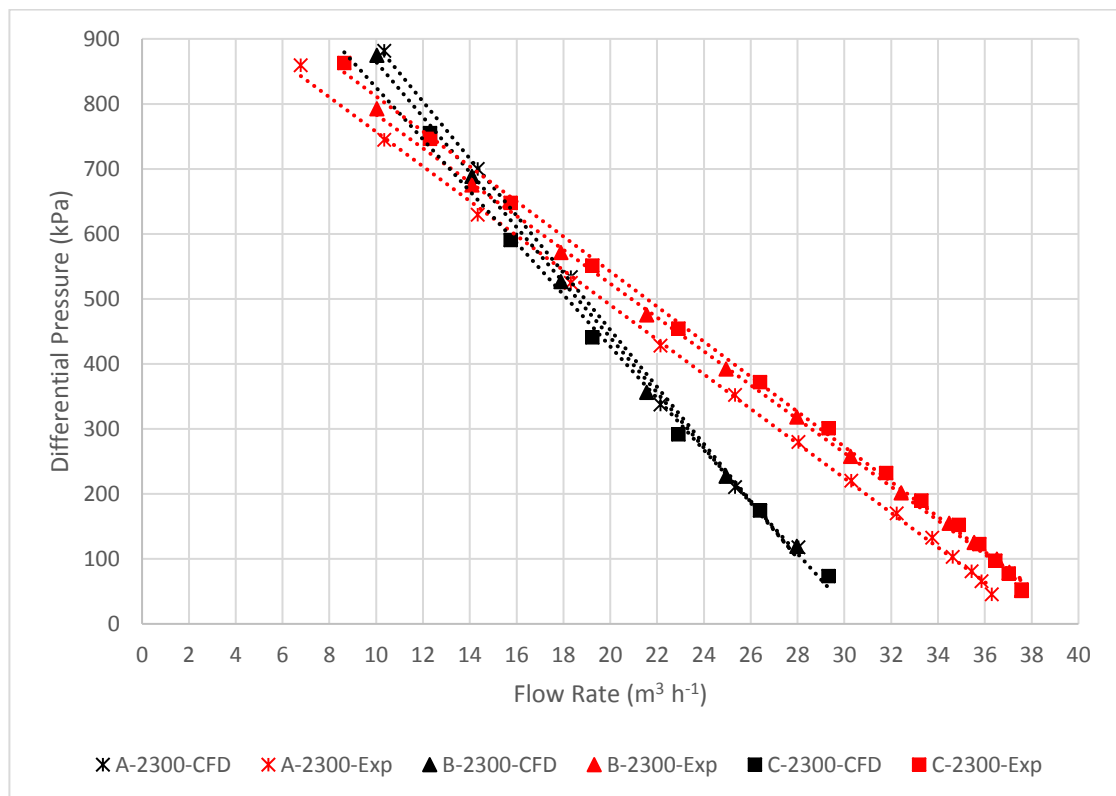


**Figure 8-1: Comparison of experimental and computational pressure head curves for pump A, B and C at 2300 rpm.**

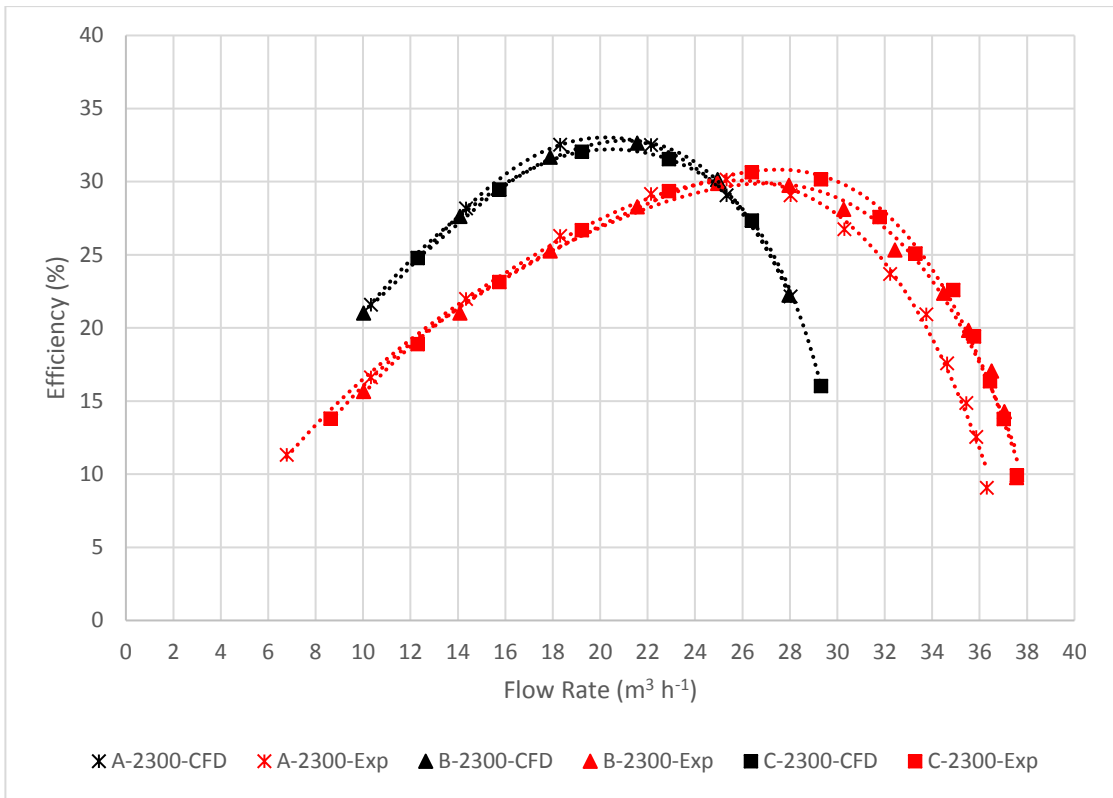


**Figure 8-2: Comparison of experimental and computational efficiency curves for pump A, B and C at 2300 rpm.**

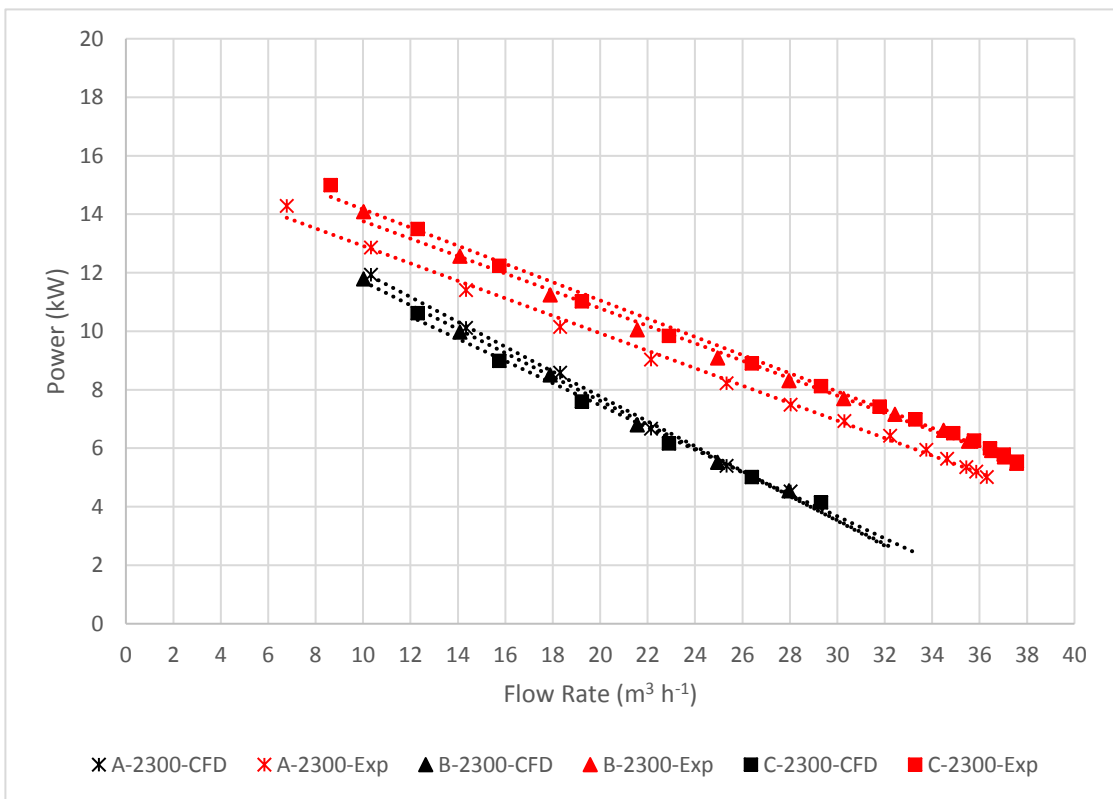


**Figure 8-3: Comparison of experimental and computational power curves for pump A, B and C at 2300 rpm.**

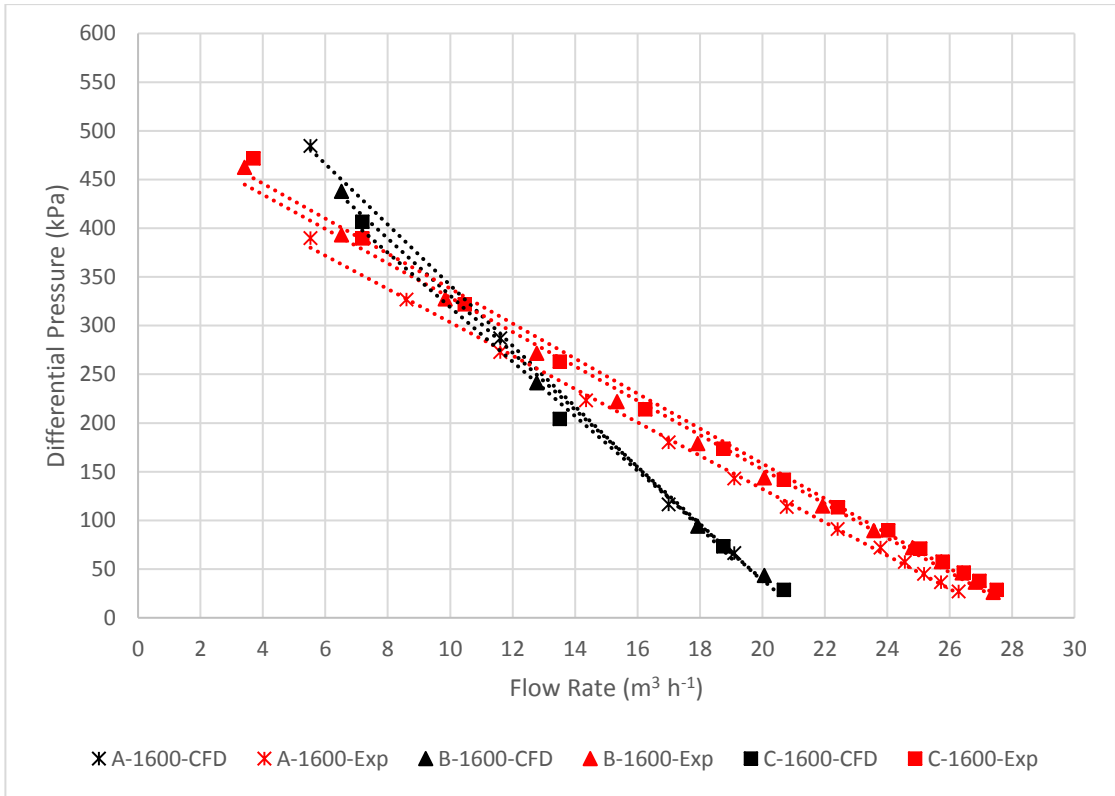


**Figure 8-4: Comparison of experimental and computational pressure head curves for pump A, B and C at 1600 rpm.**

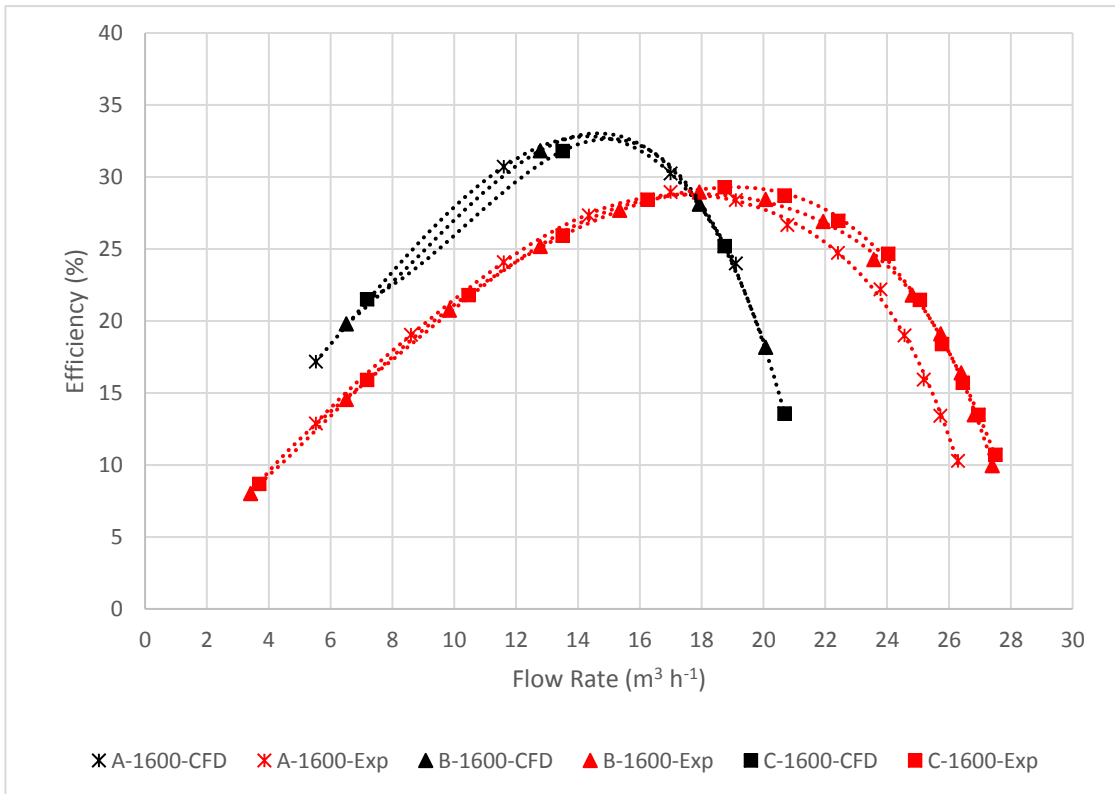


**Figure 8-5: Comparison of experimental and computational efficiency curves for pump A, B and C at 1600 rpm.**

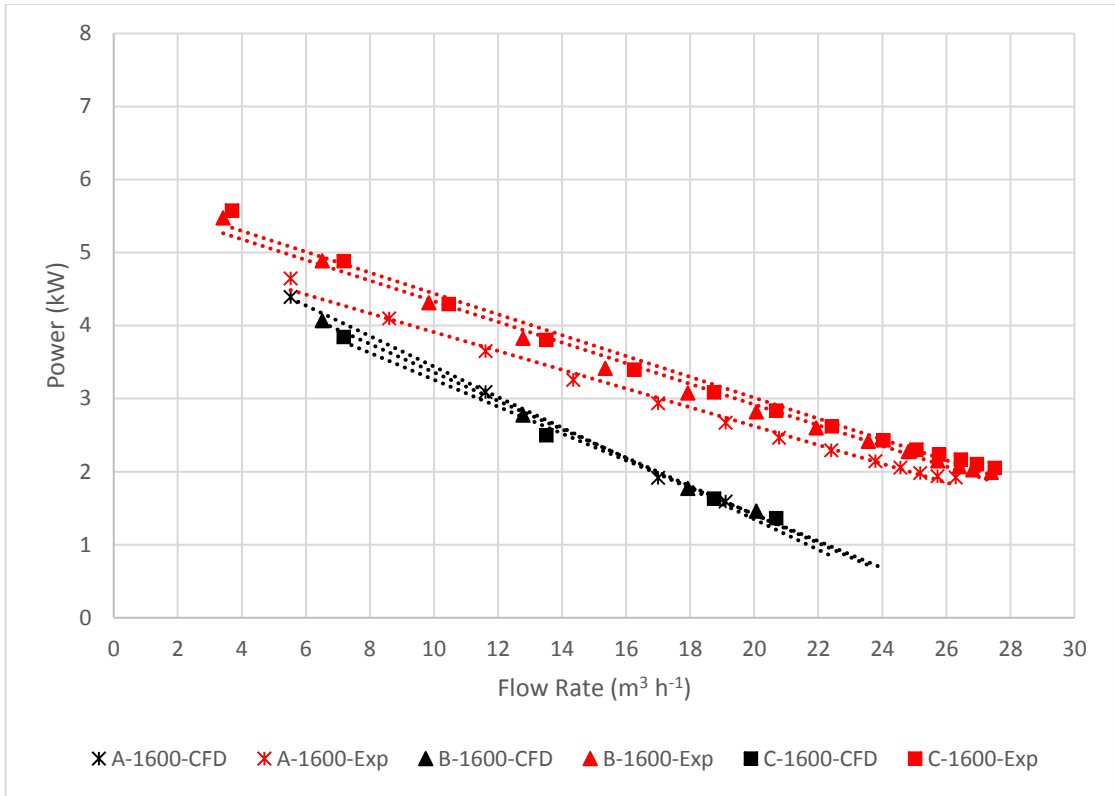


Figure 8-6: Comparison of experimental and computational power curves for pump A, B and C at 1600 rpm.

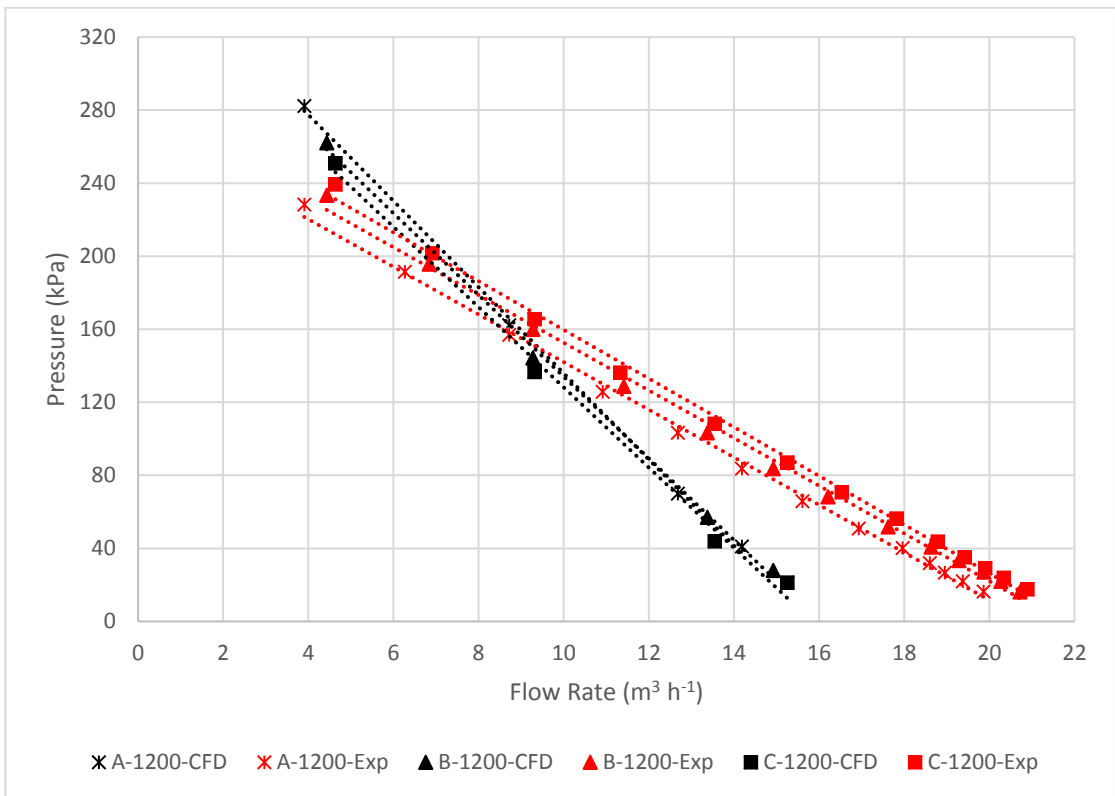


Figure 8-7: Comparison of experimental and computational pressure head curves for pump A, B and C at 1200 rpm.

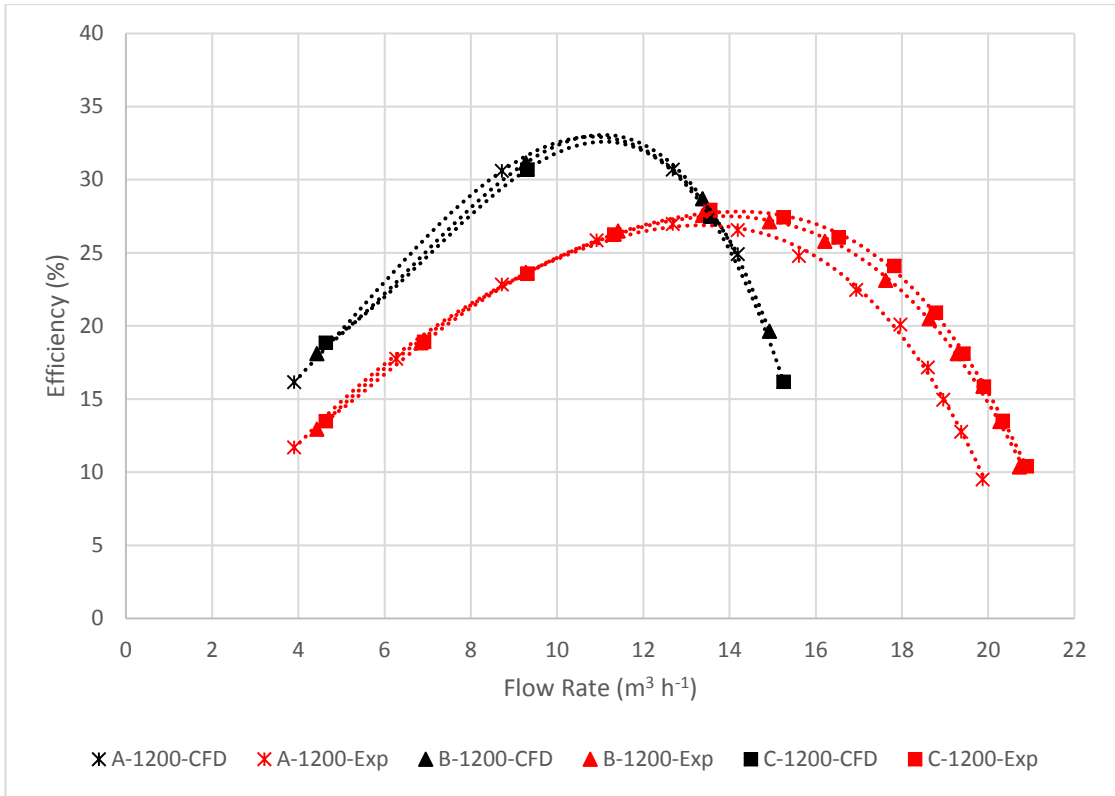


Figure 8-8: Comparison of experimental and computational efficiency curves for pump A, B and C at 1200 rpm.

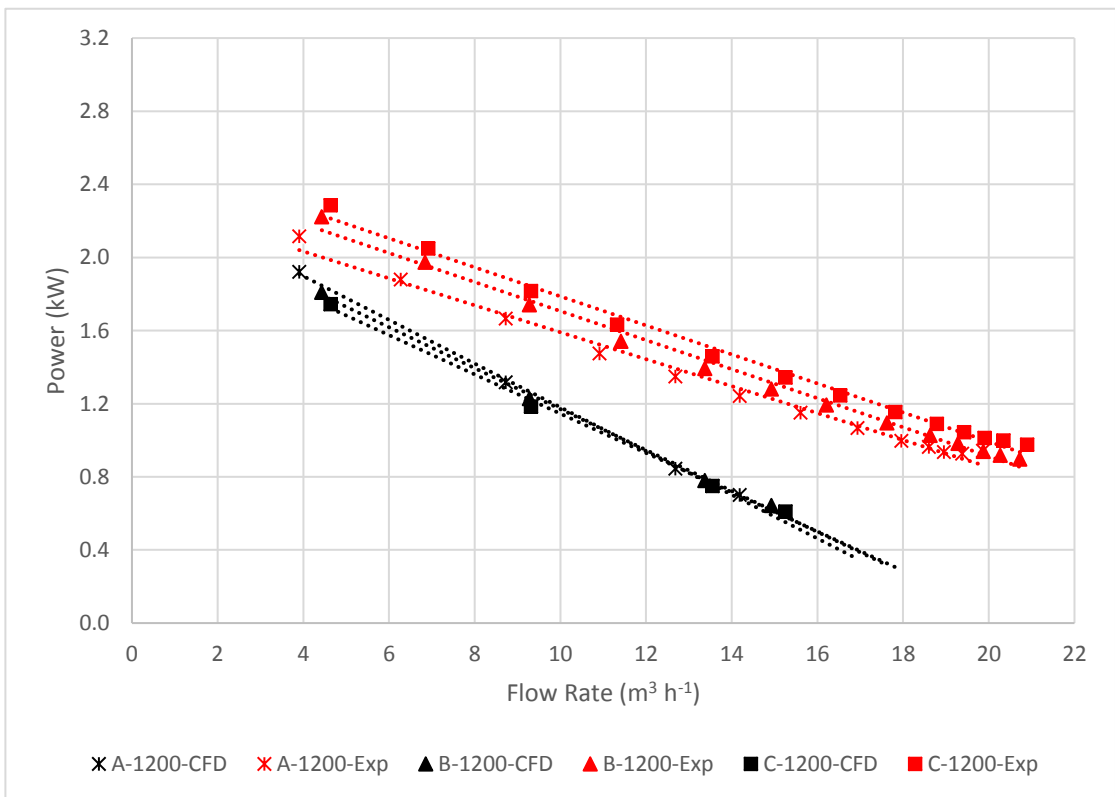


Figure 8-9: Comparison of experimental and computational power curves for pump A, B and C at 1200 rpm.

In almost all experiments, pump C can be observed to have a higher flow rate and differential pressure at all the rotational speeds tested, while pump A generated the lowest pressure head. The opposite pressure trend can be observed for the computational modelling which is most likely due to a combination of clearance sensitivity at higher flow rates and dynamic conditions not captured by the computational model. In light of these results, conclusions of the parametric clearance study might not be valid for the models featuring small DE clearances. Nonetheless, without this study the experimental testing would not have been carried out.

## 8.2 Discussion of Uncertainties and Errors

In this section the various uncertainties and errors of the experimental testing and computational simulations are discussed in order to better understand the discrepancy between the results.

### 8.2.1 Mechanical Losses

Mechanical losses that were excluded in the computational calculations but were present in the experimental testing are:

1. Disk friction losses due to friction between the rotating faces of the impeller hub and the liquid; and
2. Losses due to frictional forces within the bearings.

The mechanical losses,  $P_m$ , can be estimated for each operating point according to equation (8-1) as more accurate information is not available (Gülich, 2010):

$$P_m = 0.0045 \times \left(\frac{Q_{Ref}}{Q}\right)^{0.4} \times \left(\frac{n_{Ref}}{n}\right)^{0.3} \quad (8-1)$$

Where the reference values are  $Q_{Ref} = 1\text{ms}^{-3}$  and  $n_{Ref} = 1500$  rpm.

The mechanical losses as a percentage against the flow rates are plotted in Figure 8-10. The losses increase with decreasing flow rates due to the larger power requirements at higher pressure heads.

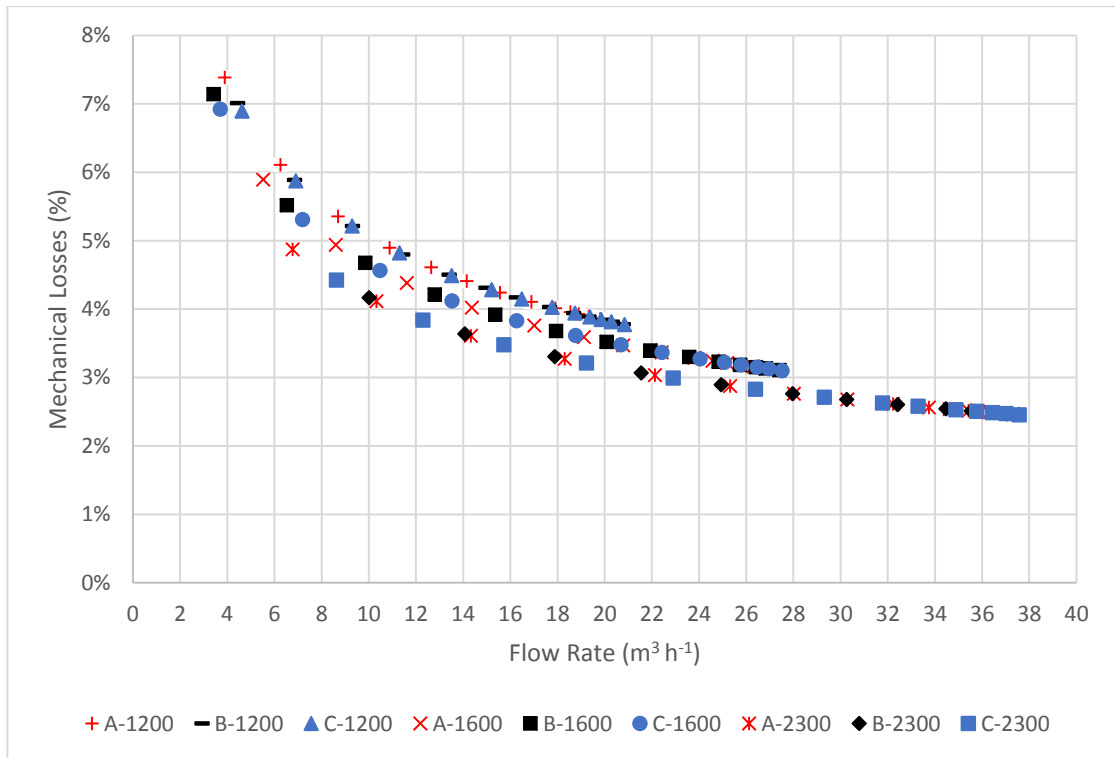


**Figure 8-10: Mechanical losses as percentage of power at BEP.**

A second method proposed by Papantonis (2009) using empirically derived factors produces similar results to the above. The mechanical losses can be calculated using equation (8-2):

$$P_m = P_e + P_s \tag{8-2}$$

Where  $P_e$  are the bearing losses and can be approximated using equation (8-3), and  $P_s$  are the rotating disk losses and can be estimated using equation (8-4)

$$P_e = 0.02 \times P \tag{8-3}$$

$$P_s = 0.00622 \times \left( \frac{\omega x r^2}{\nu} \right)^{-0.2} \times 500 \omega^3 r^5 \tag{8-4}$$

Where  $P$  is the power,  $\omega$  is the angular velocity,  $r$  is the radius of the impeller and  $\nu$  is the kinematic viscosity of water.



The mechanical losses do not offer a satisfactory explanation of the discrepancy between the computational and experimental results.

### **8.2.2 Critical Review of the Experimental Testing**

The experimental test programme that was undertaken contains information relating to the performance of the three test pumps. However, it is important to highlight the limitations of this work and to appreciate the uncertainties this causes.

Firstly, the testing was carried out by a Gilkes employee and so the author did not have any control over the testing. Furthermore, the pumps were the first ones to be tested in the new testing facility and as such there was not time to fine tune the testing procedure or to become fully acquainted with the software. As a result, a second round of testing had to be carried out to improve the quality of the measurements, particularly the sampling interval. In addition, as far as the author is aware no calibration tests were carried out on the instruments to verify that the complete data acquisition (DAQ) system represents the measured quantity within the specified limits. Because the first set of tests were of poor quality they could not be compared to the second set in order to estimate the random element in the experiments. This creates an unquantifiable uncertainty. A program of planned commercial tests and deadlines meant that no further experiments could be carried out to correct this.

The overall uncertainty for each operating point was discussed in *6.7.3 Overall Uncertainty*. The values are well within the permissible values for overall uncertainties (Grade 1) as defined by BS EN ISO 9906:2012, however it was observed that there is a higher degree of uncertainty of torque in particular at higher flow rates, and subsequently power and efficiency which could also contribute to the difference between computed predictions and measured data.

Secondly, the test pumps all feature median axial envelope (drive end and non-drive end combined) and radial clearance values. Although this indicates that pumps are manufactured to median tolerance values it does not provide a wide range of values and as a result it has not been possible to experimentally investigate the extreme ends of the manufacturing tolerances.

Another limitation of the experimental testing and perhaps the most significant, is that the static pressure transducers installed in the test rig are not able to capture the characteristic

pressure pulsation phenomenon observed in the computational modelling and reported by other researchers (Weise & Beilke, 1998; Böhle & Müller, 2009; Fleder & Böhle, 2015; Zhang, et al., 2016). The blade passing frequency (BPF) of the RLR pump at 2300 rpm is equal to 760 Hz, which corresponds to a blade pass period of 0.0013 s. The response time of the pressure transducers is 333 Hz while the sampling rate of the DAQ system is 1 Hz. To experimentally investigate if the pressure is affected by the BPF it is necessary to install piezoelectric dynamic pressure transducers that can measure frequencies up to 2 kHz and a DAQ system capable of digitalising the analogue signal with at least 4 kHz sampling frequency.

The amplitudes of these pressure pulsations are relatively large, and an average value differs from the experimental value by a significant amount at higher flow rates. The computational pressure pulsation history for pumps A, B and C at 2300 rpm at 1.1BEP, BEP, 0.9BEP and 0.6BEP (similar trends at 1600 and 1200 rpm) are plotted against the measured pressure head in Figure 8-11, Figure 8-12, Figure 8-13 and Figure 8-14, respectively, over half a revolution of the impeller. As the flow rate decreases, the experimental pressure head is shifted towards the middle of the pressure pulsations as seen in Figure 8-14. At this point the correlation between the average transient computational pressure pulsations and the experimental results are relatively good, particularly for pump A.

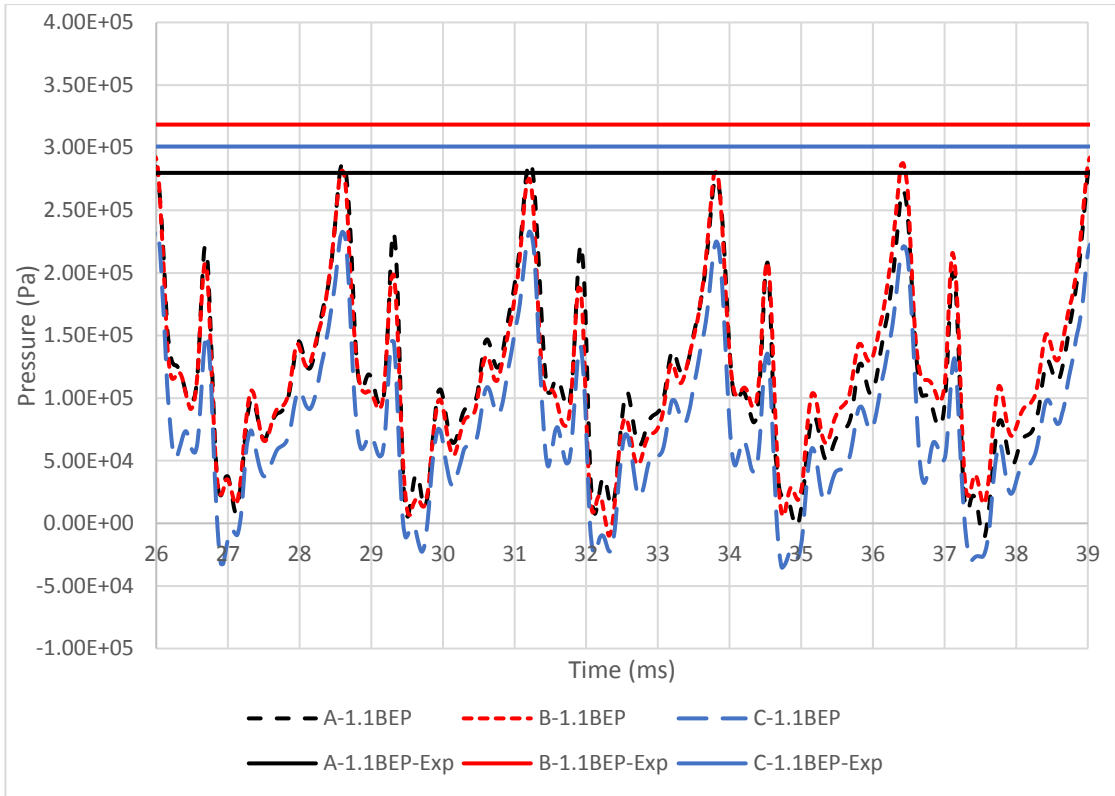


**Figure 8-11: Comparison of computed pressure pulsation history and experimental value at 1.1BEP at 2300 rpm.**

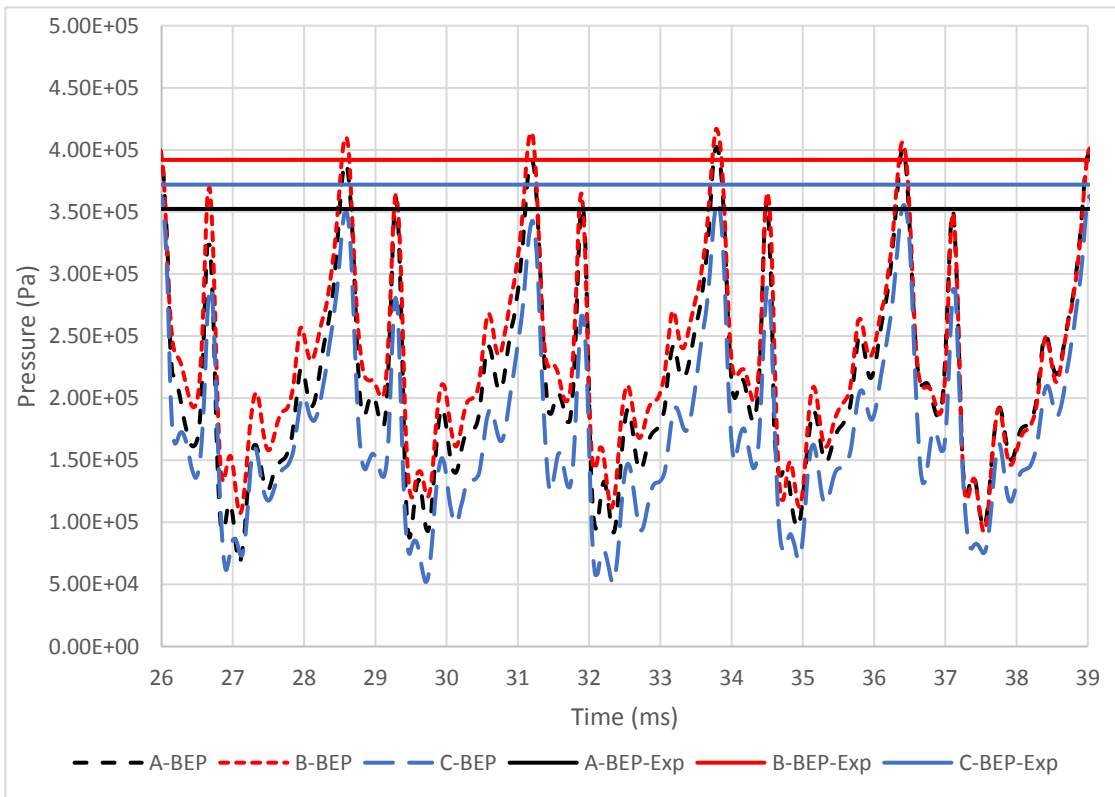


**Figure 8-12: Comparison of computed pressure pulsation history and experimental value at BEP at 2300 rpm.**

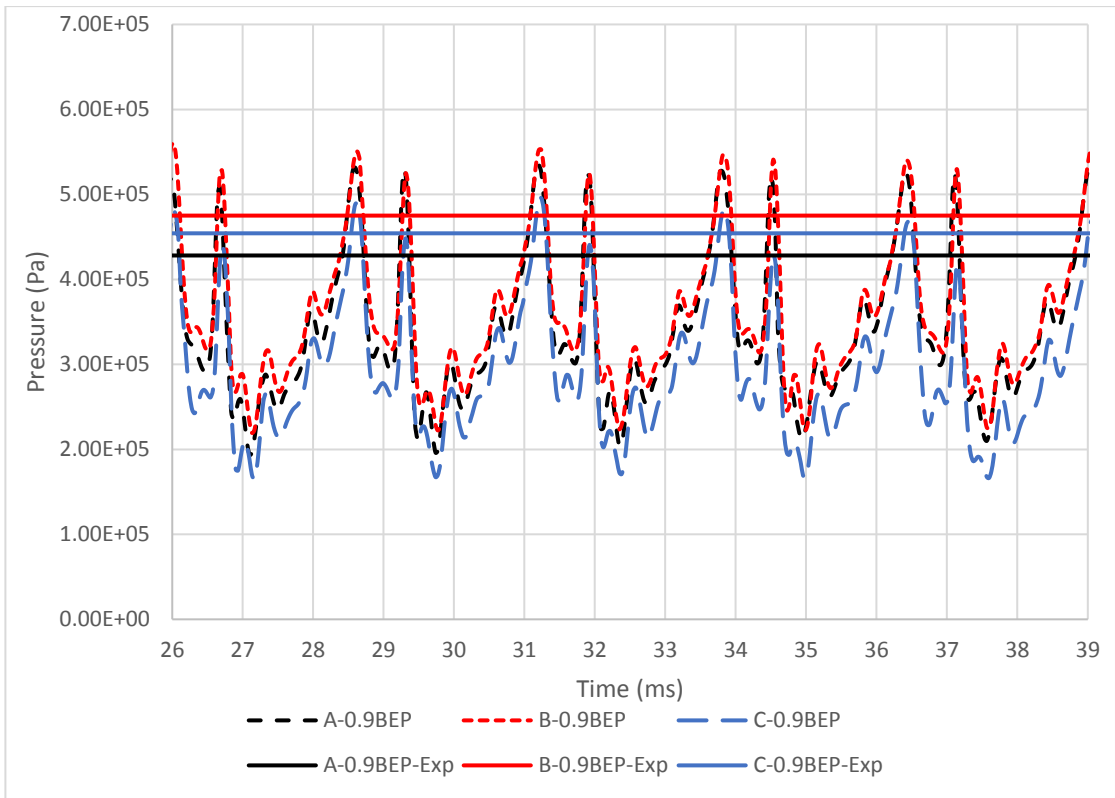


**Figure 8-13: Comparison of computed pressure pulsation history and experimental value at 0.9BEP at 2300 rpm.**

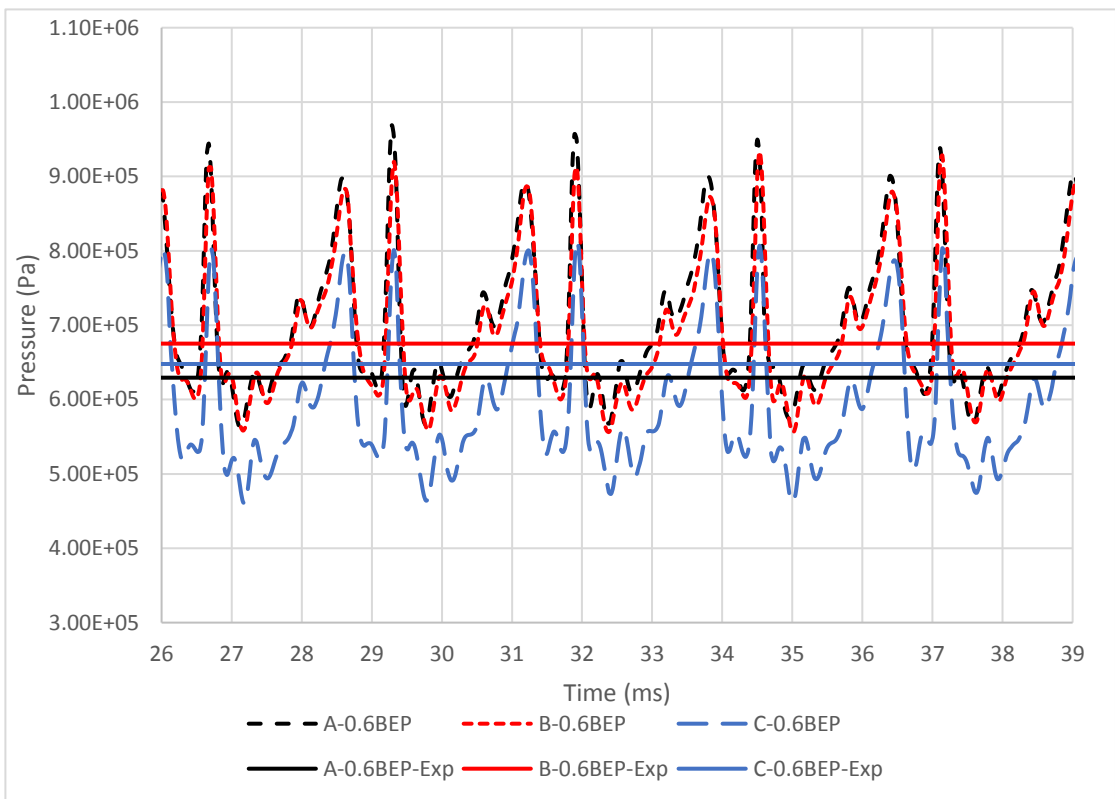


**Figure 8-14: Comparison of computed pressure pulsation history and experimental value at 0.6BEP at 2300 rpm.**

The impeller blade passing period ranges from 0.0013 to 0.0025 seconds (2300 to 1200 rpm) and subsequently a full revolution of the impeller takes between 0.026 to 0.05 seconds, respectively. In other words, at 2300 rpm the impeller rotates nearly 39 times per second. Depending on the characteristics of the DAQ system, the recorded values could either be a direct measurement or an average of a set of measurements over the sampling period. It would be interesting to know whether the values recorded by the DAQ system correspond to peak pressure values. If this is the case the computational model is predicting the performance quite well around the BEP as seen in Figure 8-11 and Figure 8-12, which is generally the case for pumps, whilst over-predicting at lower flow rates. This could of course be incidental. However, without experimental pressure pulsation traces it is not possible to know for certain.

The experimental testing has been valuable nonetheless, particularly in providing data for analysing the difference between the three different test pumps.

### **8.2.3 Uncertainties due to Manufacturing Tolerances**

The focus of this research has been to determine the variations in clearances due to manufacturing tolerance bands on machined parts and the effects these variations have on the pump performance. There are however other factors that will result in parts deviating from the ideal geometry used in the computational studies, such as casting tolerances, surface roughness and variations in machining.

The relationship between the variations in casting volume of the side channels and the effects on the pump performance is unknown. The more water that is retained inside the side channel ring, the better the pressure head and priming performance will be. Gilkes has had a foundry 3D scan the drive end (DE) and non-drive end (NDE) parts of a random pump and compared these to the CAD model which Gilkes has on their system. The results are shown in Figure 8-15 (NDE body) and Figure 8-16 (DE body).

The images on the left-hand side are based on the scale on the left, showing the difference between the Gilkes casting and the CAD model in millimetres. The blue areas are where the casting is smaller than the model, while the red areas show where there is extra material. The right-hand images follow a scale above 0 mm as these images are showing the CAD model overlaid with the casting. Therefore, the blue sections show the CAD model itself rather than the difference between the two. In other words, the results show that the side channels of

this particular cast are larger than that of the CAD model. If the same is true for the test pumps, this could help to explain some of the divergence between the experimental data and computational results.

The measured flow rate is a product of the designs of the impeller and the casing. In almost all the test cases pump C was observed to have the highest flow rate at a given operating point (partial and full loads). Unfortunately, the tested pumps have not been 3D scanned so it is not possible to do a direct comparison. The casting volume of the side channels therefore create an unknown uncertainty. One can also assume that casting variations introduce errors in the other parts of the pump assembly too.

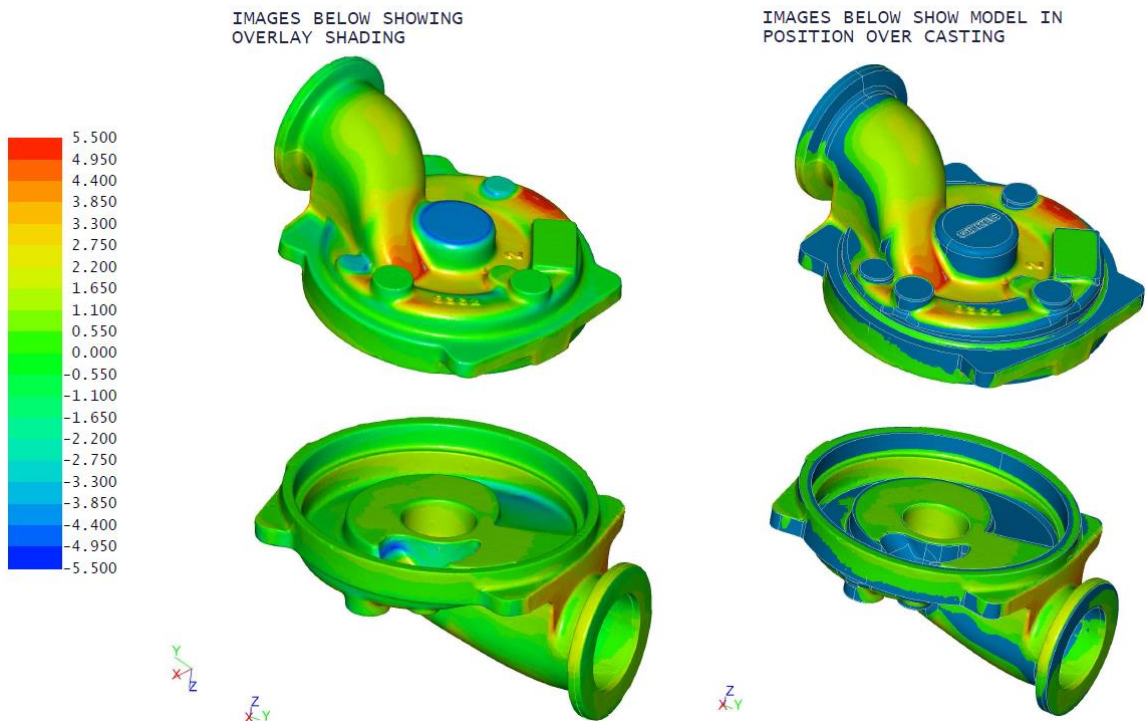
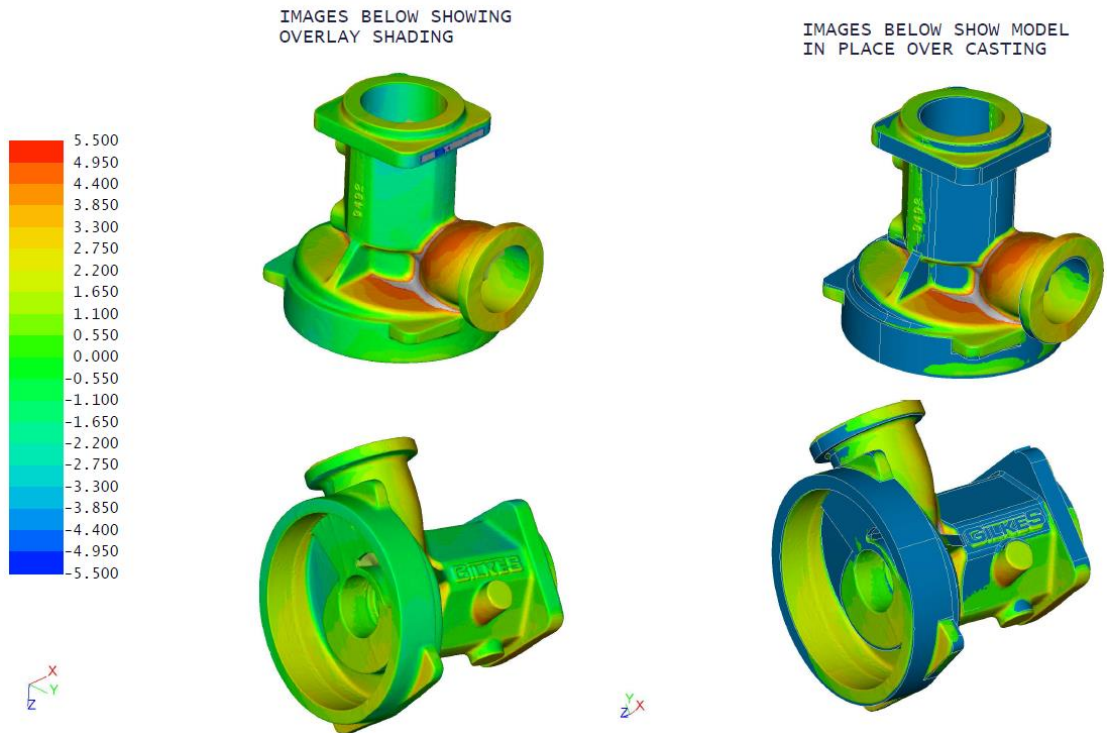


**Figure 8-15: Comparison of 3D scanned NDE body and CAD model.**



Variations in machining could also lead to non-uniform distance between parts, which has been assumed to be uniform in the computational model. This could be augmented by dynamic operating conditions such as noise and vibration. Even small changes in the impeller diameter will have a disproportionately large effect on the disk friction torque (Gülich, 2010), which increases with the fifth power of the diameter.

#### 8.2.4 Uncertainties due to Surface Roughness

The pump impellers are also sand cast. Although the important features, such as the blade edges in contact with the clearances, are machined to a set tolerance, the remaining faces of the impeller are subject to casting variations and also feature rough surfaces in between the blades. Surface roughness will affect the pump performance negatively. During the early stages of the research, a surface roughness study was carried out to assess the effects on the pump performance. The roughness of the impeller and the casing was estimated based on the manufacturing process and the surface material. In ANSYS® CFX®, the specified roughness height in the wall boundary section is the equivalent sand-grain roughness height, which is not equal to the geometric roughness height of the surface under consideration. Adam, et al.

(2012) propose a simple equation to relate surface roughness to equivalent sand-grain roughness in equation (8-5):

$$\varepsilon = 5.863 \times R_A \quad (8-5)$$

Where  $R_A$  is the average roughness of the surface in relation to the manufacturing process. Vorburger & Raja (1990) give a range of tolerances for the average surface roughness for sand casting, the values are included in Table 8-1.

**Table 8-1: Roughness values based on manufacturing process.**

		Tolerance Bands		
		<i>Lower</i>	<i>Average</i>	<i>Higher</i>
<b>Roughness Average, <math>R_A</math>, for sand casting</b>	[ $\mu\text{m}$ ]	6.3-12.5	12.5-25	25-50
<b>Estimated surface roughness for pump parts</b>		10	20	40
<b>Equivalent sand-grain roughness, <math>\varepsilon</math></b>		58.63	117.26	234.52

Schlichting, et al. (1955) provide a range of equivalent sand-grain roughness values based on the material and condition of the part in question, see Table 8-2.

**Table 8-2: Roughness values based on surface material.**

Material	State	Pump Surface	Equivalent sand-grain roughness, $k_{\text{seq}}$ [ $\mu\text{m}$ ]
Aluminium Bronze	<i>smooth, without deposition</i>	Impeller	<i>&lt; 30</i>
Cast Iron	<i>new</i>	Casing	<i>250</i>
	<i>rusted</i>		<i>1000 to 1500</i>
	<i>encrusted</i>		<i>&gt; 1500</i>
	<i>bituminized<sup>13</sup>, new</i>		<i>30 to 50</i>

Due to the complexity of the geometry of the impeller and the casing, quantifying the surface roughness was challenging with limited equipment available for measuring intricate

<sup>13</sup> Convert into, impregnate with, or cover with bitumen.



geometries. However, attempts were made to estimate the casing using the outer surface (assumed same as inside), which gave an approximate roughness value of 12.76  $\mu\text{m}$ , which is close to the average value provided in Table 8-1.

A range of equivalent sand-grain roughness values were simulated to account for any uncertainties, the results normalised against a computational model without surface roughness are shown in Figure 8-17. The simulation scenarios feature a combination of impeller and casing roughness from average to worst-case scenario (i.e. erosion or rust). It should be noted that the same roughness is applied to all the impeller walls, however the maximum value does not exceed the lower value provided in Table 8-1.

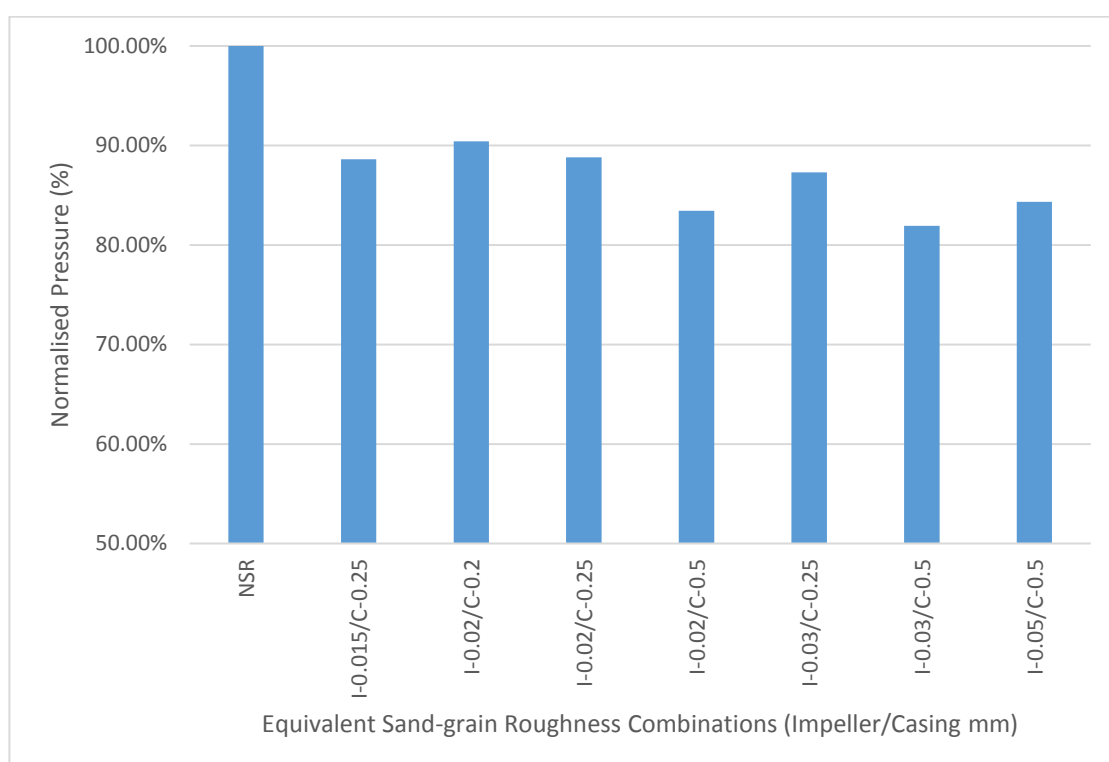


**Figure 8-17: Surface roughness study, results normalised against model with no surface roughness (NSR).**

The results indicate that the roughness of the casing has a larger effect on the performance of the pump than the roughness of the impeller. This is most likely due to a combination of the higher roughness height of the casing surface, approximately ten times higher than that of the impeller surface, and the increased friction the fluid has to overcome in the side channels. The low efficiency of these pumps can be explained by the large power loss due to sustaining the circulatory flow against the resistance caused by the fluid friction and turbulence and by the shock losses as the fluid moves between the channel and impeller (Sixsmith & Altmann, 1977).

The true effect of the surface roughness should be examined in further detail.

### **8.2.5 Limitations of the CFD Model**

Physical modelling, mesh generation, computational solution and post-processing of results harbour a number of uncertainties. The various uncertainties and errors that can exist within a computational simulation are summarised as follows (NASA, 2008; Gülich, 2010):

1. Physical approximation error due to uncertainty in the formulation of the model (physical modelling error) and deliberate simplifications of the model (geometry modelling error).
2. Computer round-off errors develop with the representation of floating point numbers on the computer and the accuracy at which the numbers are stored. When compared with other errors these are often considered to be negligible.
3. Iterative convergence error exists because the iterative methods used in the simulation must have a stopping point eventually.
4. The discretisation errors are those that occur from the representation of the governing flow equations and other physical models as algebraic expressions in a discrete domain of space and time.
5. Computer programming errors are “bugs” and mistakes made in programming or writing the code.
6. User errors are caused by negligence, lack of knowledge of the complex computational code and of physical phenomena as simplifications are made due to computational cost and lack of resources.

The computational methodology has been systematic, followed established guidelines and recognised methods, and wherever possible further simulations have been carried out to estimate uncertainties. The total computational error calculated using the root-sum-square method is 0.46% (see *4.6 Summary of Computational Modelling Methodology*). However, there might be further errors imposed by the choice of turbulence modelling. The pump experiences recirculation and the flow field is complex by nature; these types of flows are difficult to model correctly. The choice of turbulence model needs to be considered carefully and whether a Reynolds-Averaged Navier-Stokes style model is capable of modelling this type of flow at all. The under-performance of the CFD model may be due to the fact that it is not capturing enough detail and as a result the turbulence may be under resolved. Although the chosen turbulence model was compared to other Two-Equation URANS models, it was not

compared to a Scale Resolving Simulation model such as Large Eddy Simulation, Scale Adoptive Simulation and Detached Eddy Simulation which would be more accurate but also computationally more expensive.

Discretisation errors caused by the mesh are unpredictable but can be severe. This error can be quantified and reduced considerably by carrying out successive mesh refinement, using different types of meshes and searching for mesh-independent solutions. A recognised method for the analysing mesh independence (Roache, 1994) was performed in *4.5 Mesh Independence Study* and the solutions were well within the asymptotic range. However, the mesh is unstructured due to a combination of limitations imposed by the ANSYS® Meshing® software and the complex geometry, and as such any discretisation errors could be carried forward through the mesh independence study. Furthermore, the difference in volume ratio of the elements close to the domain interfaces of the axial clearance bodies were larger than the thickness of the elements in the clearances. The size of the interface elements was reduced to improve the mesh quality in this aspect, but the problem was only partially solved. A good quality mesh can be obtained with fewer elements for a structured mesh in comparison to an unstructured mesh but it requires the use of a more advanced mesh generation software.

Attempts were made to create a hexahedral impeller mesh in order to quantify potential errors of the tetrahedral mesh. Before creating a hexahedral mesh, the volume of each of the basic impeller parts (i.e. the fluid between the blades, of which there are 10 bodies) had to be split into five smaller volumes (see Figure 8-18). By splitting the basic impeller element into five volumes, they should be able to be discretised using a swept mesh. To still be able to use the swept mesh method on the clearance volumes the faces need to match those of the impeller volumes, hence why the axial clearance volumes have also been split along the same circular axis as seen in Figure 8-19.

However, the ANSYS® Meshing® tool does not allow the user as much freedom as more advanced mesh generation software. The sweep meshing method restricts the use of inflation layers. The 'MultiZone' method (see Figure 8-20) therefore seems to be more suitable, however the addition of inflation layers impacts the quality negatively. Furthermore, an improved boundary layer resolution results in a mesh with a higher ratio of tetrahedral elements to hexahedral elements.

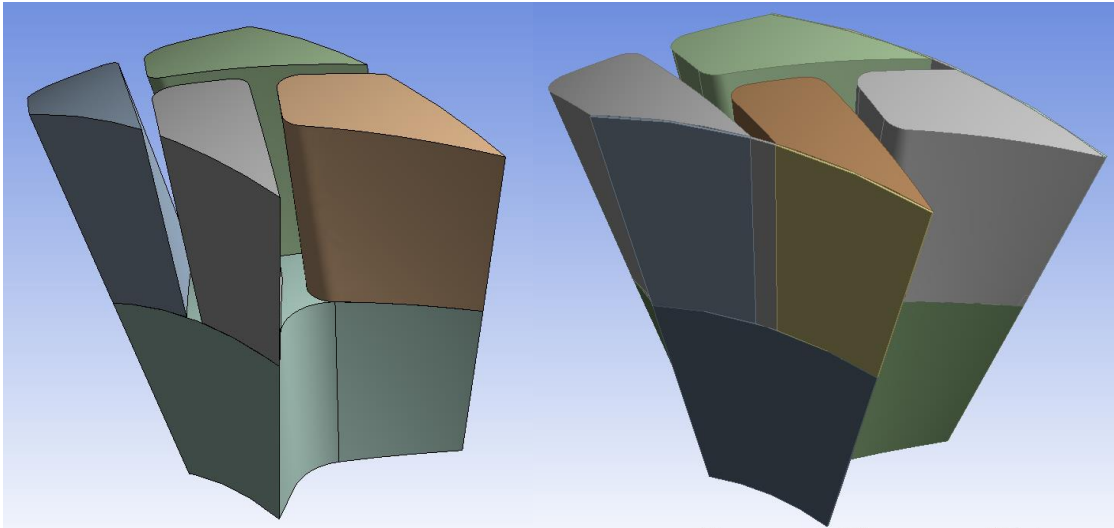


**Figure 8-18: Volume splitting of a basic impeller element.**

**Figure 8-19: Volume splitting of axial clearance elements.**



**Figure 8-20: MultiZone mesh of an impeller fluid volume.**

The computational model captures the basic trend of torque versus rotational frequency even though quantitative differences are observed, particularly at higher flow rates. This is in part due to the mechanical losses excluded in the computational prediction, but geometrical inaccuracies which were not included in the computational model can also be influential. The simplification of the inner axial clearance ‘disks’ as detailed 4.2.1.2 *Axial Clearance Reduction* was done to reduce complexity and streamline the geometry generation for the parametric

clearance study. A test case showed that only small differences in pressure exist. However, there were no experimental torque values to compare against. A case featuring one of the experimental test pumps with the added inner clearance disks has been simulated to evaluate the effects on the predicted torque. As before, the inner clearance disks are assumed to be uniform in thickness. The results show however that there is hardly any difference in the predicted torque with and without these clearance disks.

The inherent, periodically unsteady, flow-induced impeller oscillations occurring in the regenerative pump; coupled with high rotational speeds lead to undesired effects such as mechanical vibration, noise and impeller deformation. These dynamic conditions occurring during operation are not captured by the computational model and so a Finite Element Analysis was carried out to investigate the deformation of the experimental test impellers. The study is presented in the next chapter and provides further insight into the disparity between the computational and experimental results.

### **8.3 Summary of Computational and Experimental Comparison**

In this chapter, the computational and experimental results are discussed and compared. The factors leading to discrepancies between the results can be summarised as inconsistencies in experimental testing, uncertainties due to manufacturing, such as casting variations, and limitations of the computational models and techniques developed during this research. Industry cannot only rely on CFD to create new products; experimental testing is still necessary despite the expense. The RLR pump is unique (especially the Gilkes arrangement) and requires further comparison studies between experimental testing and computational analysis. This is particularly important to be able to fully understand the pressure pulsation characteristics and the effects of tighter design tolerances on the DE side, which were not captured sufficiently by the computational model. As far as the author is aware only Weise & Beilke (1998) have published a comparative study of computational and experimental pressure pulsations (for a fan), which confirmed that pressure pulsations also occur experimentally, and they show the same periodic characteristic trend as the computational calculations. Other researchers (Böhle & Müller, 2009; Fleder & Böhle, 2015; Zhang, et al., 2016) have documented computational pressure pulsations only, with comparison against 'static' experimental data, however all the studies feature radial bladed impellers in contrast to the pump analysed in this research which has a chevron shaped impeller.

## 9 Finite Element Analysis (FEA)

The RLR pump requires tight clearances around the impeller to ensure optimum performance which is confirmed in literature and studies discussed in previous chapters in this thesis. The magnitude of these clearances is very small, often less than 0.5 mm, and they are sensitive to operational wear of internal components over time due to fluid contamination and debris, which affects both the reliability and performance of the pump. As discussed in the previous chapter, high rotational speeds and pressure loads induce undesired effects such as mechanical vibration and noise, which is likely to cause some deformation of the impeller and subsequently the shape and the thickness of the clearances.

A full Finite Element Analysis (FEA) is carried out using ANSYS® Mechanical® within Workbench to investigate the deformation on the experimental test impellers A, B and C by importing pressure profiles from the corresponding CFD simulations detailed in Chapter 7 *Computational Performance Modelling*. The impeller deformations are then compared against the computational and experimental pressure heads to explain the inconsistency between them. The dimensions of the impellers are included in Figure 9-1 and Table 9-1.

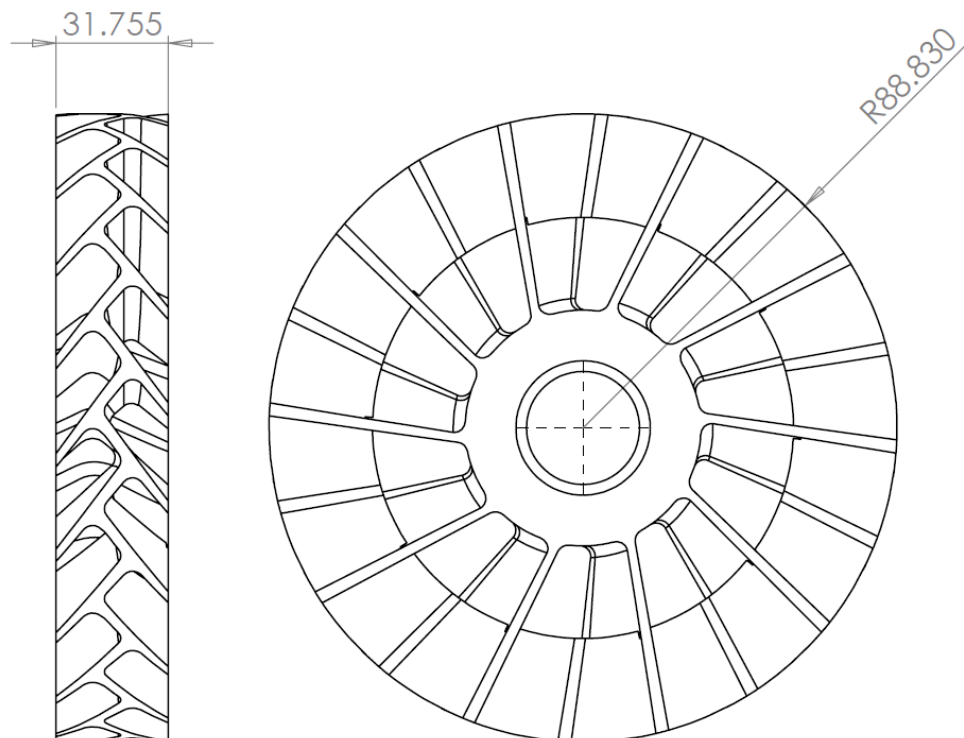


**Figure 9-1: Width and diameter of 2.5" SX impeller for pump A.**

**Table 9-1: Impeller dimensions for pump A, B and C.**

<b>Impeller [-]</b>	<b>Width [mm]</b>	<b>Diameter [mm]</b>
A	31.755	177.660
B	31.750	177.660
C	31.740	177.650

The effects of centrifugal force and pressure loads are evaluated for each impeller at:

1. The best efficiency point (BEP) at 2300, 1600 and 1200 rpm.
2. 0.7BEP at 2300, 1600 and 1200 rpm.
3. 0.6BEP and 0.4BEP at 2300 rpm.

The points are chosen to provide a deeper understanding of the operational performance of the test pumps over a wide operating range and to offer an improved insight into computational and experimental differences.

The impeller material is aluminium bronze BS1400 AB2. Some of the material characteristics are included in Table 9-2.

**Table 9-2: 2.5" SX impeller material characteristics**

	<b>Unit</b>	<b>Value</b>
Young's Modulus	[N mm <sup>-2</sup> ]	110,000
Mass Density	[kg m <sup>-3</sup> ]	7,530
Poisson's Ratio	N/A	0.32

The impeller is expected to deflect radially outwards due to the centrifugal force and axially inwards due to compression forces from the drive end (DE) and the non-drive end (NDE) as illustrated in Figure 9-2.

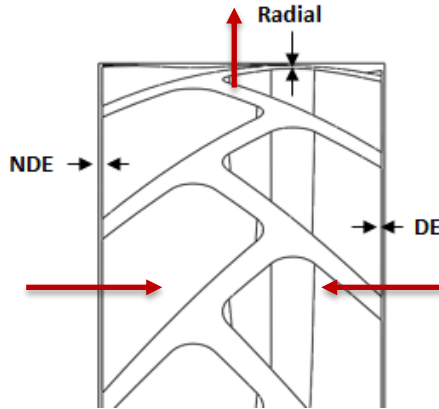


**Figure 9-2:** Cut-out of impeller showing the expected direction of impeller deformation in relation to the location of the clearance geometries.

### 9.1 Simulation Setup and Analysis

Due to the location of the inlet and outlet ports and the lack of symmetry in pressure fields this causes, the full impeller must be analysed. A one-way Fluid-Structure Interaction (FSI) approach is used, where the CFD-calculated pressure loads from one specific time step are applied to the mechanical load model and a structural analysis to determine the stresses and deflections is carried out (see Figure 9-3). The imported pressure profiles correspond to a time step at peak pressure after two full revolutions of the impeller to assess the extreme end of deflection. In a two-way FSI analysis the effects of fluid and mechanical loads are analysed simultaneously, along with the coupled effects of one type of load upon the other. However, a full FSI requires large computational resources and timescales, which was deemed to be impractical.

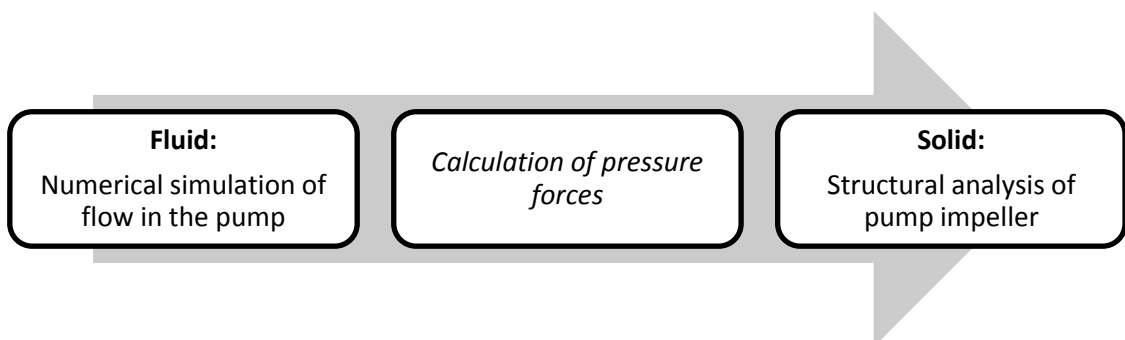


**Figure 9-3:** One-way Fluid-Structure Interaction schematic.



The 3D CAD model of the solid impeller (see Figure 1-6) is imported into the Mechanical solver for FEA. The fixed support corresponds to where the impeller is mounted on the shaft and the direction of rotational speed is shown in in Figure 9-4.



**Figure 9-4: Impeller FEA setup showing rotational speed direction (viewed from NDE).**

The stresses and deformation in the impeller as a result of pressure forces are analysed by importing the pressure profiles calculated in CFD on the impeller surface, the NDE side, the DE side and the periphery of the impeller (see Figure 9-5).

In order to study strain and stress results as a function of the number of pressure profiles set as boundary conditions, three other scenarios were also investigated:

1. Impeller only
2. Impeller, DE and NDE
3. Impeller, DE, NDE and radial
4. DE, NDE and radial

The results of the maximum total deformation and maximum von-Mises stresses and corresponding solve times are shown in Table 9-3, while the deformation and stress contours can be seen in Figure 9-6 and Figure 9-7, respectively. The impeller only version generates the highest deformation while the complete combination (i.e. 3) has the highest concentration of stress and the longest solve time. Combination 3 also has a smaller deformation which is most likely due to the axial and radial pressure profiles counteracting some of the deformation. The values of the total deflection and stress concentration are the smallest for arrangement 4. The contours of the stress distribution indicate that combinations 2 and 3 have a similar profile,

however the contours of the total deformation show a more distinct difference between the combinations. Combination 3 features the highest number of areas of maximum deformation. Based on these findings it was decided to use combination 3 for the FEA simulations.

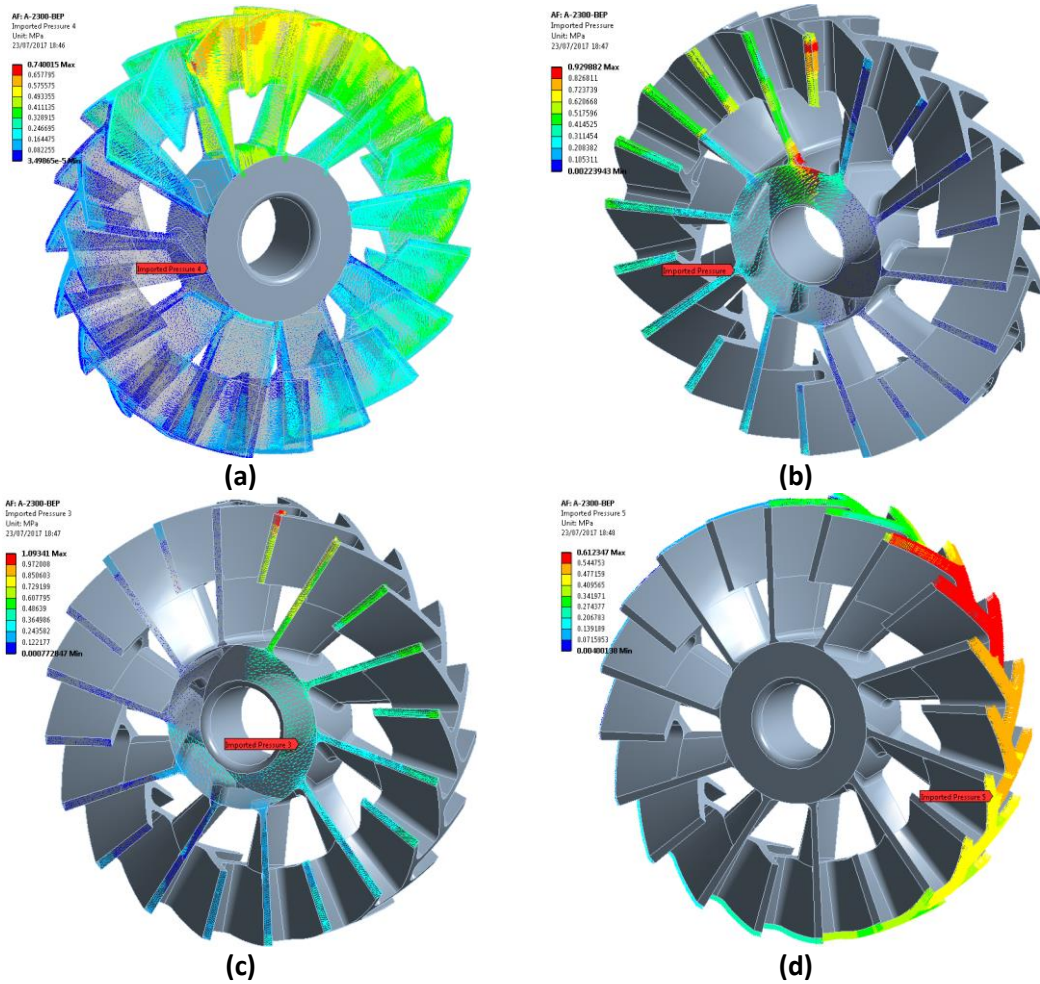
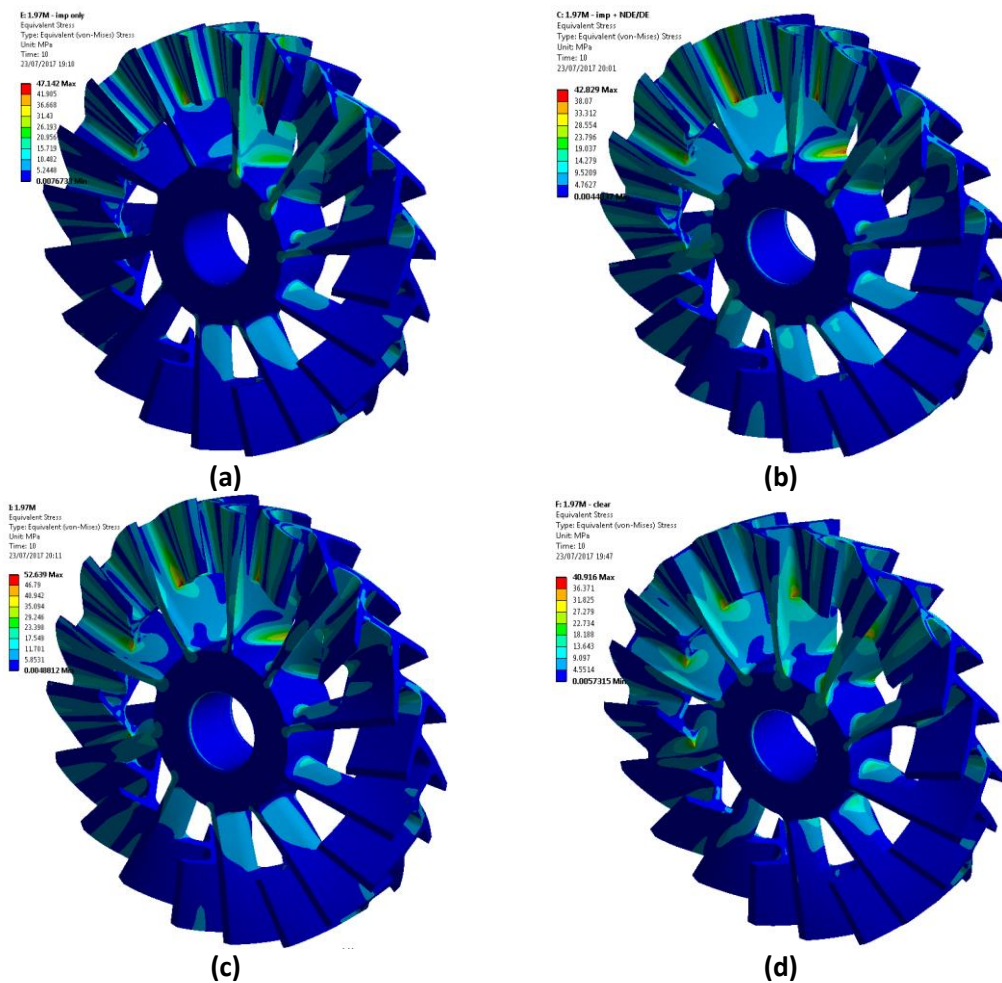


Figure 9-5: Imported pressure profiles on (a) impeller surface, (b) NDE, (c) DE and (d) impeller periphery.

**Table 9-3: Results and solve time for imported pressure profile combinations.**

Pressure Profile Combination		1	2	3	4
No. Elements	[M]	1.97			
Rotational Velocity	[rpm]	2300 <sup>14</sup>			
Max. Total Deformation	[mm]	0.054	0.043	0.044	0.032
Max. von-Mises Stress	[MPa]	47.142	42.829	52.639	40.196
Solve time	[h, min]	1h, 26min	1h, 30min	1h, 58min	1h, 27min



**Figure 9-6: Equivalent stress contours for imported pressure profile combinations for (a) impeller only, (b), impeller, DE & NDE, (c) impeller, DE, NDE & radial and (d) DE, NDE & radial.**

<sup>14</sup> Steady rotor with inertia forces.

The process of importing the CFD-calculated pressure profiles is a time-consuming process as the software must match the pressure loads to the nodes of the solid model. This is part of the motivation for limiting the investigation to two operating points at each speed as well as using the CFD results from only one time step. However, an additional two points at 2300 rpm were also included in the analysis.

Because the CFD-calculated pressure profiles imported into FEA are from one specific time step and impeller position, it was deemed that a static structural analysis would be sufficient for analysing the impeller deformations at the given time step.

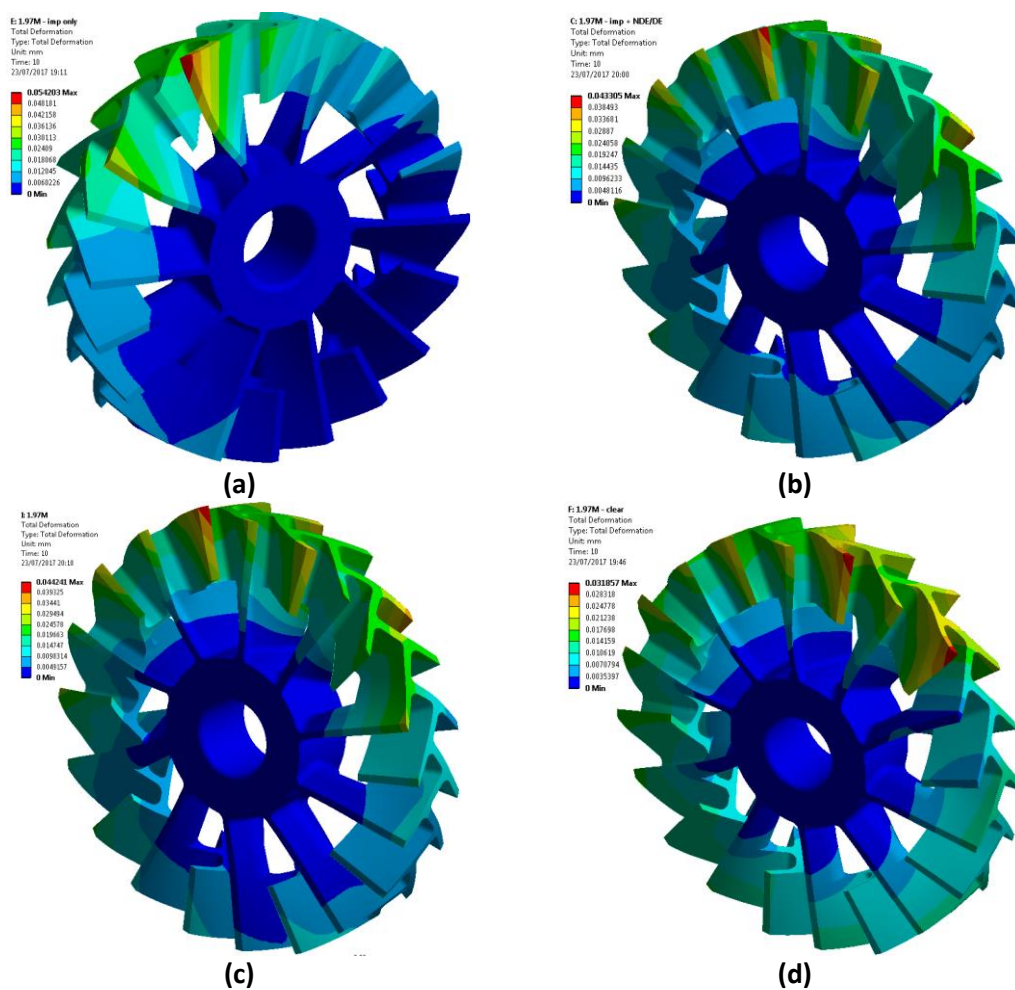


**Figure 9-7: Total deformation contours for imported pressure profile combinations (a) impeller only, (b) impeller, DE & NDE, (c) impeller, DE, NDE & radial and (d) DE, NDE & radial.**



## 9.2 Mesh Refinement Study

A mesh refinement study was carried out on the pump A impeller using the best efficiency point conditions with a rotational speed of 2300 rpm. Although the size of the impeller is different for each test pump, the differences are very small and the geometrical features remain the same. A refinement ratio of 1.5 was applied to generate four meshes, the coarsest mesh consisting of 0.28M elements and the finest mesh of 3.95M elements. The mesh density was altered by increasing the mesh size on the edges of the impeller blades in accordance with the refinement ratio, see Figure 9-8 below.

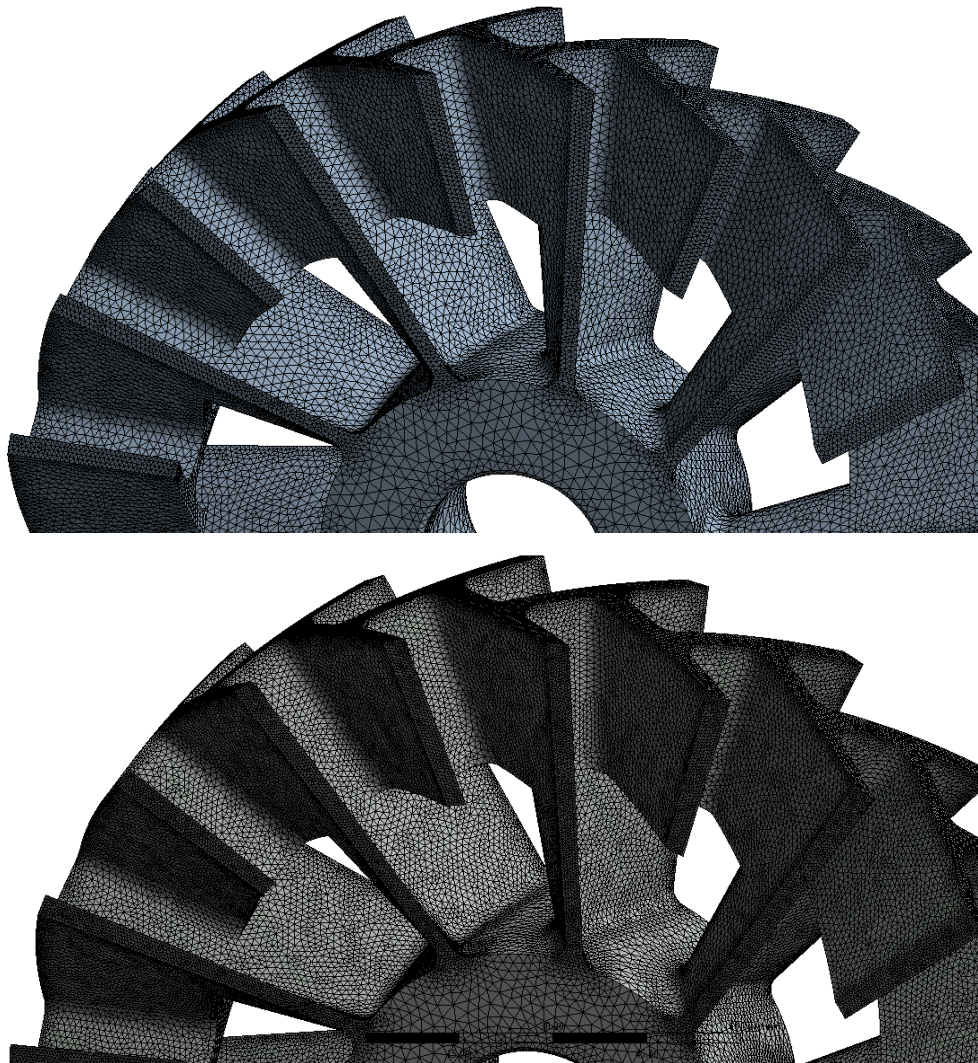


*Figure 9-8: Impeller mesh showing refinement on blade edges for Mesh 2 (top) and Mesh 4 (bottom).*

The results of the four meshes are normalised to the coarsest mesh are shown in Table 9-4 along with the solve times. The results show that there is only a small difference of

approximately 3% between the coarsest and finest mesh in terms of total deformation while the change in maximum stress value for the finest mesh is as large as 17%. However, the solve time for the finest mesh is nearly twice that of Mesh 3. Furthermore, the solve times given here do not represent the time it takes to import the pressure profiles, which increases significantly with mesh density. The main area of interest for the FEA is to assess the impeller deformation and do comparisons between the three test pumps. If considering Mesh 1, 2 and 3 in isolation the difference between the medium and finest mesh is miniscule. It was therefore decided that Mesh 2 is accurate for comparative purposes.

**Table 9-4: Results of the FEA mesh refinement study, normalised to the coarsest mesh.**

		<b>Mesh 1</b>	<b>Mesh 2</b>	<b>Mesh 3</b>	<b>Mesh 4</b>
<b>Number of Elements</b>	[M]	0.28	0.71	1.97	3.95
<b>Rotational Velocity</b>	[rpm]	2300			
<b>Normalised Max. Total Deformation</b>	[%]	100.00	101.16	102.31	102.08
<b>Normalised Max. von-Mises Stress</b>	[%]	100.00	104.98	104.83	117.72
<b>Solve Time</b>	[h, min]	19 min	54 min	1h, 58min	3h, 39min

The von-Mises stress and deformation are plotted against each mesh in Figure 9-9.

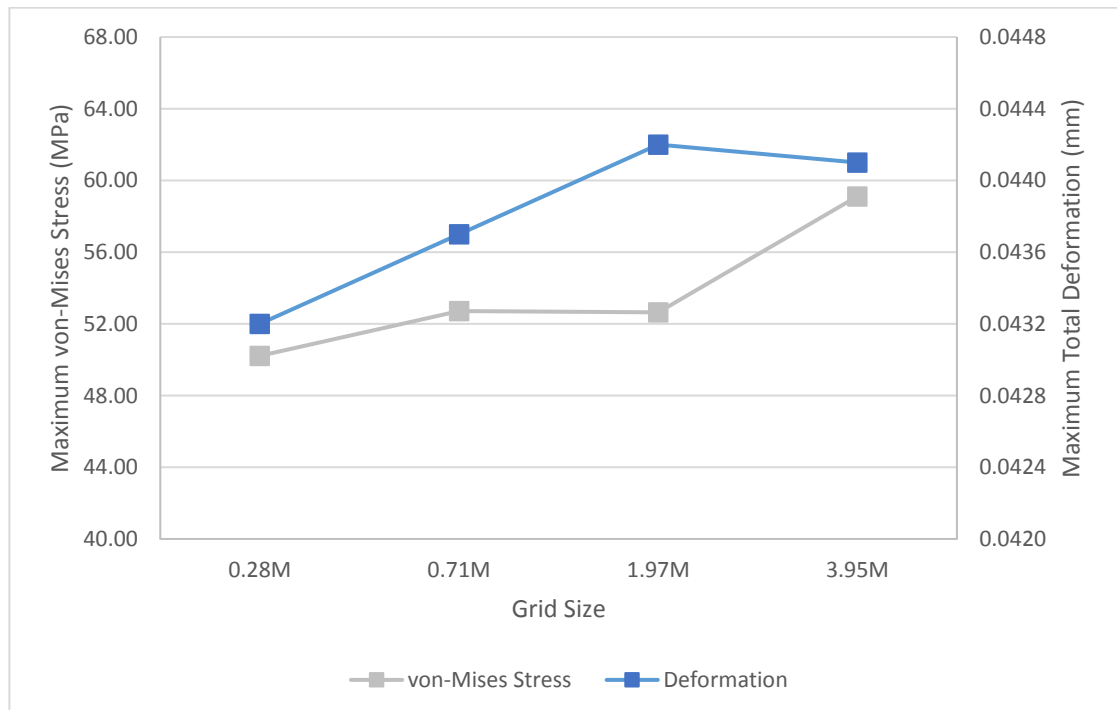


**Figure 9-9: Results of FEA mesh refinement study, von-Mises stress and deformation against mesh size.**

### 9.3 Results and Discussion

Once the simulation was completed, the results were processed. The FEA was carried out to investigate possible operational effects of variations in the radial and axial clearances. It is likely that deformation of the impeller due to both rotational speeds and pressure loads over time can change the shape and the width of the clearances. Therefore, the primary output from these simulations is the deformation on the impeller. However, areas of stress concentration are also of interest due to the inherent capabilities of regenerative pumps to create very large pressure heads. In addition, as far as the author is aware no other fluid-structural interaction studies on regenerative pumps exist in the public domain.

The outputs of the simulations are first evaluated in terms of maximum total deformation, deformation in the axial and radial directions and maximum von-Mises stresses. The deformation values are then used to compare the extreme ends of the operational impeller width and diameter dimensions against the manufacturing tolerance bandwidths. Moreover, the deformed impeller dimensions can be assessed against the experimental and computational pressure heads to shed some light on the disparity between these.

#### 9.3.1 Impeller Deformation and Stress Analysis

The total deformation is a scalar quantity of the directional vectors, see equation (9-1) below.

$$\delta_{total} = \sqrt{\delta_x^2 + \delta_y^2 + \delta_z^2} \quad (9-1)$$

It then follows that the total radial deformation is a scalar quantity of the deformation in the x- and y-directions. The total axial deformation corresponds to the deformation in the z-direction. The maximum deformation (total, radial and axial) and the maximum von-Mises stresses of the three test pumps are plotted in Figure 9-10 for the points evaluated at 2300 rpm and in Figure 9-11 for those evaluated at 1600 and 1200 rpm.

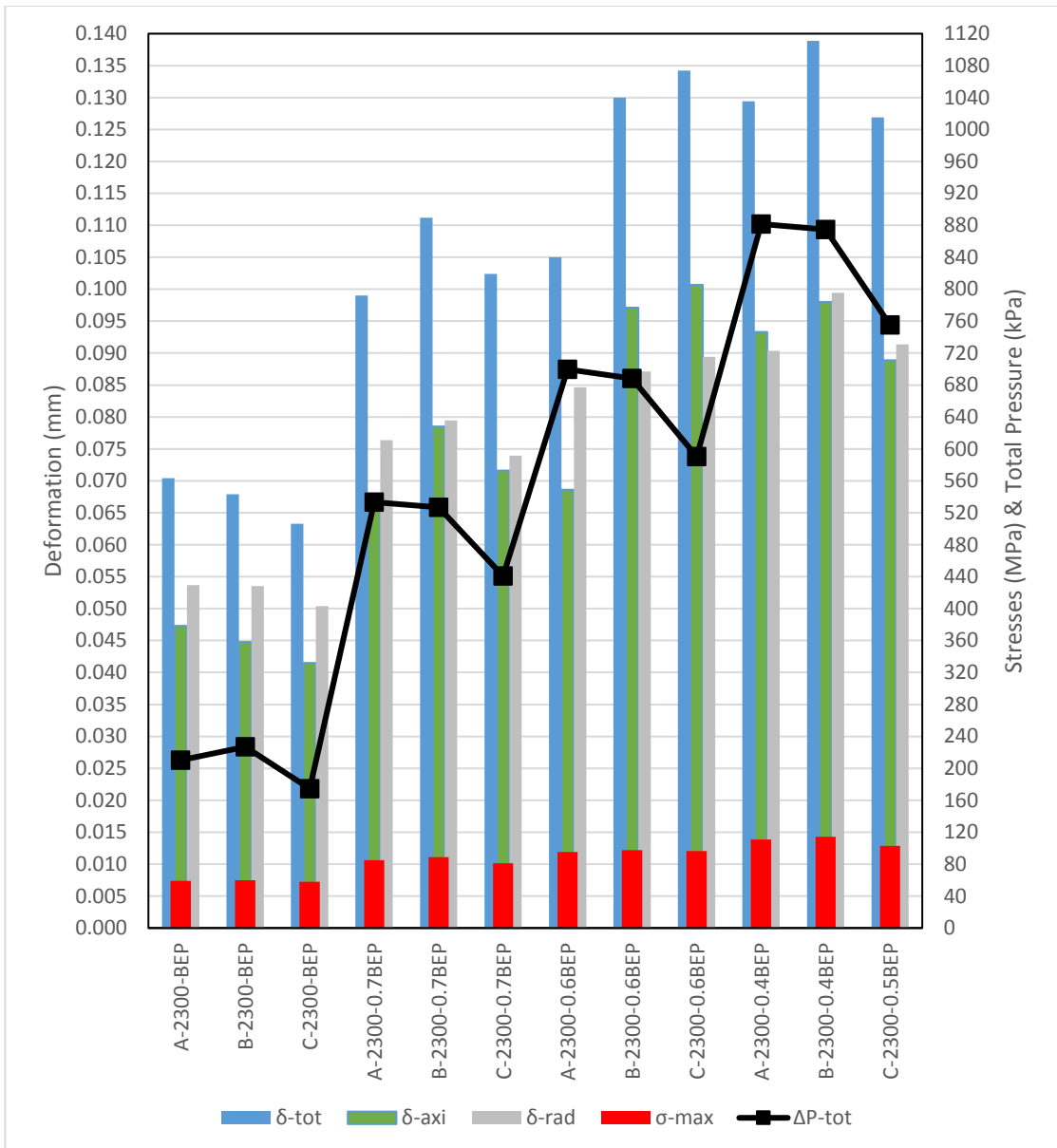


**Figure 9-10: Comparison of deformation and stress at maximum pressure pulsation against the corresponding average CFD-calculated pressure head at 2300 rpm.**

It is clear that the deformation of the impellers increases with lower flow rates, which can be put down to characteristic higher pressure heads at lower flow rates, and decrease with lower operational speeds. Generally, the largest deformation occurs in the radial direction, particularly at 2300 rpm, which is most likely due to the effect of the centrifugal force applied to the impeller when the shaft starts turning in combination with the radial pressure distribution imported from CFD. From the results it can be deduced that the impeller with the largest radial deformation also has the highest maximum stress, which corresponds to the



theory of deformation of a solid due to stress, i.e. strain which is related to stress as shown in equation (9-2):

$$\varepsilon = \frac{\sigma}{E} \tag{9-2}$$

Where  $\sigma$  is stress and  $E$  is Young's Modulus, which is a property of the impeller material and remains constant for the three pumps.

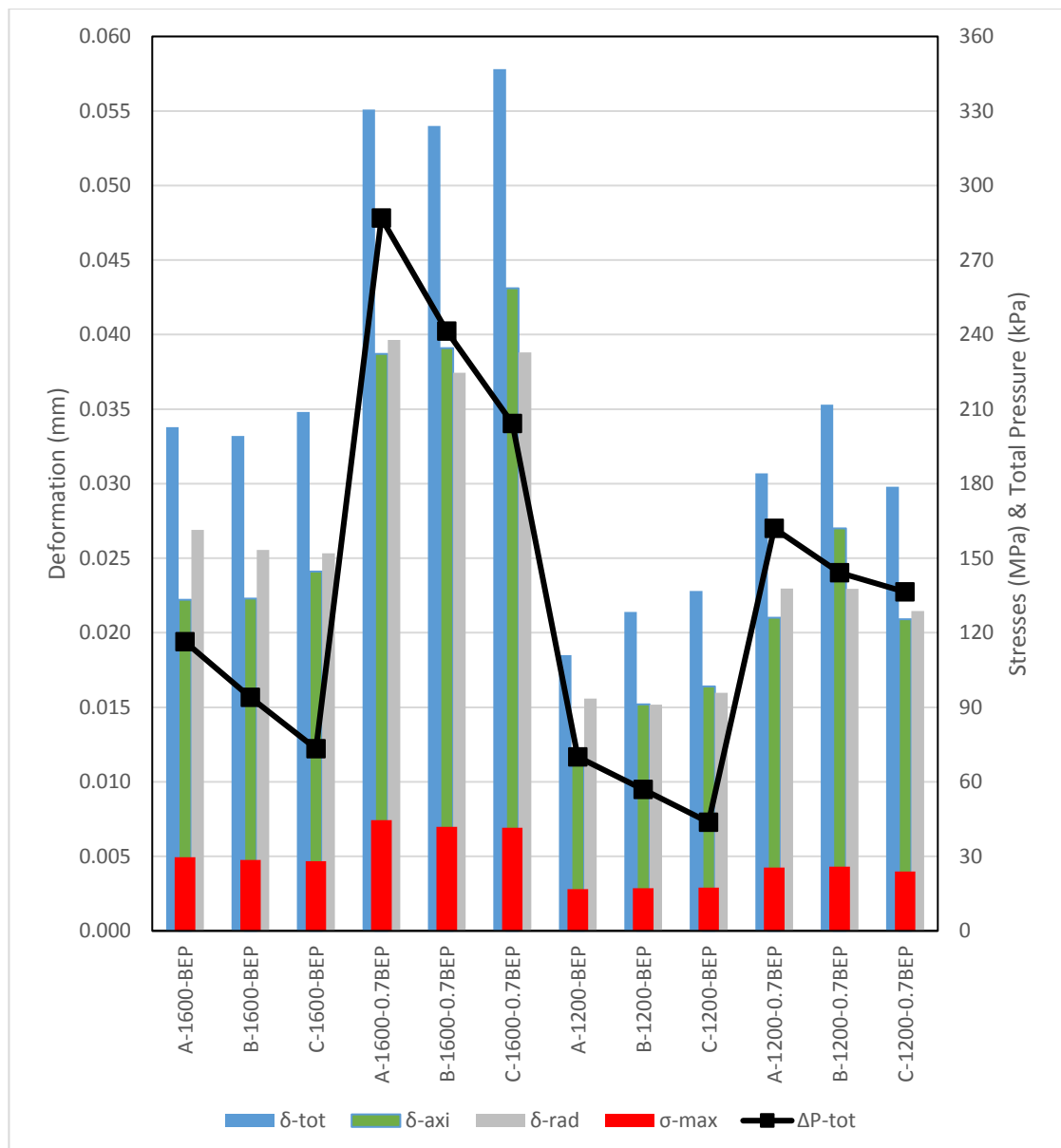
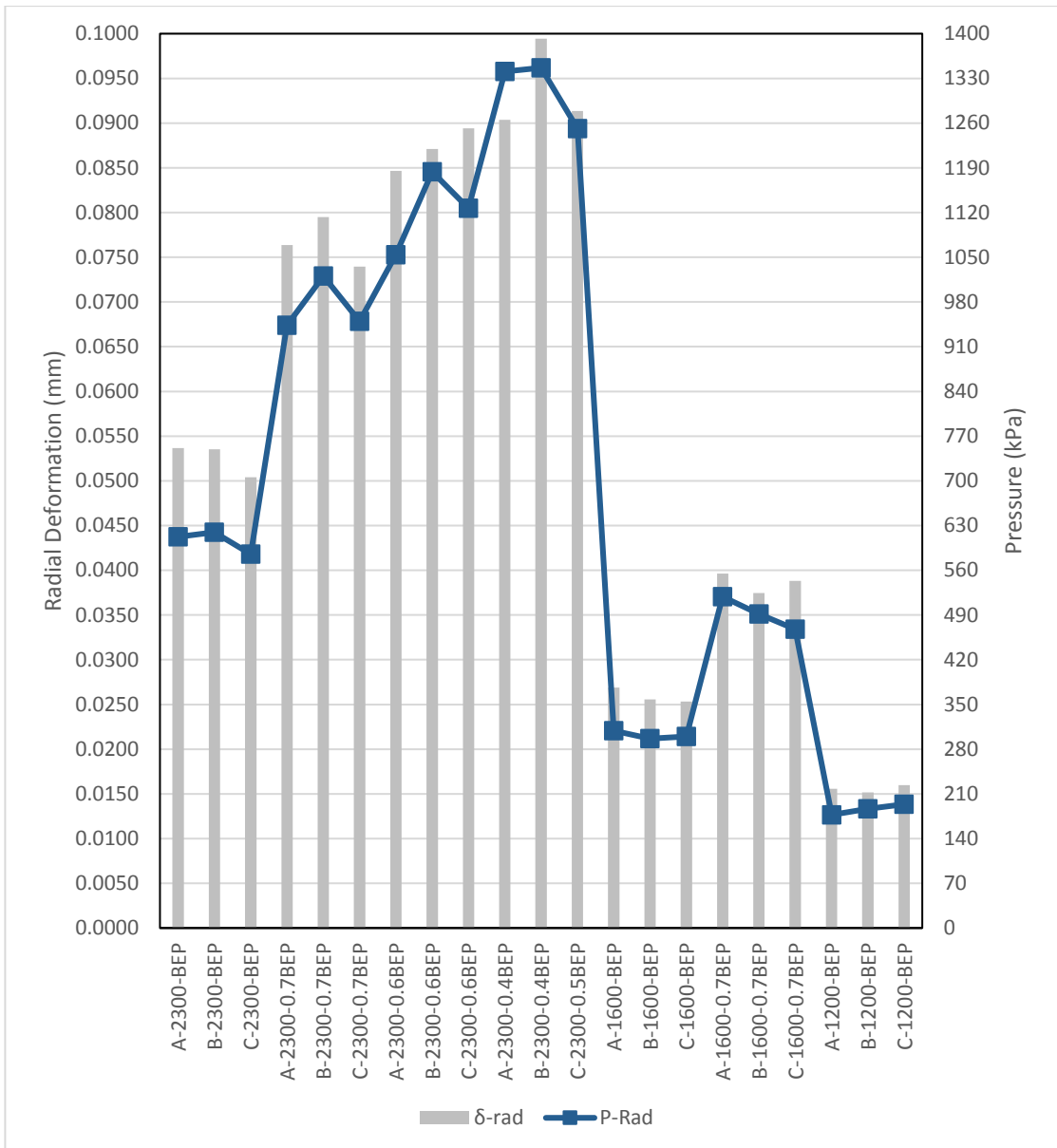


Figure 9-11: Comparison of deformation and stress at maximum pressure pulsation against the corresponding average CFD-calculated pressure head at 1600 and 1200 rpm.



**Figure 9-12: Relationship between radial deformation and imported radial pressure profile.**

A correlation between the pressure head and the radial deformation can be observed at the BEP at all the operational speeds; the pump that generates the highest total pressure also has the largest radial deformation. In 7.3 *Performance Effects due to Axial and Radial Clearance Pressure* it was concluded that the radial clearance is the primary driver for the total pressure head. The same relationship between the pump pressure and the radial deformation can also be seen at 0.7BEP at 1200 rpm, however there is no apparent trend for the other operating points. The relationship between the radial deformation and the imported radial pressure profile in terms of maximum value is shown Figure 9-12, clearly showing how the pressure profile affects the deformation.

There is no obvious link between the axial deformation and the pressure head or the maximum stress in Figure 9-10. This could be due the more complex combined effects of pressure forces acting on both the DE side and the NDE side of the impeller. However, if plotting the axial deformation against the maximum pressure on the imported DE and NDE profiles, it can be observed that the deformation generally corresponds to the maximum DE pressure, see Figure 9-13. At this time step the maximum pressure on the DE is higher than that on the NDE.

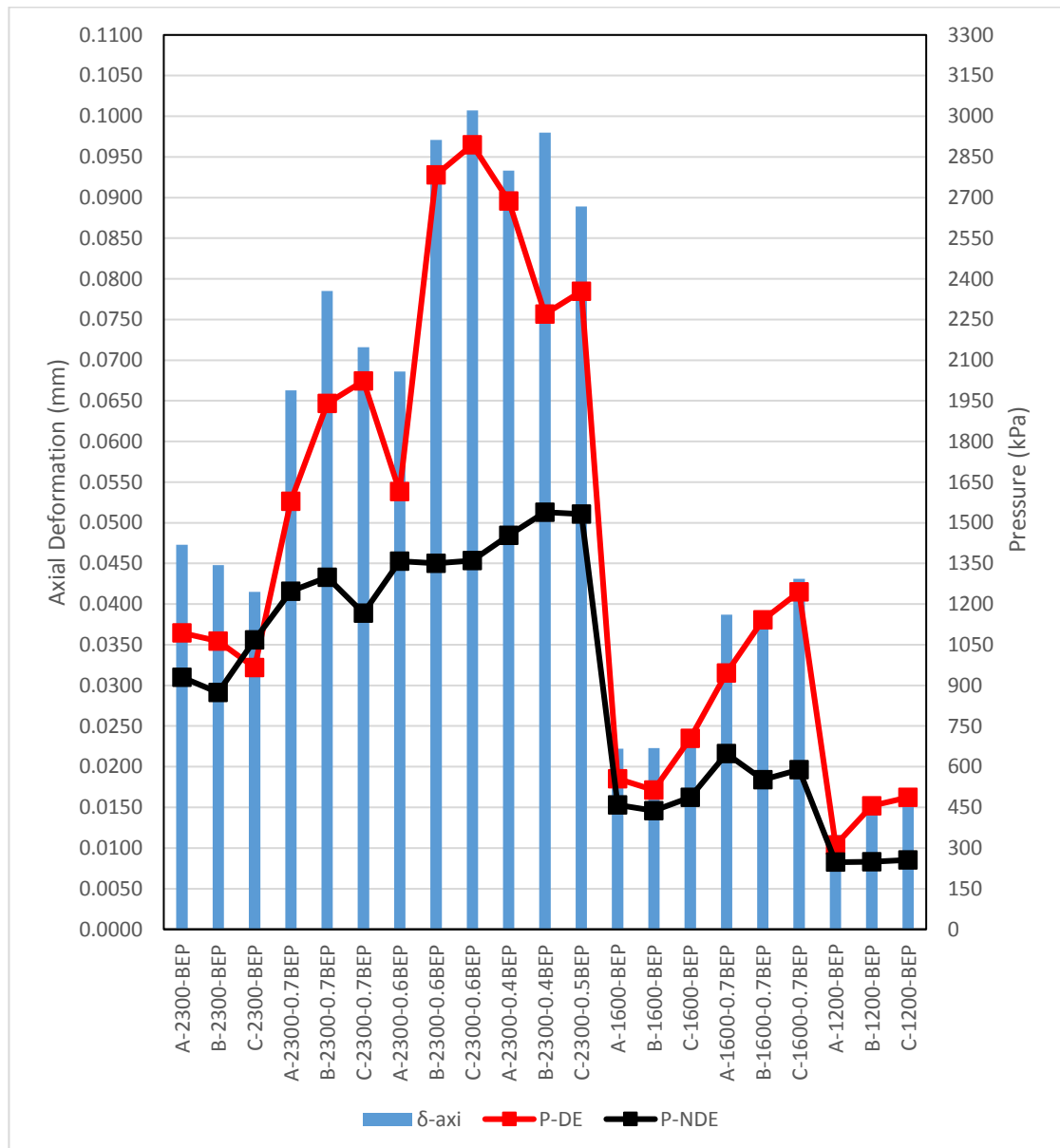


**Figure 9-13: Relationship between axial deformation and imported DE and NDE pressure profiles.**

The maximum total axial deformation is located on the DE of the impeller for all the pumps as illustrated in Figure 9-14. The maximum displacement occurs along the blade edge tip right

before it meets the port plate, corresponding to higher local pressure regions on the radial and DE pressure profiles. The impeller is under compression in both the DE and NDE due to the pressure forces acting in those directions. The maximum displacement in the radial direction also occurs at the tip of the impeller blade and corresponds to pressure distribution of the imported radial profile.

On average, impeller A has the highest radial deformation while impeller C has the highest axial deformation. It should however be noted that at certain points the difference in radial deformation between the impellers is very small. Pump C has the smallest impeller in both width and diameter compared to the other two impellers, however the difference between them is more notable for the width. The difference between impellers is minimal and the deformation values are even smaller in relation to the size of each impeller, however the difference is still noteworthy in relation to the axial and radial clearance sizes. A smaller impeller is expected to deflect more due to less stiffness to withstand the forces acting on it, particularly along the blade edges. The thickness of the blades is due to a combination of the casting and machining tolerance, should the blades themselves be thinner they will deflect significantly more. As seen in Figure 9-13, impeller C generally has the highest maximum pressure acting on it from the DE side. This could be due to the sudden increase in area as the height of the side channel increases significantly at this point. The increase in area will be even more noticeable for pump C as its DE clearance is approximately 25% and 16% smaller than that of pump A and B, respectively.

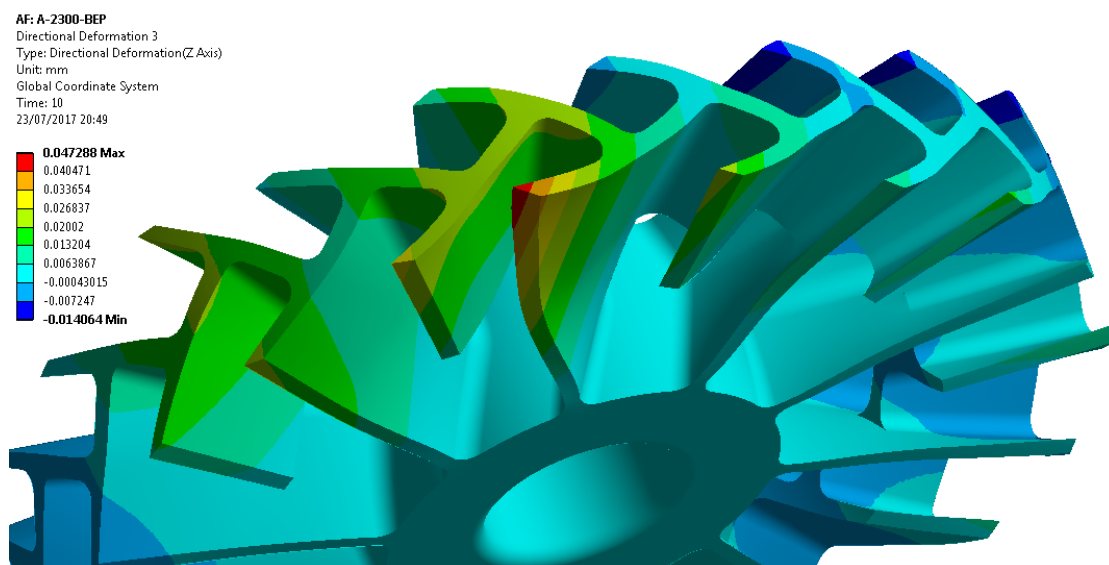


**Figure 9-14: Axial deformation in impeller A at BEP at 2300 rpm.**

Figure 9-15 shows the distribution of the total impeller deformation for the three impellers at BEP and 0.7BEP at 2300 rpm, viewed from the DE. The pattern clearly correlates to the pressure profiles shown in Figure 9-5 as well as showing signs of centrifugal force acting radially outwards, increasing the diameter of the impeller. The majority of the impeller is compressed inwards in the axial direction, also visible in Figure 9-14, essentially decreasing the width of the impeller during operation. The maximum deformation is visible in the second quadrant of the impeller (viewed from DE), in line with the pressure distribution. The deformation then decreases with the rotational direction before it increases again at the end of the first quadrant. The deformation distribution is quite similar for most of the cases, however in almost every case the impeller with the highest total deformation value has the largest overall region of zero deformation (corresponding to the dark blue colour), most prominent in quadrant three and four. This is clearly illustrated in Figure 9-15 at the BEP; impeller A has the largest total deformation value, but impeller C has the smallest overall region of zero deformation.

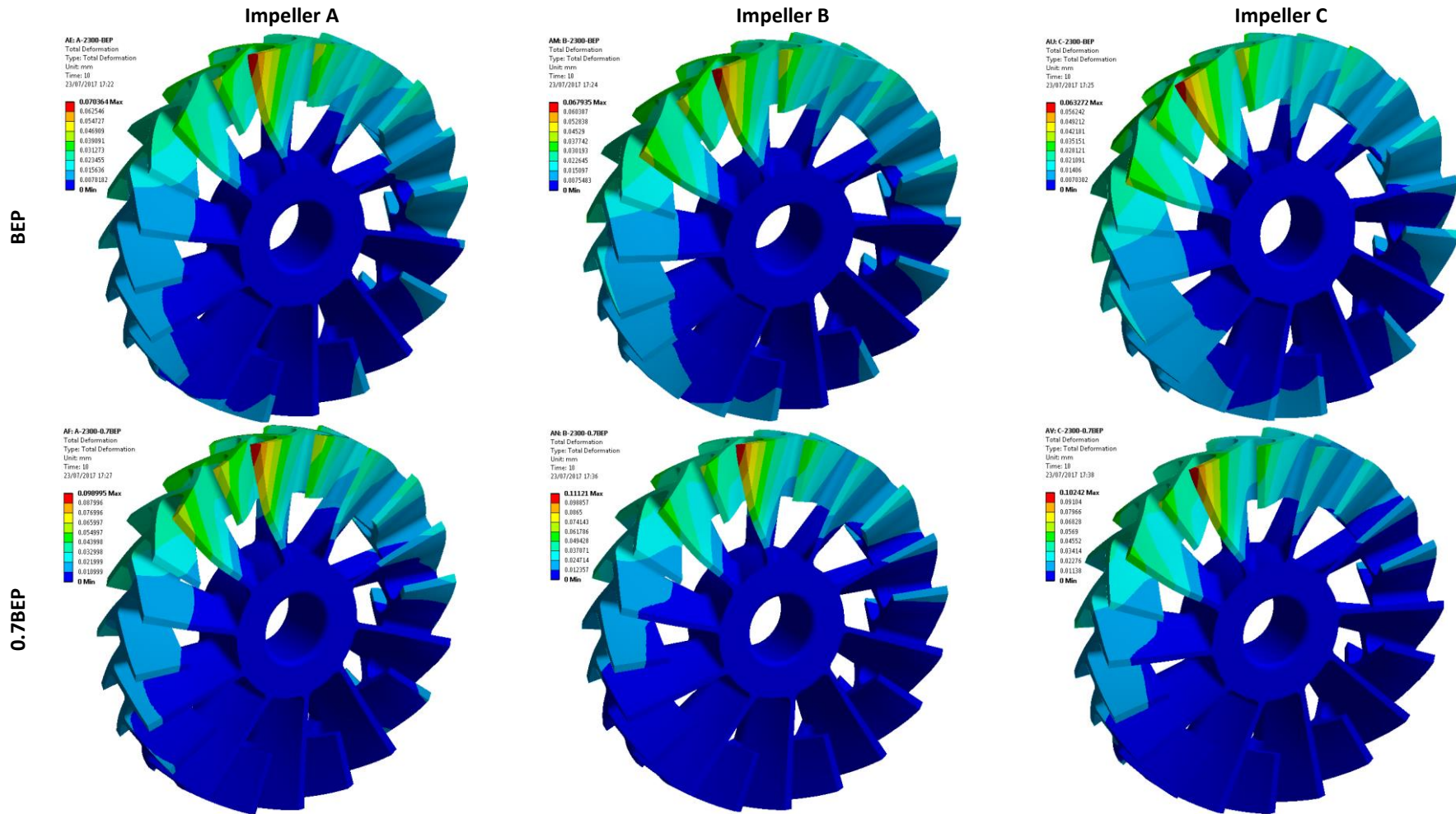
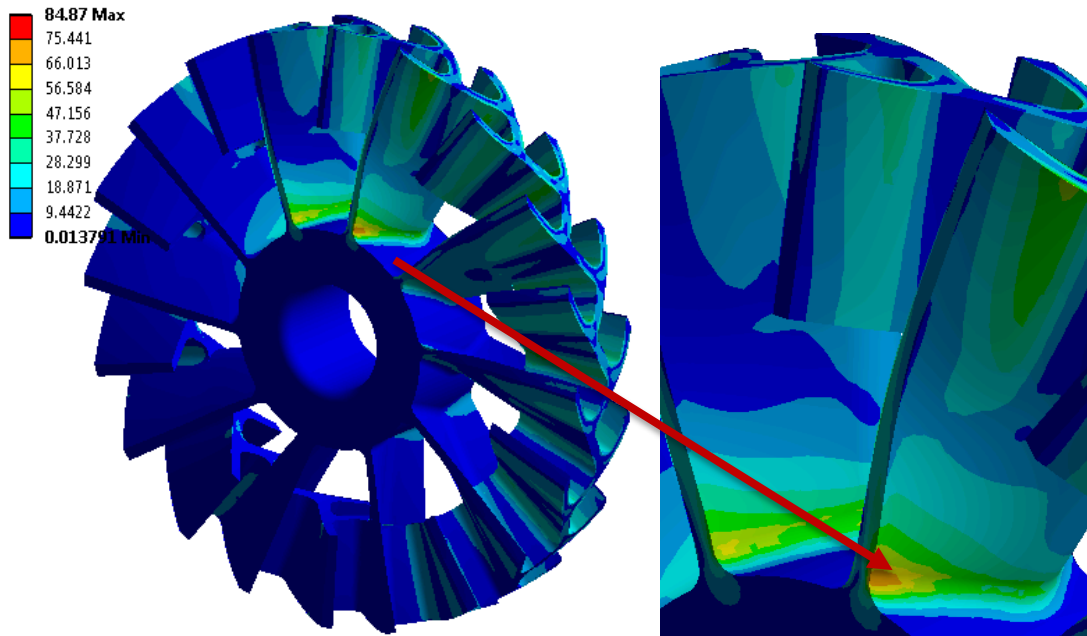
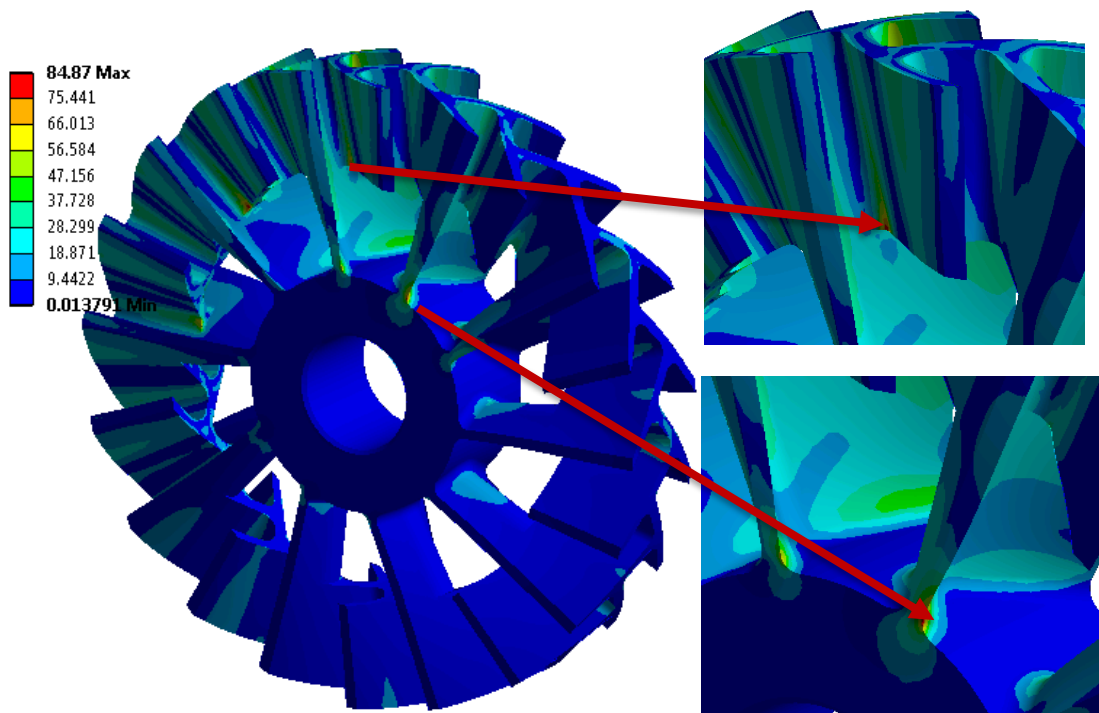


Figure 9-15: Total impeller deflection at maximum pressure point at 2300 rpm for BEP and 0.7BEP.

Areas of stress concentration can be observed in the contact points between the root of the full blades and the impeller hub, and where the half blades meet the full blades, see Figure 9-16 and Figure 9-17. The areas correspond to the higher pressure regions, indicating potential fatigue points, which are quantitatively shown to increase with decreasing flow rate.



*Figure 9-16: Stress concentration on DE of impeller A at 0.7BEP at 2300 rpm.*



*Figure 9-17: Stress concentration on NDE of impeller A at 0.7BEP at 2300 rpm.*

Although not the main focus of this study, attention in future designs should be given to the root of the blades as shown above. Internal Gilkes teardown reports indicate that these areas are particularly subjected to operational wear, as well as the inlet and outlet edges of the blades, which will negatively affect the life span of the components and the pump performance. This could subsequently decrease the losses in tolerance due to higher deflection.

### 9.3.2 Comparison of Impeller Deformation and Manufacturing Tolerances

In Figure 9-18 and Figure 9-19, the impeller width and diameter after deformation is plotted against the minimum and maximum drawing manufacturing tolerances, respectively. A worst-case scenario is assumed, where the maximum axial compression deformation value is used to calculate the impeller width while the maximum radial outwards deflection value is used to estimate the impeller diameter.

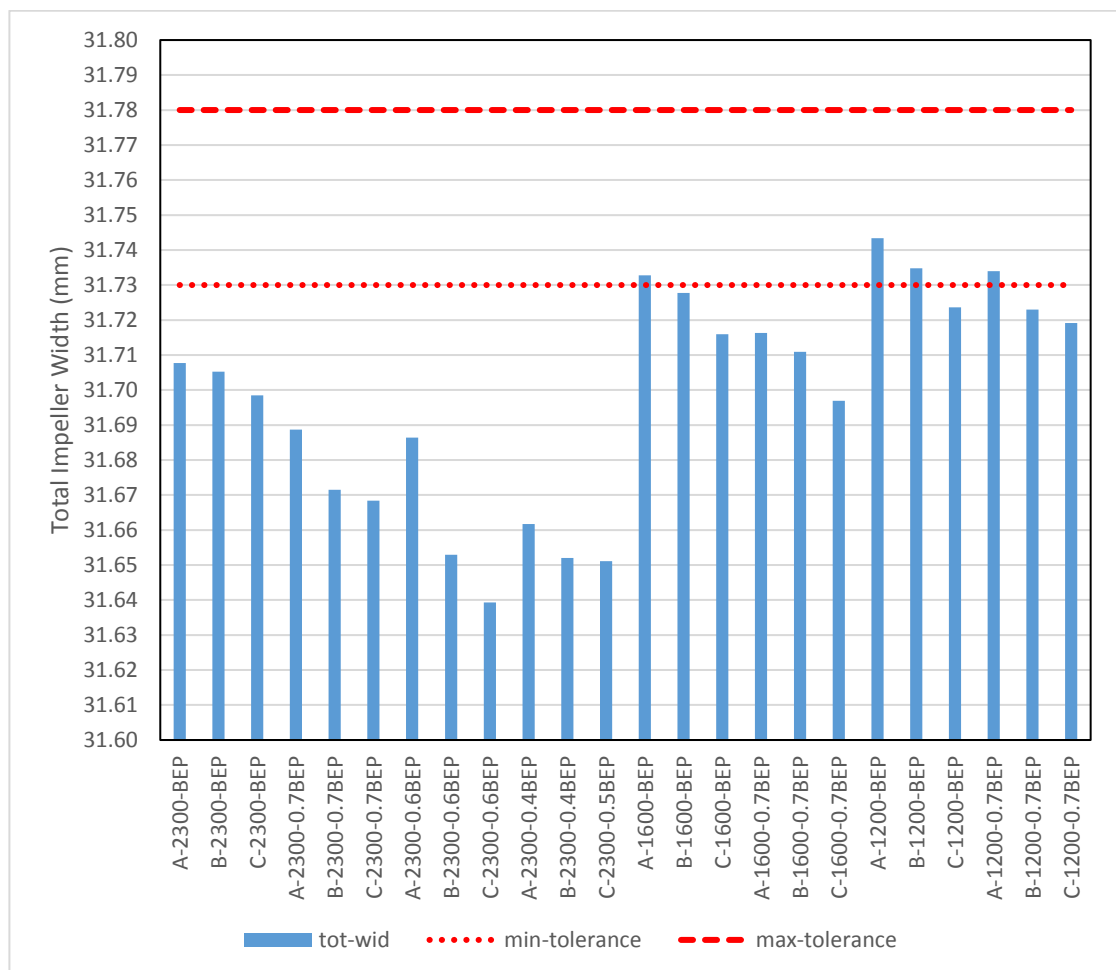


Figure 9-18: Impeller width after deformation against minimum and maximum manufacturing tolerances.



For most of the cases the “operational” impeller width is outside the manufacturing tolerance bandwidth, which should have a negative effect on the pump performance due to an increase in axial clearance.

Conversely, the “operational” impeller diameter for most of the cases is greater than the maximum impeller diameter achievable from the manufacturing tolerances, which should improve the performance of the pump due to a decrease in radial clearance. It could perhaps be that the decrease in impeller width is offset by the increase in impeller diameter, however the operational effects on the width of the impeller is more complex due the importance of original position of the impeller in relation to the DE and NDE.

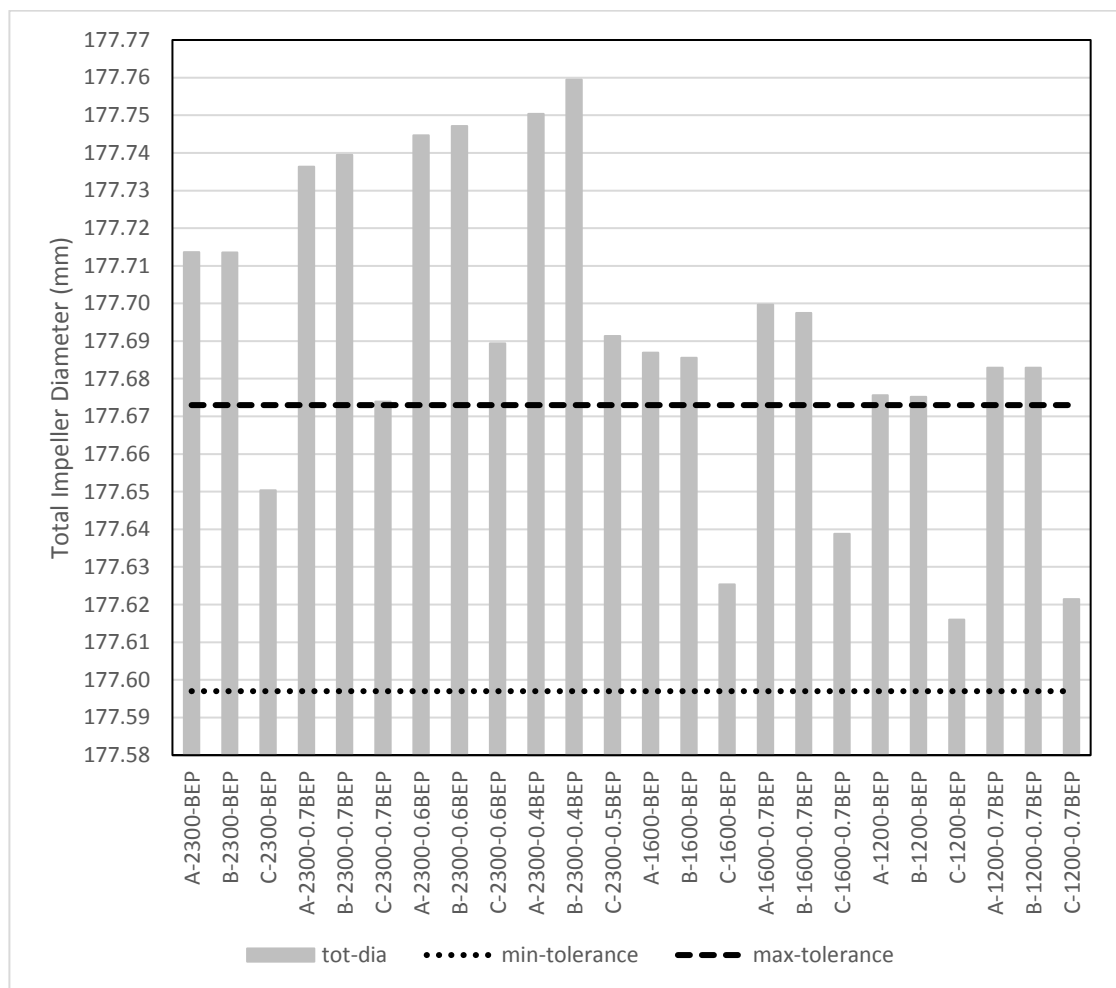


Figure 9-19: Impeller diameter after deflection against minimum and maximum manufacturing tolerances.

### 9.3.3 Comparison of Numerical Predictions and Experimental Measurements

The comparison of numerical predictions (CFD and FEA) and experimental measurements is focused on pumps A and B due to similar flow rates and the relatively good agreement between experimental and computational results at 0.7BEP, 0.6BEP and 0.4BEP at 2300 rpm. In addition, 0.7BEP at 1600 and 1200 rpm are also included. The diameter of impellers A and B are identical; however, the width of impeller A is slightly larger than that of impeller B. The impeller width and diameter after deformation are plotted against the generated experimental and computational differential pressure in Figure 9-20 and Figure 9-21.



**Figure 9-20: Comparison of total operational impeller width against computational and experimental differential pressure.**

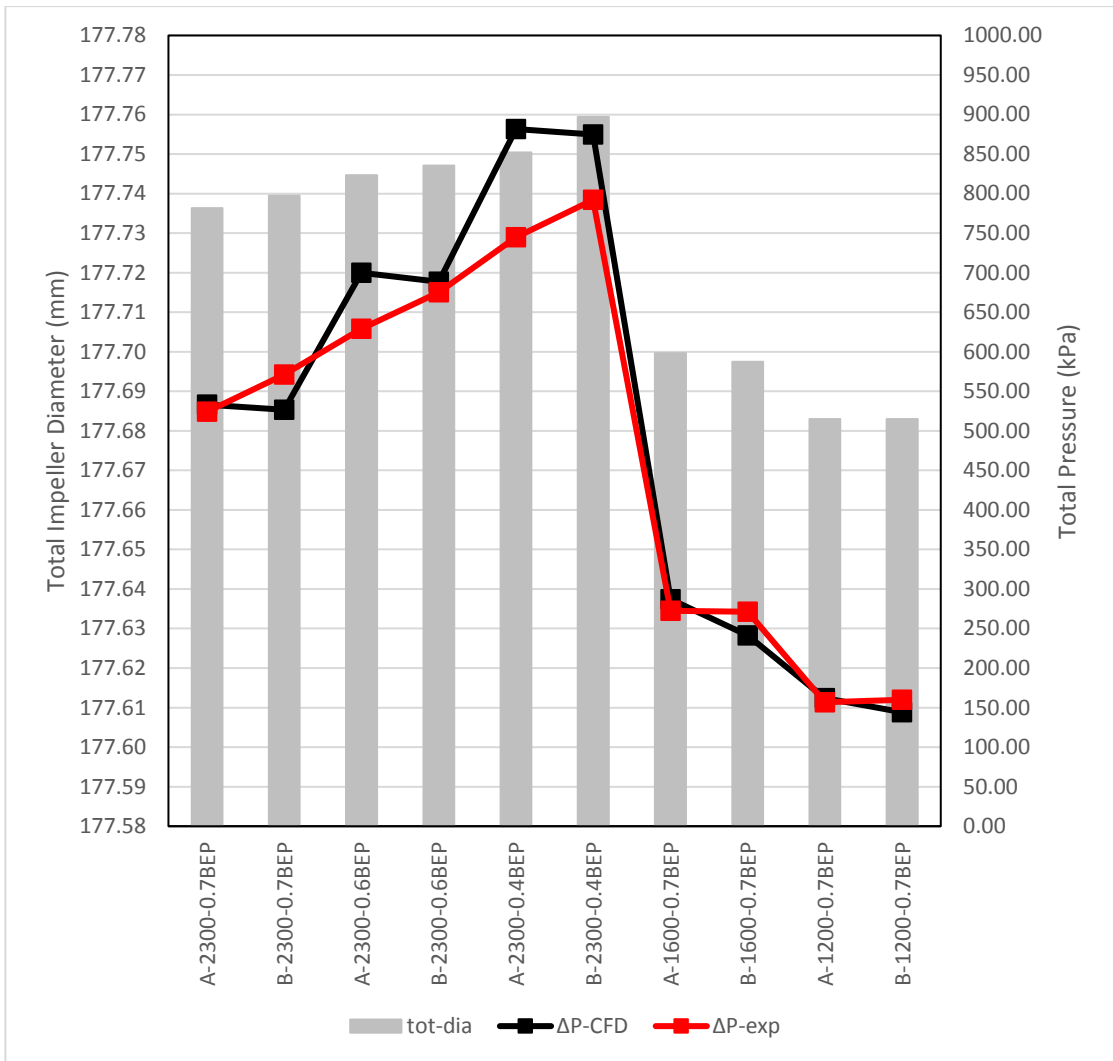


**Figure 9-21: Comparison of total operational impeller diameter against computational and experimental differential pressure.**

In almost all the cases, impeller B has a larger deformation in both axial and radial directions. The deformation is a function of the geometry and because impeller B has a smaller width it is likely that the deformation should be larger. The larger radial deformation observed in impeller B is most likely due to a combination of its smaller width and radial clearance as well as the radial pressure which is a function of the clearance dimension. Experimentally, pumps B and C produced very similar pressure heads despite the relatively large difference in DE and NDE clearance sizes, however the difference in radial clearance is almost negligible. Pump A on the other hand has a larger radial clearance in comparison. Combined with the fact that pump B has a smaller manufactured radial clearance and a larger deflection of the impeller in the radial direction, this provides pump B with an even smaller operational radial clearance. This could very well be the reason for a higher experimental pressure head when compared

to pump A. At 1600 and 1200 rpm the differences in impeller deformation and correlation between computational and measured pressure heads are very small.

Although pump A and B have relatively similar DE and NDE clearance values, the larger radial clearance of A combined with a larger DE clearance than pump C, results in pump A categorically producing a lower experimental pressure head than the other two pumps. The performance is the result of a combination of the axial and radial clearance tolerances, but it is clear that the radial clearance has the largest effect. These findings suggest that the radial design clearance should be no larger than 0.25 mm, corresponding to the pump B design tolerance. With this radial design tolerance, it appears that the DE and NDE clearances have a lower impact on the performance. However, the size of the DE clearance for pump A is 0.344 mm, which is very close to the maximum assembly tolerance of 0.35 mm (the axial alignment of the impeller in relation to the casing). This suggests that as well as a lower maximum radial tolerance, the maximum assembly tolerance should be less than 0.30 mm.

Based on these results one could therefore conclude that the pressure head performance of the pump is more sensitive to variations in radial clearance than axial clearances. This reiterates the results in *5 Parametric Clearance Analysis* showing that the radial clearance has a significant effect on both the pump efficiency and generated pressure. This further supports that the radial clearance is the primary driver for the total pressure head as concluded in *7.3 Performance Effects due to Axial and Radial Clearance Pressure*. More importantly, the dynamic conditions documented by the FEA study explain some of the disparity between the predicted and measured performance. These dynamic conditions are not captured by the computational model. In particular, the conditions could help explain the difference in trend as pump A performs better computationally than pump B at 2300 rpm while the trend is reversed experimentally.

#### **9.4 Summary and Conclusions**

The FEA study provides an indication of the deformation behaviour of the test pumps and areas of stress concentration. The maximum total deformation and maximum equivalent stress in the impeller are greatly influenced by the flow rate and the rotational speed. Their values increase with decreasing flow rate and increasing pressure. The total deformation of the impeller is greater near the edge of the blade, near its tip, where the maximum value can

be found. The stress on the other hand is more prominent near the root of the blades, where the maximum value is observed. The deformation in the blades decreases from the leading to the trailing edge in a circular fashion. Similarly, the deformation increases radially outwards from the hub to the tip of the impeller blades.

Assuming a worst-case scenario of deformation, the operational impeller width and diameter dimensions are shown to be outside the manufacturing tolerance bandwidths for most of the cases analysed. This could affect the performance negatively due to an increase in axial clearance, however the decrease in radial clearance could potentially offset this. The dynamic conditions documented by the FEA study explain some of the disparity between the predicted and measured performance. These dynamic conditions are not captured by the computational model. In particular, the conditions could help explain the difference in trend as pump A performs better computationally than pump B at 2300 rpm while the trend is reversed experimentally.

However, it is important to highlight the limitations of these simulations and to appreciate the uncertainties this causes. Impeller deformation can take place due to shrink-fit deformation as well as centrifugal force and impeller pressure loading. During operation, the shaft can expand due to friction heat, which in turn can cause impeller growth in the radial direction. This has however not been analysed in this study. In addition, the dynamic characteristic of the bearings during pump operation has not been considered either. Furthermore, the pressure loads from only one specific time step were analysed. Other time steps, particularly at minimum pressure, and further operational points should be investigated. In addition, a coupled analysis, i.e. full FSI, will paint a clearer picture of interaction between structural, thermal and hydraulic loads. The results should be verified with experimental testing measuring the strains on the impeller. The FEA results have nonetheless offered valuable insight into the operational behaviour of the pumps and the significance that the deformation behaviour has on clearances.

## 10 Conclusions and Recommendations

The overall aim of this industry funded research was to better understand the effects of manufacturing tolerances on critical components, and subsequently variations in impeller-casing clearance sizes on the performance of a Gilkes RLR pump, more specifically the 2.5" SX design. This was carried out using the modern Computational Fluid Dynamics (CFD) code ANSYS® CFX® coupled with ANSYS® Mechanical® for Finite Element Analysis (FEA) and experimental testing.

The design of the regenerative machine has evolved over many decades and improvements have been made in the design. However, very few published works are available that investigate other design aspects such as radial and axial clearances, and more crucially most researchers tend to investigate these elements in isolation. Furthermore, the studies feature relatively simple geometries with radial blades. The chevron shaped impeller in the Gilkes design has a complex geometry and a larger wetted surface in the peripheral circumference. The novel scope of this research has been to systematically investigate the effects on pump performance over a large range of impeller-casing clearance combinations and the significance that the dynamic operational behaviour may have on the clearances.

### 10.1 Conclusions

The parametric impeller-casing clearance study covered a wide range of axial and radial clearances, derived from the minimum, median and maximum values of the manufacturing tolerances of the drawings for the impeller, the casing on the drive end (DE) side, the casing on the non-drive end (NDE) side and the drive shaft. The different clearance combinations resulted in 27 models which were simulated at the duty point. The results showed that the radial clearance has a significant effect on both the pump efficiency and generated pressure indicating that there could be a potential variation in pressure head performance by as much as 25% for a newly built pump.

The study also highlighted the need to test a number of pumps with a representative range of manufacturing tolerances. This resulted in three 2.5" SX test pumps being measured to determine their exact manufacturing tolerances and clearance magnitudes, and then tested to evaluate their performance. Based on the results of the experimental testing it appears that

a pump with a larger NDE clearance and smaller DE clearance (i.e. pump C) gives the highest best efficiency point for the three different speeds tested. The radial clearance of pump A is 0.01 mm larger than that of pump C and 0.015 mm larger than that of pump B, so the difference between pump B and C is very small. The difference in DE and NDE clearances are however more significant (refer to Table 6-1), leading one to conclude that the radial clearance ultimately has a greater effect on the pump performance.

Due to the high sensitivity of the clearance magnitude under impeller deformation and the inability of the CFD model to simulate the flow in the deformable clearances, an FEA using a one-way Fluid-Structure Interaction (FSI) approach was carried out to illuminate the operational behaviour of the pumps and the effects on the clearances under deforming conditions. Firstly, the FSI showed that the maximum total deformation and maximum equivalent stress in the impeller are greatly influenced by the flow rate and the rotational speed. Their values increased with decreasing flow rate and increasing pressure. In addition, the total deformation of the impeller was observed to be greater near the edge of the blade, near its tip, where the maximum value can be found. The deformation in the blades decreased from the leading to the trailing edge in a circular fashion as well as increasing radially outwards from the hub to the tip of the impeller blades.

Assessing the deformation against the computational and experimental pressure, the results of the FSI analysis indicate that the maximum allowable radial design clearance should be reduced by 35%. Furthermore, with this radial design tolerance the magnitudes of the DE and NDE clearances have a lower impact on the performance.

Based on the complicated nature of the 2.5" SX impeller geometry and relatively low efficiency, the author wonders how the design has developed over time as it cannot have emerged 'organically'. More likely it has been the result of several design changes over the years to meet the specific customer needs on a particular project, therefore in the first instance simplifications can be made to the impeller. Double-sided impellers, with a "web" between the blades, have been found to promote equal pressure distribution which is likely to decrease wear and undesired effects such as mechanical vibration and noise. During operation, there will be leakage through the stripper clearance due to the pressure differential between the suction and discharge ports. To avoid excessive backflow it is well known that the stripper clearance must be kept to a minimum. However, an "open" impeller such as the

one used in this study is likely to increase the backflow between the discharge (NDE) and suction (DE) sides. Therefore, the impeller should be redesigned to feature a web. Although chevron shaped impellers have been shown to provide improved performance compared with radial blades, the complexity of the design could indeed exacerbate the turbulence and reduce the efficiency.

Overall this research has determined the maximum manufacturing tolerances of a 2.5" SX pump to ensure a consistent pump performance, providing Gilkes with the tools to better tailor their designs to meet the needs of their customers. For example, one option could be to accept a less expensive pump knowing that performance could vary across the purchased orders. The second option would be a more expensive pump knowing to a higher degree of certainty the exact performance to be quoted. Furthermore, the research has for the first time investigated and shown how the deformation behaviour of the impeller during operation may affect the magnitude of the axial and radial clearances, highlighting an area for further study to better understand the exact flow mechanism of this kind of pump.

## **10.2 Recommendations for Future Work**

The regenerative pump is a very specialised fluid machinery design which has been applied to a range of industries and applications in one of its many forms. In order to fully understand the operational behaviour and be able to accurately model the highly complex and turbulent flow field within these pumps, it will be important in future to explore different numerical tools, such as more computationally complex turbulence models, to try to reduce the discrepancy between simulation and experimental results. Particularly, the academic community will benefit from advanced numerical modelling. Increased numerical capability will also benefit related industries through design improvements and abilities to make changes in an iterative fashion. In a competitive market there has been a renewed focus on enhancing pump efficiency and extending the lifespan through improved design based on manufacturers' concerns over pump lifetime reliability. It is clear from this research that the effects dynamic condition modelling have on the pump performance and lifetime reliability must be explored. Anticipated future work could combine the findings with a performance-cost analysis to better understand the life cycle of an RLR pump from manufacture to decommissioning and ensure optimum impeller-casing clearances from inception. Some of the work required to achieve these developments are discussed in this section.



### **10.2.1 Advanced Numerical Modelling**

As discussed in *8.2.5 Limitations of the CFD Model* there might be errors imposed by the choice of turbulence modelling. The pump experiences recirculation and the flow field is complex by nature; these types of flows are difficult to model correctly. The choice of turbulence model needs to be considered carefully and work is required to assess whether Reynolds-Averaged Navier-Stokes models, in which all the scales of the turbulence are modelled rather than solved, are capable of modelling this type of flow at all. Scale Resolving Simulation (SRS) options, such as Large Eddy Simulation, Scale Adaptive Simulation and Detached Eddy Simulation, need to be investigated. Despite the computationally expensive simulations which use up large quantities of data, these models can resolve the large energy-containing scales while also modelling the influence of the small scales. The SRS method is more accurate when it is important to resolve the large scales. However, it necessitates the use of a very fine mesh and small timesteps to capture the eddy formation.

Discretisation errors caused by the mesh are unpredictable but can be severe. This error can be quantified and reduced considerably by carrying out successive mesh refinement, using different types of meshes and searching for mesh-independent solutions. It is important to improve on existing mesh generation techniques to be able to capture the required level of detail to resolve the turbulent flows, particularly in the clearances often measuring less than 0.5 mm.

### **10.2.2 Experimental Investigation of Pressure Pulsation Phenomenon**

As discussed in *8.2.2 Critical Review of the Experimental Testing* the inherent, periodically unsteady, flow-induced impeller oscillations documented to be occurring in the regenerative pump are not captured by the static pressure transducers in the test rig. Therefore, future work is required to address this limitation. It is suggested to install piezoelectric dynamic pressure transducers that can measure frequencies up to 2 kHz and a DAQ system capable of digitalising the analogue signal with at least 4 kHz sampling frequency. These frequency values are required to capture the maximum blade passing frequency of 760 Hz at 2300 rpm. Furthermore, it would be highly beneficial to manufacture a purpose-built test pump with holes in the casing for measuring the pressure pulsations at different locations of the pump. This should then be compared against the computationally observed pressure characteristics.

In order to ensure statistical consistency and conform to best practice, a larger number of pumps should be tested. The measurements should be repeated three times for both increasing and decreasing flow rates to ensure repeatability.

### **10.2.3 Two-way Fluid-Structure Interaction**

The manufactured clearances between the impeller and the casing change during operation due to thermal deformation and pressure forces. The FEA using a one-way Fluid-Structure Interaction (FSI) approach provided an indication of the deformation behaviour of the test pumps and areas of stress concentration, however the effects these dynamic conditions have on the computational results should also be investigated. Therefore, a two-way FSI analysis should be performed to evaluate the effects of fluid and mechanical loads simultaneously, along with the coupled effects of one type of load upon the other.

The pump also has more surfaces that are not machined, it would therefore be interesting to combine a two-way FSI analysis with variations in surface roughness due to sandcasting and how this might influence the results. Equally a worn pump can be studied which may help validate the models. The parts can be 3D scanned and analysed computationally. Furthermore, it would also be interesting to investigate the effects of manufacturing tolerance on the structural integrity (i.e. one impeller blade is slightly larger due to manufacturing tolerances). In the current study the tolerances are assumed uniform.

One aspect which could be explored further could be to analyse the effects of oscillation on the structure under dynamic loading and combine this with modal analysis to assess the effects of the structure's resonant frequencies. In modal analysis the overall mass and stiffness of a structure are used to determine the points at which it will naturally resonate, which can be destructive to its integrity. Dynamic analysis can then be used to investigate the deformation of the impeller at its critical natural frequencies.

### **10.2.4 Further Experimental Testing of Clearances**

The test pumps all feature median axial envelope (drive end and non-drive end combined) and radial clearance values. Although this indicates that pumps are manufactured to median tolerance values it does not provide a wide range of values and as a result it has not been possible to experimentally investigate the extreme ends of the manufacturing tolerances. This

is particularly important to fully understand the effects of tighter design tolerances on the drive end (DE) side, which were not captured sufficiently by the computational model. It is also recommended to test a larger number of pumps, with a representative range of clearances, to establish a statistical trend for the true manufacturing tolerances. This will also paint a clearer picture of the operational behaviour of the clearances.

#### **10.2.5 Priming Behaviour**

A study on priming behaviour and suction performance in relation to clearances, particularly the DE clearance should be carried out. This necessitates the use of multiphase flow instead of single phase for computational analysis, which will require increased computational resources, particularly for a fluid domain size where the whole region has to be modelled. For multiphase simulations a much finer, structured mesh will be required to obtain the necessary quality for accurate results.

#### **10.2.6 Cavitation Erosion**

When the local static pressure in the flow stream drops below its vapour pressure, vapour filled cavities are created. When these bubbles implode close to solid surfaces they can damage the internal components. Gilkes teardown reports show evidence of cavitation erosion on the impeller; a distinct pattern of the damage is visible on both the DE and NDE of the impeller. It is not known if the engine cooling water is contaminated or if the damage is due to internal debris passing through the system. The effects of the cavitation erosion can be analysed computationally by either 3D scanning the damaged impellers or replicating the pattern in the CAD geometry.

Computational cavitation modelling should be coupled with experimental Net Performance Suction Head (NPSH) and durability testing as well as flow visualisation. Without having any controlled 'damage' tests it will be very difficult to determine causes of failure in a way that can be compared with computational modelling. Experimental validation is also imperative to certify that a working tool is available for computational cavitation detection in a regenerative pump, particularly as studies in the public domain focus on centrifugal pumps.

### **10.2.7 Manufacturing Methods**

The manufacture of the RLR pump can be improved to reduce the cost of construction, improve the precision of the design components and the finishing of the clearance contact surfaces. The current manufacturing methods of the casing introduce uncertainties, particularly in the volume of the side channels. Therefore, 3D scanning of the side channel volumes of a range of test pumps should be carried out to determine the effects these have on the performance of the pump. This can then be complemented with a computational study. The results can provide recommendations on casting methods where perhaps tighter tolerances should be demanded.

In addition, a performance-cost analysis should be carried out. Larger clearances are likely to reduce the rate of internal wear and increase the operational life of the pump. In contrast, tighter clearances provide improved performance at the cost of an increased rate of wear, as well as an increase in cost due to higher manufacturing specification. Further investigation into optimum machining tolerances on critical components should be carried out. In order to achieve operational excellence, the current maximum tolerances are too high. For priming pumps a larger manufacturing tolerance allowance can be applied, although the suction performance might be compromised.

The use of new materials can be investigated with the aim to reduce the cost of manufacturing and improve pump performance. New alloys or surface coatings can be applied to reduce the surface friction and erosion wear, which can prolong the lifetime of the impeller when subjected to contaminated pumping fluid. Surface roughness studies of different materials can also be carried out.

### **10.2.8 Reliability**

Despite efforts by various researchers throughout the last 60 years, the efficiency of RLR pumps still remains low. Due to the inherent fluid mechanics of this kind of pump it is possible that the maximum efficiency might be physically limited to values in the region of 50% and that future developments should therefore focus on improving other desirable aspects of the pump, such as reliability and self-priming. Product warranty is not only beneficial for increased customer satisfaction and reduced total cost of ownership, it also plays a crucial role in the current economic and environmental climate. For different applications, it becomes important

to identify parameters that affect component wear and consequently performance as these will directly affect how the energy consumption will change over time, with the added benefit of improving pump reliability.

Ensuring that proper maintenance of existing pumps is carried out can also make substantial energy savings. Replacing worn pump parts will reduce internal leakage and maintain pump performance. An added benefit of this is the reduction of the life cycle impact on the environment by refurbishing rather than replacing the whole pump. A recognised wear limit should be established to determine when losses due to worn parts make pumps less economic and warrant replacement of components. This could be achieved by analysing worn pumps against key performance parameters and cataloguing the wear rate of their parts.

## References

- Abdallah, H., 1981. *A theoretical and experimental investigation of the regenerative pump with aerofoil blades*, UK: Royal Military College of Science.
- Adams, T., Grant, C. & Watson, H., 2012. A simple algorithm to relate measured surface roughness to equivalent sand-grain roughness. *Journal ISSN: 2929-2724*, 1(1), pp. 66-71.
- Addison, H., 1954. *A Treatise on Applied Hydraulics*. 4th ed. London: Chapman and Hall.
- Aggidis, G., 2002. *Regenerative liquid ring pumps experimental modelling and flow visualisation*, Kendal, UK: Gilbert Gilkes & Gordon Ltd.
- Andrew, D., 1990. The calculation of flow in regenerative turbomachines by a streamline curvature method. *Proceedings of the Institution of Mechanical Engineers, Part A: Journal of Power and Energy*, 204(2), pp. 121-129.
- ANSYS, Inc., 2013. *ANSYS CFX Introduction, Release 15.0*, Canonsburg, PA, USA: s.n.
- ANSYS, Inc., 2013. *ANSYS CFX-Solver Modeling Guide*, Canonsburgh, PA, USA: s.n.
- ANSYS, Inc., 2013. *ANSYS CFX-Solver Theory Guide*, Canonsburgh, PA, USA: s.n.
- Badami, M., 1997. Theoretical and experimental analysis of traditional and new periphery pumps. *SAE Technical Paper No 971074*.
- Badami, M. & Mura, M., 2012. Comparison between 3D and 1D simulations of a regenerative blower for fuel cell application. *Energy Convers Manage*, Volume 55, pp. 93-100.
- Bartels, J., 1947. *Performance of a peripheral pump*, New York, USA: Polytechnic Institute of Brooklyn.
- Batchelor, G. K., 2012. *An Introduction to Fluid Dynamics*. s.l.:Cambridge University Press.
- Bicard, R., 1957. *Investigation of the inlet design of the regenerative pump*, Cambridge, Massachusetts: Massachusetts Institute of Technology.
- Biheller, H., 1976. Special Variants of Dynamic Pumps. In: I. Karassik, W. Krutzsch, W. Fraser & J. Messina, eds. *Pump Handbook*. USA: McGraw-Hill, pp. 2.202-2.203.
- Böhle, M., Fleder, A. & Mohr, M., 2016. *Study of losses in fluid machinery with the help of entropy*. Honolulu, Hawaii, ISROMAC.
- Böhle, M. & Müller, T., 2009. *Evaluation of the flow inside a side channel pump by the application of an analytical model and CFD*. Colorado, USA, American Society of Mechanical Engineers, pp. 11-18.
- British Standards Institution, 2012. *BS EN ISO 9906:2012. Rotodynamic pumps - Hydraulic performance acceptance tests - Grades 1, 2 and 3*, s.l.: BSI Standards Limited.
- Burton, D., 1962. *Review of regenerative compressor theory*. Tennessee, Oak Ridge National Laboratory, pp. 228-242.
- Burton, J., 1966. *A Theoretical and Experimental Analysis of the Flow in Regenerative Pumps and Turbines*, Southampton, UK: University of Southampton.

- Burton, J., 1967. *The prediction and improvement of regenerative turbo-machine performance*. Cranfield, BHRA .
- Burton, J., 1972. *The prediction and improvment of regenerative turbo-machine performance*. s.l., BHRA.
- Choi, W., Yoo, I., Park, M. & Chung, M., 2013. Experimental study on the effect of blade angle on regenerative pump performance. *Proc. IMechE, Part A: J Power Energy*, 227(5), pp. 585-592.
- Cone, J., 1980. "Pump energy conservation techniques. Texas A & M University, Proc. 9th Turbomachinery Symposium, pp. 83-101.
- Cooper, P., 2001. *Sealless integral-motor pump with regenerative impeller disk*. USA, Patent No. 628015728.
- Crewdson, E., 1956. Water-ring self-priming pumps. *Proceedings of the Institution of Mechanical Engineers*, 170(1), pp. 407-425.
- Dewitt, D., 1957. *Rational design and development of the regenerative pump*, s.l.: Massachusetts Institute of Technology.
- El Hag, A., 1979. *A theoretical analysis of the flow in regenerative pumps*, UK: University of Bath.
- Engeda, A., 2003. *Flow analysis and design suggestions for regenerative flow pumps (Keynote)*. Hawaii, USA, Proceedings of the American Society of Mechanical Engineers, pp. 1847-1858.
- Engels, H., 1940. *Investigations of Ring pumps*, Germany: Tech Hoch Hannover.
- European Commission, 2001. *Study on improving the energy efficiency of pumps February 2001*, The Netherlands: JRC Institute for Energy and Transport.
- Fleder, A. & Böhle, M., 2012. *Numerical and experimental investigation of the influence of the blade shape of industrial side channel pumps*. In: *Proceedings of the international rotating equipment conference*. Dusseldorf, Germany, 27-28 September 2012, Pumps & System Association.
- Fleder, A. & Böhle, M., 2015. A systematical study of the influence of blade length, blade width and side channel height on the performance of a side channel pump. *Journal of Fluids Engineering*, 137(12), p. 121102.
- Grabow, G., 1975. *Influence of the number of vanes and vane angle on the suction behaviour of regenerative pumps*. In: , Budapest, Hungary, 14-20 September 1975: pp. 351-364.. Budapest, Hungary, s.n., pp. 351-364.
- Gülich, J. F., 2010. *Centrifugal pumps*. 2nd ed. Berlin: Springer.
- Hollenberg, J. & Potter, J., 1979. An Investigation of Regenerative Blowers and Pumps. *ASME J. Eng. Ind. Trans*, 101(2), pp. 147-152.
- Horiguchi, H. et al., 2009. Study for the Increase of Micro Regenerative Pump Had. *International Journal of Fluid Machinery and Systems*, 2(3), pp. 189-195.
- Hübel, M., Blättel, B. & Strohl, W., 1995. Investigation on Fluid Mechanics of the Regenerative Pump Used in Gasoline Injection Systems. *SAE Technical Paper 950077*, pp. 131-139.

- Imray, J., 1874. *The Helical Pump*. Cardiff, Martin Billing, Son & Co, pp. 289-296.
- International Electrotechnical Commission, 1999. *IEC 60193:1999. Hydraulic turbines, storage pumps and pump-turbines - Model acceptance tests*, Switzerland: Empresas Publicas de Medellin.
- Iversen, H., 1955. Performance of the periphery pump. *Trans ASME*, Volume 77, pp. 19-28.
- Kang, S., Lim, H. & Ryu, S., 2004. *Performance evaluation of a regenerative pump of small size*. Charlotte, North Carolina, USA, Proceedings of HT-FED04, pp. 1171-1178.
- Karenth, V. & Sharma, N., 2014. *CFD Analysis of a Regenerative Pump for Performance Enhancement*. Kathmandu, Nepal, s.n.
- Karlsen-Davies, N. & Aggidis, G., 2016a. Regenerative liquid ring pumps review and advances on design and performance. *Applied Energy*, Volume 164, pp. 815-825.
- Karlsen-Davies, N. & Aggidis, G., 2016b. *Computational analysis of the effects of manufacturing tolerances on the performance of a regenerative liquid ring (RLR) pump*. In: *Proceedings of the 13th European Fluid Machinery Congress*. The Hague, The Netherlands 3-4 October 2016, Institution of Mechanical Engineers, pp. 47-57.
- Karlsen, N. & Aggidis, G., 2014. *Review and state of the art of regenerate liquid ring pumps*. In: *Proceedings of the the 12th European Fluid Machinery Congress 6-7 October 2014*. Edinburgh, UK 6-7 October 2014, Woodhead Publishing, pp. 125-134.
- Kidger, J., Cumming, R. & Gibbons, J., 1995. *Pumps*. USA, Patent No. U.S. Patent 5,435,692.
- Krutzsch, W. C. & Cooper, P., 1986. *Introduction: classification and selection of pumps*. s.l.:Pump Handbook.
- Kusagaya, K. et al., 2004. *Impeller and turbine type fuel pump*. USA, Patent No. U.S. Patent 6767179.
- Lazarkiewicz, S. & Troskolanski, A., 1965. Self-Priming Pumps. In: *Impeller Pumps*. Warsawa: Pergamon Press Ltd., pp. 567-590.
- Lazo, L. & Hopkins, T., 1953. *Theoretical and experimental analysis of a regenerative turbine pump*, USA: Massachusetts Institute of Technology.
- Lutz, G., 1953. *Experimental investigation of the pressure distribution in a regenerative turbine pump*, USA: Massachusetts Institute of Technology.
- Lytron, 2015. *Maintaining your Regenerative Turbine Pump*. [Online] Available at: <http://www.lytron.com/Tools-and-Technical-Reference/Application-Notes/Regenerative-Turbine-Pumps> [Accessed 14 Aug 2015].
- Lytron, 2015. *Regenerative Turbine Pumps*. [Online] Available at: <http://www.lytron.com/Tools-and-Technical-Reference/Application-Notes/Regenerative-Turbine-Pumps> [Accessed 7 Aug 2015].
- Marty, T., 2012. Side Channel Sealless Magentic Drive Pumps. *Pumps & Systems*, November, pp. 2-4.



- Mason, S., 1957. *Influence of internal geometry upon regenerative pump performance*, Cambridge, Massachusetts, USA: Massachusetts Institute of Technology.
- Meakhal, T. & Park, S., 2005. An improved theory for regenerative pump performance. *Proc. IMechE, Part A: J Power Energy*, 219(3), pp. 213-222.
- Menter, F. R., Kuntz, M. & Langtry, R., 2003. Ten years of industrial experience with the SST turbulence model. *Turbulence, heat and mass transfer*, 4(1), pp. 625-632.
- MEPCO, 2014. *Regenerative Turbines*. [Online] Available at: <http://www.mepcollc.com/products.html> [Accessed 5 Jul 2015].
- Molloy, E., ed., 1953. *Modern pumps: A comprehensive survey of modern pumping equipment and practice*. s.l.:Newnes.
- Moss, N. & Czarnowski, R., 1996. *Extended range regenerative pump with modified impeller and/or housing*. USA, Patent No. U.S. Patent 5,527,149.
- MTH Pumps, 2014. *Regenerative Turbine Principles*. [Online] Available at: <http://www.mthpumps.com/turbine.html> [Accessed 14 March 2014].
- Mueller, S., 2004. Consider regenerative pumps for low-flow/low-NPSH applications. *Hydrocarbon Processing*, August, pp. 55-57.
- Mulley, R., 2004. *Flow of Industrial Fluids - Theory and Equations*. USA: CRC Press.
- NASA, 2008. *Uncertainty and Error in CFD Simulations*. [Online] Available at: <https://www.grc.nasa.gov/www/wind/valid/tutorial/errors.html> [Accessed 9 August 2017].
- Nesbitt, B., 2006. *Handbook of Pumps and Pumping: Pumping Manual International*. Oxford: Elsevier and Rolls & Associates.
- Oeirich, J., 1953. *Development of an analysis of a regenerative pump*, Cambridge, Massachusetts: Massachusetts Institute of Technology.
- Papantonis, D., 2009. *Hydrodynamic machines, hydrodynamic transmissions (in Greek)*. Athens, Symeon Publications.
- Parker, D. B., 1994. *Positive displacement pumps-performance and application*. Turbomachinery Laboratories, Department of Mechanical Engineering, Texas A&M University, In Proceedings of the 11th International Pump Users Symposium.
- Pfaff, H., 1961. Comparative investigations on side channel pumps with and without inducer. *Transl. from: Production Engineering Research Association*.
- Quail, F., Scanlon, T. & Baumgartner, A., 2012. Design study of a regenerative pump using one-dimensional and three-dimensional numerical techniques. *Eur J of Mech B/Fluids*, Volume 31, pp. 181-187.
- Quail, F., Scanlon, T. & Stickland, M., 2011a. A one-dimensional numerical model for the momentum exchange in regenerative pumps. *J. Eng. Gas Turbines Power*, 133(9).

- Quail, F., Scanlon, T. & Stickland, M., 2011b. Design optimisation of a regenerative pump using numerical and experimental techniques. *Int J Number Method H*, 21(1), pp. 95-111.
- Quail, F., Scanlon, T. & Strickland, M., 2010b. Development of a regenerative pump impeller using rapid manufacturing techniques. *Rapid Prototyping Journal*, 16(5), pp. 337-344.
- Quail, F., Stickland, M. & Baumgartner, A., 2010a. *Design study of a novel regenerative pump using experimental and numerical techniques*. Edinburgh, s.n.
- Quail, F., Stickland, M. & Scanlon, T., 2010c. *Numerical and experimental design study of a regenerative pump*. London, AIP Conference Proceedings, pp. 165-180.
- Raheel, M. & Engeda, A., 2002. *Current Status, Design and Performance Trends for the Regenerative Flow Compressors and Pumps*. s.l., s.n., pp. 99-110.
- Raheel, M. & Engeda, A., 2005. Systematic Design Approach for Radial Blade Regenerative Turbomachines. *J Propul Power*, 21(5), pp. 884-892.
- Roache, P. J., 1994. Perspective: A Method for Uniform Reporting of Grid Refinement Studies. *ASME J. Fluids Eng.*, 116(3), pp. 405-413.
- Roth Pump Company, 2015. *Bulletin 1C99: Regenerative Turbine Chemical Pumps for the Process Industry*. [Online] Available at: <http://www.rothpump.com/technical.html> [Accessed 6 August 2015].
- Schlichting, H., Gersten, K., Krause, E. & Oertel, H., 1955. *Boundary layer theory*. 7th ed. New York: McGraw-Hill.
- Senoo, Y., 1948. Theoretical research on friction pump. *Institute of Fluid Engineering*, 5(1), pp. 23-48.
- Senoo, Y., 1954. Influences of the suction nozzle on characteristics of peripheral pump and an effective method of their removal. *Rep Res Inst Appl Mech*, 3(11).
- Senoo, Y., 1956. A comparison of regenerative pump theories supported by new performance data. *Trans ASME*, Volume 78, pp. 1091-1102.
- Shimosaka, M., 1960. Research on the characteristics of regenerative pump. *Bull of JSME*, 3(10), pp. 191-199.
- Shimosaka, M. & Yamazaki, S., 1960. Research on the characteristics of regenerative pump. *Bull of JSME*, 3(10), pp. 185-190.
- Shirinov, A. & Oberbeck, S., 2011a. *Optimisation of the high vacuum side channel pump*. London, UK, IMechE.
- Shirinov, A. & Oberbeck, S., 2011b. High vacuum side channel pump working against atmosphere. *Vacuum*, 85(12), pp. 1174-1177.
- Sixsmith, H., 1981. *The theory and design of a regenerative compressor*, Surrey: Wallington.
- Sixsmith, H. & Altmann, H., 1977. A regenerative compressor. *Trans ASME*, 99(3), pp. 637-647.
- Škerlavaj, A., Škerget, L., Ravnik, J. & Lipej, A., 2011. Choice of a turbulence model for pump intakes. *Proceedings of the Institution of Mechanical Engineers, Part A: Journal of Power and Energy*, 225(6), pp. 764-778.

- Song, J., Engeda, A. & Chung, M., 2003. A modified theory for the flow mechanism in a regenerative flow pump. *Proceedings of the Institution of Mechanical Engineers, Part A: Journal of Power and Energy*, 217(3), pp. 311-321.
- Song, J., Raheel, M. & Engeda, A., 2003. A compressible flow theory for regenerative compressors with aerofoil blades. *Proc. IMechE Part, C: J. Mechanical Engineering Science*, Volume 217, pp. 1241-1257.
- Spence, R. & Amaral-Teixeira, J., 2008. Investigation into pressure pulsations in a centrifugal pump using numerical methods supported by industrial tests. *Computers & Fluids Journal*, 37(6), pp. 690-704.
- Spence, R. & Amaral-Teixeira, J., 2009. A CFD parametric study of geometrical variations on the pressure pulsations and performance characteristics of a centrifugal pump. *Computers & Fluid Journal*, 38(6), pp. 1243-1257.
- Tomita, Y., Yamazaki, S. & Sasahara, T., 1973. The scale effect and design method of the regenerative pump with non-radial vanes. *Bull of JSME*, 16(98), pp. 1176-1183.
- Versteeg, H. & Malalasekera, W., 2007. *An Introduction to Computational Fluid Dynamics*. 2nd ed. Harlow, UK.: Pearson Education Limited.
- Vorburger, T. V. & Raja, J., 1990. *Surface Finish Metrology Tutorial*, Gaithersburg, MD, US: National Institute of Standards and Technology.
- Weise, V. & Beilke, J., 1998. 3D flow in a peripheral fan. *International Journal of Computer Applications in Technology*, 11(3-5), pp. 203-210.
- Wendt, J. F. e., 2008. *Computational fluid dynamics: an introduction*. s.l.:Springer Science & Business Media.
- Wilson, W., Santalo, M. & Oelrich, J., 1955. A theory of the fluid dynamic mechanism of regenerative pumps. *Trans ASME*, 77(8), pp. 1303-1316.
- Yamazaki, S. & Tomita, Y., 1971. Research on the performance of the regenerative pump with non-radial vanes. *Bull of JSME*, 14(77), pp. 1178-1186.
- Yamazaki, S., Tomita, Y. & Sasahara, T., 1972. Research on the performance of the regenerative pump with non-radial vanes. *Bull of JSME*, 15(81), pp. 337-343.
- Yamazaki, S. & Y, T., 1974. Research on the performance of the regenerative pump with non-radial vanes. *Bull of JSME*, 17(104), pp. 459-466.
- Yoo, I., Park, M. & Chung, M., 2005. Improved momentum exchange theory for incompressible regenerative turbomachines. *Proc. IMechE, Part A: J Power and Energy*, 219(7), pp. 567-581.
- Zhang, F., Fleder, A., Böhle, M. & Yuan, S., 2016. Effect of suction side blade profile on the performance of a side channel pump. *J Power and Energy*, 0(0), pp. 1-12.
- Zozulya, I., 1982. Effect of the indentation profile shape on the regenerative-pump parameters. *Chemical and Petroleum Engineering*, 18(6), pp. 224-226.